



Institut für Erd- und Umweltwissenschaften
Mathematisch-Naturwissenschaftliche Fakultät
Universität Potsdam



Signals stored in sediment

Fluvial sediments as records of landscape evolution

Stefanie Tofelde

Kumulative Dissertation

zur Erlangung des akademischen Grades

"doctor rerum naturalium" (Dr. rer. nat.)

in der Wissenschaftsdisziplin "Geologie"

eingereicht an der

Mathematisch-Naturwissenschaftlichen Fakultät

Institut für Erd- und Umweltwissenschaften

der Universität Potsdam

Potsdam, November 2018

Published online at the
Institutional Repository of the University of Potsdam:
<https://doi.org/10.25932/publishup-42716>
<https://nbn-resolving.org/urn:nbn:de:kobv:517-opus4-427168>

Erklärung zur Eigenständigkeit

Hiermit erkläre ich, dass ich die Dissertation „*Signals stored in sediment - Fluvial sediments as records of landscape evolution*“ selbstständig angefertigt und keine anderen, als die von mir angegebenen Quellen und Hilfsmittel verwendet habe.

Die Stellen der Dissertation, die anderen Quellen entnommen wurden, sind durch Angaben der Herkunft kenntlich gemacht.

Bereits in einer Fachzeitschrift publizierte oder zur Publikation eingereichte Kapitel sind eindeutig gekennzeichnet.

Ich erkläre weiterhin, dass die Dissertation bisher nicht in dieser oder anderer Form in einem anderen Prüfungsverfahren vorgelegt wurde.

Potsdam, 26. November 2018

Stefanie Tofelde

Acknowledgments

I am deeply thankful to so many people who have contributed to this thesis in one or the other way. Clearly, without your help and support, this thesis would not have been realized.

First and foremost, I would like to thank my main supervisor, Taylor Schildgen, for her continuous support, her patience, the constructive and fast feedback at any time, and the endless proof-reading. Thank you, for the confidence and trust you placed in me and the freedom to always follow my own ideas! I would like to thank my second supervisor, Manfred Strecker, first of all for his engagement for my admission to the geoscience master program in Potsdam despite my non-geoscientific background. Without that opportunity, this thesis would have never been written. Also, for his continuous encouragement, support and guidance through the Andes in Argentina.

I would like to thank two of my co-authors, Andy Wickert and Sara Savi, with whom I spent weeks in the field, in the chemistry lab or at SAFL shuffling sand and dyeing water. It has been a joy! Thanks for your endless time of discussing data, ideas and solve any kind of problems.

I would also like to thank Heiko Pingel, Alexander Rohrmann, Yanina Rojo, Walter Düsing, Philipp Weissmann and Ricardo Alonso for all their support during field work in Argentina. For your efforts in getting permissions, finding places to stay even in the most remote areas and of course for your help in collecting all the samples and discussing ideas in the field.

The preparation and analysis of the samples in the laboratory would not have been possible without the help and support of Hella Wittmann, Catrin Schulz, Martin Lang, Philine Thöle, Lilian Pollozek, Jan Schürmann and Anna Rosner.

I am very thankful to Niels Hovius for his open door, his encouragement and the honest feedback and discussions.

I would like to thank the entire section 5.1 for the fun times and their valuable feedback on data, ideas or presentations. In particular, I would like to thank Jens Turowski for his willingness to discuss and help at any time. And Duna Roda-Boluda, Mitch D'Arcy and Aaron Bufe, thank you for your friendship.

Thomas, Anne, Mara, Janosch, Klaus, Tina, Maré, Stevie, Katrin and Richard - life in Potsdam wouldn't have been the same without you, you made it a home.

And finally, I would like thank my parents, Monika and Rolf, my brother Michael, and Georg for their endless support, trust and love at any time. Thanks for always making me feel I can and should do what makes me happy.

Table of Contents

Table of Contents	IV
List of Figures	VIII
List of Tables	X
List of Abbreviations	XI
Abstract.....	XIII
Zusammenfassung.....	XV
1. Introduction.....	1
1.1. Sediment routing system	2
1.2. Sediment characteristics & Signal propagation	4
1.2.1. Sediment geochemical composition (^{10}Be).....	5
1.2.2. Sediment discharge (Q_s).....	8
1.3. Channel profiles and fluvial fill terraces	10
1.3.1. From boundary conditions to channel responses and terrace formation	10
1.3.2. Reconstructions of boundary conditions from fill terraces	14
1.4. Emerging research questions	16
1.5. Thesis structure	18
1.6. Publications and author contributions	19
2. ^{10}Be concentrations in fluvial sand and gravel.....	22
2.1. Introduction.....	23
2.2. Study area.....	26
2.3. Methods.....	26
2.3.1. Cosmogenic radionuclide analysis.....	26
2.3.2. Hillslope-process inventory	28

2.3.3.	Topographic analysis	30
2.4.	Results.....	30
2.4.1.	Denudation rates and hillslope processes.....	30
2.4.2.	Normalized sand-gravel index	32
2.5.	Discussion	33
2.5.1.	Correlation between denudation rates and hillslope processes	33
2.5.2.	Normalized sand-gravel index	34
2.6.	Conclusion	40
3.	Terrace formation and channel response to external perturbation	42
3.1.	Introduction.....	43
3.2.	Formation of fluvial fill terraces	45
3.2.1.	Sediment to water discharge ratio ($Q_{s,in}/Q_w$).....	45
3.2.2.	Base-level change	46
3.2.3.	Complex response and autogenic processes	46
3.3.	Methods.....	47
3.4.	Results.....	51
3.5.	Discussion	58
3.5.1.	Channel response to perturbations and conditions of terrace formation	58
3.5.2.	Preservation of channel profiles.....	60
3.5.3.	Differences in terrace surface slopes	62
3.5.4.	Signal propagation and implications for stratigraphy	63
3.6.	Summary and Conclusions.....	66
4.	Fluvial fill terraces in the Quebrada del Toro	69
4.1.	Introduction.....	70
4.2.	Study area.....	73

4.2.1.	Geological and geomorphic setting.....	73
4.2.2.	Climatic setting	74
4.3.	Methods.....	76
4.3.1.	Cosmogenic radionuclide dating.....	76
4.3.2.	U-Pb zircon geochronology	77
4.4.	Results.....	78
4.4.1.	Terrace tread exposure dating.....	78
4.4.2.	Depositional ages	81
4.5.	Discussion	82
4.5.1.	Reliability and interpretation of terrace exposure	82
4.5.2.	Cut-and-fill cycles within the Toro Basin.....	82
4.5.3.	Potential causes of terrace formation	85
4.5.4.	Impacts of global climate change on sedimentary systems	88
4.6.	Conclusions.....	90
5.	Discussion and Synthesis	92
5.1.	Summary of key findings.....	93
5.2.	Fluvial fill terraces	94
5.2.1.	First insights on terrace formation in the Quebrada del Toro	94
5.2.2.	Reconstruction of paleo sediment supply ($Q_{s,in}$)	96
5.2.3.	Reconstruction of paleo water discharge (Q_w).....	100
5.2.4.	Concluding remarks on terrace formation in the Quebrada del Toro	108
5.3.	Signal propagation in fluvial sediments.....	109
5.3.1.	Chemical composition (^{10}Be) signals.....	109
5.3.2.	Sediment discharge (Q_s) signals.....	113
5.4.	Emerging research questions	117

6. Bibliography	119
Appendix A	140
Appendix B	149
Appendix C	156

List of Figures

Fig. 1.1 Sediment routing system, sediment characteristics & signal propagation..	3
Fig. 1.2 Photo of the train bridge crossing the Yacoraite river in the Quebrada de Humahuaca.....	11
Fig. 1.3 Mechanisms of fluvial fill terrace formation.....	12
Fig. 1.4 Photo of the fluvial cut-and-fill terrace sequence in the Quebrada del Toro.....	15
Fig. 2.1 Schematic diagram showing the derivation of the normalized sand-gravel index (<i>NSGI</i>) and hypothesized dependence on erosion processes..	24
Fig. 2.2 Geological map of the Quebrada del Toro.	25
Fig. 2.3 The hillslope-process inventory is based on mapping in Google Earth.	29
Fig. 2.4 Sampling sites for detrital sand and gravel.....	31
Fig. 2.5 Relationship between <i>NSGI</i> values and catchment	35
Fig. 2.6 Slope distributions of the five mapped hillslope processes	36
Fig. 2.7 The evolution of [¹⁰ Be] in sand and gravel during transport and storage within the catchment. ...	37
Fig. 2.8 Comparison of <i>NSGI</i> and catchment morphological parameters	39
Fig. 3.1 Experimental setup, data collection and analysis.	48
Fig. 3.2 Fill terraces formed during experimental runs.	51
Fig. 3.3 Evolution of cross-sections in the upper part of the reach.....	52
Fig. 3.4 Evolution of longitudinal river profiles.....	53
Fig. 3.5 Input parameters and evolution of channel slope, channel width and sediment discharge at the outlet during the experiments.	56
Fig. 3.6 Elevation profile and slope comparison of terrace surfaces and active channels.	57
Fig. 3.7 Schematic model of the evolution of signals at the outlet stored in either sediment volume or the chemical composition of the sediment.	64
Fig. 4.1 Rainfall of the Central Andes and regional topography of NW Argentina.	71
Fig. 4.2 Detailed overview of the Toro Basin and the fill terraces.....	72
Fig. 4.3 Field pictures of the Terrace Conglomerates.....	75
Fig. 4.4 Distribution of ¹⁰ Be concentration with depth for the nine profiles and sedimentary logs of the sampled pit walls.....	79
Fig. 4.5 Simplified overview of the spatial sample distribution and the temporal evolution of the fill terraces.....	83
Fig. 4.6 Comparison of aggradation and incision phases in the Toro Basin with regional and global climate proxies.....	87
Fig. 4.7 Correlation of recorded climate cyclicality and river length.	89

Fig. 5.1 Modern versus paleo-denudation rates in the Quebrada del Toro.....	99
Fig. 5.2 Discharge measurements at Campo Quijano and estimated annual mean discharge for the CRN sampling locations.....	103
Fig. 5.3 Paleo Q_w reconstructions from terrace surface slopes and CRN-derived paleo- Q_s estimates.	105
Fig. 5.4 Quantitative paleo-hydrological reconstructions from the Central and Eastern Andes.....	107
Fig. 5.5 Summary on new insights into signal propagation.....	110
Fig. A1 Basin mean denudation rates compared to topographic and climatic parameters.	143
Fig. A2 Geological maps of all sampled catchments.....	147
Fig. A3 ^{10}Be concentration of the sand and gravel pairs compared to median basin slope..	148
Fig. C1 Field photos of the four $^{26}\text{Al}/^{10}\text{Be}$ burial sites..	159
Fig. C2 Overview of the three different approaches for the terrace surface age estimations.....	160
Fig. C3 Age-frequency plots of the ^{10}Be depth-profiles.....	161
Fig. C4 Height of the terrace surfaces above the current channel compared to their exposure age.	162

List of Tables

Table 2.1 Cosmogenic nuclide samples.	27
Table 3.1 Water and sediment inputs to the experiments.	49
Table 4.1 Summary of terrace surface exposure ages based on the three different approaches.	80
Table 4.2 Burial ages based on paired ^{10}Be and ^{26}Al measurements.	81
Table 5.1 Cosmogenic nuclide samples for calculation of paleo-denudation rates.	97
Table 5.2 Calculation of paleo-discharge from terraces in the Quebrada del Toro.	102
Table A1 Surface area affected by each of the mapped hillslope processes.	140
Table A2 Topographic and climatic characteristics of the catchments.	143
Table A3 Detailed list of cosmogenic nuclide studies that have measured ^{10}Be concentrations in a sand and a gravel fraction for the same location.	144
Table B1 Evolution of height, slope and sediment discharge at the outlet in the Ctrl_1 experiment.	149
Table B2 Evolution of height, slope and sediment discharge at the outlet in the Ctrl_2 experiment.	150
Table B3 Evolution of height, slope and sediment discharge at the outlet in the IQ_w experiment.	151
Table B4 Evolution of height, slope and sediment discharge at the outlet in the DQ_w _ IQ_w experiment.	152
Table B5 Evolution of height, slope and sediment discharge at the outlet in the $\text{DQ}_{s,\text{in}}$ experiment.	153
Table B6 Evolution of height, slope and sediment discharge at the outlet in the $\text{IQ}_{s,\text{in}}$ _ $\text{DQ}_{s,\text{in}}$ experiment.	154
Table B7 Evolution of height, slope and sediment discharge at the outlet in the BLF experiment.	155
Table C1 Depth profile samples.	163
Table C2 Burial samples.	164
Table C3 ^{10}Be and ^{26}Al blanks processed during sample preparation.	165
Table C4 Terrace surface ages calculated with the Monte Carlo depth profile simulator based on the ‘St’-scaling-scheme.	165
Table C5 Terrace surface ages calculated with the Monte Carlo simulator based on the calculated ‘Lm’-scaling-scheme.	166
Table C6 Comparison of muogenic and spallogenic production rates.	167
Table C7 Terrace surface ages based on the surface-pebbles samples.	167
Table C8 Raw data of volcanic ash zircon grains.	168

List of Abbreviations

$[^{10}\text{Be}]$	^{10}Be concentration [atoms/g]
$[^{10}\text{Be}]_{\text{gravel}}$	^{10}Be concentration in the gravel fraction [atoms/g]
$[^{10}\text{Be}]_{\text{sand}}$	^{10}Be concentration in the sand fraction [atoms/g]
AMS	Accelerator mass spectrometer
BLF	Base-level fall
C_0	Concentration at the surface [atoms/g]
CRN	Cosmogenic radio nuclide
DEM	Digital elevation model
ε	Catchment-mean denudation rate [mm/yr]
ε	Excess shear stress at bankfull flow [-]
GSD	Grain-size distribution
I	Intermittency [-]
k_b	Threshold river-width coefficient [-]
k_{Qs}	Sediment discharge coefficient ($=k_{qs} k_b$) [-]
k_{qs}	Specific sediment-discharge coefficient [-]
k_{sn}	Normalized channel-steepness index (slope-area coefficient) [$\text{m}^{2\theta}$]
NSGI	Normalized sand-gravel index
OSL	Optically stimulated luminescence
$P(\mu)$	Muon production rate [atm/(g yr)]
$P(sp)$	Spallation production rate [atm/(g yr)]
P_0	Production rate at the surface [atm/(g yr)]
Q_s	Sediment discharge or sediment supply [m^3/s]
$Q_{s,in}$	Sediment supply at the inlet of a reach [m^3/s]

$Q_{s,out}$	Sediment supply at the outlet of a reach [m^3/s]
Q_w	Water discharge [m^3/s]
S	Slope [-]
<i>SALLJ</i>	South American low-level jet
<i>SASM</i>	South American Summer Monsoon
<i>TCN</i>	Terrestrial cosmogenic nuclide
w	Channel width [m]
λ	^{10}Be decay rate [atoms/(g yr)]
A	Attenuation coefficient [g/cm^2]
ρ	Density [g/cm^3]
τ_b	Basal shear stress at bankfull discharge [Pa]
τ_c	Critical shear stress [Pa]

Abstract

Tectonic and climatic boundary conditions determine the amount and the characteristics (size distribution and composition) of sediment that is generated and exported from mountain regions. On millennial timescales, rivers adjust their morphology such that the incoming sediment ($Q_{s,in}$) can be transported downstream by the available water discharge (Q_w). Changes in climatic and tectonic boundary conditions thus trigger an adjustment of the downstream river morphology. Understanding the sensitivity of river morphology to perturbations in boundary conditions is therefore of major importance, for example, for flood assessments, infrastructure and habitats. Although we have a general understanding of how rivers evolve over longer timescales, the prediction of channel response to changes in boundary conditions on a more local scale and over shorter timescales remains a major challenge. To better predict morphological channel evolution, we need to test (i) how channels respond to perturbations in boundary conditions and (ii) how signals reflecting the persisting conditions are preserved in sediment characteristics. This information can then be applied to reconstruct how local river systems have evolved over time.

In this thesis, I address those questions by combining targeted field data collection in the Quebrada del Toro (Southern Central Andes of NW Argentina) with cosmogenic nuclide analysis and remote sensing data. In particular, I (1) investigate how information on hillslope processes is preserved in the ^{10}Be concentration (geochemical composition) of fluvial sediments and how those signals are altered during downstream transport. I complement the field-based approach with physical experiments in the laboratory, in which I (2) explore how changes in sediment supply ($Q_{s,in}$) or water discharge (Q_w) generate distinct signals in the amount of sediment discharge at the basin outlet ($Q_{s,out}$). With the same set of experiments, I (3) study the adjustments of alluvial channel morphology to changes in Q_w and $Q_{s,in}$, with a particular focus in fill-terrace formation. I transfer the findings from the experiments to the field to (4) reconstruct the evolution of a several-hundred meter thick fluvial fill-terrace sequence in the Quebrada del Toro. I create a detailed terrace chronology and perform reconstructions of paleo- Q_s and Q_w from the terrace deposits. In the following paragraphs, I summarize my findings on each of these four topics.

First, I sampled detrital sediment at the outlet of tributaries and along the main stem in the Quebrada del Toro, analyzed their ^{10}Be concentration ($[^{10}\text{Be}]$) and compared the data to a detailed hillslope-process inventory. The often observed non-linear increase in catchment-mean denudation rate (inferred from $[^{10}\text{Be}]$ in fluvial sediment) with catchment-median slope, which has commonly been explained by an adjustment in landslide-frequency, coincided with a shift in the main type of hillslope processes. In addition, the $[^{10}\text{Be}]$ in fluvial sediments varied with grain-size. I defined the normalized sand-gravel-index (*NSGI*) as the ^{10}Be -concentration difference between sand and gravel fractions divided by their summed concentrations. The *NSGI* increased with median catchment slope and coincided with a shift in the prevailing hillslope processes

active in the catchments, thus making the *NSGI* a potential proxy for the evolution of hillslope processes over time from sedimentary deposits. However, the *NSGI* recorded hillslope-processes less well in regions of reduced hillslope-channel connectivity and, in addition, has the potential to be altered during downstream transport due to lateral sediment input, size-selective sediment transport and abrasion.

Second, my physical experiments revealed that sediment discharge at the basin outlet ($Q_{s,out}$) varied in response to changes in $Q_{s,in}$ or Q_w . While changes in Q_w caused a distinct signal in $Q_{s,out}$ during the transient adjustment phase of the channel to new boundary conditions, signals related to changes in $Q_{s,in}$ were buffered during the transient phase and likely only become apparent once the channel is adjusted to the new conditions. The temporal buffering is related to the negative feedback between $Q_{s,in}$ and channel-slope adjustments. In addition, I inferred from this result that signals extracted from the geochemical composition of sediments (e.g., [^{10}Be]) are more likely to represent modern-day conditions during times of aggradation, whereas the signal will be temporally buffered due to mixing with older, remobilized sediment during times of channel incision.

Third, the same set of experiments revealed that river incision, channel-width narrowing and terrace cutting were initiated by either an increase in Q_w , a decrease in $Q_{s,in}$ or a drop in base level. The lag-time between the external perturbation and the terrace cutting determined (1) how well terrace surfaces preserved the channel profile prior to perturbation and (2) the degree of reworking of terrace-surface material. Short lag-times and well preserved profiles occurred in cases with a rapid onset of incision. Also, lag-times were synchronous along the entire channel after upstream perturbations (Q_w , $Q_{s,in}$), whereas base-level fall triggered an upstream migrating knickzone, such that lag-times increased with distance upstream. Terraces formed after upstream perturbations (Q_w , $Q_{s,in}$) were always steeper when compared to the active channel in new equilibrium conditions. In the base-level fall experiment, the slope of the terrace-surfaces and the modern channel were similar. Hence, slope comparisons between the terrace surface and the modern channel can give insights into the mechanism of terrace formation.

Fourth, my detailed terrace-formation chronology indicated that cut-and-fill episodes in the Quebrada del Toro followed a ~ 100 -kyr cyclicity, with the oldest terraces ~ 500 kyr old. The terraces were formed due to variability in upstream Q_w and Q_s . Reconstructions of paleo- Q_s over the last 500 kyr, which were restricted to times of sediment deposition, indicated only minor (up to four-fold) variations in paleo-denudation rates. Reconstructions of paleo- Q_w were limited to the times around the onset of river incision and revealed enhanced discharge from 10 to 85% compared to today. Such increases in Q_w are in agreement with other quantitative paleo-hydrological reconstructions from the Eastern Andes, but have the advantage of dating further back in time.

Zusammenfassung

Tektonische und klimatische Bedingungen bestimmen die Menge, Größenverteilung und Zusammensetzung von Sedimenten, welche in Gebirgsregionen produziert und von dort exportiert werden. Über Jahrtausende hinweg passen Flüsse ihre Morphologie an, um den Sedimenteintrag ($Q_{s,in}$) mit dem verfügbaren Wasserabfluss (Q_w) flussabwärts zu transportieren. Änderungen in den klimatischen oder tektonischen Randbedingungen lösen flussabwärts eine Anpassung der Flussmorphologie aus. Ein besseres Verständnis darüber, wie sensitiv Flüsse auf Perturbationen in den Randbedingungen reagieren, ist entscheidend, um beispielsweise Überflutungspotential besser abschätzen zu können. Obwohl wir generell ein gutes Verständnis für die Entwicklung von Flüssen auf langen Zeitskalen haben, können wir durch veränderte Randbedingungen ausgelöste Flussdynamiken lokal und auf kurzen Zeitskalen nur schwer vorhersagen. Um die Entwicklung der Flussmorphologie besser zu verstehen, beziehungsweise vorhersagen zu können, müssen wir testen, (1) wie Flüsse auf veränderte Randbedingungen reagieren und (2) wie Signale, welche die vorherrschenden Bedingungen reflektieren, in Sedimenten konserviert werden. Diese Informationen können wir nutzen, um die Entwicklung von lokalen Flusssystemen zu rekonstruieren.

In der vorliegenden Arbeit adressiere ich diese Fragen durch die Analyse von kosmogenen Nukleiden und Fernerkundungsdaten in der Quebrada del Toro (südliche Zentralanden in NW Argentinien). Insbesondere untersuche ich, wie (1) Informationen über Hangprozesse in der ^{10}Be Konzentration (geochemische Zusammensetzung) von Flusssedimenten gespeichert werden und wie diese Signale durch den Transport flussabwärts überprägt werden. Ich ergänze diesen geländebasierten Ansatz mit physikalischen Experimenten im Labor, mit welchen ich untersuche, wie (2) Veränderungen in der Sedimentzufuhr ($Q_{s,in}$) oder der Abflussmenge (Q_w) eindeutige Signale in der Menge an Sedimentaustag ($Q_{s,out}$) am Beckenauslass generieren. Mit denselben Experimenten untersuche ich (3) die Anpassung der Flussmorphologie auf Veränderungen in Q_w und $Q_{s,in}$ mit einem speziellen Fokus auf der Entstehung von Flussterrassen. Ich übertrage die Erkenntnisse von den Experimenten ins Gelände und (4) rekonstruiere die Entstehung von einer mehreren hundert Meter mächtigen Terrassensequenz in der Quebrada del Toro. Ich erstelle eine detaillierte Terrassenchronologie und führe mit Hilfe der Terrassenablagerungen Rekonstruktion von Q_s und Q_w für die Vergangenheit durch. In den folgenden Paragraphen fasse ich meine Ergebnisse zu den vier Forschungsschwerpunkten dieser Arbeit zusammen.

Erstens habe ich Flusssedimente an den Mündungen von Nebenflüssen, sowie entlang des Hauptflusses in der Quebrada del Toro beprobt, die jeweilige ^{10}Be Konzentration ($[^{10}\text{Be}]$) bestimmt und die Daten mit einem detaillierten Hangprozess-Inventar verglichen. Der häufig beobachtete, nicht-lineare Anstieg der durchschnittlichen Denudationsrate des Einzugsgebietes (abgeleitet aus der $[^{10}\text{Be}]$ der Flusssedimente) mit der Hangneigung eines Einzugsgebietes fiel mit einer Verschiebung der wesentlichen,

aktiven Hangprozesse zusammen. Zusätzlich variierte die [^{10}Be] der Flusssedimente mit den Korngrößen. Ich habe den normalisierten Sand-Schotter-Index (*NSGI*) definiert, welcher sich aus der Differenz der [^{10}Be] zwischen der Sand- und der Kiesfraktion, geteilt durch ihre summierte Konzentration, berechnet. Der *NSGI* stieg mit dem Median der Hangneigung eines Einzugsgebietes und fiel wiederum mit einer Verschiebung der vorherrschenden Hangprozesse im jeweiligen Einzugsgebiet zusammen. Diese Beobachtung qualifiziert den *NSGI* als einen potentiellen Proxy, um die Entwicklung von Hangprozessen über die Zeit aus Sedimentablagerungen zu rekonstruieren. Es ist jedoch einzuschränken, dass der *NSGI* durch den Transport flussabwärts auf Grund von temporärer Sedimentablagerung, lateraler Sedimentzufuhr, größenselektivem Sedimenttransport und Abrasion überprägt werden kann.

Zweitens haben die Laborexperimente gezeigt, dass der Sedimentaustrag am Beckenauslass ($Q_{s,out}$) auf Grund von Veränderungen in $Q_{s,in}$ oder Q_w variiert. Während Veränderungen in Q_w ein eindeutiges Signal in $Q_{s,out}$ während der transienten Anpassungsphase des Flusses an die neuen Randbedingungen hervorriefen, wurden durch $Q_{s,in}$ ausgelöste Signale während der transienten Anpassungsphase gepuffert. Sie werden vermutlich erst sichtbar, nachdem der Fluss sich an die neuen Randbedingungen angepasst hat. Das zeitliche Puffern ist mit der negativen Rückkopplung zwischen $Q_{s,in}$ und dem Flussgradienten zu erklären. Zusätzlich deuten die Ergebnisse darauf hin, dass sich Signale, welche in der geochemischen Zusammensetzung von Sediment gespeichert sind (z.B. [^{10}Be]), in Phasen der Flussaufsotterung mit einer höheren Wahrscheinlichkeit die heutigen Bedingungen repräsentieren. Dagegen sind Signale in Zeiten der Flusseinschneidung aufgrund von Mischung mit älteren, remobilisierten Sedimenten gepuffert.

Drittens haben dieselben Experimente gezeigt, dass Flusseinschneidung, Flussbettverengung sowie Terrassenbildung entweder durch eine Zunahme an Q_w , eine Abnahme in $Q_{s,in}$ oder durch ein Absinken der Flussbasis initiiert werden konnte. Die Zeitverzögerung zwischen der Perturbation der Randbedingungen und der Terrassenformation bestimmt (1) wie gut Terrassenoberflächen das Flussprofil vom Zeitpunkt unmittelbar vor der Störung repräsentieren und (2) den Grad an Umschichtung des Terrassenoberflächenmaterials. Kurze Verzögerungszeiten und gut erhaltende Profile konnten in Fällen eines schnellen Einsetzens der Flusseinschneidung beobachtet werden. Außerdem waren die Verzögerungszeiten entlang des Flusslaufes synchron im Falle einer Perturbation im Flussoberlauf (Q_w , $Q_{s,in}$), während ein Abfallen der Flussbasis einen flussaufwärts migrierenden Knickpunkt ausgelöst hat, sodass die Verzögerungszeiten in flussaufwärts Richtung zunahmten. Terrassen, welche durch Perturbationen im Flussoberlauf (Q_w , $Q_{s,in}$) gebildet wurden, waren steiler im Vergleich zum aktiven Fluss, nachdem dieser sich an die neuen Randbedingungen angepasst hat. In dem Experiment, bei welchem die Flussbasis abgesenkt wurde, waren die Neigung der Terrassenoberflächen und des aktiven Flussesbettes

ähnlich. Daher können Vergleiche zwischen der Neigung der Terrassenoberflächen mit dem aktiven Flussbett auf den Mechanismus der Terrassenformation hinweisen.

Viertens hat die detaillierte Terrassenchronologie gezeigt, dass die Einschneide- und Ablagerungsepisoden in der Quebrada del Toro einem ~100 ka Zyklus folgen, beginnend mit der ersten Terrasse vor ca. 500 ka. Die Terrassen wurden durch Variabilität in Q_w und $Q_{s,in}$ gebildet. Rekonstruktionen von Q_s über die letzten 500 ka, beschränkt auf die Zeiten von Sedimentablagerung, zeigten eine eher geringe Variabilität (maximal vierfach) in Denudationsraten an. Rekonstruktionen des Abflusses waren beschränkt auf die Zeitpunkte um das Einsetzen der Flusseinschneidung herum und deuteten auf vermehrten Abfluss zwischen 10 und 85% im Vergleich zu heutigen Bedingungen hin. Vermehrter Abfluss in dieser Größenordnung stimmt mit anderen quantitativen Rekonstruktionen zur Hydrologie der Ost-Anden überein, diese Methode hat jedoch den Vorteil, dass sie zeitlich weiter zurück reicht.

1. Introduction

The Earth's surface is continuously reshaped by processes that create and destroy topographic relief. Over geological timescales tectonic processes generate relief through a combination of tectonic uplift and subsidence (Suess, 1875; Wilson, 1968). The created relief can be strongly modified by denudation – the transformation of solid rock into sediment and the subsequent removal of sediment from its site of production – with higher relief generally causing faster denudation rates (Ahnert, 1970; Davis, 1899; Gilbert, 1877; Milliman and Syvitski, 1992). The rate of erosion may additionally be strongly affected by climate (Bookhagen and Strecker, 2012; DiBiase and Whipple, 2011; Huntington, 1907; Lague et al., 2005; Moon et al., 2011; Penck and Brückner, 1909; Roe et al., 2008). As such, tectonic and climatic boundary conditions determine the amount and also the characteristics (size distribution, composition) of sediment that is generated and removed from mountain regions. On millennial timescales (10^3 - 10^6) rivers adjust their morphology such that the incoming sediment can be transported downstream by the available water discharge (Blom et al., 2017, 2016; Lane, 1955; Mackin, 1948; Schumm, 1977; Wickert and Schildgen, 2018). As rivers are sensitive to variability in boundary conditions, changes in incoming sediment or water have a fundamental control on downstream river morphology (Allen et al., 2013; Church, 2006; Fryirs, 2017; Sinha and Friend, 1994). On human timescales, the evolution of river channel morphology is of great importance for flood assessments, infrastructure but also riparian and aquatic habitats (see review by Buffington, 2012). Although we have a general understanding of how rivers will respond to changes in sediment supply and/or water discharge on longer timescales, predicting how changes in boundary conditions will affect the course of a river on a local scale and over short time periods remains a major challenge.

If boundary conditions change, rivers require time to adjust to the new conditions (Allen, 2008a; Allen and Densmore, 2000; Castelltort and Van Den Driessche, 2003; Howard, 1982; Métivier and Gaudemer, 1999; Paola et al., 1992a; Simpson and Castelltort, 2012). A major challenge in predicting channel response to changes in boundary conditions is that during those phases of adjustment – transient phases – rivers can behave differently compared to equilibrium phases, when they are adjusted to the persisting conditions (Bull, 1991; Mackin, 1948). An additional complexity is the degree of freedom of the morphological change. Gravel-bed rivers, for example, can adjust their slope, their width and depth, but also their grain size distribution or channel roughness following a change in forcing (Buffington, 2012; Church, 1995; Dade et al., 2011; Lane, 1955; Schumm, 1977). Furthermore, neither sediment transport by rivers (Coulthard and Wiel, 2007; Jerolmack and Paola, 2010; Romans et al., 2016; Van de Wiel and Coulthard, 2010) nor denudation on hillslopes (Bennett et al., 2016; Binnie et al., 2007; Burbank et al.,

1996; DiBiase and Whipple, 2011; Larsen and Montgomery, 2012; Ouimet et al., 2009) are linear processes, but instead are commonly controlled by internal system threshold behavior (Schumm, 1979, 1973).

Although there have been a great advances in the modelling of landscape evolution in response to changes in boundary conditions (e.g., Braun et al., 2015; Coulthard et al., 2005; Godard et al., 2013; Simpson and Castellort, 2012; Tucker and Slingerland, 1997; Wobus et al., 2006), the models do not incorporate all the complexities listed above. To better understand how landscapes respond to changes in boundary conditions even on shorter timescales, there is a need for empirical studies that quantify hillslope and channel responses of landscapes to changes in boundary conditions either through space or time. High mountain landscapes, as for example the Andes, offer a great opportunity for such work, as they experience strong topographic and climatic gradients over relatively short distances. In additions, the presence of fluvial fill terraces – the remnants of former channel floodplains – indicate that past boundary conditions substantially differed from today and can be potentially reconstructed from those terraces (e.g., Bookhagen et al., 2006; Litty et al., 2016; Poisson and Avouac, 2004; Schaller et al., 2004).

In this thesis, I address these challenges by investigating hillslope processes, sediment discharge, and the formation of fluvial fill terraces in the Quebrada del Toro, an intermontane basin in the southern Central Andes of NW Argentina. I combine targeted field data collection, cosmogenic nuclide analysis and remote-sensing data in my field area to gain insights that I further complement with physical laboratory experiments.

A broad background to this work is laid out in sections 1.1 to 1.3 of this introductory chapter, which serves as a general introduction that is not particularly tailored to the Andes. The emerging research aims and questions are summarized in section 1.4 and an overview of the thesis structure is provided in section 1.5

1.1. Sediment routing system

The Earth's surface undergoes cycles of mountain building by endogenic processes (e.g. folding, faulting, volcanism), followed by relief reduction through denudation (Ahnert, 1970; Davis, 1899; Gilbert, 1877; Milliman and Syvitski, 1992; Suess, 1875; Wilson, 1968). Denudation is the combination of physical and chemical disintegration of rocks in place (weathering) and the subsequent removal of mobile material from its site of production (erosion) (e.g., Atkinson, 2004). The mobilized sediment can be redistributed across the Earth's surface by rivers, glaciers and periglacial processes, wind, or purely by gravity (Ahnert, 1998). Although sediment can be temporarily stored within the terrestrial realm, deep-marine basins are the ultimate sink of sediment produced on land (Allen, 2008b, 2017). Dynamical systems that include a

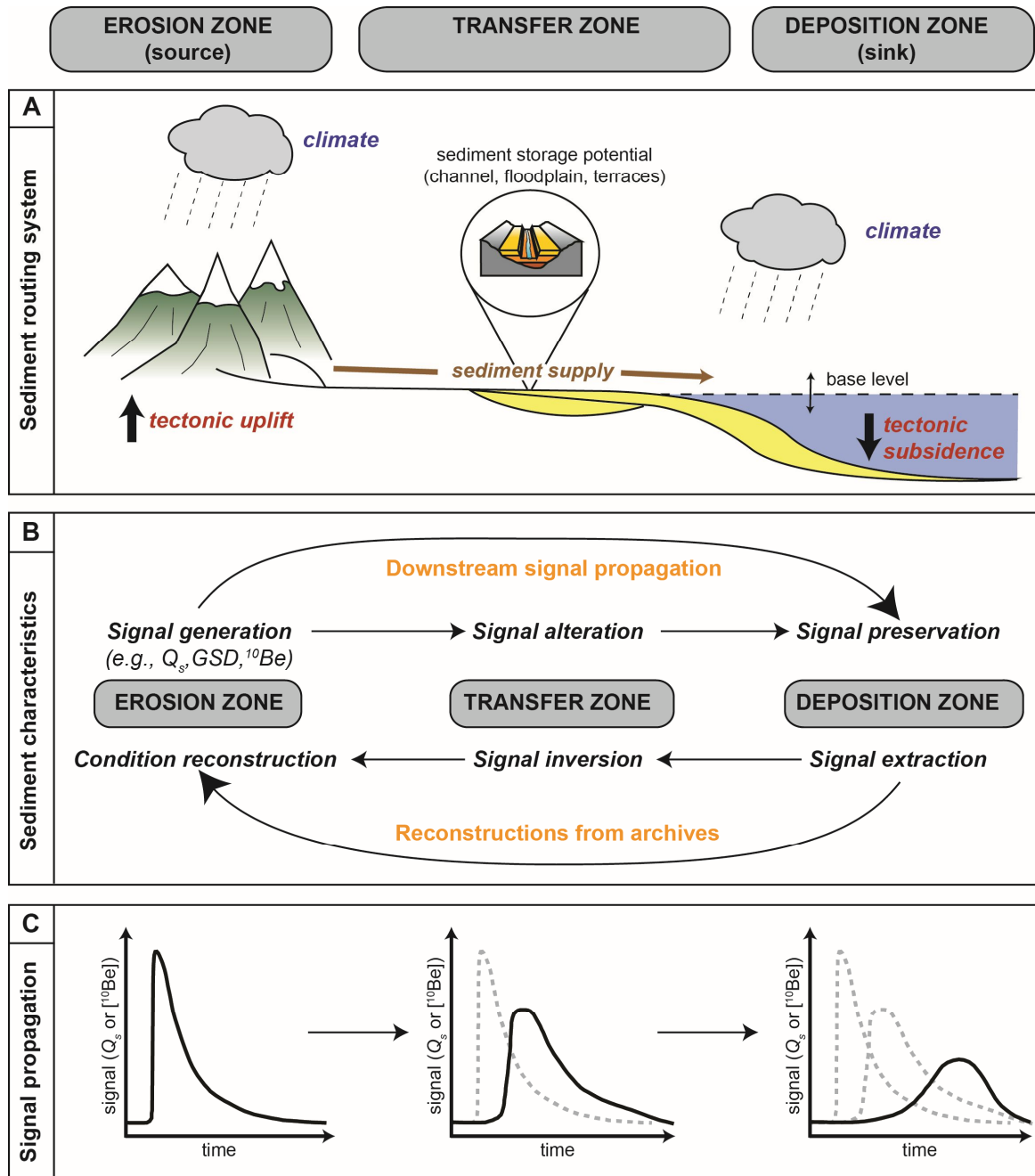


Fig. 1.1 Sediment routing system, sediment characteristics & signal propagation. (A) Sediment routing systems or source-to-sink systems (Allen 2017) can be subdivided into the erosion zone, the transfer zone and the deposition zone (modified after Castelltort and van den Driessche 2003 and Romans et al., 2016). (B) Sediment characteristics including the amount of sediment (Q_s), the grain-size distribution or its composition, as for example the cosmogenic ^{10}Be concentration, vary with the forcing conditions in the erosion zone and create a distinct signal (C). These signals or sediment characteristics can be altered during downstream transport through the transfer zone and potentially even further after deposition. However, if we understand which signals are generated under certain conditions in the erosion zone and how those signals are altered afterwards, we can invert the signals stored in sedimentary deposits to reconstruct past conditions in the erosion zone. Panel C modified after Romans et al. (2016).

sediment cascade from a zone of production to a zone of deposition, including intermittent storage, are named sediment routing systems (Allen, 2008b, 2017; Einsele et al., 1996; Hinderer and Einsele, 2001). Sediment routing systems can be subdivided into three subsystems: the erosion zone, the transfer zone, and the deposition zone (**Fig. 1.1A**; Castellort and Van Den Driessche, 2003; Meade, 1982; Romans et al., 2016; Schumm, 1977). The erosion zone describes areas of sediment production, with hillslopes being the typical sediment feeder to adjacent channels (Allen, 2017; Castellort and Van Den Driessche, 2003; Schumm, 1977). The transfer zone is the region of sediment bypass or temporary storage. It comprises river channels, floodplains, levees, terraces, bars, shorelines, deltas and the continental shelf (Allen, 2017; Castellort and Van Den Driessche, 2003). Finally, the deposition zone is the region of eventual sedimentation, in most cases deep ocean basins or submarine fans (Allen, 2017; Castellort and Van Den Driessche, 2003). On a continental scale, sediment routing systems include the entire sediment cascade from mountainous regions, through foreland areas to final deposition in ocean basins. For instance, the Amazon river connects the eastern part of the northern Andes with the Amazon shelf, from where it is transported further to adjacent deep marine basins (Kuehl et al., 1986; Meade et al., 1985). Typically, a sediment routing system acts as a unidirectional cascade that connects source and sink areas and consequently participates in a range of global biogeochemical cycles; for example, they participate in the global carbon cycles by transporting particulate organic matter to the ocean (France-Lanord and Derry, 1997; Galy et al., 2008) and by supplying the coastal regions with nutrients (Datta et al., 1999).

1.2. Sediment characteristics & Signal propagation

Sediment is continuously transported along sediment routing systems in the form of dissolved load, suspended load or bedload (Allen, 2017). However, the characteristics of the transported sediment are not constant through time. Sediment characteristics that may be modified through time or space include (1) the amount of sediment discharge (Q_s), (2) the grain-size distribution (GSD), and (3) the composition of the sediment including, for example, lithologic components, organic content or the geochemical composition of the minerals, such as the concentration of the cosmogenic isotope ^{10}Be (**Fig. 1.1B**; Allen, 2017 and references therein). Variability in transported sediment can be caused by two main mechanisms. First, the sediment (and its characteristics) produced within the erosion zone vary with local environmental conditions such as climate, tectonics, or land use (e.g., Armitage et al., 2011; Attal et al., 2015; Bookhagen and Strecker, 2012; Coulthard and Van de Wiel, 2017, 2013; D'Arcy et al., 2016; Lague et al., 2005; Larsen and Montgomery, 2012; Schildgen et al., 2016; Sklar et al., 2017). Certain environmental conditions in the erosion zone are thought to generate a distinct signals (e.g., Q_s or ^{10}Be concentration) within the sediment (**Fig. 1.1C**; Castellort and Van Den Driessche, 2003; Romans et al., 2016). Second, this signal can be

altered due to non-linear sediment transport along the sediment routing system (e.g., Coulthard and Wiel, 2007; Jerolmack and Paola, 2010; Romans et al., 2016; Van de Wiel and Coulthard, 2010). After deposition, the sediment characteristics can be further modified by diagenetic processes (Lynn and Bonatti, 1965; Wetzel, 1984), such that the signal stored in the sediment becomes even less recognizable. Climatically or tectonically driven variability in sediment characteristics in the sediment-production zone enables us, in theory, to reconstruct the environmental conditions of the past from sedimentary deposits; this is one of the oldest principles of the geological sciences, which has been constantly refined, particularly following the advent of geochemical and isotope geological techniques (Allen, 2008b; Gilbert, 1877; Lyell, 1830; Penck and Brückner, 1909; Whittaker, 2012; Wobus et al., 2006). However, to reliably reconstruct conditions of the past from sedimentary deposits, we have to understand (1) how conditions in the erosion zone impact sediment signals ; (2) how the signals are altered during transport along the sediment routing system prior to deposition; and (3) how the signals are altered over time after deposition. In the following, I will focus in particular on two types of sedimentary signals – the geochemical composition, in particular the ^{10}Be concentration, and the amount of sediment discharge (Q_s). I will summarize what is known about the generation of those signals in the erosion zone and how they may be altered during transport, and finally I will highlight open questions.

1.2.1. Sediment geochemical composition (^{10}Be)

1.2.1.1. Sediment ^{10}Be concentration in the erosion zone

Over the last two decades, the ^{10}Be concentration ($[^{10}\text{Be}]$) in fluvial sediment, mainly in quartz, has become an important tool to estimate the average denudation rate of catchments (Bierman and Steig, 1996; Binnie et al., 2007; Brown et al., 1995; Codilean et al., 2018; Granger et al., 1996; Lal, 1991; Lupker et al., 2012; Ouimet et al., 2009; Portenga and Bierman, 2011; Schildgen et al., 2016; von Blanckenburg, 2005; Willenbring et al., 2013; Wittmann et al., 2007). ^{10}Be in quartz is produced *in-situ* by interaction with cosmic ray particles (Dunai, 2010; Gosse and Phillips, 2001 and references therein) and the production rates varies locally as a function of altitude, latitude and the secular variation of the Earth's magnetic field (Desilets et al., 2006; Dunai, 2001, 2000; Lal, 1991; Lifton et al., 2005; Nishiizumi et al., 1989; Stone, 2000). At a given site on the Earth's surface, the *in-situ* production rate of ^{10}Be is highest at the surface and decreases exponentially with depth (Lal, 1991). At about 2 m depth, the production rate is close to zero. Hence, long residence times of sediment on hillslopes results in high $[^{10}\text{Be}]$ in sediments and vice versa for short residence times. As long as hillslopes erode steadily and by diffusional processes (e.g. soil creep), and under the assumption that each part of the catchment is equally represented in fluvial sediments at the

catchment outlet, the [^{10}Be] in fluvial sediments is inversely correlated with the hillslope denudation rate (Bierman and Steig, 1996; Brown et al., 1995; Lal, 1991).

Recently, however, several studies have shown that deep-excavation processes (e.g. landslides, rock falls) can remove several meters of hillslope material instantly and dilute the [^{10}Be] in eroded sediment with low [^{10}Be] material from deeper layers, which would result in higher calculated denudation rates (Kober et al., 2012; Niemi et al., 2005; Puchol et al., 2014; West et al., 2014; Yanites et al., 2009). Although these stochastic inputs should be negligible given sufficiently large catchment areas (Niemi et al., 2005; Yanites et al., 2009), substantial variability in [^{10}Be] has been measured in modern sediment from the Ganga Plains, which has been attributed to stochastic input of sediments from deep-excavation events and variability in evacuation timescales of different sediment deposits (Dingle et al., 2018). Other studies have measured different [^{10}Be] in different grain sizes (e.g., Aguilar et al., 2014; Belmont et al., 2007; Carretier et al., 2015; Puchol et al., 2014; Schildgen et al., 2016). Lower concentrations in the sand fraction compared to the gravel fraction has been attributed to longer transport times of gravel in gentle slopes (Codilean et al., 2014). In contrast, higher concentrations in sand compared to the gravel fraction have commonly been explained as a result of coarser grain sizes being primary exhumed from deeper, lower [^{10}Be] layers during deep-excavation events (e.g., Aguilar et al., 2014; Belmont et al., 2007; Brown et al., 1995; Puchol et al., 2014). Although our knowledge on grain-size distributions (GSD) on hillslopes is still limited, GSDs tend to coarsen with depth (Puchol et al., 2014; Ruxton and Beery, 1957) and have been reported to coarsen with steeper, faster eroding hillslopes (Attal et al., 2015; Litty et al., 2017; Riebe et al., 2015). Also, GSDs have been shown to vary with hillslope processes, with landslides and debris-flows producing coarser material relative to processes like soil-creep (Attal et al., 2015; Attal and Lavé, 2006; Roda-Boluda et al., 2018; Sklar et al., 2017). These observations complicate the interpretation of [^{10}Be] in detrital sediment in terms of catchment-mean denudation rates, but they also raise the possibility that the differences in [^{10}Be] among different grain-sizes are indicative of the types of hillslope processes active in the catchment. Although a range of studies has already suggested that the difference in [^{10}Be] can be explained by certain hillslope processes (e.g., Aguilar et al., 2014; Belmont et al., 2007; Brown et al., 1995; Carretier et al., 2015; Puchol et al., 2014), we still lack a systematic comparison of [^{10}Be] in different detrital grain sizes with a detailed hillslope process inventory to address the question: **Do hillslope processes create a distinct and traceable ^{10}Be signal in clastic sediments with differing grain-sizes?**

1.2.1.2. Sediment ^{10}Be concentration in the transfer zone

The identification of distinct ^{10}Be signals in fluvial sediment created by certain hillslope processes would provide a valuable tool to trace the evolution of hillslope processes through time from sedimentary

deposits. The signal stored in the [^{10}Be] difference between grain sizes, however, might be altered during transport through the transfer zone and even after deposition. Although the [^{10}Be] in fluvial sediment is, to a first order, a function of location, erosion rate, and erosion process, ^{10}Be production continues as long as the grain is exposed to cosmic rays. Often, the transport times in the fluvial system are short compared to hillslope residence times and can be neglected (e.g., Hippe et al., 2012; Wittmann et al., 2016; Wittmann and von Blanckenburg, 2009). However, if the sediment is transiently stored along a sediment routing system over longer timescales, for example in an alluvial fan, within a fluvial terrace deposit or within floodplains, the ^{10}Be concentration can increase if the material is located within the production zone (upper few meters), or decrease (due to nuclide decay) if it is shielded from cosmic rays (e.g., Hippe et al., 2018; Wittmann et al., 2011; Wittmann and von Blanckenburg, 2009). The decay-rate of ^{10}Be is $4.99 \cdot 10^{-7} \text{ yr}^{-1}$, which corresponds to a half-life of $\sim 1.4 \text{ Ma}$ (Chmeleff et al., 2010; Korschinek et al., 2010). Hence, whether or not sediment storage can alter the ^{10}Be signal depends on the duration of storage and the initial concentration after erosion.

In addition to changes in the ^{10}Be concentration in individual grains, a signal that is defined by the concentration difference between two grain sizes can also be altered if the grain-size distribution (GSD) in the river changes. Whereas the sediment produced on hillslopes sets the initial GSD in the sediment routing system, several secondary controls can alter the GSD during downstream transport. First, downstream fining is driven by size-selective transport and sediment deposition where accommodation space is available (Ferguson et al., 1996; Paola et al., 1992b). On a larger scale, the availability of accommodation space for long-term sediment deposition is driven by the spatial distribution of tectonic subsidence rates (e.g., Duller et al., 2010; Heller and Paola, 1992). Second, grain-sizes are reduced during transport by abrasion (Attal and Lavé, 2009, 2006; Bradley, 1970; Dingle et al., 2017; Kodama, 1994; Kuenen, 1956). Abrasion includes different processes, for example the production of clay-sized particles, silt and sand by attrition (pebbles scraping against each other), but also the production of different size fragments by splitting, breaking or chipping (Attal and Lavé, 2009; Kodama, 1994; Kuenen, 1956). Attal and Lavé (2006) measured abrasion rates between 0.15 and 31%/km for different Himalayan rock types in a circular flume. Dingle et al. (2017) considered abrasion as the main process responsible for the disappearance of coarse gravel in Himalayan rivers within 10-40 km of the rivers entering the Ganga Plain. The abrasion of grains during transport results in an over-representation of grains from low-elevation, where ^{10}Be production rates are lower, such that concentration differences between grain-sizes will be affected (Belmont et al., 2007; Lupker et al., 2017; Matmon et al., 2003; Olen et al., 2015). Third, although GSDs typically fine downstream (Sternberg, 1875), downstream coarsening has been observed in some cases and was explained by local, lateral input from tributaries or sedimentary deposits like landslides or moraines (Attal and Lavé, 2006). The alteration of [^{10}Be] in individual grains as well as changes in GSDs in downstream directions raise the question: **How is**

a potential hillslope-process signal stored in the [^{10}Be] difference between grain sizes altered during propagation along the sediment routing system?

1.2.2. Sediment discharge (Q_s)

Changes in the amount of sediment produced within the erosion zone through time are thought to vary with changes in local climatic conditions, tectonic forcing, and/or land use (Armitage et al., 2011; Attal et al., 2015; Bookhagen and Strecker, 2012; Coulthard and Van de Wiel, 2017, 2013; D'Arcy et al., 2016; Lague et al., 2005; Larsen and Montgomery, 2012; Schildgen et al., 2016; Sklar et al., 2017). If changes in sediment discharge (Q_s) from the erosion zone are preserved through the transfer zone, then variability in sediment deposition in sink areas can be used to reconstruct tectonic and climatic conditions of the past (e.g., Alloway et al., 2007; Zhang et al., 2001). This approach, however, requires a detailed understanding of how Q_s -signals are transferred and altered within the transfer zone (Romans et al., 2016 and references therein). Up to now, few, and sometimes contrasting, results have been presented on whether climatic or tectonic signals are faithfully transmitted through the transfer zone.

Field studies have shown that the amount of sediment produced in the erosion zone varies with (1) rainfall intensity (Bookhagen and Strecker, 2012; Moon et al., 2011) and variability in rainfall (DiBiase and Whipple, 2011; Lague et al., 2005), (2) the presence of glaciers (Koppes and Montgomery, 2009), (3) freeze-thaw cycles (Walder and Hallet, 1985) and (4) vegetation cover (Garcin et al., 2017; Langbein and Schumm, 1958; Olen et al., 2016; Torres Acosta et al., 2015). With regards to tectonic activity, already in 1877, G. K. Gilbert suggested that erosion rates are highest where slopes are steepest, implying that high uplift rates cause high erosion rates. More quantitative analyses have corroborated this observation (Ahnert, 1970; Milliman and Syvitski, 1992; Portenga and Bierman, 2011) and have identified a non-linear increase in denudation rates with increasing slopes, which is attributed to the onset of landslide activity once hillslopes have reached a threshold slope of $\sim 30^\circ$ (Bennett et al., 2016; Binnie et al., 2007; Burbank et al., 1996; Larsen and Montgomery, 2012; Montgomery and Brandon, 2002; Ouimet et al., 2009; von Blanckenburg et al., 2004). On shorter timescales, co-seismic waves can induce landslides (Keefer, 1994; Meunier et al., 2007), and enhanced landslide activity has been observed to continue several years after co-seismic activity has ceased (Hovius et al., 2011; Marc et al., 2015).

However, whether any of those signals produced within the erosion zone is preserved during propagation along a sediment routing system has been shown to depend on a range of factors including (1) the nature of the perturbation (Q_s or Q_w), (2) its frequency and (3) the degree of buffering due to non-linear sediment transport within the fluvial system. Regarding the first point, an experimental study by van den Berg van Saparoea and Postma (2008) as well as a 1D numerical model study by Simpson and Castelltort

(2012) showed that changes in water discharge (Q_w) leave a distinct signal in the sediment outflux ($Q_{s,out}$), whereas variability in the upstream sediment supply ($Q_{s,in}$) is buffered within the channel reach and less detectable in the sediment flux at the outlet ($Q_{s,out}$). Their explanation is a strong positive coupling between Q_w and channel gradient and a negative coupling between $Q_{s,in}$ and channel gradient, such that higher Q_w requires a lower channel slopes and thus remobilizes sediment from within its bed, thereby creating a clear signal in $Q_{s,out}$ (Simpson and Castelltort, 2012; van den Berg van Saparoea and Postma, 2008). In contrast, an increase in $Q_{s,in}$ requires a steeper slope, such that the additional sediment is deposited within the channel and therefore not visible in the $Q_{s,out}$ signal. Coulthard and Van de Wiel (2013) predicted with a 2D landscape evolution model (CAESAR) that even a moderate increase in Q_w (10-20%) can be detected in $Q_{s,out}$, while substantial changes in uplift are not detectable in $Q_{s,out}$. Hence, $Q_{s,out}$ signals created by changes in Q_w are more distinct than those created by variability in $Q_{s,in}$.

Second, boundary conditions are not static, but constantly undergo changes, often in cyclic patterns (e.g. Milankovitch cycles; Milankovitch, 1941). As alluvial rivers adjust their channel morphology to the prevailing environmental conditions (Lane, 1955; Mackin, 1948; Schumm, 1977), changes in climate or tectonics also drive changes in channel morphology (Blom et al., 2017; Buffington, 2012; Church, 1995; Curtis et al., 2010; Dade et al., 2011; Wickert and Schildgen, 2018). During the adjustment phase (transient phase) to new equilibrium conditions, sediment can be deposited in or remobilized from the channel bed to adjust the gradient; consequently $Q_{s,in}$ does not equal $Q_{s,out}$ during the adjustment phase. Paola et al. (1992a) proposed that the characteristic adjustment time, or response time, for a 1D fluvial profile is a function of the system length and the diffusivity. Based on the response time equation proposed by Paola et al. (1992a), Métivier and Gaudemer (1999) predicted response times of > 1 Myr for large Asian alluvial rivers. Castelltort and Van Den Driessche (2003) calculated the response times of more than 90 rivers globally and found that the response times of large rivers are on the order of 10^5 - 10^6 years. If the frequency of the forcing is shorter than the response time of the system, no clear Q_s signal will be transmitted (Allen, 2008a; Castelltort and Van Den Driessche, 2003; Métivier and Gaudemer, 1999; Paola et al., 1992a).

Third, a distinct signal generated in the erosion zone can be altered by non-linear sediment transport along the transfer zone, that is several phases of sediment deposition and later remobilization (Coulthard and Wiel, 2007; Jerolmack and Paola, 2010; Romans et al., 2016; Van de Wiel and Coulthard, 2010). Studies in large mountain ranges, such as the Himalaya and the Andes, have revealed that sediment can be transiently stored for thousands to millions of years within the transfer zone before it reaches the ocean (Blöthe and Korup, 2013; Hippe et al., 2012; Hoffmann, 2015; Strecker et al., 2009; Wittmann et al., 2011). Temporary storage zones within the fluvial system include the channel bed itself (Coulthard et al., 2005; Simpson and Castelltort, 2012), floodplains (Coulthard and Van de Wiel, 2013; Wittmann et al., 2011),

fluvial terraces (Schildgen et al., 2016), alluvial fans (Allen and Densmore, 2000; D'Arcy et al., 2016; Mason et al., 2018) or entire valley fills (Hilley and Strecker, 2005). Non-linear sediment transport along sediment routing systems has been attributed to a range of processes and feedback mechanisms within the transfer zone. First, mobilization of sediment is a function of the transport capacity of the river (Young et al., 2001), such that in cases where the supplied sediment increases the local transport capacity, the excavation of that sediment is stretched over longer time periods and therefore reduces the Q_s -amplitude (Hovius et al., 2000). Second, the local water discharge, in particular its velocity, determines the maximum grain size that can be transported by the fluvial system (Shields, 1936). Larger grain sizes require more water to initiate grain entrainment (Tucker, 2004). Consequently, the largest boulders are only moved during extreme events, such that different grain sizes have different transport rates (Howard et al., 1994). Third, the armor layer, a coarser bed-surface layer overlying finer sediment, protects the underlying, fine material from entrainment. But once the armor layer is destroyed, the underlying, fine material is also mobilized, resulting in a sudden pulse of transported sediment (Van de Wiel and Coulthard, 2010). The consequence of threshold-driven, non-linear sediment transport within the fluvial system is the alteration or 'shredding' of sediment discharge ($Q_{s,out}$) signals (Jerolmack and Paola, 2010; Romans et al., 2016; Van de Wiel and Coulthard, 2010).

As a consequence of all those factors - the nature of the perturbation, its frequency and non-linear sediment transport - signals can be strongly altered during transport. Although it is also a matter of time and spatial scale, predictions range from signal buffering over transmission to amplification (Armitage et al., 2013; Braun et al., 2015; Godard et al., 2013; Jerolmack and Paola, 2010; Simpson and Castelltort, 2012; Van de Wiel and Coulthard, 2010; van den Berg van Saparoea and Postma, 2008). Because the understanding of signal propagation is crucial for the inversion of paleo-environmental conditions from sedimentary deposits, we ask the question: **Does variability in $Q_{s,in}$ and Q_w create a distinct signal in $Q_{s,out}$, and how do these signals differ from one another?**

1.3. Channel profiles and fluvial fill terraces

1.3.1. From boundary conditions to channel responses and terrace formation

1.3.1.1. Alluvial channels

Alluvial rivers constantly adjust their channel morphology (slope, width, depth) according to the prevailing environmental conditions (Blom et al., 2017; Buffington, 2012; Church, 1995; Curtis et al., 2010; Dade et al., 2011; Lane, 1955; Mackin, 1948). Changes in the course of a river channel or its bed elevation are of major importance, such as for infrastructure and buildings adjacent to the channel. In the



Fig. 1.2 Photo of the train bridge crossing the Yacoraite river in the Quebrada de Humahuaca. Due to bed elevation rise and repeated destruction of the tracks, the train tracks were abandoned in the 1990s.

Quebrada de Humahuaca, an intermontane basin within the Eastern Cordillera of the southern Central Andes (NW Argentina), fast bed-elevation rise during the last few decades and repeated overwash has led to the abandonment of the entire train network in the basin in the 1990s (**Fig. 1.2**). As such, understanding how alluvial channels respond to changes in climatic and tectonic boundary condition is important for the infrastructure maintenance and future development of such regions.

The longitudinal profile of a river is typically concave-upward in shape, with a decreasing channel slope and increasing discharge in the downstream direction (**Fig. 1.3**; Bagnold, 1977; Leopold and Bull, 1979; Mackin, 1948). The slope (S) of an alluvial channel at a given location along the profile is a function of water discharge (Q_w), sediment discharge (Q_s) and GSD (Blom et al., 2017, 2016; Hack, 1973; Lane, 1955; Schumm, 1977; Wickert and Schildgen, 2018). Alluvial rivers adjust their slope by sediment deposition (aggradation) or excavation (incision), such that the available Q_w can transport the incoming Q_s ($Q_{s,in}$) downstream (Gilbert, 1877; Lane, 1955; Mackin, 1948). Adjusted channel profiles, whereby the incoming sediment ($Q_{s,in}$) equals the outgoing sediment ($Q_{s,out}$), are considered *graded* or *equilibrium* profiles (Mackin, 1948). Several relationships between S , Q_s and Q_w have been proposed (e.g., Blom et al., 2016; Lane, 1955; Parker, 1998, 1979; Wickert and Schildgen, 2018). Both 1D numerical models of

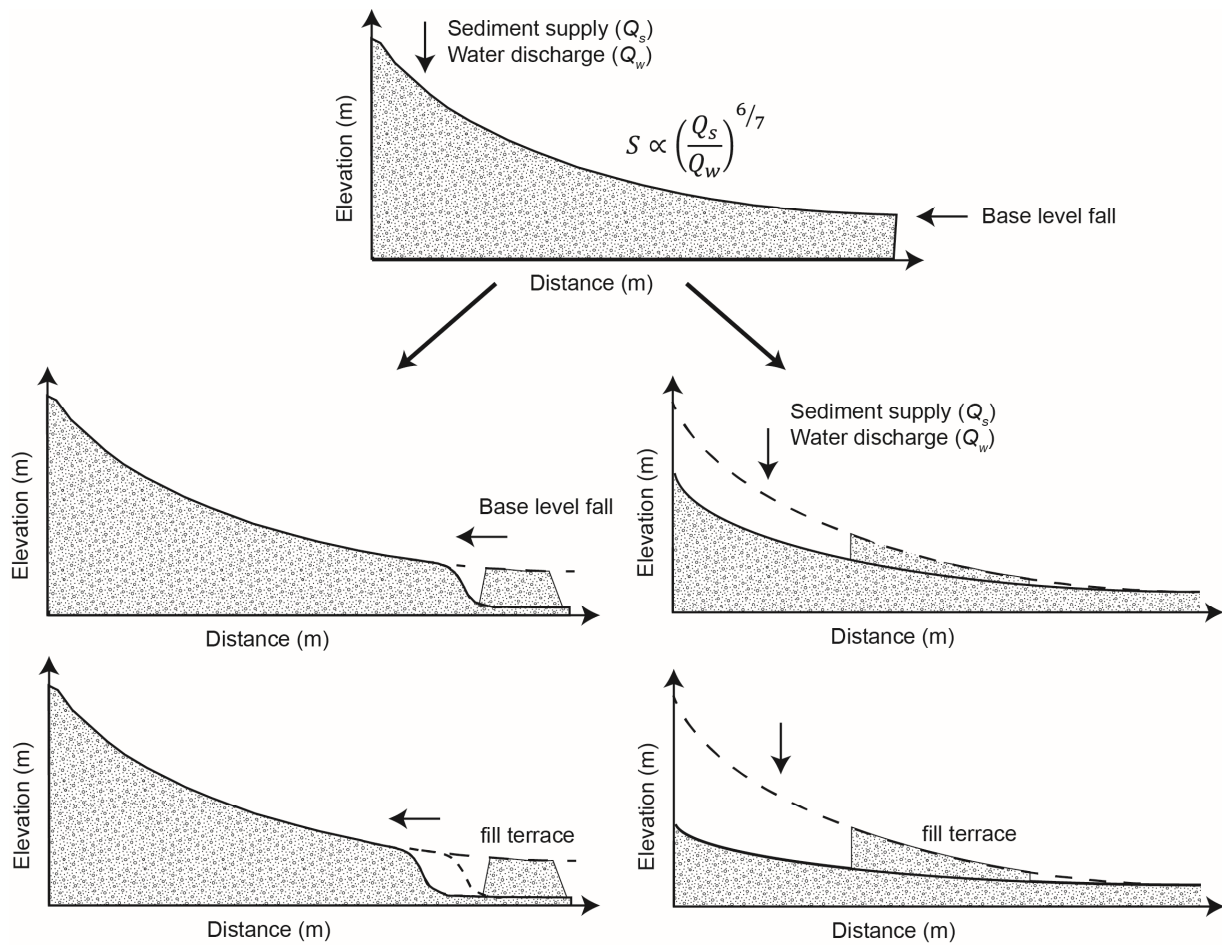


Fig. 1.3 Mechanisms of fluvial fill terrace formation. Alluvial rivers commonly have a concave-up longitudinal profile with the local gradient being a function of sediment supply, water discharge and GSD. The slope scaling given in the upper profile is based on Wickert and Schildgen (2018). Fluvial fill terraces are former channel floodplains that have been abandoned and preserved adjacent to the modern channel. Fluvial fill terraces are the result of major changes in bed elevation, which can be caused by either variability in the upstream sediment supply or water discharge (left) or changes in the downstream base level (right). Not shown are potential autogenic or more complex response scenarios for fill terrace formation.

the longitudinal channel profile (Blom et al., 2016; Simpson and Castelltort, 2012) and physical experiments (van den Berg van Saparoea and Postma, 2008) show that either a reduction in Q_w or an increase in $Q_{s,in}$ cause aggradation, while an increase in Q_w or a reduction in $Q_{s,in}$ cause incision. However, because alluvial channels also adjust their width in response to changes in forcing (e.g., Buffington, 2012; Church, 1995; Curtis et al., 2010; Dade et al., 2011), changes in bed-elevation and width must be investigated simultaneously to reliably predict channel evolution. A recent derivation, allowing for self-adjusting channel width and channel roughness by combining equations of flow and sediment transport in

an equilibrium-width channel (Parker, 1978), proposed the following scaling between Q_s , Q_w and S (**Fig 1.3**; Wickert and Schildgen, 2018):

$$S \propto \left(\frac{Q_s}{Q_w} \right)^{6/7} \quad (1.1)$$

But as the equations used in numerical modelling studies are simplifications of the processes acting in real landscapes that do not necessarily accurately capture the dynamics of transient adjustment phases, physical experiments can provide further insights into the response of channel morphology to changes in external boundary conditions. I designed a series of physical experiments with a focus on the following question: **How does an alluvial-channel reach adjust its morphology (longitudinal profile, width) in response to changes in boundary conditions?**

1.3.1.2. Fluvial fill terraces

Alternating phases of channel aggradation and incision can form fluvial fill terraces (**Fig. 1.3**; e.g., Bull, 1990; Burbank and Anderson, 2011; Merritts et al., 1994; Pazzaglia, 2013). If several terrace surfaces are cut into a single fill unit, the highest terraces is called ‘*fill terrace*’, while the lower ones are sometimes referred to as ‘*cut terraces*’ (e.g., Merritts et al., 1994). As the channel-bed gradient is always a function of the prevailing conditions (Q_s , Q_w , GSD), the preservation of former channel beds as terraces offer the opportunity to reconstruct conditions of the past from those geomorphic landforms (Bridgland and Westaway, 2008; Bull, 1990; Merritts et al., 1994).

The formation of fluvial fill terraces can occur through several different mechanisms (**Fig. 1.3**). Either changes in upstream $Q_{s,in}$ or Q_w can cause aggradation, or incision and the abandonment of a fill-terrace surface (Dey et al., 2016; Fuller et al., 1998; Hanson et al., 2006; Huntington, 1907; Penck and Brückner, 1909; Scherler et al., 2015; Schildgen et al., 2016; Steffen et al., 2010, 2009). Variability in $Q_{s,in}$ can either be the result of changes in hillslope erosion rates due to, for example, increased seismic activity (Marc et al., 2015; McPhillips et al., 2014), climatic changes in the catchment that affect surface erosivity (Dey et al., 2016; Fuller et al., 1998; Steffen et al., 2010, 2009) or land-use changes (Milliman et al., 1987). Variations in Q_w are often climatically related, but can also be the result of land-use changes (Macklin and Lewin, 2003; Malatesta et al., 2018; Schildgen et al., 2002). Alternatively, base-level changes can affect the channel-bed elevations at the downstream end (e.g., Frankel et al., 2007; Gardner, 1983; Grimaud et al., 2015). A rise in base-level leads to local reduction in channel slope upstream of the base-level control point, which will trigger sediment deposition until the channel returns to its equilibrium profile. In turn, a drop in base-level results in the upstream migration of a wave of incision, marked by a knickzone, which may leave

behind terraces as traces of the former channel bed (**Fig. 1.3**; Farabaugh and Rigsby, 2005; Fisk, 1944; Shen et al., 2012). Base-level control can either be tectonic, for example if the river crosses an active fault (e.g., Hilley and Strecker, 2005) or climatic, if the river drains into a lake or the ocean (Farabaugh and Rigsby, 2005; Fisk, 1944; Merritts et al., 1994). All of those river-incision mechanisms described above -- increase in Q_w , decrease in $Q_{s,in}$ or a drop in base-level -- are externally triggered (allogenic). But channel bed-elevation changes may also occur due to “autogenic” internal feedbacks within the fluvial system (Erkens et al., 2009; Gonzalez, 2001; Limaye and Lamb, 2016; Womack and Schumm, 1977) or more complex responses to allogenic perturbation (Schumm, 1979, 1973). A detailed description of the different fill terrace formation mechanisms can be found in chapter 3.2.

In summary, the presence of fluvial fill terraces as a result of bed-elevation changes can be an indicator of alterations in either Q_s , Q_w and/or base level, all of which are typically driven by variability in the climatic or tectonic boundary conditions, and potentially land-use on shorter time-scales. For this reason, fill terraces have been used for reconstructions of paleo catchment-mean denudation rates (Bookhagen et al., 2006; Schaller et al., 2004, 2002; Schildgen et al., 2016) or paleo-discharge variability (Leopold and Miller, 1954; Litty et al., 2016; Poisson and Avouac, 2004). However, to reliably reconstruct that information from fill terraces, it is essential to first identify the terrace formation mechanism. Because fluvial cut-and-fill terraces are often thousands of years old (Schaller et al., 2004, 2002, Schildgen et al., 2002, 2016, Steffen et al., 2010, 2009), the process of terrace formation can rarely be observed in nature. Instead, numerical models (Bogaart and van Balen, 2000; Boll et al., 1988; Tebbens et al., 2000; Veldkamp, 1992; Veldkamp and Van Dijke, 2000) and laboratory experiments (Baynes et al., 2018; Frankel et al., 2007; Gardner, 1983; Lewis, 1944; Mizutani, 1998; Schumm and Parker, 1973; Wohl and Ikeda, 1997) have provided important insights into terrace formation. However, no numerical or experimental set-up so far has systematically compared the different mechanisms of fill-terrace formation or investigated the differences in the resulting terraces, regarding, for example, lag-times between the time of perturbation and the abandonment of a terrace surface or slope-differences between the resulting terrace surfaces. To address this knowledge gap, I perform physical laboratory experiments to address the questions: **Under which conditions are fill terraces formed? And how do the resulting terraces differ from one another with regards to lag-times compared to the onset of forcing and surface slopes?**

1.3.2. Reconstructions of boundary conditions from fill terraces

In NW Argentina, several intermontane basin between the high-elevated Puna Plateau to the west and the low-elevated foreland to east, including the Quebrada de Humahuaca and the Quebrada del Toro, are characterized by thick sedimentary fill units, which preserve several cycles of sediment deposition and



Fig. 1.4 Photo of the fluvial cut-and-fill terrace sequence in the Quebrada del Toro, NW Argentina. The terrace sequence extends ~20 km along the Río Toro main stem. The most prominent terrace level shown in the photo is ~110 m above the current river bed. Photo taken by S.Savi.

subsequent fluvial incision (Alonso et al., 2006; Hilley and Strecker, 2005; Marrett and Strecker, 2000; Mortimer et al., 2007; Tchilinguirian and Pereyra, 2001). Dating of individual sedimentary deposits in those basins, with for example optically stimulated luminescence (OSL) and cosmogenic ^{10}Be exposure dating, indicated that major changes in bed elevation have occurred since the late Pleistocene (Robinson et al., 2005; Sancho et al., 2008; Savi et al., 2016; Schildgen et al., 2016; Spencer and Robinson, 2008). In addition, lacustrine sediments document the existence of several landslide-dammed paleo-lakes and thus the partial closure of those intermontane basins (Hermanns et al., 2000; Trauth et al., 2003a, 2003b; Trauth et al., 2000; Trauth and Strecker, 1999). As ^{14}C ages of those lacustrine deposits correlate with wetter phases on the Altiplano-Puna Plateau (Baker et al., 2001; Baker and Fritz, 2015; Bobst et al., 2001; Fritz et al., 2004; Placzek et al., 2006, 2013), landslides-initiation has been related to increased rainfall and pore-pressure (Hermanns et al., 2000; Trauth et al., 2003a; Trauth et al., 2000; Trauth and Strecker, 1999). Other

studies, however, suggested that seismic activity might also have triggered enhanced landsliding (Hermanns et al., 2000; Strecker and Marrett, 1999). Whether climatically or tectonically induced, quantitative information on how sediment discharge (Q_s) and water discharge (Q_w) have varied over time would significantly improve our understanding on the dynamic evolution of those basins. Schildgen et al. (2016) dated fluvial terraces in the Quebrada de Humahuaca and found that aggradation and incision cycles correlate with the 21-kyr precessional cycles, indicating changes in climate to be a major control factor. However, quantitative paleo-hydrological reconstructions for the area are limited to a paleo-lake-extent modelling study from the Santa Maria Basin further to the south, which suggested about 10-15% higher precipitation at about ~30 ka (Bookhagen et al., 2001). In addition, reconstructions of glacial extents based on ^{10}Be derived moraines ages on the Nevado de Chañi (located on the dividing range between the Quebrada de Humahuaca and the Quebrada del Toro) indicated colder and wetter conditions at ~52-39 ka, ~23 ka, ~15 ka and ~12 ka (Martini et al., 2017). Both paleo-hydrological reconstructions, however, are limited to the last ~50 ka. Paleo-hydrological constructions from fluvial terraces, if they can be done accurately, hold the potential to reach further back in time.

While the fluvial terraces in the Quebrada del Humahuaca are mainly located at confluences of tributaries with the main stem, a several-hundred-meter thick fluvial cut-and-fill terrace sequence in the Quebrada del Toro (**Fig. 1.4**), which extents for ~20 km along the Río Toro main stem, offers an opportunity to reconstruct paleo- Q_s and paleo Q_w . The terraces were first described by Schwab and Schäfer (1976), and are known to be the result of a major valley filling and re-incision phase sometime after ~ 1Ma (Hilley and Strecker, 2005; Marrett et al., 1994). But so far, no chronology of the individual aggradation and incision events exists. To use the terraces for the reconstruction of paleo-environmental conditions, the following questions need to be addressed: **When were the terraces in the Quebrada del Toro formed (individual aggradation and incision times)? By which mechanism were the terraces formed (Q_s , Q_w , base level or autogenic/ complex response)? What information regarding paleo- Q_s and paleo- Q_w can be extracted from those terraces?**

1.4. Emerging research questions

Based on the open research questions described above, this thesis focuses on four principal research topics – two related to signal propagation and two related to alluvial-channel response and terrace formation. Each topic is subdivided into one to three questions. The topics and questions are:

Topic 1) Signals in the geochemical composition of sediment: (A) Do hillslope processes create a distinct and traceable ^{10}Be signal in clastic sediments with differing grain-sizes? (B) How is a potential hillslope-process signal stored in the ^{10}Be difference between grain sizes altered during propagation along the sediment routing system? Recent studies have demonstrated that different hillslope-erosion processes produce different grain-size distributions. Other studies have observed that detrital ^{10}Be concentrations vary with grain size. This research question focuses on the important issue of whether or not ^{10}Be -concentration differences associated with different grain sizes preserve information on the type of hillslope processes that mobilized the sediment. To address the first question, I collected 13 fluvial sand-and-gravel pairs in the Quebrada del Toro, NW Argentina and analyzed their ^{10}Be . Because the basin is characterized by a strong gradient in hillslope angles from north to south, we observed a range of different hillslope-processes. I mapped these hillslope processes in Google Earth to compare their distribution to the geochemical signal stored in the sediment. Furthermore, I will discuss how those signals are potentially altered during transport considering the findings on other studies regarding the downstream evolution of ^{10}Be in fluvial sediment.

Topic 2) Signals in the sediment discharge amount (Q_s): Does variability in $Q_{s,in}$ and Q_w create a distinct signal in $Q_{s,out}$, and how do these signals differ from one another? Previous studies have investigated the propagation of Q_s signals through the transfer zone. It has been debated, mainly based on numerical model results, whether alluvial channels buffer, preserve, or amplify sedimentary signals originating from hillslopes. I performed physical experiments at Saint Anthony Falls Laboratory, USA in which I could control the base level and the amount of water discharge and sediment supply separately. As such, I could trace the evolution of sediment discharge at the basin outlet in response to changes in any of those parameters.

Topic 3) From boundary conditions to channel responses and terrace formation: (A) How does an alluvial-channel reach adjust its morphology (longitudinal profile, width) in response to changes in boundary conditions? (B) Under which conditions are fill terraces formed? (C) And how do the resulting terraces differ from one another with regards to lag-times compared to the onset of forcing and surface slopes? Fill terrace formation has been linked to changes in upstream (Q_s , Q_w) and downstream (base level) boundary conditions. However, so far there has not been a systematic comparison of the different terrace formation mechanism and the resulting terraces. Also, many of the numerical models that investigate alluvial channel profile evolution and terrace formation do not take changes in channel width into account. To address this gap, I use the same set of physical

experiments that were analyzed to address Topic 2. Data was acquired by tracing the evolution of the channel with overhead photos and regular laser-scans.

Topic 4) Reconstructions of boundary conditions from fill terraces: (A) When were the terraces in the Quebrada del Toro formed (individual aggradation and incision times)? (B) By which mechanism were the terraces formed (Q_s , Q_w , base level or autogenic/ complex response)? (C) What information regarding paleo- Q_s and paleo- Q_w can be extracted from those terraces? Once a terrace sequence has been dated and the formation mechanism is identified, information on paleo-environmental conditions could potentially be extracted from the terraces. For the terrace sequence in the Quebrada del Toro, NW Argentina, I generated a terrace formation chronology by combining cosmogenic radionuclide dating with U-Pb dating of volcanic ashes. After discussing by which mechanism those terraces were formed, I calculated paleo-denudation rates from ^{10}Be concentration in terrace sediments and used that information combined with terrace surface-slope measurements to estimate paleo-discharge. On this topic, I aim to understand what quantitative paleo-climatic information can be extracted from sequences of fill terraces in mountainous environments. This question is particularly relevant in regions where variability in the climatic and tectonic forcing conditions may have substantial impacts on sediment production, storage and removal.

1.5. Thesis structure

The thesis is structured in three chapters (2 to 4) comprising manuscripts that are either published or currently under review in international peer-reviewed journals, and a final discussion chapter (5). In chapter 5, I will present new analyses and combine data and findings from different parts of chapters 2 through 4 to answer the questions that were not addressed in those chapters. I will shortly elaborate which of the research questions listed above is addressed in which part of the thesis.

Chapter 2 comprises the manuscript *Effects of deep-seated versus shallow hillslope processes on cosmogenic ^{10}Be concentrations in fluvial sand and gravel* (in press at *Earth Surface Processes and Landforms*) and addresses Topic 1, in particular the questions of whether hillslope processes create a distinct and traceable ^{10}Be signal in clastic sediments when different grain-sizes are compared.

Chapter 3 comprises the manuscript titled *Alluvial channel response to environmental perturbations: Fill-terrace formation and sediment-signal disruption* (submitted to *Earth Surface Dynamics*). In this chapter I investigate Topics 2 and 3. I investigate signals stored in the sediment discharge

amount ($Q_{s,out}$) and I address the response of alluvial channels and the formation of fill terraces to external perturbations.

Chapter 4 consists of the manuscript *100 kyr fluvial cut-and-fill terrace cycles since the Middle Pleistocene in the southern Central Andes, NW Argentina* (published in *Earth and Planetary Science Letters*) in which mainly the first question of Topic 4, the chronology of the terraces in the Quebrada del Toro, is addressed.

Chapter 5 is the final discussion chapter, and I start by continuing with Topic 4. I discuss in detail by which mechanism the terraces in the Quebrada del Toro formed, followed by new analyses on plaeo- Q_s and paleo- Q_w estimates extracted from those terraces. Next, I broaden my scope and return to overall implications of this work regarding signal generation and signal propagation in the sediment routing system (Topics 1 and 2). First, I will address how a potential geochemical signal on hillslope processes is altered during fluvial transport (Topic 1) and second, I will elaborate in more detail on the amount of sediment discharge ($Q_{s,out}$) as a signal.

1.6. Publications and author contributions

The majority of the work described in the following chapters has been performed by the author. Chapter 2 and 4 are published in international peer-reviewed journals. Chapter 3 has been submitted.

Chapter 2 **Tofelde, S.,** Duesing, W., Schildgen, T., Wickert, A., Wittmann, H., Alonso, R. and Strecker, M., 2018. Effects of deep-seated versus shallow hillslope processes on cosmogenic ^{10}Be concentrations in fluvial sand and gravel. *Earth Surf. Process. Landforms*. doi: 10.1002/esp.4471

S.T., W.D., T.S. and M.S. conducted field work. S.T., W.D. and T.S. prepared the CRN samples. S.T. analyzed the CRN data. S.T. created the hillslope-process inventory. S.T. and T.S. designed the manuscript. All authors discussed interpretations and commented on the manuscript. S.T. designed all artwork.

Chapter 3 **Tofelde, S.,** Savi, S., Wickert, A.D., Bufe, A., Schildgen, T.F.. Alluvial channel response to environmental perturbations: Fill-terrace formation and sediment-signal disruption. *Submitted to Earth Surf. Dyn. Discuss.*

S.T., S.S. and A.W. designed and built the experimental setup. S.T. and S.S. performed the experiments. S.T. analyzed the data with the help of S.S., A.W. and A.B. All authors discussed the data, designed the manuscript and commented on it. S.T. designed the artwork.

Chapter 4 **Tofelde, S.**, Schildgen, T.F., Savi, S., Pingel, H., Wickert, A.D., Bookhagen, B., Wittmann, H., Alonso, R.N., Cottle, J., Strecker, M.R., 2017. 100 kyr fluvial cut-and-fill terrace cycles since the Middle Pleistocene in the southern Central Andes, NW Argentina. *Earth Planet. Sci. Lett.* 473, 141–153. doi:10.1016/j.epsl.2017.06.001

S.T., S.S., A.W., H.P., T.S. and M.S. conducted field work. S.T., S.S. and H.W. performed the preparation of the CRN samples. H.P. prepared the volcanic ash samples, which were measured by J.C. and analyzed by H.P. S.T. analyzed the CRN samples. R.A. supported field work and sample collection. S.T., T.S., H.P., S.S., A.W., B.B., H.W. and M.S. designed and wrote the manuscript; all authors discussed interpretations and commented on the manuscript. S.T. designed all artwork.

During the course of my PhD, I have contributed to further publications that are published or are in review in international peer-reviewed journals.

Schwanghart, W., Bernhardt, A., Stolle, A., Hoelzmann, P., Adhikari, B.R., Andermann, C., **Tofelde, S.**, Merchel, S., Rugel, G., Fort, M., 2016. Repeated catastrophic valley infill following medieval earthquakes in the Nepal Himalaya. *Science*. 351 (6269), 147-150. doi:10.1126/science.aac9865

Savi, S., Schildgen, T.F., **Tofelde, S.**, Wittmann, H., Scherler, D., Mey, J., Alonso, R.N., Strecker, M.R., 2016. Climatic controls on debris-flow activity and sediment aggradation: The Del Medio fan, NW Argentina. *J. Geophys. Res. Earth Surf.* 2424–2445. doi:10.1002/2016JF003912

Schildgen, T.F., Robinson, R.A.J., Savi, S., Phillips, W.M., Spencer, J.Q.G., Bookhagen, B., Scherler, D., **Tofelde, S.**, Alonso, R.N., Kubik, P.W., Binnie, S.A., Strecker, M.R., 2016. Landscape response to late Pleistocene climate change in NW Argentina: Sediment flux modulated by basin geometry and connectivity. *J. Geophys. Res. Earth Surf.* 121, 392–414. doi:10.1002/2015JF003607

Nieto-Moreno, V., Rohrmann, A., van der Meer, M.T.J., Sinninghe Damsté, J.S., Sachse, D., **Tofelde, S.**, Niedermeyer, E.M., Strecker, M.R., Mulch, A., 2016. Elevation-dependent changes in n-alkane δD and soil GDGTs across the South Central Andes. *Earth Planet. Sci. Lett.* 453, 234–242. doi:10.1016/j.epsl.2016.07.049

Introduction

Rohrman, A., Sachse, D., Mulch, A., Pingel, H., **Tofelde, S.**, Alonso, R.N., Strecker, M.R., 2016. Miocene orographic uplift forces rapid hydrological change in the southern central Andes. *Sci. Rep.* 6, 35678. doi:10.1038/srep35678

D'Arcy, M., Mey, J., Duesing, W., Wittmann, H., Alonso, R. N., Schildgen, T.F., **Tofelde, S.**, Weissmann, P., Strecker, M.. Timing of past glaciation at the Sierra de Aconquija, northwestern Argentina, and throughout the Central Andes. *Accepted in Quaternary Science Reviews*.

Bufe, A., Turowski, J.M., Burbank, D., Paola, C., Wickert, A.D., **Tofelde, S.**, The influence of valley-wall height and downstream sediment discharge on the rate and extent of lateral channel migration. *In review at Earth Surface Processes and Landforms*.

2. ¹⁰Be concentrations in fluvial sand and gravel

Published as:

Tofelde, S., Duesing, W., Schildgen, T., Wickert, A., Wittmann, H., Alonso, R. and Strecker, M., 2018. Effects of deep-seated versus shallow hillslope processes on cosmogenic ¹⁰Be concentrations in fluvial sand and gravel. *Earth Surf. Process. Landforms*. doi: 10.1002/esp.4471

Keywords:

*cosmogenic nuclides,
grain size,
hillslope processes,
erosion,
Andes*

Abstract

Terrestrial cosmogenic nuclide (TCN) concentrations in fluvial sediment, from which denudation rates are commonly inferred, can be affected by hillslope processes. TCN concentrations in gravel and sand may differ if localized, deep-excavation processes (e.g. landslides, debris flows) affect the contributing catchment, whereas the TCN concentrations of sand and gravel tend to be more similar when diffusional processes like soil creep and sheetwash are dominant. To date, however, no study has systematically compared TCN concentrations in different detrital grain-size fractions with a detailed inventory of hillslope processes from the entire catchment. Here we compare concentrations of the TCN ¹⁰Be in 20 detrital sand samples from the Quebrada del Toro (southern Central Andes, Argentina) to a hillslope-process inventory from each contributing catchment. Our comparison reveals a shift from low-slope gully and scree production in slowly denuding, low-slope areas to steep-slope gully and landsliding in fast-denuding, steep areas. To investigate whether the nature of hillslope processes (locally excavating or more uniformly denuding) may be reflected in a comparison of the ¹⁰Be concentrations of sand and gravel, we define the normalized sand-gravel index (*NSGI*) as the ¹⁰Be-concentration difference between sand and gravel divided by their summed concentrations. We find a positive, linear relationship between the *NSGI* and median slope, such that our *NSGI* values broadly reflect the shift in hillslope processes from low-slope gully and scree production to steep-slope gully and landsliding. Higher *NSGI* values characterize regions affected by steep-slope gully or landsliding. We relate the large scatter in the relationship, which is exhibited particularly in low-slope areas, to reduced hillslope-channel connectivity and associated transient sediment storage within those catchments. While high *NSGI* values in well-connected catchments are a reliable signal of deep-excavation processes, hillslope excavation processes may not be reliably recorded by *NSGI* values where sediment experiences transient storage.

2.1. Introduction

Terrestrial cosmogenic nuclides (TCN) have enabled the measurement of catchment-mean denudation rates over 10^2 – 10^6 year timescales (Bierman and Steig, 1996; Brown et al., 1995; Granger et al., 1996) and the tracking of changes in past denudation rates (e.g. Balco and Stone, 2005; Garcin et al., 2017; Schaller et al., 2004, 2002). However, it has been shown that the concentration of the TCN ¹⁰Be ($[^{10}\text{Be}]$) in detrital sediment, from which catchment-mean denudation rates are commonly inferred, is affected by hillslope processes such as landslides (Puchol et al., 2014; West et al., 2014) and debris flows (Kober et al., 2012). In several cases, $[^{10}\text{Be}]$ in detrital sediment has been shown to vary with grain size, which has been suggested to result from different hillslope processes mobilizing different grain-size distributions (Aguilar et al., 2014; Belmont et al., 2007; Carretier et al., 2015; Puchol et al., 2014; Schildgen et al., 2016). These observations imply that $[^{10}\text{Be}]$ in fluvial sediments not only track denudation rates and their changes through time, but also preserve information about hillslope processes within the contributing catchment area. To date, however, there has been no systematic study comparing $[^{10}\text{Be}]$ in different grain sizes to an inventory of hillslope processes within each contributing catchment.

Both TCN concentrations and grain-size distributions vary with depth. The *in-situ* production of ¹⁰Be is greatest at the Earth's surface and decreases approximately exponentially with depth (**Fig. 2.1A**; Lal, 1991). At ~3 m depth, the production rate is close to zero. In addition, grain-size distributions tend to coarsen with depth (Puchol et al., 2014; Ruxton and Beery, 1957). While the abundance of sand tends to be higher close to the surface and decreases with depth, the abundance of gravel tends to increase with depth due to less chemical weathering in deeper layers (Paasche et al., 2006; Puchol et al., 2014). In soil-mantled landscapes grain size distributions can deviate from this theoretical distribution due to the presence of a mixing layer (Riebe and Granger, 2013). If the surface is denuded uniformly and steadily throughout a catchment, the $[^{10}\text{Be}]$ in fluvial sediment is inversely related to the mean denudation rate (Bierman and Steig, 1996; Brown et al., 1995; Granger et al., 1996; Lal, 1991). Deep-excavation processes such as landsliding can remove several meters of material instantly, and consequently contribute sediment with low $[^{10}\text{Be}]$ to channels, resulting in higher catchment-mean denudation rates inferred from detrital sediment concentrations (Niemi et al., 2005; Puchol et al., 2014; West et al., 2014; Yanites et al., 2009). Landsliding or debris-flow activity also tends to produce coarser detrital material relative to processes like soil creep, because their mobilized material comprises a larger proportion of deeply-sourced, less-weathered, coarser material (**Fig. 2.1B**; Attal et al., 2015; Attal and Lavé, 2006; Roda-Boluda et al., 2018; Sklar et al., 2017). Consequently, $[^{10}\text{Be}]$ in detrital gravel and sand fractions should be affected by hillslope erosion processes. We define the normalized sand-gravel index (*NSGI*) as the ¹⁰Be concentration-difference between sand ($[^{10}\text{Be}]_{\text{sand}}$) and gravel ($[^{10}\text{Be}]_{\text{gravel}}$) normalized to their summed concentrations (**Fig. 2.1C**):

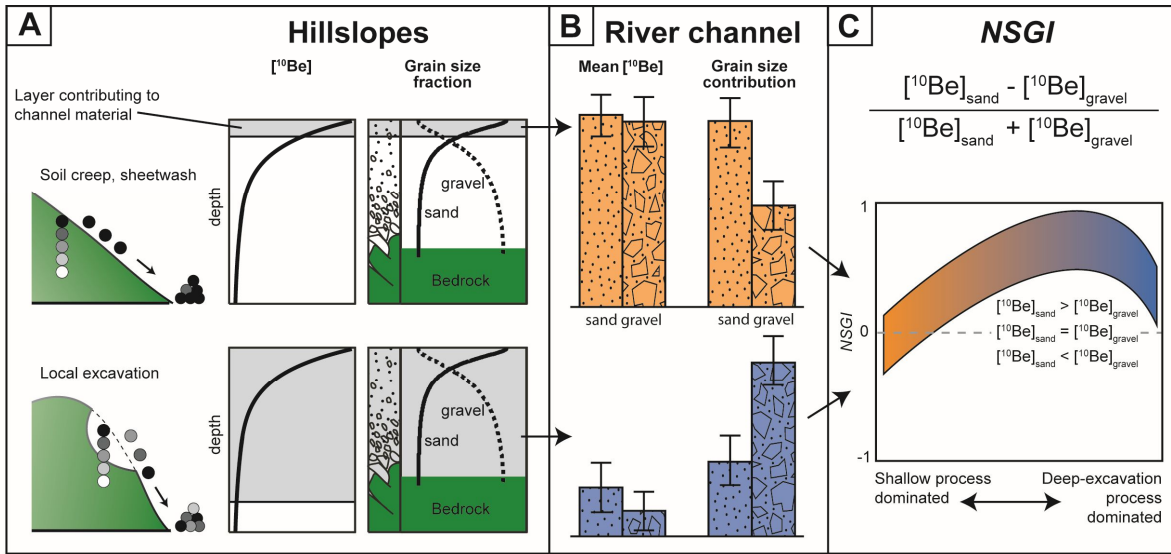


Fig. 2.1 Schematic diagram showing the derivation of the normalized sand-gravel index (*NSGI*) and hypothesized dependence on erosion processes. (A) ^{10}Be concentration ($[^{10}\text{Be}]$) of hillslope material decreases exponentially with depth (black to white circles and solid lines). The sand fraction is most abundant at the surface and decreases with depth, whereas gravel is more abundant in deeper layers less affected by weathering. (B) In soil creep or sheetwash dominated areas, the $[^{10}\text{Be}]$ in detrital sand and gravel is higher than in areas influenced by local excavation processes, where the removal of deeper material results in the dilution of ^{10}Be in detrital sediments. Diffusional processes can mobilize more sand than gravel, whereas local excavation processes typically mobilize more gravel than sand. (C) For purely soil creep and sheetwash dominated areas, a *NSGI* of 0 ($[^{10}\text{Be}]_{\text{sand}} = [^{10}\text{Be}]_{\text{gravel}}$) to -1 is expected. Negative values may result from slower hillslope transport of gravel compared to sand (e.g., Codilean et al., 2014). An increased abundance of local excavation processes should shift the *NSGI* toward more positive values. Highest *NSGI* values are expected when the majority of the gravel is contributed by deeper excavation events with low $[^{10}\text{Be}]_{\text{gravel}}$ and the majority of the sand contributed by shallow processes. The *NSGI* decreases again if deep-excitation events dominate the sampled sediment, and provide the majority of both the sand and gravel. The graphs of column A were modified from Puchol et al., (2014).

$$NSGI = \frac{[^{10}\text{Be}]_{\text{sand}} - [^{10}\text{Be}]_{\text{gravel}}}{[^{10}\text{Be}]_{\text{sand}} + [^{10}\text{Be}]_{\text{gravel}}} \quad (2.1)$$

In areas dominated by diffusive hillslope processes like soil creep and sheetwash, fluvial sand and gravel is mainly sourced from near-surface layers with similar $[^{10}\text{Be}]$, resulting in an *NSGI* of around 0 (**Fig. 2.1C**). If our assumptions about deep-excitation processes contributing coarser sediment with lower $[^{10}\text{Be}]$ are correct, an increased contribution of those processes will lead to more positive *NSGI* values. The *NSGI* will peak near 1 when the majority of sand comes from diffusional processes with high $[^{10}\text{Be}]_{\text{sand}}$, while the majority of the gravel is contributed by deeper layers with low $[^{10}\text{Be}]_{\text{gravel}}$ that are mobilized by deep excavation processes. The *NSGI* should decrease again if deep-excitation events dominate the sampled sediment, and provide the majority of both the sand and gravel (e.g. landslide deposits). For such deposits, the *NSGI* would reflect the local $[^{10}\text{Be}]$ difference of the sand and gravel fractions due to their sourcing from different depth layers (**Fig. 2.1A**). In areas characterized only by diffusive hillslope processes like soil creep and sheetwash, $[^{10}\text{Be}]_{\text{sand}}$ should be equal to or lower than $[^{10}\text{Be}]_{\text{gravel}}$ (*NSGI* = -1 to 0). Higher

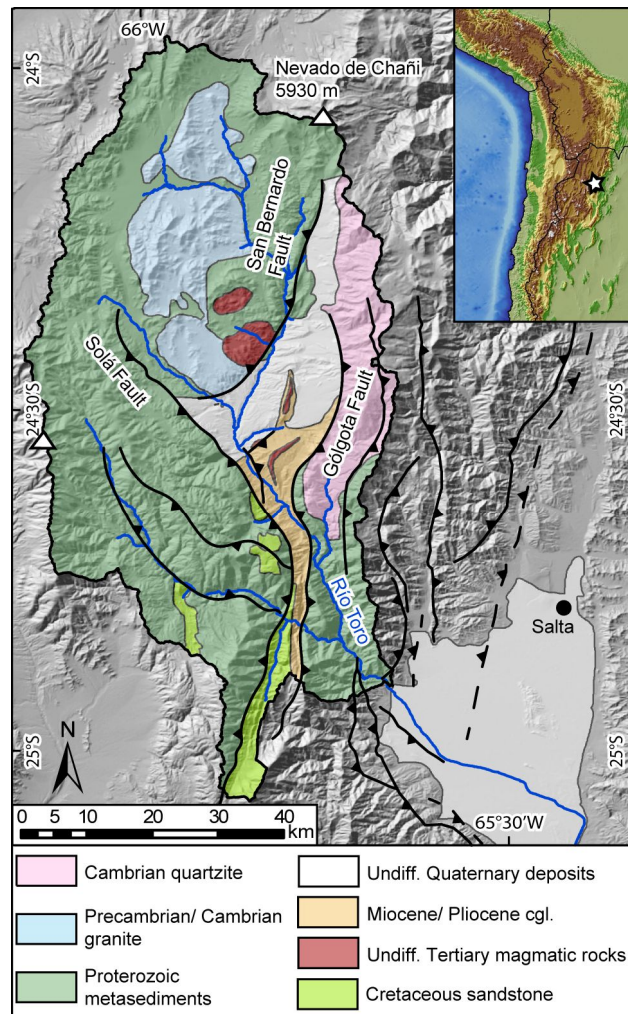


Fig. 2.2 Geological map of the Quebrada del Toro (modified after García et al., 2013; Hilley and Strecker, 2005; Tofelde et al., 2017). The intermontane basin is located within the Eastern Cordillera of the southern Central Andes (insert), with the Puna Plateau to its west and the foreland to its east.

^{10}Be in gravel relative to sand, which would result in negative *NSGI* values, has rarely been reported, but has been attributed to the accumulation of ^{10}Be during slower transport of gravel compared to sand on gentle slopes (Codilean et al., 2014).

As a preliminary test of how different hillslope processes affect ^{10}Be in different grain sizes, we first compare ^{10}Be measured in fluvial sands collected from the Quebrada del Toro in the southern Central Andes to our mapped inventory of five distinct hillslope processes to investigate potential correlations among hillslope gradient, denudation rate, and hillslope processes. Second, we address whether a signal of hillslope processes is reflected in comparisons of ^{10}Be in sand and gravel fractions, such that variations in erosion processes may be traced in sedimentary archives.

2.2. Study area

The Quebrada del Toro is a N-S oriented intermontane basin in the Eastern Cordillera of NW Argentina, which narrows southward where it traverses late Proterozoic basement rocks (**Fig. 2.2**). The basin is located between the arid Altiplano-Puna Plateau to the west and the humid foreland to the east, and it is bordered by reverse-fault bounded basement ranges. Activity on the Solá Fault in the west began in late Miocene time (Hilley and Strecker, 2005); to the northeast is the Gólgota Fault, which has been active since the Miocene and delimits the Sierra Pasha, a formerly glaciated range that forms an orographic barrier to precipitation (Marrett and Strecker, 2000). Exposed lithologic units in the ranges include late Proterozoic quartz-bearing metasediments, late Precambrian to early Cambrian granites, Cambrian quartzites, Cretaceous to Tertiary continental sandstones, Cretaceous shallow marine limestones, Miocene to Pliocene conglomerates, and Quaternary gravels (Omarini et al., 1999; Reyes and Salfity, 1973; Schwab and Schäfer, 1976). The basin covers ~4000 km² between elevations of 1500 to 5900 m asl and is drained by the braided Río Toro. The region is subjected to ongoing deformation (García et al., 2013) and frequent, low-magnitude earthquakes (Hain et al., 2011).

2.3. Methods

2.3.1. Cosmogenic radionuclide analysis

We collected 15 detrital sand samples (250 – 500 µm) for ¹⁰Be analysis along the Río Toro main stem (n = 4; sample prefix “M”) and its tributaries (n = 11; sample prefix “T”) to quantify denudation rates (**Table 2.1**). In 13 of those locations, we additionally sampled pebbles (1-3 cm, >65 clasts for each sample). The drainage areas of the main-stem samples range from 1495 to 2962 km², whereas the tributary catchments range from 9 to 779 km². Tributaries were sampled sufficiently far upstream to avoid admixing by main-stem material during flooding. In addition, we re-analyzed the ¹⁰Be data from five previously published detrital sand samples from the Quebrada del Toro using an updated reference production rate (C1, C2, C3, C5, C6; Bookhagen and Strecker, 2012).

The sand and gravel samples were collected in March 2014. Mineral separation and quartz purification was carried out at the University of Potsdam, Germany. Sample preparation followed standard procedures (von Blanckenburg et al., 2004). First, samples were crushed (in the case of pebbles) and sieved. Next, quartz grains from the sand (250 – 500 µm) and crushed-pebble (250 - 1000 µm) samples were concentrated through magnetic separation. Subsequent chemical treatments with HCl and H₂O₂ dissolved carbonate and organic components. To dissolve non-quartz minerals and remove meteoric ¹⁰Be, the samples were leached three times with a 1% HF/HNO₃ solution in an ultrasonic bath for 12 h each. Column

¹⁰Be concentration in fluvial sand and gravel

Table 2.1 Cosmogenic nuclide samples. CC= pebble samples, CS= sand samples, P(mu)= muon production rate, P(sp)= spallation production rate. Catchment mean denudation rates calculated with a reference spallation production rate of 4.00 atoms/(g*yr) (Borchers et al., 2016) and the time-dependent scaling scheme of Lal (1991) and Stone (2000). All calculations were performed using the 07KNSTD ¹⁰Be standard.

Sample name	Latitude (°S)	Longitude (°W)	Drainage area (km ²)	Measured ¹⁰ Be / ⁹ Be	Error (%)	¹⁰ Be ± 1σ (atm/g)	Topo. shield	P(mu) (atm/g/yr)	P(sp) (atm/g/yr)	Denudation rate ± 1σ (mm/yr)
M08_CC	24.54671	65.86952	2196	4.611e-12	3.07	939112 ± 28862				
M08_CS	24.54671	65.86952	2196	4.411e-12	3.06	869576 ± 26639	0.99	0.24	42.66	0.028 ± 0.0027
T11_CC	24.54951	65.86073	130	1.331e-12	3.16	247465 ± 7863				
T11_CS	24.54951	65.86073	130	8.935e-13	3.2	171990 ± 5559	0.99	0.22	36.81	0.112 ± 0.0105
M15_CC	24.49079	65.85755	1665	4.632e-12	3.06	916547 ± 28076				
M15_CS	24.49079	65.85755	1665	3.529e-12	3.08	691466 ± 21329	0.99	0.24	43.18	0.035 ± 0.0033
T26-CC	24.89980	65.67305	33	7.583e-15	15.06	1259 ± 1103				
T26-CS	24.89980	65.67305	33	1.329e-14	10.41	9547 ± 3383	0.95	0.18	23.13	1.232 ± 0.5100
T27-CC	24.84270	65.71425	9	7.286e-15	33.47	990 ± 1131				
T27-CS	24.84270	65.71425	9	1.873e-14	7.94	7457 ± 1697	0.96	0.16	19.17	1.337 ± 0.3398
T28-CC	24.64685	65.80950	114	3.048e-13	3.77	201980 ± 7977				
T28-CS	24.64685	65.80950	114	8.65e-13	3.38	189445 ± 6467	0.97	0.23	38.56	0.106 ± 0.0100
T32-CC	24.75050	65.74763	11	9.847e-14	4.96	27877 ± 1695				
T32-CS	24.75050	65.74763	11	2.525e-13	3.98	81981 ± 3462	0.95	0.20	28.49	0.181 ± 0.0174
T35-CC	24.36600	65.79750	100	2.119e-12	3.2	690382 ± 22155				
T35-CS	24.36600	65.79750	100	3.249e-12	3.13	445592 ± 13970	0.98	0.26	51.27	0.061 ± 0.0058
T43-CC	24.80866	65.80130	770	2.871e-14	8.41	7850 ± 1226				
T43-CS	24.80866	65.80130	770	4.288e-13	3.56	37265 ± 1365	0.97	0.23	42.01	0.541 ± 0.0513
T44-CC	24.81043	65.80020	176	7.568e-15	15.06	2169 ± 1906				
T44-CS	24.81043	65.80020	176	2.066e-13	4.04	18858 ± 826	0.96	0.23	40.40	1.033 ± 0.1009
M48_CS	24.79751	65.72750	2962	1.597e-12	3.13	322541 ± 10139	0.98	0.23	40.67	0.067 ± 0.0064
T59-CC	24.40490	65.82160	99	2.511e-12	3.16	768568 ± 24342				
T59-CS	24.40490	65.82160	99	1.349e-11	3.08	2173832 ± 66975	0.99	0.22	38.14	0.010 ± 0.0010
M60_CS	24.40700	65.81952	1495	4.673e-12	3.07	955189 ± 29355	0.99	0.24	44.15	0.026 ± 0.0025
T68_CC	24.49691	65.87763	474	4.856e-12	3.07	986599 ± 30319				
T68_CS	24.49691	65.87763	474	9.427e-12	3.05	1413630 ± 43136	0.98	0.23	42.39	0.017 ± 0.0017
T69_CC	24.56590	65.86406	79	4.562e-12	3.06	901168 ± 27606				
T69_CS	24.56590	65.86406	79	1.197e-12	3.17	943985 ± 30117	0.97	0.23	40.90	0.025 ± 0.0024
C1*	24.50169	65.86240	1672			745690 ± 14250	0.99	0.24	43.11	0.032 ± 0.0030
C2*	24.52355	65.87348	493			1510820 ± 18610	0.98	0.23	41.97	0.016 ± 0.0015
C3*	24.55461	65.86698	130			402260 ± 4590	0.99	0.22	36.77	0.050 ± 0.0045
C5*	24.72431	65.75522	178			314670 ± 5950	0.98	0.23	41.19	0.070 ± 0.0063
C6*	24.84070	65.72560	1011			38220 ± 1030	0.97	0.23	40.53	0.511 ± 0.0467
Blanks										
ST_Blk2**				3.061e-15	19.48					
ST_Blk3**				1.953e-15	23.14					
ST_Blk4**				9.654e-15	11.58					
ST_Blk1**				6.839e-15	15.91					
SS_Blk6**				6.898e-16	44.82					
BLK1				2.279e-15	25.19					
BLK2				1.678e-15	26.9					
ST_Blk6				6.701e-15	16.51					
MDBLK1				8.26e-16	37.92					
ST_Blk5**				5.113e-15	21.5					
mean				3.879e-15						

* Samples previously published (Bookhagen and Strecker, 2012). ¹⁰Be concentrations were extracted from the original publication, all further calculations were redone.

** Previously published blanks (Tofelde et al., 2017).

chemistry and target preparation was performed at the GeoForschungsZentrum (GFZ) Potsdam, Germany, following standard procedures (i.e. von Blanckenburg et al., 2004). Prior to dissolution, 150 µg of a ⁹Be carrier was added to each sample. Quartz was digested with concentrated HF (48%), and Be(OH)₂ was isolated via column chemistry. Be(OH)₂ was oxidized to BeO, mixed with Niobium, and prepared as targets for ¹⁰Be/⁹Be measurement with an accelerator mass spectrometer (AMS). AMS measurements were performed at the Department of Geology and Mineralogy, University of Cologne, Germany. The AMS standards used were KN01-6-2 and KN01-5-3; these have nominal ¹⁰Be/⁹Be ratios of 5.35*10⁻¹³ and 6.32*10⁻¹², respectively. Blank corrections were performed using the average value of all 10 blanks processed during sample preparation (**Table 2.1**; a mean ¹⁰Be/⁹Be ratio of 3.88*10⁻¹⁵ was used for blank corrections of ¹⁰Be/⁹Be sample ratios).

The ¹⁰Be concentration of fluvial sediment can be used to calculate catchment-mean denudation rates (ε) using the following equation (Lal, 1991):

$$\varepsilon = \left(\frac{P_0}{C_0} - \lambda \right) \frac{A}{\rho} \quad (2.2)$$

with P being the catchment-mean ¹⁰Be production rate [atm/(g*yr)] and C the measured ¹⁰Be concentration [atoms/g]; the subscript 0 on both refers to the surface (depth of zero). λ is the ¹⁰Be decay rate [atoms/(g*yr)], A is the attenuation coefficient [g/cm²] and ρ is the density of the eroding material [g/cm³]. To solve this equation, we used the script of Scherler et al. (2014), which calculates the production rate first for each pixel within a catchment based on the reference production rate, the scaling scheme, and local shielding. Next, the script computes a catchment-mean production rate. For our analysis, we used a reference spallation-production rate of 4.00 atoms/(g*yr) (Borchers et al., 2016) and the time-dependent scaling scheme of Lal (1991) and Stone (2000), commonly known as the Lm-scaling scheme (Balco et al., 2008). In addition, we used the decay rate for ¹⁰Be of $4.99 \pm 0.043 \cdot 10^{-7} \text{ yr}^{-1}$ (Chmeleff et al., 2010; Korschinek et al., 2010), an attenuation coefficient of 160 g/cm², and a rock density of 2.7 g/cm³. All calculations were performed using the 07KNSTD ¹⁰Be standard. We report 1 σ uncertainties for the denudation rates. The uncertainties are equivalent to the external uncertainties given by the CRONUS-Earth calculator (Balco et al., 2008) and include the analytical uncertainty of the ¹⁰Be AMS measurement and the uncertainties of the reference spallation and muogenic production rates.

2.3.2. Hillslope-process inventory

We compared the ¹⁰Be concentrations to a hillslope-process inventory that we created from Google Earth imagery, by mapping four non-diffusive, gravel-producing hillslope processes with a total of >8,500

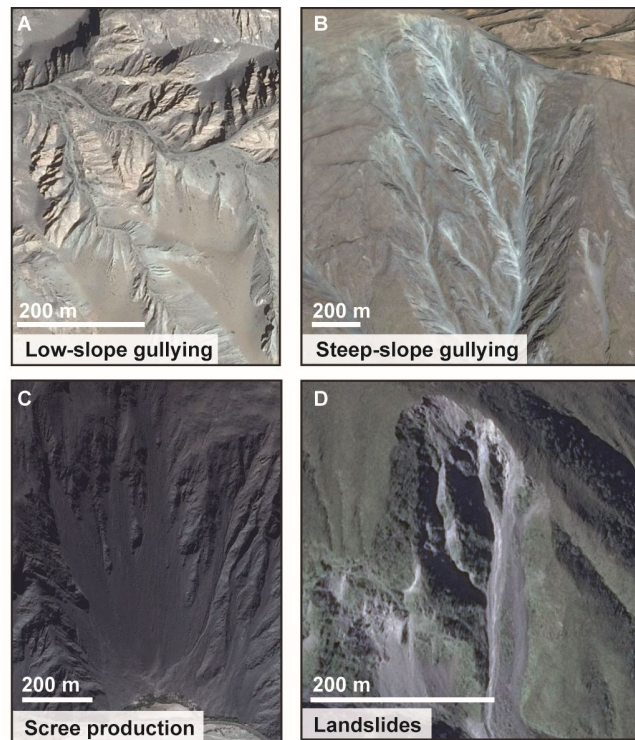


Fig. 2.3 The hillslope-process inventory is based on mapping in Google Earth. The four gravel-producing processes are (A) low-slope gullying (Image: Google, CNES/ Airbus, 2017), including the incision of first-order streams into Miocene to Quaternary sedimentary deposits; (B) gullying on steep slopes (Image: Google, CNES/ Airbus, DigitalGlobe, 2017), mostly associated with debris flows; (C) scree production (Image: Google, Google, CNES/ Airbus, 2017), mostly as a product of river undercutting followed by the formation of talus slopes, and (D) deep-seated landsliding (Image: Google, DigitalGlobe, 2017), characterized by stochastic events that instantly remove hillslope material up to several meters beneath the surface.

polygons. We used the available historical imagery, with most images starting between 2003 and 2009. We named the four processes that we observed in the Quebrada del Toro *low-slope gullying*, *scree production*, *steep-slope gullying*, and *deep-seated landsliding* (**Fig. 2.3**; KML files containing our hillslope-process inventory can be found in the supplementary material). *Low-slope gullies* form rills in gently sloping sedimentary deposits (mostly Miocene to Quaternary in age) and mobilize gravel close to the surface. *Steep-slope gullies* occur on steep slopes and are associated with debris-flows, which remove material from depths of up to several meters. *Scree production* occurs on steep slopes and is often related to river undercutting. *Deep-seated landslides* are rare, but tend to occur on steep slopes, where they mobilize rock from up to several meters depth. Moraine deposits visible in several locations above ~3700 m elevation indicate the former presence of glaciers. We mapped the extent of glaciers based on moraines and glacially carved valleys. However, the previously glaciated parts of the landscape today appear mainly diffusive, or are otherwise mapped as one of the areas characterized by the four non-diffusional processes. We summed the total area of each non-diffusive erosion process for each catchment using ArcGIS and defined the remaining

area as characterized by diffusional processes, i.e., soil creep or sheetwash (**Table A1**). We make the assumption that the spatial distribution of those processes today is representative for the timescale over which the denudation rates average (10^2 to 10^5 yr).

2.3.3. Topographic analysis

Our stream network and slope analysis are based on the ~30-m-resolution SRTM digital elevation model (DEM) (data available from the U.S. Geological Survey). Slope is calculated for each pixel as the maximum rate of change in elevation between that pixel cell and its neighboring 8 cells. Based on that map, the slope distribution for each catchment and for the hillslope processes can be extracted. Then, a median slope value for the catchments and hillslope processes is calculated. We calculate the median rather than the mean slope due to the non-normal slope distributions, but the values differ by only 1 to 3 degrees for each catchment, and the choice of either does not affect the observed trends (**Table A2**). Previous studies have shown that the standard deviation of the slope depends on the resolution of the DEM (Ouimet et al., 2009). Instead of reporting the standard deviation, we additionally show the entire slope distribution from SRTM ~30-m data. Longitudinal river profiles were extracted in Matlab using the FLOWobj- and STREAMobj- functions provided by the TopoToolbox (Schwanghart and Scherler, 2014).

2.4. Results

2.4.1. Denudation rates and hillslope processes

Catchment-mean denudation rates derived from the sand samples range from 0.01 ± 0.001 to 1.34 ± 0.34 mm/yr (**Fig. 2.4A, Table 2.1**). Five additional denudation rates (C1, C2, C3, C5, C6) were recalculated from ¹⁰Be data previously reported by Bookhagen and Strecker (2012). Three of those sites (C1, C2 and C3) were sampled near our sample locations; the associated denudation rates either agree within uncertainty (C1, C2) or within a factor of ~2 (C3) of our calculated rates. This difference is minor compared to the increase in denudation rates from N to S across the field area, which spans two orders of magnitude (**Fig. 2.4A insert**).

Catchment-mean denudation rates increase non-linearly with catchment-median slope (**Fig. 2.4B**). In detail, denudation rates increase linearly with median slope up to around 25°, beyond which they increase approximately exponentially. Denudation rates also increase non-linearly with normalized channel steepness index (k_{sn}) (e.g. Wobus et al., 2006) and relief, but those relationships show a weaker correlation (**Fig. A1, Table A2**).

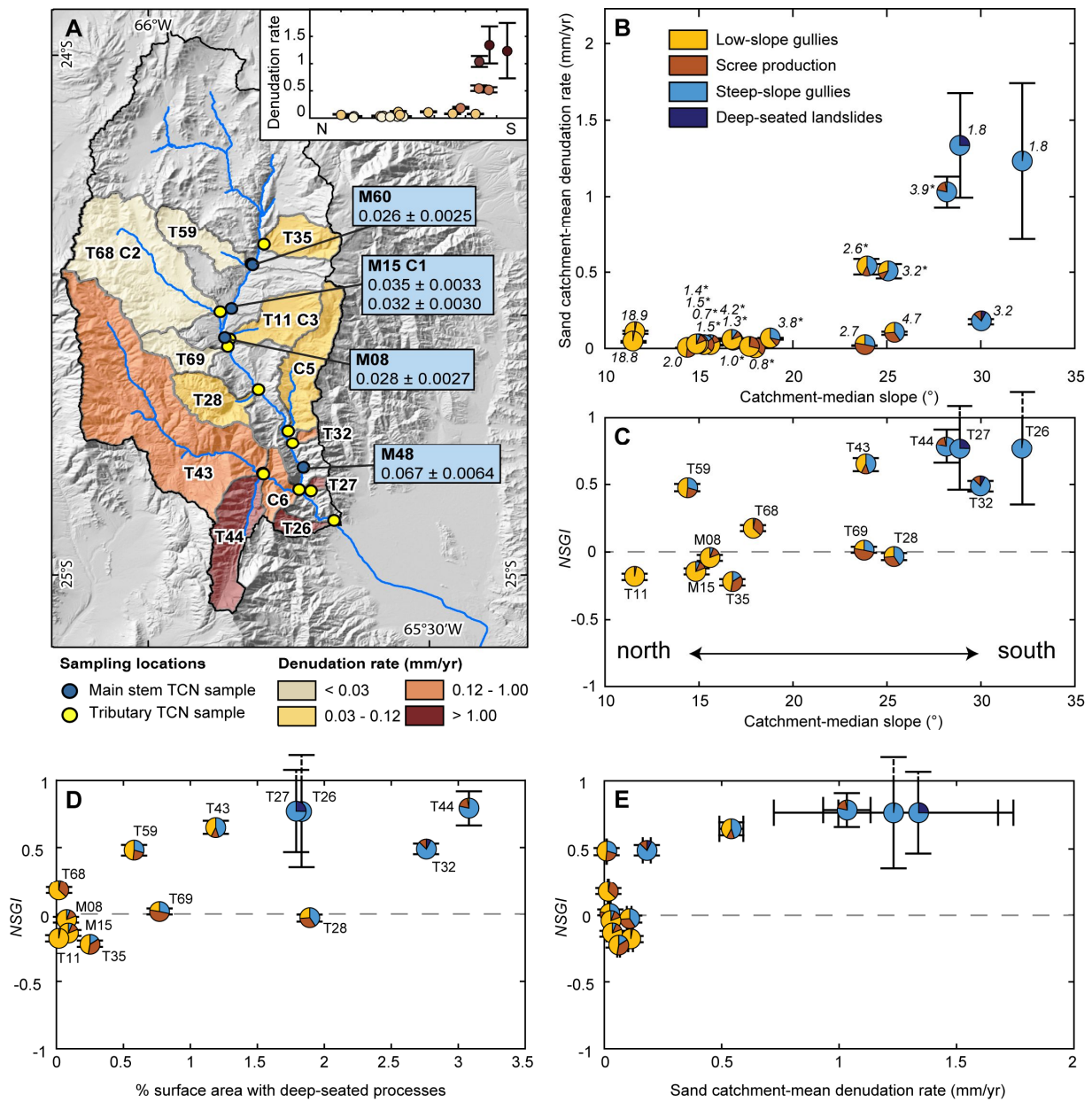


Fig. 2.4 (A) Sampling sites for detrital sand ($n=20$) and gravel ($n=13$, names of gravel sample sites given in C) along the main stem (blue, sample prefix “M”) and tributaries (yellow, sample prefix “T”). Samples with the prefix “C” were recalculated from a previously published dataset (Bookhagen and Strecker, 2012). The catchments are colored according to mean denudation rates, which were calculated from ^{10}Be in sand samples. The inset shows the increase in denudation rates by two orders of magnitude from N to S. (B) Catchment-mean denudation rates correlate non-linearly with catchment-median slope. Pie charts indicate the relative surface area influenced by low-slope gully, scree production, steep-slope gully, and deep-seated landsliding. The numbers depict the percentage catchment area affected by those four processes. Numbers with asterisks indicate the presence of moraines in the catchment. (C) The NSGI increases positively with catchment-median slope, and it increases overall with the occurrence of steep-slope gully and landsliding. (D) The NSGI increases with percentage of catchment area affected by deep-seated processes, such as landslides or steep-slope gully. (E) The NSGI shows a non-linear relationship with catchment-mean denudation rates derived from the sand fraction. Whereas slowly denuding areas experience some scatter in their NSGI, NSGI values become consistently larger than 0.5 and increase with higher denudation rates once catchment-mean denudation rates exceed ~ 0.2 mm/yr.

Our hillslope-process inventory allows us to investigate how denudation rates and topographic metrics vary with hillslope processes. The pie charts (**Fig. 2.4B**) represent the proportional area covered by *low-slope gullying*, *steep-slope gullying*, *scree production*, and *deep-seated landsliding*. The numbers indicate the percentage of the catchment area covered by those four processes; the remaining area in each catchment is characterized by diffusional hillslope processes (soil creep or sheetwash). An asterisk indicates the presence of moraines in the catchment. Previously glaciated regions range from ~0.2 to ~15.7% of the catchment areas. We found no relationship between the formerly glaciated area and denudation rates, but we found a gradual shift in the type of erosion processes with increasing denudation rates and slopes. Apart from soil creep or sheetwash, low-gradient areas with low denudation rates are influenced by *low-slope gullying*. With increasing hillslope angles and denudation rates, *scree production* becomes more important, and when hillslope angles increase further, *steep-slope gullying* becomes more prevalent. Evidence for present-day *deep-seated landsliding* is sparse.

The total area covered by any of those four non-diffusive processes is small (0.7 to 18.8% of the catchment areas; **Table A1**). However, we only mapped areas with clear remnants of any of those four processes. The time for the visible recovery of the landscape after any localized mass-wasting event, however, is likely shorter than the recovery of the steady-state ¹⁰Be depth profile in the bedrock. The mapped areal extents of non-diffusive processes are therefore likely underestimated with respect to the averaging timescale of the cosmogenic method.

2.4.2. Normalized sand-gravel index

We measured *NSGI* values between -0.22 and 0.79 (**Fig. 2.4C**, **Table A2**). The index values, although showing substantial scatter, increase linearly with catchment-median slope, indicating an increasing contribution of low [¹⁰Be]_{gravel} on steeper hillslopes. Negative *NSGI* values only occur in catchments characterized by low-gradient slopes, low denudation rates, and *low-slope gullying*, whereas positive values close to 1 occur in steep, rapidly eroding catchments influenced by *steep-slope gullying* and *deep-seated landsliding*. Furthermore, despite some scatter, we find that the *NSGI* increases with the proportion of the catchment surface area affected by *landslides* and *steep-slope gullies* (**Fig. 2.4D**). Overall, < 3.5 % of the total catchment areas are affected by these deep-seated process, but, we expect these numbers to be underestimated due to the restriction of the hillslope-process mapping to the last ~10 years of available imagery.

The non-linear increase of denudation rate with slope and the linear increase of *NSGI* with slope result in a non-linear relationship between denudation rate and *NSGI* (**Fig. 2.4E**). Slowly denuding areas

reveal a range of *NSGI* values between -0.22 and 0.5. Once denudation rates exceed ~0.2 mm/yr, *NSGI* values exceed 0.5 and increase with higher denudation rates.

2.5. Discussion

2.5.1. Correlation between denudation rates and hillslope processes

The non-linear increase in ¹⁰Be-derived catchment-mean denudation rates with catchment-median slope in our dataset (**Fig. 2.4B**) is in agreement with earlier studies (e.g. Binnie et al., 2007; Carretier et al., 2013; DiBiase et al., 2010; Ouimet et al., 2009; von Blanckenburg et al., 2004). As noted by those studies, whereas the mean or median hillslope gradient tracks catchment-mean denudation rates for lower slopes, this topographic metric becomes insensitive to changes in erosion rate in steeper areas, when hillslopes reach threshold angles. It has been suggested that once river incision creates hillslopes steep enough to initiate landsliding, any further increase in river down-cutting is accommodated by an increase in landslide frequency and not by further steepening of slopes (Burbank et al., 1996). Field studies have supported this idea, by showing that despite having similar mean hillslope angles, inventory-based landslide erosion rates are highly variable and correlate well with exhumation rates (Bennett et al., 2016; Larsen and Montgomery, 2012). Both modeling studies and empirical observations support the idea that landslide activity influences the [¹⁰Be] in fluvial sediments by introducing low-concentration material to channels, resulting in higher inferred denudation rates (Niemi et al., 2005; Puchol et al., 2014; West et al., 2014; Yanites et al., 2009).

In our study area, recent deep-seated *landslides* are rarely observed, despite the non-linear increase in denudation rates in steeper areas. We find a gradual shift in hillslope processes with increasing hillslope angles from *low-slope gullying*, to *scree production*, and finally to *steep-slope gullying* and *landsliding* (**Fig. 2.4B**). In particular, we find *steep-slope gullying* to be the most common process characterizing threshold hillslopes, rather than deep-seated *landsliding*.

We assume that all mapped hillslope processes erode to a different average depth per event, have different recurrence intervals, and consequently affect the [¹⁰Be] in fluvial sediment to a different degree. To quantify the impact of those individual hillslope processes on [¹⁰Be] in mobilized sediment, we would not only need to know the average depth per event and average recurrence, but also the vertical distribution of grain sizes. Because the current knowledge on grain size-distributions associated with various hillslope processes is limited (Attal et al., 2015; Attal and Lavé, 2006; Marshall and Sklar, 2012; Sklar et al., 2017), we cannot yet quantify the contribution of the individual hillslope processes to our measured [¹⁰Be], nor can we quantify the sediment flux associated with each process. However, our dataset suggests that the non-

linearity in the relationship between ¹⁰Be-derived denudation rates and slope is not only linked to changing landslide frequency, but also to a shift in the type of hillslope processes occurring within the catchments.

2.5.2. Normalized sand-gravel index

To our knowledge, 17 studies to date have performed ¹⁰Be analyses of both detrital sand (< 2 mm) and gravel (>1 cm) (detailed list in **Table A3**). In most cases, those studies found significant differences between [¹⁰Be]_{sand} and [¹⁰Be]_{gravel}. Carretier et al. (2015) and Aguilar et al. (2014) summarized different mechanisms that may explain the common occurrence of lower [¹⁰Be]_{gravel} compared to [¹⁰Be]_{sand} (*NSGI* > 0). These are: (1) a large contribution of glacial pebbles with low [¹⁰Be] due to shielding by ice (e.g. Wittmann et al., 2007); (2) lithological variations leading to gravel production mainly at lower elevations, where ¹⁰Be production rates are lower (e.g. Palumbo et al., 2009); (3) an over-representation of gravels from low elevations, because high-elevation gravels are comminuted during transport (e.g. Belmont et al., 2007; Matmon et al., 2003) (4) deep-excavation events exhuming coarse material with low [¹⁰Be] (e.g. Belmont et al., 2007; Brown et al., 1995; Puchol et al., 2014); (5) coarse material being primarily derived from steep, faster eroding slopes (e.g. Carretier et al., 2015; Riebe et al., 2015); or (6) the alteration of [¹⁰Be] in sand and gravel due to temporary storage within the catchment (e.g. Schildgen et al., 2016). Conversely, [¹⁰Be]_{sand} can be lower than [¹⁰Be]_{gravel} (*NSGI* < 0) when gravels are transported more slowly than sand across low-gradient slopes (Codilean et al., 2014). In the following, we will discuss for each of those processes (i) how the different mechanisms affect [¹⁰Be], (ii) if those mechanisms apply to our study area and, (iii) if they can explain the positive trend of *NSGI* with catchment-median slope in our dataset (**Fig. 2.4C**).

Glacial debris can increase the *NSGI* value, if the glacial deposits contribute more gravel than sand and if those gravels have a lower [¹⁰Be] than the hillslope material due to shielding by glacial ice (Wittmann et al., 2007). In our study area, glacial moraines are present (as indicated in **Fig. 2.4B**), but we found no systematic relationship between *NSGI* and previous glacial cover: the catchments with the highest *NSGI* values experienced no visible glacial overprint.

Lithological variability can explain positive *NSGI* values, if gravel is exclusively derived from a rock type that only occurs at low elevations in the catchment, where ¹⁰Be production rates are lower. Lithological variations are present in our study area (**Fig. 2.2**), but cannot explain the observed systematic increase in *NSGI* from north to south. In several catchments, only one lithology crops out - Proterozoic metasediments (**Fig. A2**). Among those catchments, we measured both very high *NSGI* values close to 1 (T26, T27) and low *NSGI* values close to 0 (T69, T28) (**Fig. 2.4C**).

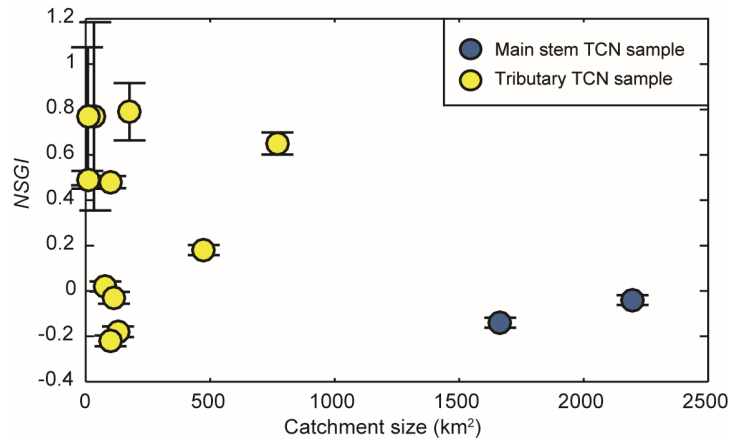


Fig. 2.5 Relationship between NSGI values and catchment size for tributary samples (yellow) and main-stem samples (blue); no correlation is observed. As such, attrition and upstream sediment storage, which are assumed to be more effective in larger catchments, cannot be the main drivers for the positive linear relationship between NSGI and catchment-median slope.

Comminution of gravels during transport would result in an over-representation of gravel from lower elevations, where ^{10}Be production rates are lower. This mechanism probably affected our samples, but likely only to a minor degree. Attal and Lavé (2009, 2006) experimentally measured mean abrasion rates between 0.15 and 0.4 %/km for Himalayan quartzites, quartzitic sandstones, and granites. The lengths of our sampled tributaries range from ~4 to ~75 km. These lengths would imply a maximum possible grain-size reduction of 30% through abrasion, but in most cases less than 10% for the farthest-transported gravel. In another study from the Tsangpo-Brahmaputra catchment, Lupker et al. (2017) modelled abrasion to explain observed dilution in fluvial [^{10}Be]. They predicted that the effects of abrasion become apparent after 50 to 150 km, which is longer than the majority of our catchments. If the variations in NSGI in our study area were explained by an over-representation of gravels derived from low-elevations, we would expect a correlation between the NSGI and catchment size, but such a correlation does not occur in our dataset (**Fig. 2.5**).

The increase of NSGI values with median catchment slope in our dataset implies a higher contribution of low [^{10}Be]_{gravel} in steep areas. Those steep areas are characterized by *steep-slope gullying* and *deep-seated landsliding* (**Fig. 2.4C**). As we assume that all hillslope processes contribute to the fluvial sand and gravel fractions, but that deep seated processes produce relatively more gravel and diffusional hillslope processes produce relatively more sand (**Fig. 2.1B**), two mechanisms can achieve lower [^{10}Be]_{gravel} relative to [^{10}Be]_{sand}. One possibility is that the erosion depth and/or recurrence interval of deep-excavation processes increases with steeper slopes (Puchol et al., 2014), such that the [^{10}Be]_{gravel} is diluted by deeply sourced gravel with low [^{10}Be]. Because deep-seated processes contribute relatively less sand, the [^{10}Be]_{sand} is diluted less, and the difference between [^{10}Be]_{gravel} and [^{10}Be]_{sand} increases. Alternatively, the percentage

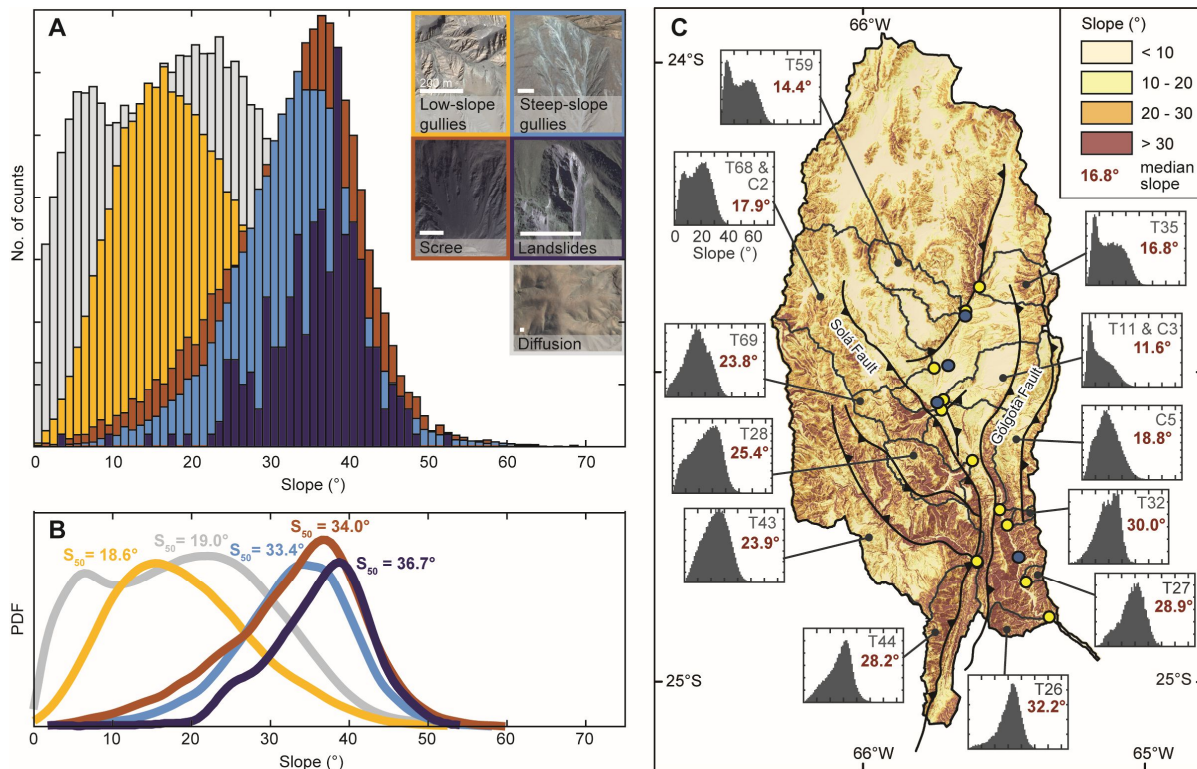


Fig. 2.6 Slope distributions of the five mapped hillslope processes represented as histograms (A) and best-fitted curves (B) together with the median slope for each process. Due to the great variability in abundance, the y-axes of (A) and (B) are scaled differently for each process for comparability. (C) Slope map of the Quebrada del Toro. Low-slope areas in the north are limited by the Solá and Gólgota faults. Insets show histograms of slope distributions for the sampled tributary catchments. Number indicates the median basin slope. Tributary slope distributions evolve from bimodal and with lower median slopes in the north to unimodal and higher median slopes in the south.

of catchment surface area affected by deep-seated processes increases with steeper slopes (Fig. 2.1C moving to the right). Although we have no field measurements (e.g. landslide depths) to demonstrate the depths of the hillslope processes, it is probable that *landslides* erode to a greater depth per event than, for example, *scree production*. Previous studies have measured coarser sediment in landslides compared to non-landsliding hillslope processes, indicating greater erosional depths in landslides (Attal et al., 2015; Roda-Boluda et al., 2018; Whittaker et al., 2010). Thus, an increasing depth per erosion event and/or shorter recurrence intervals of excavation events with steeper slopes could help explain the linear increase of *NSGI* with catchment-median slope. We also observe an increase in *NSGI* with the proportion of the catchment surface-area affected by deep-seated processes (Fig. 2.4D). Hence, both mechanisms are likely to help explain the observed variations in *NSGI*.

If gravel-producing processes are not equally distributed throughout the catchment, but instead occur preferentially on steeper, faster eroding slopes, then the [¹⁰Be] in gravel would be on average lower

^{10}Be concentration in fluvial sand and gravel

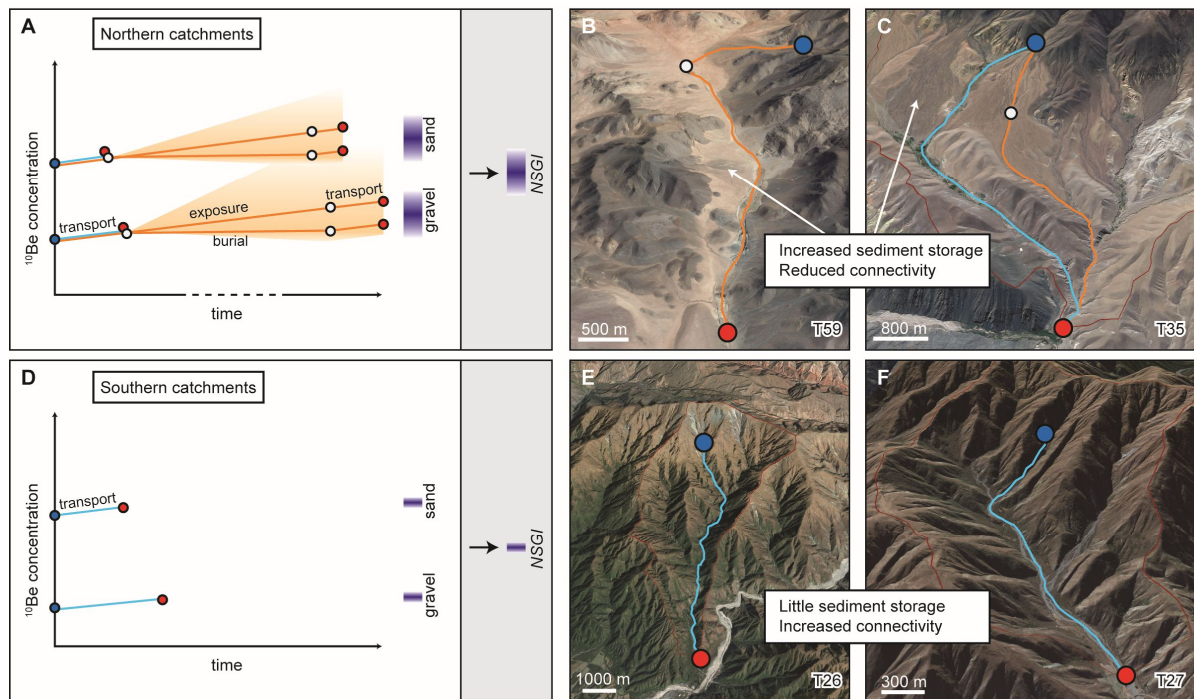


Fig. 2.7 (A) The evolution of [^{10}Be] in sand and gravel during transport and storage within the catchment. If gravel is derived, on average, from deeper in the profile, its [^{10}Be] is lower than that of the sand fraction. If those sediments are transported rapidly (blue line) from the hillslope (blue circle) to the catchment outlet (red circle), then additional accumulation of ^{10}Be during fluvial transport is low. The downstream transport of gravel is often slower compared to sand. However, if sediments are transiently stored in alluvial fans or fluvial terraces (white circle) and only later remobilized, the [^{10}Be] can significantly increase due to surface exposure, or slowly decrease when buried due to shielding from cosmic rays and subsequent nuclide decay. The sand grains or pebbles sampled at the outlet can consequently have diverse exposure and/or burial histories, which results in scatter of the NSGI. (B, C) Catchments in the north are characterized by significant sediment storage, which can reduce the hillslope-channel connectivity (Image A: Google, CNES/Airbus, 2018; Image B: Google, Digital Globe, CNES/Airbus, 2018). (D) Sand grains and pebbles collected at outlets experience a very similar transport history, such that [^{10}Be] signatures from the hillslopes remain largely unchanged and the NSGI values are consequently less scattered. (E, F) The catchments in the south show very little evidence for sediment storage, allowing for efficient downstream transport (Image D & E: Google, Digital Globe, CNES/Airbus, 2018).

than in sand. The mapped non-diffusive hillslope processes in the Quebrada del Toro tend to occur on different hillslope angles (**Fig. 2.6A**). Whereas *low-slope gullying* mainly occurs on lower slopes (median slope 18.6° ; **Fig. 2.6B**), the median hillslope angles increase for *steep-slope gullying* (33.4°), *scree production* (34.0°) and *deep-seated landsliding* (36.7°). The median slopes of *scree production*, *steep-slope gullying*, and *landsliding* are all higher than the median slope of the steepest catchment (T26: 32.2°). Thus, the processes that we infer to preferentially produce gravel tend to occur on steeper, faster eroding slopes within the catchments. The slope distributions of the catchments reveal a change from bimodal slope distributions in the north (e.g. T59, T68, T35) to unimodal distributions in the south with a shift towards a higher percentage of steeper slopes (e.g. T26, T27, T32, T44) (**Fig. 2.6C**). To explain higher NSGI values from the steeper catchments in the south, the gravel must be sourced primarily from deep-seated erosion

processes occurring in areas of faster erosion, whereas the sand must be sourced more uniformly throughout the catchment (Aguilar et al., 2014; Carretier et al., 2015). This interpretation is supported by the fact that the change in slopes affects the [¹⁰Be]_{gravel} significantly more than [¹⁰Be]_{sand} (**Table 2.1, Fig. A3**).

Upstream deposition of gravels and sand during transport can alter the [¹⁰Be] in different ways. Transient sediment storage can result in prolonged sediment exposure and accumulation of ¹⁰Be during slow transport, or it can result in a decrease in [¹⁰Be] due to ¹⁰Be decay during long-term burial (**Fig. 2.7A**). Consequently, in areas of low connectivity between hillslopes and river channels, the ¹⁰Be signature of deep-excavation processes could be overprinted by inefficient sediment transport through the catchment. In contrast, low sediment storage space enables fast downstream transport of sediment with minimal effects on the [¹⁰Be] in sand and gravel, and preservation of the original [¹⁰Be] signatures in the sediment delivered from the hillslopes (**Fig. 2.7D**). In the field we observe a greater potential for sediment storage in the northern part of the study area, where Quaternary deposits in the form of alluvial fans and fluvial fill terraces are common (**Fig. 2.2, Fig. 2.7B & C**), while little sediment storage can be observed in the southern catchments (**Fig. 2.7E & F**). Topographic analysis confirms that the southern catchments, having relatively high *NSGI* values, show unimodal slope distributions with relatively high median slopes and concave-up river profiles, ensuring good connectivity between hillslopes and channels, which facilitates continuous transport of sediment downstream (**Fig. 2.6C, Fig. 2.8**). In contrast, the northern catchments, with relatively low *NSGI* values, are characterized by bimodal slope distributions, lower median slopes, and convex segments within their river profiles (especially T68 and T59) (**Fig. 2.6C, Fig. 2.8**). These convex segments are characterized by sedimentary fill in the form of Quaternary fluvial fill terraces (Tofelde et al., 2017), mass-failure of hillslopes (Marrett and Strecker, 2000; Mikuz, 2003), preserved lake sediments (Marrett and Strecker, 2000; Trauth and Strecker, 1999), and widespread alluvial-fan deposits (**Fig. 2.2, Fig. A2**). Overall, this evidence points to more transient sediment storage and a higher alteration potential of [¹⁰Be] in the northern catchments. As such, upstream deposition of sediment does not explain the positive linear *NSGI*-slope trend, but is likely to explain why scatter in the relationship between *NSGI* and slope is larger in the northern catchments compared to the southern catchments (**Fig. 2.4C**).

Negative *NSGI* values were only measured in catchments with median slopes below 25° and are predominantly found in the northern, slowly denuding areas. We suggest that these negative values are a result of slower transport of gravel compared to sand on the gentle slopes, as has been noted in other low-slope regions (Codilean et al., 2014). If transient sand and gravel are equally distributed with depth in the temporary sedimentary deposits, such that they are exposed to similar ¹⁰Be production rates during downstream transport, then negative *NSGI* values could potentially be used to infer relative differences in sand and gravel residence times.

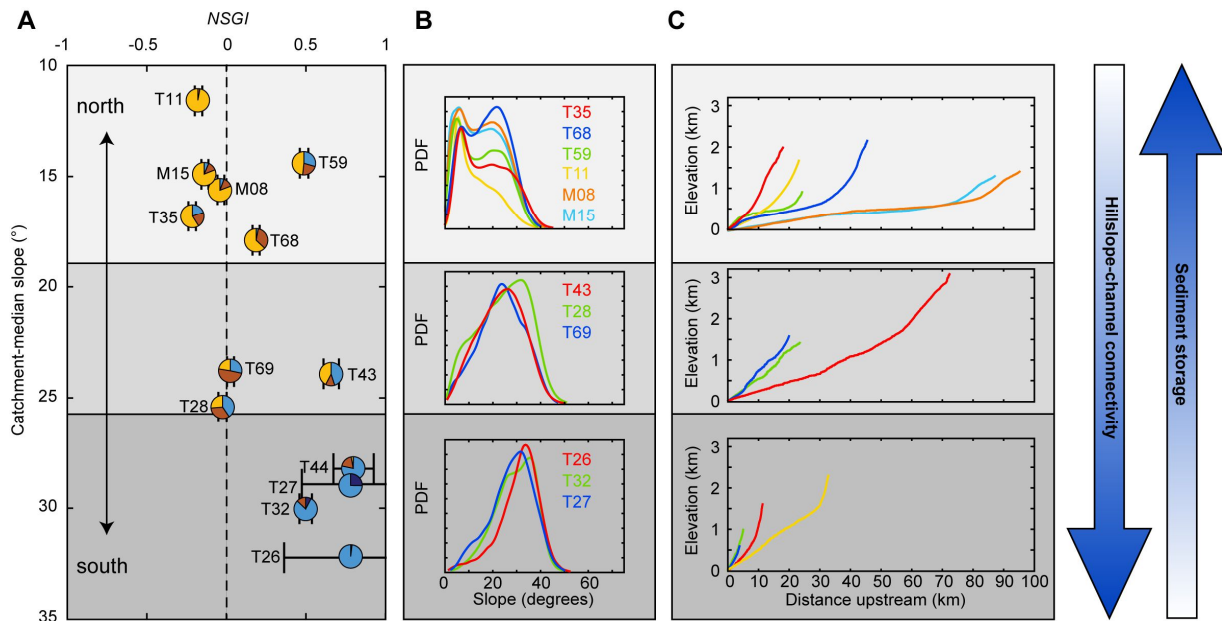


Fig. 2.8 (A) *NSGI* increases with catchment-median slope (same as Fig.2.4C). Separation of samples into three distinct domains based on their differences in *NSGI*, slope distributions, and river profiles (light grey to dark grey). (B) Best-fit slope distributions from all sample sites where sand and gravel were collected. The slope distributions evolve from a bimodal distribution with lower median slopes in the north to a unimodal distribution with higher median slopes in the south. (C) Longitudinal river profiles of the catchments. Elevations are relative to the sampling location. Profile shapes evolve from gentle, partly convex profiles in the north to steeper, concave-up profiles in the south. We interpret the channel geometries as an increase in hillslope-channel connectivity and increased uplift rates from north to south, while sediment storage within the catchments increases from south to north.

We infer that several previously described mechanisms that can alter [¹⁰Be] in sand and gravel could have affected our samples. Only three of those mechanisms, however – (1) increasing depth and/or shorter recurrence intervals together with a rising percentage of surface area covered by deep-excavation events with increasing slopes, (2) gravel being primarily produced on steeper, faster eroding slopes, and (3) slow transport of gravel on gentle slopes – can explain the linear increase of *NSGI* with catchment-median slope. We suggest that transient sediment storage and the consequent alteration of [¹⁰Be] in sand and gravel, particularly in the northern part of the catchment, explain the majority of the observed scatter of the *NSGI*-slope relationship. We do not find clear evidence that glacial pebbles, lithological variation, or comminution affect the *NSGI*. However, we cannot rule out their contribution to the scatter in the *NSGI*-slope relationship.

In summary, in the Quebrada del Toro, the effects of deep-excavation processes in the southern catchments are captured well by high *NSGI* values. Lower *NSGI* values in the north partly reflect less prevalent deep-excavation processes (based on our hillslope-process inventory), but those samples are likely to have been affected by transient sediment storage and overprinting of the ¹⁰Be signal in fluvial sand and gravel.

Catchment-mean denudation rates inferred from [¹⁰Be] are typically measured in the sand fraction (e.g. Bookhagen and Strecker, 2012; Granger et al., 1996; Ouimet et al., 2009; Scherler et al., 2014; Wittmann et al., 2007), which is commonly assumed to be uniformly sourced throughout the catchment (Aguilar et al., 2014; Carretier et al., 2015). The non-linear relationship between *NSGI* and catchment-mean denudation rates reveals that the highest *NSGI* values coincide with the highest denudation rates (**Fig. 2.4E**). As originally hypothesized, most of these fast denuding catchments (T26, T27, T44 and T43) with high *NSGI* are characterized by a higher abundance of deep-seated processes (**Fig. 2.4D**), which not only contribute large amounts of gravel with low [¹⁰Be], but also sand with low [¹⁰Be]. Consequently, the calculated denudation rates for those catchments based on [¹⁰Be]_{sand} may be overestimated (e.g. Niemi et al., 2005; Yanites et al., 2009). In such cases, the *NSGI* could potentially be used not only as a tracer of hillslope processes, but also as a tool to detect biases in ¹⁰Be derived denudation rates.

2.6. Conclusion

By combining [¹⁰Be] measurements in sand and gravel with a detailed hillslope-process inventory, we demonstrate empirically a shift in hillslope erosion processes with increasing catchment-median slopes and ¹⁰Be derived catchment-mean denudation rates. Specifically, rapid increases in denudation rates as hillslopes approach threshold angles are associated with increasing importance of *steep-slope gullying*, with a minor contribution from *landsliding*. As such, we suggest that the non-linearity in the cosmogenic nuclide-derived correlations between denudation-rate and slope are not only linked to the adjustment of landslide frequency, but also to a shift in the type of hillslope processes.

We find that the normalized sand-gravel index (*NSGI*) shows a linear, albeit scattered, increase with catchment-median slope, indicating an increased contribution of low [¹⁰Be] gravel in steeper areas. By excluding other options, we conclude that the increase can only be explained if (i) non-diffusive hillslope processes contribute more gravel compared to sand, (ii) the erosion depth per event, the event frequency, and/or the affected surface area increases with higher slopes, and (iii) gravel is primarily produced on steeper, faster eroding slopes. The shift to higher *NSGI* values coincides with a shift in hillslope processes from *low-slope gullying* to *scree production* to *steep-slope gullying* and *landsliding*. As such, the *NSGI* may track changes in hillslope processes. However, the *NSGI*-slope correlation exhibits significant scatter. We explain the majority of the scatter, especially in lower-slope areas, by the limited hillslope-channel connectivity, which can delay the delivery of sediment with low [¹⁰Be] to channels, providing more time for ¹⁰Be accumulation or decay. While high *NSGI* values in the southern catchments appear to be a reliable signal of deep-excitation processes, lower *NSGI*-values in the northern catchments are a less reliable proxy

^{10}Be concentration in fluvial sand and gravel

for hillslope processes due to transient sediment storage and the potential for overprinting of [^{10}Be] in the sediment.

Acknowledgements

J. Schüürmann, L. Pollozek, D. Käter, M. Lang, and C. Schulz are thanked for help with sample processing and S. Binnie and S. Heinze for performing the AMS measurements. In addition, we would like to thank Sébastien Carretier and Maarten Lupker for highly constructive review comments. This study was funded by the Emmy-Noether-Programme of the Deutsche Forschungsgemeinschaft (DFG) grant number SCHI 1241/1-1 awarded to T.S.

3. Terrace formation and channel response to external perturbation

Submitted as:

Tofelde, S., Savi, S., Wickert, A., Bufe, A. and Schildgen, T., Alluvial channel response to environmental perturbations: Fill-terrace formation and sediment-signal disruption. *Submitted to Earth Surface Dynamics Discussion*

Keywords:

*fluvial-fill terraces,
alluvial-channel response,
aggradation-incision cycles,
signal propagation,
physical experiments*

Abstract

The sensitivity of fluvial fill terraces to tectonic and climatic boundary conditions make them potentially useful archives of past climatic and tectonic conditions. However, we currently lack a systematic understanding of the impacts of base-level, water discharge, and sediment discharge changes on terrace formation and associated sediment storage and release. This knowledge gap precludes a quantitative inversion of past environmental changes from terraces. Here we use a set of seven physical experiments to explore terrace formation and sediment export from a braided channel system that is perturbed by changes in upstream water discharge and sediment supply, or downstream base-level fall. Each perturbation differently affects (1) the geometry of terraces and channels, (2) the timing of terrace formation, and (3) the transient response of sediment discharge. In general, an increase in water discharge leads to near-instantaneous channel incision across the entire fluvial system and consequent local terrace cutting, preservation of the initial channel profile on terrace surfaces, and a transient increase in sediment export from the system that eventually returns to its pre-perturbation rate. In contrast, changes in the upstream sediment supply rate may result in longer lag-times before terrace cutting, leading to a less well-preserved pre-perturbation channel profile, and may also produce a gradual change in sediment output towards a new steady-state value. Finally, downstream base-level fall triggers the upstream migration of a knickzone, forming terraces with upstream-decreasing ages. The gradient of terraces triggered by base-level fall mimicks that of the newly-adjusted active channel, whereas gradients of terraces triggered by variability in upstream sediment or water discharge are steeper compared to the new equilibrium channel. Our findings provide guidelines for distinguishing between different types of perturbations when interpreting fill terraces and sediment export from fluvial systems.

3.1. Introduction

Sediment is moved across the Earth's surface from the production zone (mountainous regions), through the transfer zone (fluvial channels and floodplains), to the final depositional zone (continental and oceanic sedimentary basins) (Allen, 2017; Castelltort and Van Den Driessche, 2003). Because sediment production in mountainous regions is thought to vary with climatic and tectonic conditions, any changes in those conditions may be reflected in the sedimentary deposits in the transfer or depositional zones (Alloway et al., 2007; Zhang et al., 2001). However, reliable reconstructions of past conditions from sedimentary deposits require a detailed understanding of sediment transport along the sediment-routing (or source-to-sink) system, including any potential alteration of signals through the transfer zone, as well as the preservation of the sedimentary deposits and its signals over time (Romans et al., 2016 and references therein).

Fluvial fill terraces represent transient sediment storage along river channels, and therefore they are an important component of the sediment-routing system (e.g., Allen, 2008b). They are generated by variations in river-bed elevations due to sediment deposition followed by river incision into the formerly deposited sediments (Bull, 1990). As a result of incision, remnants of the former floodplain can be abandoned by the active channel and preserved as terraces, a process we refer to as “terrace cutting”. Fill terraces, as such, are an indicator of unsteadiness in the parameters that control fluvial-channel geometry. Aggradation and incision can be triggered by changing conditions at the upstream end of the river, namely the sediment to water discharge ratio, $Q_{s,in}/Q_w$ (e.g., Buffington, 2012; Gilbert, 1877; Lane, 1955; Mackin, 1948), or by base-level changes at the downstream end (e.g., Fisk, 1944; Merritts et al., 1994; Shen et al., 2012). In some cases, internal dynamics of the system, sometimes referred to as “autogenic processes”, may lead to terrace formation which cannot be directly linked to any external forcing at the upstream or downstream end of the channel (e.g., Erkens et al., 2009; Limaye and Lamb, 2016; Malatesta et al., 2017; Patton and Schumm, 1981; Womack and Schumm, 1977). The cutting of terraces can either coincide with or lag behind the onset of the perturbation that drives terrace formation. The formation of fill terraces in response to external perturbations has two major implications: (1) fill terraces potentially provide a record of past environmental conditions (e.g., Bridgland and Westaway, 2008; Bull, 1990; Merritts et al., 1994); and (2) the deposition and erosion of fill terraces can alter downstream sediment signals, complicating signal propagation from catchment headwaters to long-term depositional sinks (e.g., Allen, 2008b; Castelltort and Van Den Driessche, 2003; Romans et al., 2016).

Fill-terrace deposits have been used to infer past variability in discharge (Litty et al., 2016; Poisson and Avouac, 2004) or sediment supply (Bookhagen et al., 2006; Schaller et al., 2004). For a reliable reconstruction of such parameters, however, it is essential to understand how closely terrace formation tracks environmental perturbations. Because most studied fill terraces are thousands to millions of years

old and form over the course of years to thousands of years (e.g., Bookhagen et al., 2006; Schaller et al., 2004; Schildgen et al., 2002, 2016; Tofelde et al., 2017), fill-terrace formation can rarely be observed directly in nature. Consequently, we need alternative ways to investigate the formation of fill terraces and their impacts on downstream sediment discharge.

Numerical models provide an opportunity to predict the evolution of alluvial river-bed elevation over time (Blom et al., 2017, 2016; Simpson and Castelltort, 2012; Slingerland and Snow, 1988; Wickert and Schildgen, 2018). However, those predictions commonly are limited to the evolution of the longitudinal profile and do not take into account modifications of the channel width or the cutting of terraces (Blom et al., 2017, 2016; Simpson and Castelltort, 2012; Slingerland and Snow, 1988). Hancock and Anderson (2002) modeled bedrock strath terrace formation, a partially analogous process, but their erosional stream-power-based approach cannot be easily translated to transport-limited systems, where slope and long-profile evolution result from both sediment and water inputs.

Physical experiments provide an alternative approach to studying terrace formation (Baynes et al., 2018; Frankel et al., 2007; Gardner, 1983; Lewis, 1944; Mizutani, 1998; Schumm and Parker, 1973; Wohl and Ikeda, 1997). Most experimental studies have tested the cutting of terraces due to base-level fall (Frankel et al., 2007; Gardner, 1983; Schumm and Parker, 1973) or explained their formation through autogenic processes (Lewis, 1944; Mizutani, 1998). Only one experimental study by Baynes et al. (2018) investigated terrace formation as a response to changes in sediment supply ($Q_{s,in}$) or water discharge (Q_w), but this study focused on vertical incision into bedrock and strath-terrace cutting. Van den Berg van Saparoea and Postma (2008) performed experiments to investigate the effects of pulses in Q_w and $Q_{s,in}$ on the evolution of longitudinal channel profiles and sediment discharge at the basin outlet ($Q_{s,out}$), but they did not focus on terrace formation. To our knowledge, there are no experimental studies that systematically compare how fill terraces formed through various mechanisms may differ from one another, or investigate the impacts of terrace formation on downstream sediment discharge.

In this study, we present results from seven physical experiments of braided channels in non-cohesive sediment to test three potential mechanisms of fill-terrace cutting due to external perturbations: (1) an increase in Q_w , (2) a reduction in $Q_{s,in}$, and (3) a fall in base level. We furthermore monitor our experiments for terrace cutting related to autogenic processes. Subsequently, we discuss: (1) channel responses to perturbations in external forcing and conditions for terrace formation, (2) differences in lag-times between the onset of the perturbation and the timing of terrace cutting and consequent differences in terrace profiles, (3) the relationship between terrace surface slope and the terrace-formation mechanism, and (4) the effects of fluvial aggradation or bed incision on sediment discharge at the outlet of the river system ($Q_{s,out}$).

3.2. Formation of fluvial fill terraces

Fluvial terraces form in response to perturbations that happen either upstream ($Q_{s,in}$, Q_w), or downstream (base-level changes) along the river. Such perturbations may be the result of environmental changes (external or allogenic perturbations), or the result of internal (autogenic) dynamics within the system. For each external or internal forcing mechanism, we summarize below observations from field studies, numerical models, and physical experiments.

3.2.1. Sediment to water discharge ratio ($Q_{s,in}/Q_w$)

Alluvial rivers adjust their slopes and widths such that, in a graded (steady) state, the incoming water discharge (Q_w) can transport the incoming sediment ($Q_{s,in}$) downstream (Buffington, 2012; Gilbert, 1877; Lane, 1955; Mackin, 1948). Scherler et al. (2015) referred to terrace formation related to changes in Q_w as the ‘*discharge-driven model*’. In this model, a reduction in Q_w leads to valley aggradation due to deposition of sediment on the riverbed. A subsequent phase of increased Q_w can then cause incision. In contrast, the ‘*hillslope-driven model*’ requires variability in $Q_{s,in}$. When an increased $Q_{s,in}$ exceeds the sediment-transport capacity of the river, the excess sediment is deposited. Deposition of sediment elevates the channel bed, increases its slope, and thereby increases the sediment-transport capacity of the river until it matches the incoming sediment supply, $Q_{s,in}$. If $Q_{s,in}$ is reduced such that the sediment-transport capacity exceeds the sediment supply, the river tends to incise. The incision both supplements $Q_{s,in}$ with material from the channel bed and lowers the channel slope, thereby decreasing its transport capacity towards an equilibrium with the new $Q_{s,in}$.

Terrace formation due to variability in Q_w has mainly been related to climatic changes, such as those caused by glacial-interglacial cycles (Penck and Brückner, 1909). Field studies favor this model when times of valley aggradation coincide with drier conditions and incision coincides with wetter conditions (Hanson et al., 2006; Scherler et al., 2015; Schildgen et al., 2016; Tofelde et al., 2017). Variability in $Q_{s,in}$ to river channels can have a variety of causes, including climatically driven changes in regolith production rates on hillslopes (Bull, 1991; Norton et al., 2015; Savi et al., 2015), climatically driven vegetation growth that stabilizes sediment on hillslopes (Fuller et al., 1998; Garcin et al., 2017; Huntington, 1907), and exposure of regolith following glacier retreat (Malatesta et al., 2018; Malatesta and Avouac, 2018; Savi et al., 2014; Schildgen et al., 2002). Landslides also deliver sediment to rivers, and the rate of landsliding can vary in response to changes in tectonic rock uplift rates or precipitation (e.g., Bookhagen et al., 2006; McPhillips et al., 2014; Scherler et al., 2016; Schildgen et al., 2016). Increases in precipitation can mobilize additional sediment from hillslopes until the climate returns to a drier state (Dey et al., 2016) or until hillslopes are stripped bare (Steffen et al., 2010, 2009). All of the above interpretations are based on a

temporal link between the formation of fill terraces and climate proxy data, and suggest that variability in Q_w and/or $Q_{s,in}$ can drive terrace formation.

Numerical models have been developed to investigate the evolution of fluvial terraces in response to variable Q_w and $Q_{s,in}$ (Boll et al., 1988; Veldkamp and Vermeulen, 1989; Veldkamp and Van Dijke, 1998), and model results have been compared to different terrace sequences in Europe (Meuse River: Bogaart and van Balen, 2000; Tebbens et al., 2000; Maas River: Veldkamp and Van Dijke, 2000; Allier River: Veldkamp, 1992, Veldkamp and Van Dijke, 1998). Similarities between modeled terraces and field observations support the conclusion that terraces can form in response to variable Q_w and/or $Q_{s,in}$.

3.2.2. Base-level change

Fluvial terraces can also be the product of changes in base level at the downstream end of the river. A drop in base level locally creates a steeper channel gradient at the downstream end. To return to a steady-state profile, the channel typically incises into its bed through an upstream-propagating knickzone, which, in the case of alluvial channels, can be highly diffuse (Begin et al., 1981; Grimaud et al., 2015; Whipple and Tucker, 1999; Wickert and Schildgen, 2018). A rise in base level leads to a local reduction in channel slope at the downstream end. To return to a steady-state profile, the channel deposits sediment upstream of the location of base-level rise to increase the slope again. Fluvial fill terraces can thus be formed in response to alternating phases of base level rise and fall.

Although either tectonic or climatic forcing can lead to changes in base level, alternating rises and falls are most commonly associated with climatic forcing. Early observations in the Lower Mississippi Valley (USA) related valley aggradation to a glacio-eustatic sea-level highstand and marine transgression, whereas valley incision and consequent terrace cutting was linked to sea-level fall (Fisk, 1944; Shen et al., 2012). Other field studies have related terrace formation to climatically driven alternations of sea level (Merritts et al., 1994) or lake level (Farabaugh and Rigsby, 2005). Sediment aggradation associated with sea-level rise followed by incision during sea-level fall has also been shown by a numerical model that aimed to model the evolution of the Meuse terrace sequence in Europe (Tebbens et al., 2000; Veldkamp and Tebbens, 2001). In addition, terrace cutting following base-level drop and upstream knickzone migration has been produced in flume experiments (Frankel et al., 2007; Gardner, 1983; Schumm and Parker, 1973).

3.2.3. Complex response and autogenic processes

In addition to external (i.e., allogenic) forcing described above, internal dynamics can also drive terrace formation. Internally-driven terrace formation can result from internal feedbacks in response to a

change in boundary conditions ('complex response') or due to purely internal dynamics with constant boundary conditions ('autogenic' processes). Below, we distinguish between complex responses and autogenic processes, and we discuss how they may lead to terrace development.

A non-linear response within the channel system to a linear external change can be considered a complex response (Schumm, 1979, 1973). For example, field observations (Faulkner et al., 2016; Schumm, 1979; Womack and Schumm, 1977), physical experiments (Gardner, 1983; Schumm and Parker, 1973), and numerical models (Slingerland and Snow, 1988) indicate that several terrace levels may be cut in response to a single drop in base level. Schumm (1979, 1973) observed that incision of the main stem lowered the base level for the tributaries, which consequently started to incise and transport additional sediment to the main stem. The elevated sediment supply in turn exceeded the transport capacity of the main stem, triggering deposition in the formerly incised channel. Once the tributaries were adjusted to the new base level, sediment supply decreased, which triggered renewed incision of the main stem into the recently deposited material. Whereas the initial, externally-driven base-level drop created a first terrace level, all subsequent terraces were formed in response to internal feedbacks within the fluvial system and therefore cannot be directly linked to an external perturbation.

In contrast to a complex response, we consider autogenic terraces to be those that are formed in response to non-linear processes within the fluvial system under constant external boundary conditions. One example is a meander cut-off, which can occur without any external perturbation and leads to a local increase in channel slope. The resulting increase in bed shear stress triggers incision and subsequent terrace formation. This phenomenon has been observed in the field (Erkens et al., 2009; Gonzalez, 2001; Womack and Schumm, 1977) and has been replicated using numerical models (Limaye and Lamb, 2016). Another example is local storage and release of sediment, which results from and feeds back into locally non-uniform sediment transport rates. By storing or releasing sediment, each section of the channel changes the local boundary condition on the segment directly downstream ($Q_{s,in}/Q_w$) or upstream (bed elevation and thus slope). Consequently, sediment deposition, channel incision, and terrace formation can happen simultaneously in different parts of the channel (Lewis, 1944; Patton and Schumm, 1981).

3.3. Methods

To test the dynamics of fill-terrace formation in response to different external forcing conditions and the impact of terrace formation on sediment transport across the transfer zone of a source-to-sink system, we performed seven experiments at the Saint Anthony Falls Laboratory in Minneapolis, USA, in 2015. The experimental setup consisted of a wooden box with the dimensions of 4 m x 2.5 m x 0.4 m (**Fig. 3.1A**) that was filled with quartz sand with a mean grain size of 144 μm . At the inlet, sand and water were

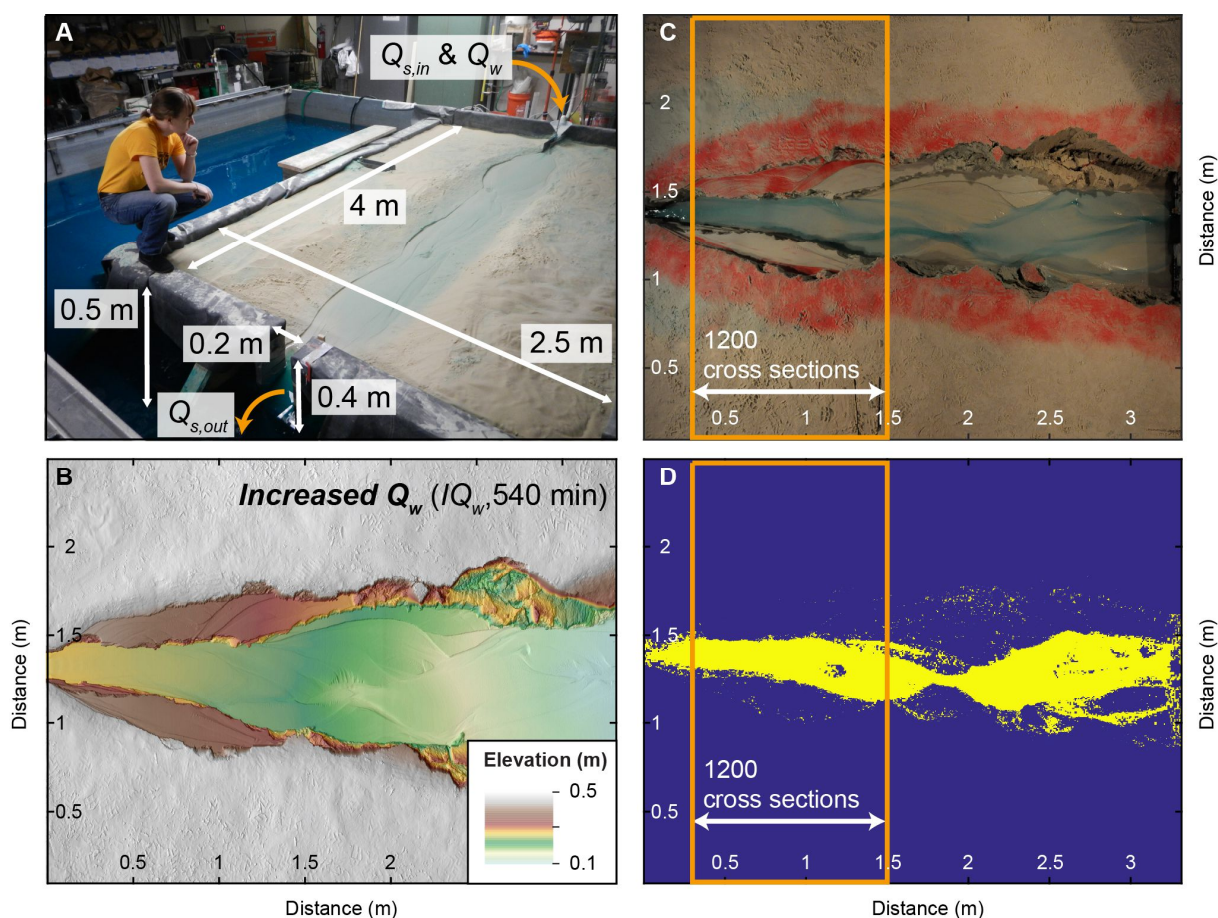
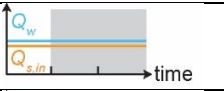
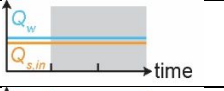
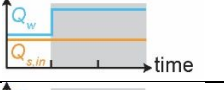
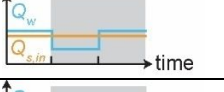
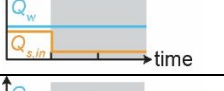
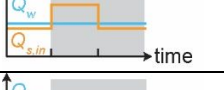
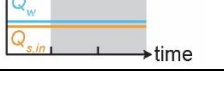


Fig. 3.1 Experimental setup, data collection and analysis. (A) Overview of experimental setup. Sediment supply ($Q_{s,in}$) and water discharge (Q_w) can be regulated separately. For all but the base level fall (BLF) experiment, the base level was fixed. Water and sediment fell off of an edge at the outlet. For the BLF experiment (shown in the picture), the base level was controlled through the water level in the surrounding basin. (B) Digital elevation model (DEM) derived from laser scans showing the final topography of the increased water (IW) experiment. (C) Overhead photograph of the IW experiment taken directly before the scan shown in B. The surface was covered with a thin layer of red sand before the instant increase in discharge was performed. The remnants of red sand on the terraces indicate no further reworking after the onset of increased discharge. (D) Overhead photographs were turned into binary (wet, dry) images from which the average channel width within the analyzed area (orange frame) can be calculated.

supplied through a cylindrical wire-mesh diffuser filled with gravel to ensure sufficient mixing of sand and water. Water discharge (Q_w) and sediment supply ($Q_{s,in}$) could be regulated separately. At the downstream end, water and sand ($Q_{s,out}$) exited the basin through a 20 cm-wide gap that opened onto the floor below. This downstream sink was required to avoid deltaic sediment deposition that would, if allowed to grow, eventually raise the base level of the upstream fluvial system. At the beginning of each experiment, an initial channel was shaped by hand (Fig. 3.1A) and the experiments were run under reference conditions ($Q_{w,ref} = 95$ ml/s, $Q_{s,ref} = 1.3$ ml/s) for 240 minutes. This runtime was sufficient to reach a quasi-steady state in which the average $Q_{s,out}$ approximately equaled $Q_{s,in}$. After this “spin-up” phase, the channel had a uniform equilibrium slope of approximately 7%.

Table 3.1 Water and sediment inputs to the experiments.

Experiment	0 – 240 min (reference conditions)		240 – 480 min		480 min until end		Graphical description
	Q_w (mL/s)	$Q_{s,in}$ (mL/s)	Q_w (mL/s)	$Q_{s,in}$ (mL/s)	Q_w (mL/s)	$Q_{s,in}$ (mL/s)	
<i>Ctrl_1</i>	95	1.3	95	1.3	95	1.3	
<i>Ctrl_2</i>	95	1.3	95	1.3	95	1.3	
<i>IQ_w</i>	95	1.3	190	1.3	190	1.3	
<i>DQ_w_IQ_w</i>	95	1.3	47.5	1.3	95	1.3	
<i>DQ_{s,in}</i>	95	1.3	95	0.22	95	0.22	
<i>IQ_{s,in}_DQ_{s,in}</i>	95	1.3	95	2.6	95	1.3	
<i>BLF</i>	95	1.3	95	1.3	95	1.3	

Every 30 min we stopped the experiments to perform a scan with a laser scanner mounted on the railing of the basin that surrounded the wooden box. Digital elevation models (DEMs) created from the scans have a horizontal resolution of 1 mm (**Fig. 3.1B**). Using those DEMs, we measured the evolution of channel cross-sectional profiles, longitudinal channel profiles, and surface slopes. Long profiles were calculated by extracting the lowest elevation point in each cross-section at 1 mm increments. By plotting elevation against the distance down the long axis of the box rather than against channel length, resulting slopes are slightly overestimated due to the minor sinuosity of the channels. To directly compare terrace and channel slopes, we extracted 5 cm wide swath profiles along the terrace surfaces and the equivalent stretch of the modern channel. The width of swath profiles had to be reduced on terraces of the $DQ_w_IQ_w$ and the $IQ_{s,in}_DQ_{s,in}$ experiments because terraces in these runs were narrower than 5 cm. Slopes were calculated based on a linear fit through the mean elevation profiles. To assess uncertainties, the root mean square error (RMSE) was calculated between the linear model and the observed data.

Overhead photos were taken every 20 s with a fish-eye lens (**Fig. 3.1C**). Distortions of the photos were ortho-rectified in Adobe Photoshop and photos were resampled at 1 mm horizontal resolution to

directly overlap with the laser scans. Photos were turned into binary images with values of 1 for wet pixels and 0 for dry pixels. This binarization was performed by transforming the *rgb* (red, green, blue) images into *hsv* (hue, saturation, value) images and then manually defining a hue cut-off for each experiment that best separates wet and dry pixels in the image (**Fig. 3.1D**). From the binary images, the number of wet pixels in each cross-section (perpendicular to the basin margin and therefore to the average flow direction) were counted. Analyses were restricted to the areas within the orange box (**Fig. 3.1C, D**), because terraces mainly developed in this part of the channel and because we considered this sector of the channel to be unaffected by the fixed location of the outlet. To calculate average channel width, the average number of wet pixels in 1200 cross sections perpendicular to the basin margin (therefore perpendicular to the average flow direction) were counted and are reported with one standard deviation. No overhead photos were taken for the *Ctrl_1* experiment, because of an error in the camera installation.

We manually measured $Q_{s,out}$ at 10-minute intervals by collecting the discharged sediment in a container over a 10-second period and measuring its volume. This approach allowed us to estimate whether the system had returned to steady state ($Q_{s,in} \approx Q_{s,out}$) during the runs. At the same 10-minute interval, we measured bed elevation at the inlet and at the outlet to estimate the spatially-averaged channel slope. We interpreted a constant slope for over more than 30 minutes as additional evidence for a graded (steady state) channel. The data can be found in the supplementary material (**Appendix B**).

We ran seven experiments to test the impacts of changes in $Q_{s,in}$, Q_w , and base level on the channel. The experiments are summarized in **Table 3.1**. To investigate the effect of Q_w , we ran two separate experiments: in one experiment we doubled Q_w (IQ_w = increase discharge) to 190 mL/s at 240 min (end of the spin-up time) and in the other experiment we first halved Q_w to 48 ml/s at 240 min and then returned to the initial 95 mL/s at 480 min (DQ_w IQ_w = decrease discharge, increase discharge). To test the effect of $Q_{s,in}$, we ran one experiment in which we reduced the $Q_{s,in}$ by 83% to 0.22 ml/s ($DQ_{s,in}$ = decrease sediment supply) at 240 min and another one in which we first doubled $Q_{s,in}$ to 2.6 ml/s at 240 min and then halved $Q_{s,in}$ again to the initial 1.3 ml/s at 480 min ($IQ_{s,in}$ $DQ_{s,in}$ = increase sediment supply, decrease sediment supply). All $Q_{s,in}$ and Q_w changes were imposed instantaneously, resulting in a step function in the forcing. Immediately before imposing these changes, we covered the near-channel surface with a thin layer of red sand to optically identify the area that is reworked after the change. We ran one experiment in which we dropped the base level by 10 cm gradually over 20 min starting at 240 min, resulting in a base-level lowering rate of 0.5 cm/min (*BLF*). For this experiment, we started with a base level higher than in the initial setting by flooding the basin surrounding the wooden box (**Fig. 3.1A**). The final base level equaled those of the other experiments. In this experiment, the red sand was applied immediately before the onset of base-level lowering. Additionally, we performed two control experiments in which we made no changes to the initial

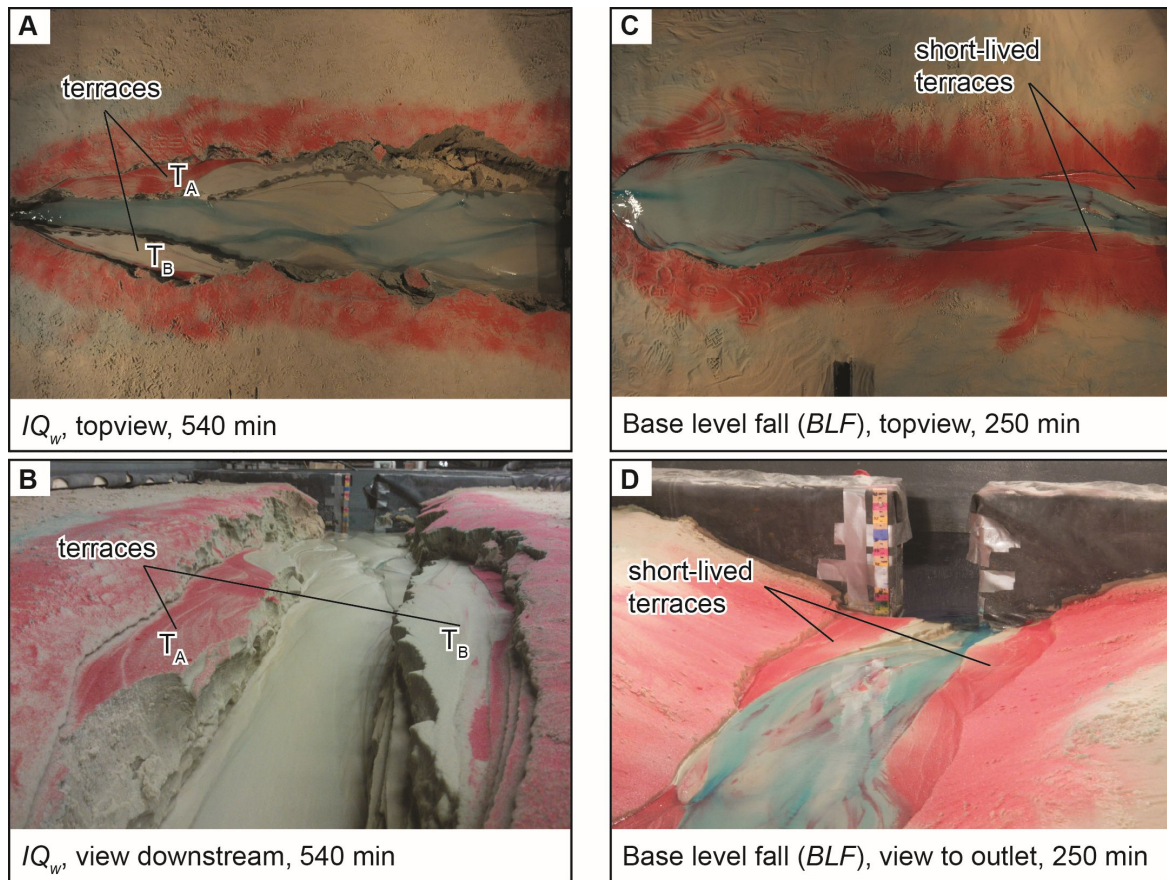


Fig. 3.2 Fill terraces formed during experimental runs. Paired terraces were formed in the Increase Q_w (IQ_w) experiment and are shown from top (A) and looking in the downstream direction (B) at the end of the experiment (540 min = 300 min after spin-up time). Remnants of red sand on the terrace surfaces indicate that those areas have not been flooded after the instant doubling in discharge. During the base-level fall (BLF) experiment, terraces at the downstream end were abandoned instantly after the onset of base level fall (250 min = 10 min after onset of BLF). Terraces are shown from above (C) and looking in the downstream direction (D). Those terraces were destroyed shortly after they were cut. A new set of terraces was formed in the upstream part ca. 120 min after the onset of BLF.

conditions in order to investigate whether terraces would form in our experiment without any change in external forcing (*Ctrl_1*, *Ctrl_2*).

3.4. Results

Fluvial terraces were cut in the experimental runs IQ_w , DQ_w - IQ_w (in the IQ_w phase), $DQ_{s,in}$, $IQ_{s,in}$ - $DQ_{s,in}$ (in the $DQ_{s,in}$ phase) and BLF (**Fig. 3.2, 3.3**). No terraces were formed after the ‘spin-up’ time of *Ctrl_1* and *Ctrl_2*. The terraces visible in the cross-section of *Ctrl_2* formed in response to incision during the ‘spin-up’ phase and did not substantially develop after 240 min (**Fig. 3.3B**, red line).

To form fill terraces, changes in channel-bed elevation and channel width are required. In our experiments, channel-elevation changes occurred by sediment deposition or incision (**Fig. 3.4**). However,

Terrace formation and channel response to external perturbation

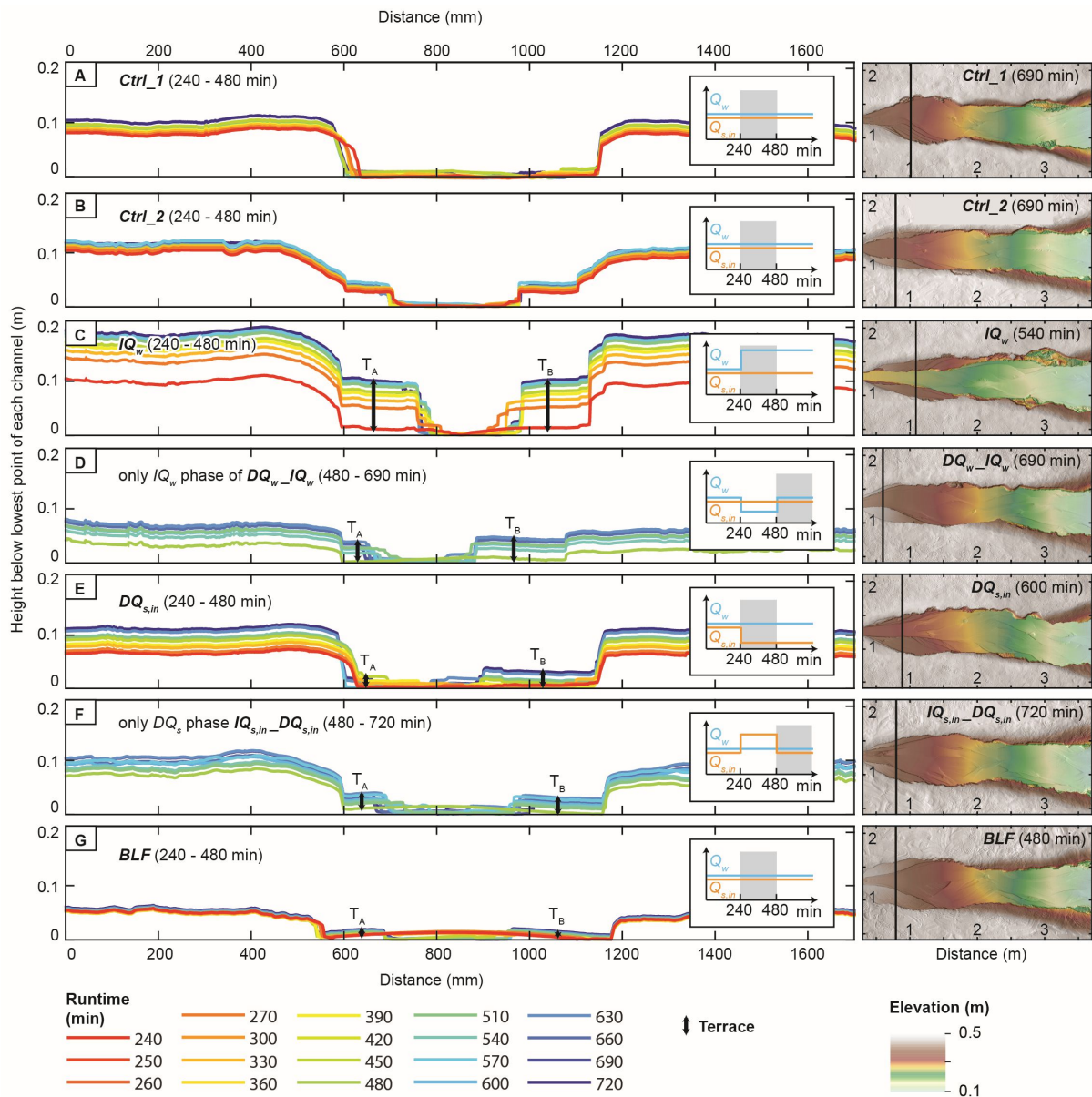


Fig. 3.3 Evolution of cross-sections in the upper part of the reach (left panel). In each cross section, the lowest point is set equal to zero to track incision. The color scheme represents time since the last change in boundary conditions (equivalent to either 240 min or 480 min experiment time). For better comparison, we plot a maximum of 240 minutes for all experiments, despite longer recordings for some of the runs. Exact location of cross sections are indicated by the black lines in the DEMs displaying the last scan of each experiment (right panel). Cross-sections have been chosen at the terrace midpoints and thus vary slightly between the experiments. The times given in parentheses are the absolute experiment runtimes.

these bed-elevation changes were not uniform along the channel reach (**Fig. 3.4**). In the runs *Ctrl_1* and *Ctrl_2*, the longitudinal profiles were stable over time and only minor lowering in bed elevation (max. 4 cm) occurred at the upstream end (**Fig. 3.4A, B**). A sudden increase in Q_w (IQ_w , and the IQ_w phase of $DQ_w_IQ_w$) or a decrease in $Q_{s,in}$ ($DQ_{s,in}$, and the $DQ_{s,in}$ phase of $IQ_{s,in}_DQ_{s,in}$) both led to river incision,

Terrace formation and channel response to external perturbation

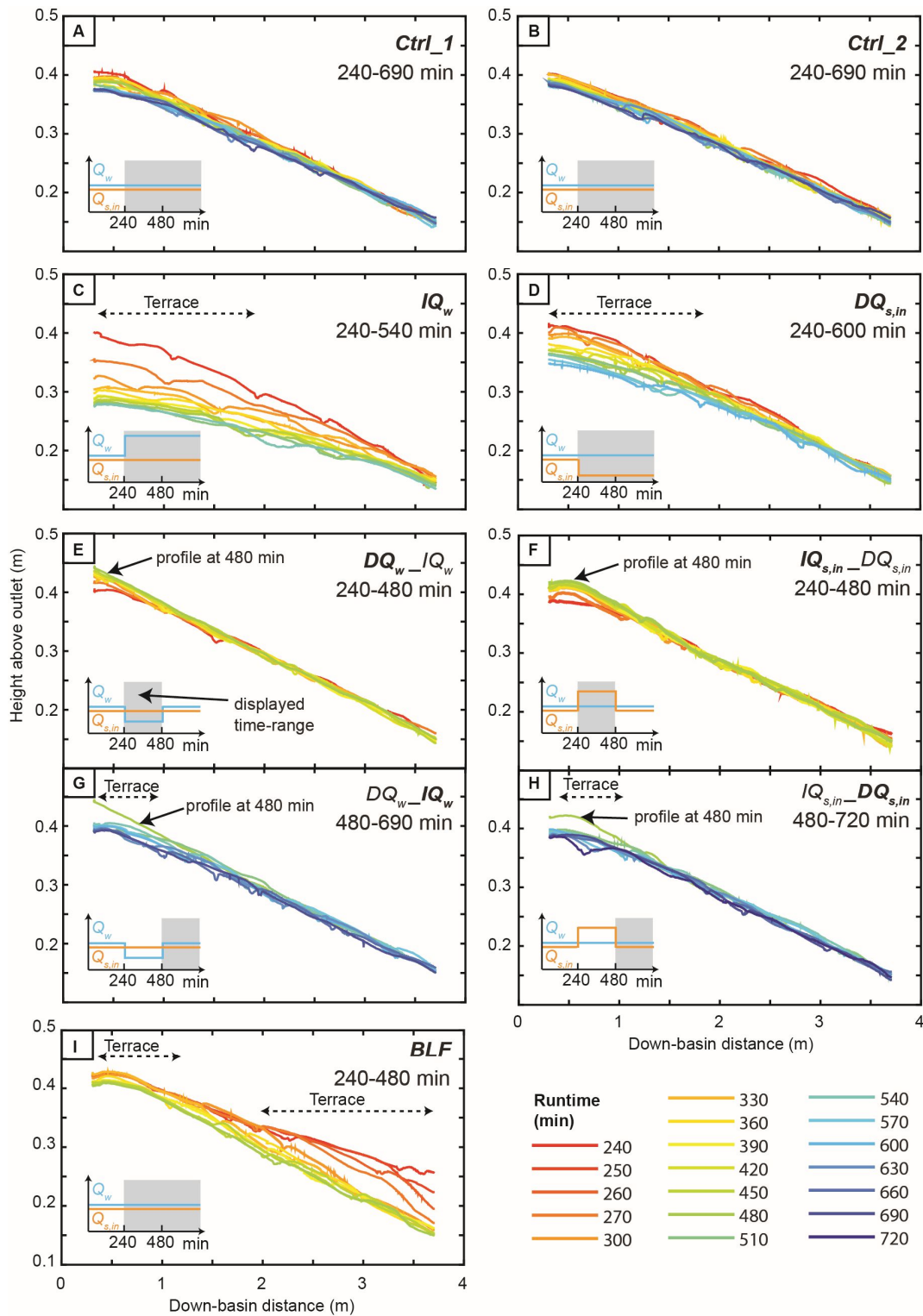


Fig. 3.4 Evolution of longitudinal river profiles from minute 240 (end of 'spin-up' phase) onwards. River profiles were extracted from the laser scans. Laser scans were recorded every 30 min, and an additional two scans at 10 and 20 minutes after the initiation of the base-level fall were conducted during the BLF experiment. Dashed arrows indicate down-basin distance along which terraces formed. Note that the DQ_w-IQ_w and $IQ_{s,in}-DQ_{s,in}$ were split into two panels each, with one panel representing each phase.

which was most pronounced at the upstream end (**Fig. 3.4C, D, G, H**) and was, in most cases, not recognizable at the downstream end (**Fig. 3.4D, G, H**), where the channel-bed elevation was fixed due to the steady base level. Sediment deposition in the channels followed a decrease in Q_w (DQ_w phase of $DQ_w_IQ_w$) or an increase in $Q_{s,in}$ ($IQ_{s,in}$ phase of $IQ_{s,in}_DQ_{s,in}$), which was again most recognizable at the upstream end of the reach (**Fig. 3.4E, F**). The drop in base level, however, caused maximum incision at the downstream end, and the incision wave migrated upstream as a knickzone (**Fig. 3.4I**).

The evolution of slope and width of the active channel were tracked through time (**Fig. 3.5**). The *Ctrl_1* and *Ctrl_2* experiments only showed a marginal decrease of channel slopes after the 240 min ‘spin-up’ time from ~ 0.074 and 0.071 to around 0.070 and 0.067 ($\sim 6\%$ reduction; **Fig. 3.5A**). As such, we consider any change in slope after the ‘spin-up’ time that is on the same order as those observed in *Ctrl_1* and *Ctrl_2* as ongoing adjustment to the reference condition as opposed to the result of an external perturbation. Channel width in the control experiments varied slowly between ca. 20 cm and 35 cm.

An instant doubling of Q_w (IQ_w ; **Fig. 3.5B**) resulted in a rapid, exponential decrease in channel slope. After approximately 480 min, the slope was reduced from ~ 0.072 to ~ 0.043 (40% reduction), and new stable conditions were reached. The doubling of Q_w also triggered an instant narrowing of the channel from ~ 35 cm to ~ 15 cm ($\sim 57\%$ decrease), followed by subsequent slow widening.

A sudden reduction in Q_w to half its initial value ($DQ_w_IQ_w$; **Fig. 3.5C**) resulted in an increase in slope from ~ 0.072 to ~ 0.085 (18% increase) between 240 and 480 min runtime, and a widening of the channel from about 25 cm to about 45 cm ($\sim 80\%$ increase) during the same time. The subsequent doubling in Q_w back to its initial value triggered a rapid (nearly exponential) reduction in slope back to the initial ~ 0.072 ($\sim 15\%$ reduction) and an instantaneous narrowing of the channel ($\sim 45\%$ reduction) followed by slow widening.

A reduction in $Q_{s,in}$ by 83% ($DQ_{s,in}$; **Fig. 3.5D**) triggered a decrease in channel slope. The rate of decrease was lower than in the IQ_w run, and the new slope stabilized around 0.06 (24% reduction). An instantaneous decrease in channel width also occurred, but this change was again less pronounced than what we observed in the IQ_w experiment ($\sim 33\%$ reduction). No subsequent widening of the channel was detectable.

An increase in $Q_{s,in}$ ($IQ_{s,in}_DQ_{s,in}$; **Fig. 3.5E**) led to an increase in channel gradient from about 0.070 to about 0.078 (11% increase) and an increase in channel width from about 30 cm to about 55 cm ($\sim 83\%$ increase). The subsequent reduction in $Q_{s,in}$ led to a decrease of the channel slope and an instantaneous channel narrowing to < 30 cm, followed by subsequent widening back to the initial width of ~ 30 cm.

Terrace formation and channel response to external perturbation

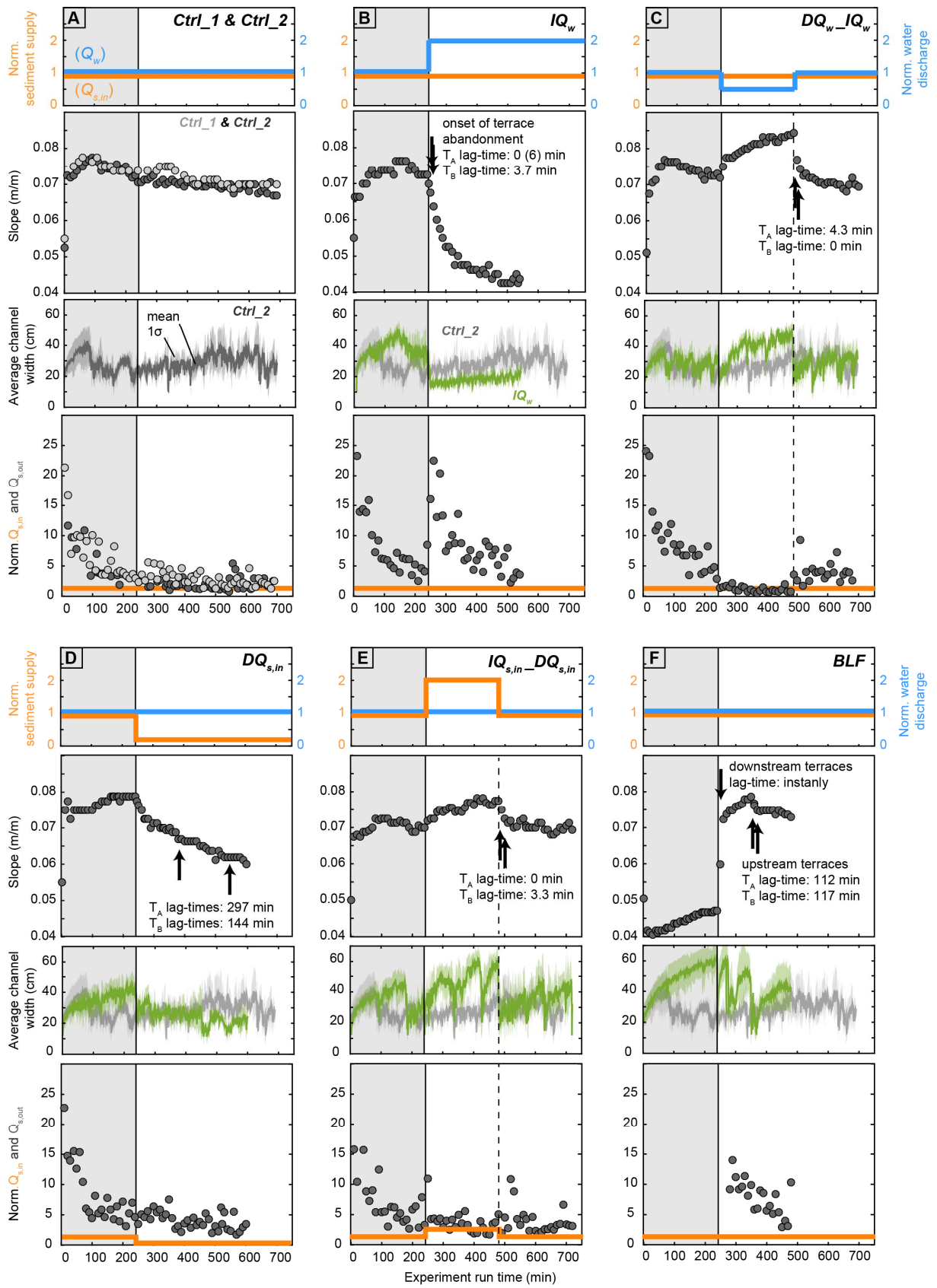


Fig. 3.5 Input parameters and evolution of channel slope and channel width during the experiments. Input sediment ($Q_{s,in}$; orange solid line) and water (Q_w ; blue solid line) discharge were normalized to the reference input values ($Q_{s,ref} = 1.3$ ml/s and $Q_{w,ref} = 95$ ml/s). Slope (S , grey circles) was calculated based on the bed elevation difference between the inlet and the outlet divided by the length of the system. Channel elevation measurements for slope calculations were performed manually during the runs. Channel width was calculated as the mean number (solid lines) of wet pixels in each of 1200 cross section within the box indicated in Fig. 3.1C, D. The colored shaded areas around the curves indicate the standard deviation of the 1200 measurements. The evolution of width without any external perturbation (Ctrl_2) is plotted for comparison with each other experiment in which external conditions were changed (B-F). Note that no measurements are available for the Ctrl_1 experiment due to issues with the installation of the overhead camera. Sediment discharge at the outlet ($Q_{s,out}$) during the experimental runs is compared to input sediment ($Q_{s,in}$; orange solid line); both were normalized to reference input values ($Q_{s,ref} = 1.3$ ml/s). The first 240 min of each experiment were adjustment to the reference settings (grey box) and were not included in the analyses. Black arrows indicate times when terraces in the upstream part of the sandbox started to be cut.

For the base-level fall experiment (*BLF*; **Fig. 3.5F**), channel slope instantly and rapidly increased after the onset of base-level fall from about 0.047 to 0.073 (55% increase), and it increased at a slower rate further to about 0.08, before lowering back to 0.072. However, these slope values are simply calculated based on the height difference at the inlet and outlet, ignoring any variability in slope along the experiment reach that is, in the *BLF* experiments, significant due to knickzone propagation. The drop in base level resulted in a sudden drop in channel width, followed by three cycles of channel widening and narrowing. In summary, we observed that an increase in Q_w and a decrease in $Q_{s,in}$, resulted in an immediate decrease in channel slope (through upstream incision) and an instant reduction in channel width, whereas a drop in base level caused an increase in channel slope (through downstream incision) and a reduction in channel width (**Fig. 3.5**).

The time of terrace cutting lagged minutes to hours behind the onset of the perturbation (**Fig. 3.5**). Lag-times were determined from overhead photos and are defined as the time interval between the onset of the perturbation (at minute 240 or 480) and the last time the future terrace surface was occupied by water. The times given in **Fig. 3.5** refer to the last occupation of the areas for which swath profiles were extracted (**Fig. 3.6** right panel). In the two experiments in which we changed Q_w and in the $IQ_{s,in} - DQ_{s,in}$ experiment, terrace cutting in the upstream reach of the channel (**Fig. 3.3** right column, **Fig. 3.4**; dashed arrows) began within ~5 minutes after the change in boundary conditions (**Fig. 3.5**; black arrows). In the IQ_w experiment, for example, the majority of the T_A terrace was cut instantly (no removal of red sand) and only a small part at the downstream end was occupied again until 6 minutes after perturbation (**Fig. 3.2A, B**). In the $DQ_{s,in}$ experiment, however, the T_A and T_B terraces were cut 297 and 144 min after the perturbation (**Fig. 3.5D**). In the *BLF* experiment, terraces in the downstream channel reach were cut immediately after the onset of base-level drop, but were mostly destroyed within 30 min (**Fig. 3.2C, D**). Terrace cutting in the upstream part of the basin began 112 and 117 min after the initial perturbation (**Fig. 3.5F**).

To analyze how well the channel-bed profiles immediately preceding the time of perturbation were preserved by the terraces, we compared the elevation profiles of the two terraces on each side of the channel (yellow and orange lines) with the channel that existed at the onset of perturbation (red line) (**Fig. 3.6**). In

Terrace formation and channel response to external perturbation

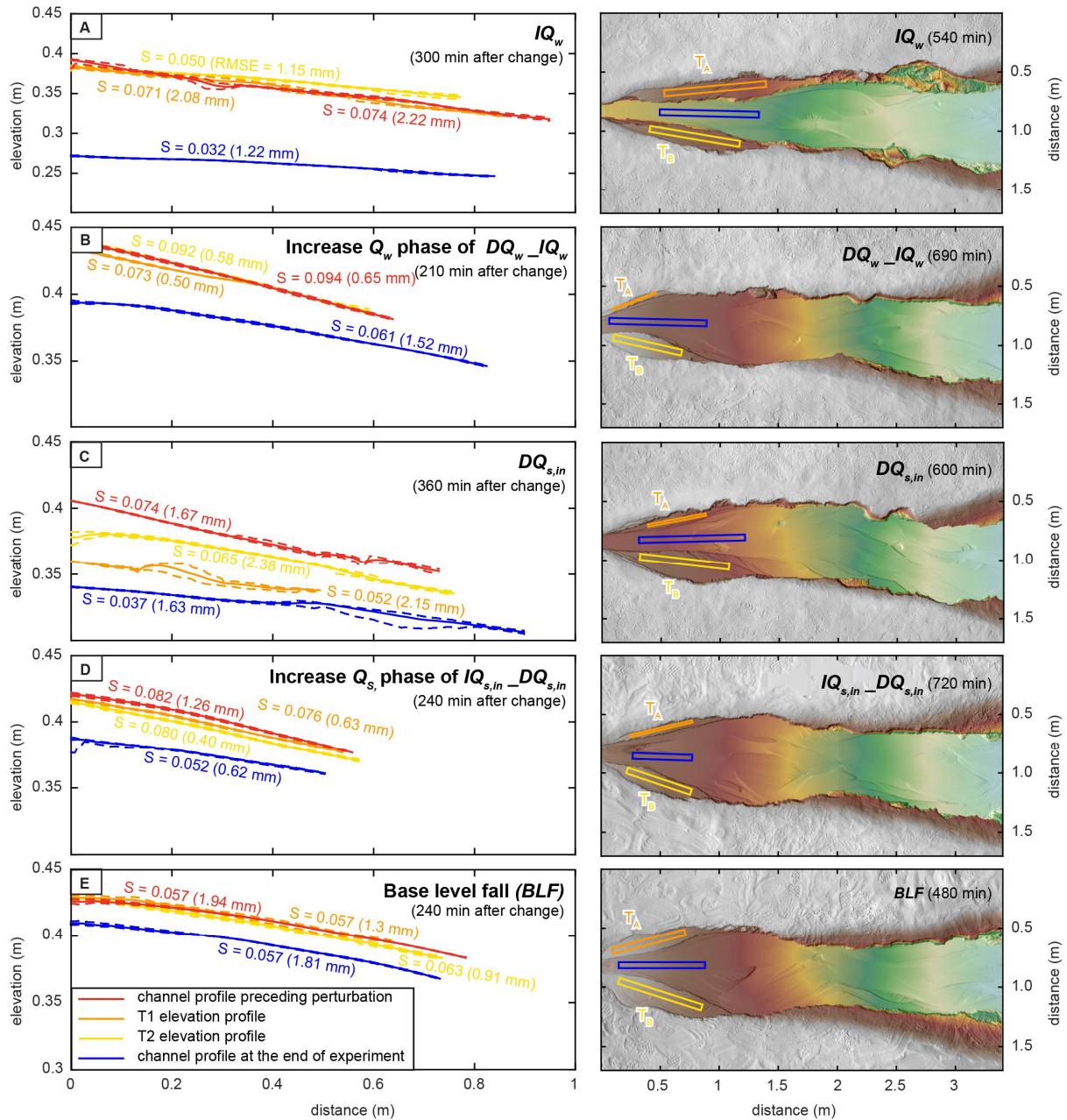


Fig. 3.6 Elevation profile and slope comparison of terrace surfaces and active channels. Elevation profiles are given as mean (solid lines) and minimum and maximum values (dashed lines), extracted along a 5 cm wide swaths as indicated on the right panel. Swath width was reduced in two cases of too narrow terraces to 1 cm ($DQ_w_IQ_w$ T_A terrace) and 2 cm ($DQ_{s,in}$ T_A terrace). T_A and T_B indicate terraces on one side each and refer to labels of lag-times given in Fig.3.5. Slopes were calculated based on a linear fit through the mean elevation profiles. Numbers in parentheses give the RMSE between the linear fit and the measured data. For the four experiments in which upstream conditions were changed (A-D), the slopes of the terraces are steeper than of the active channel at the end of the experiment. In contrast, in the BLF experiment, slopes of the terraces and the active channels are about the same. Note the different y-axis for the IQ_w run for better visibility. Colors of elevation in right panel same as in Fig. 3.3.

experiments with increasing Q_w (IQ_w , IQ_w phase of $DQ_w_IQ_w$) or base-level changes (BLF), the elevation profiles of the terraces are similar to the initial channel profile (Fig. 3.6A, B and E). In cases of changes in

$Q_{s,in}$ ($DQ_{s,in}$, $DQ_{s,in}$ phase of $IQ_{s,in}$ $DQ_{s,in}$), the terraces were cut at lower elevations than the former channel (**Fig. 3.6C, D**). In the $DQ_{s,in}$ experiment, terraces on either side of the channel formed at different elevations, with one terrace about 3 cm below the other (**Fig. 3.6C, 3E**; unpaired terraces). In contrast, terraces in the other four experiments are at approximately the same elevation (paired terraces) (**Fig. 3.4, 3.6**). Despite being paired, the slopes of the two terraces differ from each other by between 5% ($IQ_{s,in}$ $DQ_{s,in}$) and 33% (IQ_w). When comparing terrace slopes to the active channel slopes (blue lines) at the end of each run, terrace slopes are steeper in all experiments in which upstream conditions (Q_w , $Q_{s,in}$) were changed (**Fig. 3.6 A-D**). In contrast, the slopes of the terraces and the active channel in the *BLF* experiment are similar to each other (**Fig. 3.6E**).

Changes in boundary conditions also affected sediment discharge at the outlet (**Fig. 3.5**, lowest panels). An instantaneous doubling of Q_w (IQ_w ; **Fig. 3.5B**) resulted in an instant increase in $Q_{s,out}$ to more than 20 times $Q_{s,in}$. This rapid increase was followed by an exponential decay down to the initial $Q_{s,out}$ value. A sudden reduction in Q_w to half its initial value (DQ_w IQ_w ; **Fig. 3.5C**) resulted in a decrease in $Q_{s,out}$. The subsequent doubling in Q_w back to its initial value triggered a rapid increase in $Q_{s,out}$ that decayed over time. In contrast, neither the instantaneous reduction in $Q_{s,in}$ by 83% ($DQ_{s,in}$; **Fig. 3.5D**) nor the doubling in $Q_{s,in}$ ($IQ_{s,in}$ $DQ_{s,in}$; **Fig. 3.5E**) triggered a measurable change in $Q_{s,out}$. For the base-level fall experiment (*BLF*; **Fig. 3.5F**), $Q_{s,out}$ could not be measured before and during the base level drop, because the basin surrounding the wooden box was flooded for this experiment. $Q_{s,out}$ was only measured from minute 280 onwards, which corresponds to minute 40 after the ‘spin-up’ of the base level fall. At that time, $Q_{s,out}$ was still about 10 times higher than $Q_{s,in}$, and $Q_{s,out}$ decreased approximately linearly from that time onwards.

3.5. Discussion

3.5.1. Channel response to perturbations and conditions of terrace formation

The preservation of fluvial fill terraces requires that vertical incision outpaces lateral erosion on one or both sides of the active channel. Whether this occurs depends on the response of alluvial channels to changing boundary conditions, which can occur through adjustments to their slope, wetted perimeter (width and depth), and/or bed-surface texture (grain-size distribution) (Blom et al., 2017; Buffington, 2012 and references therein). Because the grain-size distribution in our experiments remained constant, we focus our discussion on the externally forced adjustments of channel slope (S) and width (w) during terrace formation.

In our experiments, river-bed aggradation and channel steepening occurred after a decrease in Q_w and after an increase in $Q_{s,in}$, whereas river incision (with terrace cutting) and channel-slope lowering were driven by an increase in Q_w , a decrease in $Q_{s,in}$, or a fall in base level (**Figs. 3.2, 3.3, 3.4**). In the case of

base-level fall, incision began at the downstream boundary and diffused upstream, producing a transient steepening. The evolution of longitudinal channel profiles in our experiments is in agreement with earlier flume studies that investigated channel response to upstream (van den Berg van Saparoea and Postma, 2008) and downstream (Begin et al., 1981; Frankel et al., 2007) perturbations, as well as with numerical models that predict the evolution of longitudinal profiles following variations in $Q_{s,in}$ or Q_w (Blom et al., 2017; Simpson and Castellort, 2012; Wickert and Schildgen, 2018). In addition to slope changes, channels can also adjust to external forcing by changing their width (**Fig. 3.5**; Buffington, 2012; Church, 1995; Curtis et al., 2010; Dade et al., 2011). In all experiments, an increase in channel width occurred during aggradation (reduced Q_w , increased $Q_{s,in}$), and an instantaneous decrease in channel width occurred at the start of incision (increased Q_w , reduced $Q_{s,in}$, *BLF*; **Fig. 3.5**). No terraces were formed during the two control experiments after the ‘spin-up’ time. However, this finding does not imply that autogenic terraces do not exist in natural systems, as meander bend cut-off (Erkens et al., 2009; Gonzalez, 2001; Limaye and Lamb, 2016; Womack and Schumm, 1977) could not be tested with our experimental setup. We observed internal variability in sediment storage and release, for example in the form of bank collapse due to lateral channel migration during the experiments. However, local lateral sediment input through bank collapse did not trigger terrace formation in our experiments. Our experimental set-up also precluded terrace formation in response to internal feedbacks between the main stem and tributaries (Schumm, 1979, 1973, Gardener 1983, Schumm and Parker 1973, Slingerland and Snow 1988).

In order to link drivers and response, we turn to the work of Wickert and Schildgen (2018), who coupled equations for flow, sediment transport, and channel morphodynamics to solve for long-profile changes in transport-limited rivers. From this work, in which channel width is allowed to self-adjust following Parker (1978), we distill the following relationships between channel width (w), slope (S) and either $Q_{s,in}$ or Q_w :

$$Q_w \propto \frac{w}{S^{7/6}} \quad (3.1)$$

and

$$Q_{s,in} \propto w \quad (3.2)$$

Eq. 3.2 predicts the observed reduction in channel width after a decrease in $Q_{s,in}$ (**Fig. 3.5**). **Eq. 3.1** predicts that slope should decrease as water discharges increases, which is consistent with the observed decrease in slope from about 0.072 to 0.043 (**Fig. 3.5B**) in the IQ_w experiment, in which water discharge doubled. However, this amount of slope decrease should be matched by an 8% increase in channel width, which runs contrary to the observed instantaneous reduction in channel width by ~57% followed by gradual widening. This response is transient, whereas Wickert and Schildgen (2018) assume an equilibrium width;

the relationship between time-evolving slope, width, and basal shear stress is the most likely cause of this discrepancy. The equilibrium-width solution used by Wickert and Schildgen (2018) assumes a constant ratio between the basal shear stress at bankfull discharge (τ_b) and the critical shear stress for the initiation of sediment motion (τ_c), which can be described by (Parker, 1978):

$$\tau_b = (1 + \varepsilon)\tau_c \quad (3.3)$$

Parker (1978) suggested that the fraction of excess shear stress at bankfull flow (ε) is about 0.2 for self-formed gravel-bed rivers with equilibrium widths. Empirical measurements have confirmed an epsilon of 0.2 in a large number of rivers across the US (Phillips and Jerolmack, 2016), but Pfeiffer et al. (2017) illustrated that ε increases in tectonically active regions. It could be that rapid uplift is analogous to incision in our experiment during its transient-response phase, causing the channel to narrow and τ_b to increase, which further accelerates incision. Our experimental results demonstrate that accurately simulating long-profile evolution may require an improved understanding of the transient response of channel width.

3.5.2. Preservation of channel profiles

A common application of fluvial-terrace mapping is to reconstruct paleo-longitudinal channel profiles from terrace remnants (e.g., Faulkner et al., 2016; Hanson et al., 2006; Pederson et al., 2006; Poisson and Avouac, 2004). Reconstructed longitudinal profiles from terrace remnants are thought to be representative of the former channel profiles, ideally of conditions immediately prior to perturbations. However, morphological adjustments of a channel to external perturbations require time, such that the geomorphological response can lag behind the changes in environmental parameters (e.g., Blum and Tornqvist, 2000; Tebbens et al., 2000; Vandenberghe, 2003, 1995). The lag-time between external perturbations and the onset of terrace cutting determines the degree of reworking of terrace material. Consequently, the shorter the lag-time, the better the preservation potential of environmental conditions that existed prior to the time of perturbation.

In our experiments, the terrace surfaces preserve the former channel elevation profiles in the two increased Q_w experiments and in the *BLF* experiment (**Fig. 3.6A, B and E**). In contrast, in the decreased $Q_{s,in}$ experiments, terrace-elevation profiles are lower than the river channel immediately preceding the perturbation and, in case of the $DQ_{s,in}$ run, the terraces are also unpaired (**Fig. 3.6C, D**). Focusing on the upstream-perturbation experiments first, we observed short lag-times between perturbations and terrace cutting in all Q_w related experiments (**Fig. 3.5B, C**), which ensured good preservation of the channel profile prior to perturbation (**Fig. 3.6A, B**). Similarly, terrace cutting in the $IQ_{s,in}DQ_{s,in}$ experiment was characterized by short (T_B) or no (T_A) lag-times (**Fig. 3.5E**). The small discrepancy between terrace slopes

and initial channel slopes is a result of slope variations between the center of the channel belt (where initial and final channel profiles were measured), and the sides of the channel belt, where the terrace slopes were measured. In contrast, terrace cutting in the $DQ_{s,in}$ experiment occurred with a several hour delay. The difference in lag-times between the T_A and T_B terrace of about two and a half hours resulted in unpaired terraces, with elevation profiles several cm below the channel profile prior to perturbation (**Fig. 3.6C**).

The length of the lag-time between the perturbation and the abandonment of a terrace surface depends on how effectively vertical incision outcompetes lateral erosion. Bufe et al. (2018) have shown that the rate of lateral channel migration scales inversely with the height of valley walls (elevation difference between a terrace surface and the active channel). As such, the higher the incision rate after perturbation, the faster wall-heights grow and the more lateral mobility is reduced. Due to this positive feedback, rapid incision after a perturbation should result in short lag-times between the onset of the perturbation and terrace cutting and a good preservation of the channel profile that existed prior to perturbation. In contrast, if the river incises more slowly, terraces may be cut long after incision initiates, and the terrace profile will not directly reflect the channel profile prior to perturbation.

The lag time between the onset of base-level fall and the cutting of terraces in the upstream part of the valley is about ~115 min (**Fig. 3.5I**), which was the time required for the knickpoint to propagate upstream. As such, for base-level-fall-related terraces, the temporal lag between base-level fall and terrace cutting increases with increasing distance to the terrace upstream. In other words, terrace surfaces created through upstream knickpoint migration are diachronous, become progressively younger upstream despite being physically a continuous unit. Faulkner et al. (2016) found decreasing OSL ages with upstream distance in a fill terrace along the Chippewa River, USA that formed in response to base-level fall. Similar conclusions were also reached by Pazzaglia (2013). In comparison, incision was initiated near-synchronously along the entire reach when incision was triggered by a change in upstream boundary conditions (IQ_w , $DQ_{s,in}$; **Fig. 3.4C, D**). In summary, lag-times between the onset of the perturbation and terrace cutting depend on the combination of local incision rates after the perturbation and the trigger for incision (base-level fall vs. a change in upstream conditions).

Lag-times between the perturbation and the onset of terrace cutting can be important when dating the surfaces of fluvial fill terraces in the field. Common methods to date the onset of river incision include the dating of terrace surface material with cosmogenic exposure dating (e.g., Schildgen et al., 2016; Tofelde et al., 2017), dating sand or silt lenses with optically stimulated luminescence close to the terrace surface (OSL; e.g., Fuller et al., 1998; Schildgen et al., 2016; Steffen et al., 2009) or dating embedded organic material with ^{14}C (Farabaugh and Rigsby, 2005; Scherler et al., 2015). When transferring our observations to a field scenario, the ~2h or more of channel material reworking before terraces were cut within the upstream part of the reach in the BLF and the $DQ_{s,in}$ experiment would result in terrace ages that are younger

than the time of perturbation. The best temporal correlations between the perturbation and the terrace surface ages are achieved by those formed by changes in Q_w due to the fast onset of vertical incision and minimal reworking of terrace surface material. To assess the significance of this time-lag in natural systems requires more work on how to scale the experiment to larger channels.

3.5.3. Differences in terrace surface slopes

To reliably use fluvial terraces to reconstruct paleo-environmental conditions (i.e., changes in base level, $Q_{s,in}$ or Q_w), the identification of the terrace formation mechanism is important. We found that for $Q_{s,in}$ or Q_w related terraces, the slopes of terrace surfaces are always steeper than the active channel (the new steady state channel after the perturbation), whereas the slope of terraces formed due to downstream perturbations is very similar to that of the active channel (**Fig. 3.6**). Similar observations have been made in the field. Poisson and Avouac (2004) measured a reduction in channel slope between terraces due to deeper incision at the upstream end of a flight of terraces in the Tien Shan. They related the changes in longitudinal profiles (inferred from the terraces) to changes in Q_w . In contrast, Faulkner et al. (2016) measured terraces in the Chippewa River, a tributary to the Mississippi River, which were created in response to base-level fall and upstream knickpoint migration due to incision of the Mississippi channel bed after deglaciation. They observed no major slope change between the longitudinal profile reconstructed from the terrace and the modern channel. According to Wickert and Schildgen (2018), the relationship between slope S , $Q_{s,in}$ and Q_w , for alluvial rivers taking self-adjusting channel width and channel roughness into account, can be described as:

$$S \propto \left(\frac{Q_{s,in}}{Q_w} \right)^{6/7} \quad (3.4)$$

According to this relationship, a decrease in $Q_{s,in}$ or an increase in Q_w results in a lower channel slope. A drop in base level should, after the signal has propagated upstream, result in a slope similar to the channel before the perturbation because the $Q_{s,in}/Q_w$ ratio is unchanged. Hence, our findings suggest that slope comparisons between the terrace surfaces and the active channel could indicate whether an upstream or a downstream perturbation caused the cutting of the terraces. However, such comparisons are only informative if the active channel is still graded to the boundary conditions that initiated incision and terrace cutting. In addition, this approach to identifying the terrace-formation mechanism requires negligible tectonic tilting of the terraces after cutting.

In tectonically active regions, both strath and fill terraces have been used to infer tectonic deformation rates (e.g., Hu et al., 2017; Lavé and Avouac, 2000; Litchfield and Berryman, 2006; Peters and van Balen, 2007). Variability in slopes over time, derived from reconstructed longitudinal channel profiles, have been used to infer local deformation rates (e.g., Hu et al., 2017; Lavé and Avouac, 2000). The observed

slope differences between terrace surfaces and the active channel after upstream perturbations in our experiments (**Fig. 3.6**), however, imply that slope differences observed in the field can only be used to infer tectonic deformation rates if one can either rule out (Lavé and Avouac, 2000) or quantify slope changes related to changing Q_w and/or $Q_{s,in}$ (Pazzaglia, 2013). Because the slope changed in our experiments of upstream perturbations, incision rates were not uniform along the channel (**Fig. 3.4**). Litchfield and Berryman (2006) also measured variable fluvial incision rates based on terrace heights at several locations along 10 major rivers located along the Hikurangi Margin, New Zealand. Accordingly, gradients in incision rates along rivers should be interpreted in the context of potential changes to the shape of the longitudinal profile.

3.5.4. Signal propagation and implications for stratigraphy

Alluvial rivers adjust their channel geometry (slope, width, and depth) with regards to incoming Q_w and $Q_{s,in}$ (Lane, 1955; Mackin, 1948). Consequently, a change in input parameters leads to an adjustment in channel geometry through the deposition or remobilization of sediment until new equilibrium conditions are reached (transient phase). The required adjustment time is referred to as the response time of the channel (Paola et al., 1992a). We expect that a change in Q_w will trigger a transient response in $Q_{s,out}$ during that adjustment phase, but $Q_{s,out}$ is expected to return to the initial value once the new steady-state channel geometry is reached (Armitage et al., 2013, 2011). In contrast, a change in $Q_{s,in}$ will result in a permanent adjustment of $Q_{s,out}$ once the channel geometry is adjusted to the new conditions (Allen and Densmore, 2000; Armitage et al., 2011).

According to Eq. 3.4, an increase in Q_w is expected to result in a lower channel slope and, therefore, to initiate river incision. In our IQ_w experiment, we observed an up to 20-fold increase in $Q_{s,out}$ after the perturbation, followed by a return to previous $Q_{s,out}$ values at about 300 min after the perturbation (equivalent to 540 min runtime; **Fig. 3.5B**). As such, the $Q_{s,out}$ signal is generated during the transient phase of slope adjustment. This pattern is schematically shown in **Fig. 3.7C**. Because $Q_{s,in}$ was held constant during the experiment, the additional sediment that reached the outlet was remobilized from within the channel, in particular from the upstream part (**Fig. 3.4C, G**). This result corroborates previous observations from physical experiments (van den Berg van Saparoea and Postma, 2008) and numerical models (Armitage et al., 2013; Simpson and Castelltort, 2012). In contrast, a decrease in Q_w requires a steeper channel gradient, which is achieved through sediment deposition within the channel (**Fig. 3.4E**). In our experiments, $Q_{s,out}$ was reduced relative to the upstream sediment supply during the transient slope-adjustment phase (**Fig. 3.5C and 3.7D**).

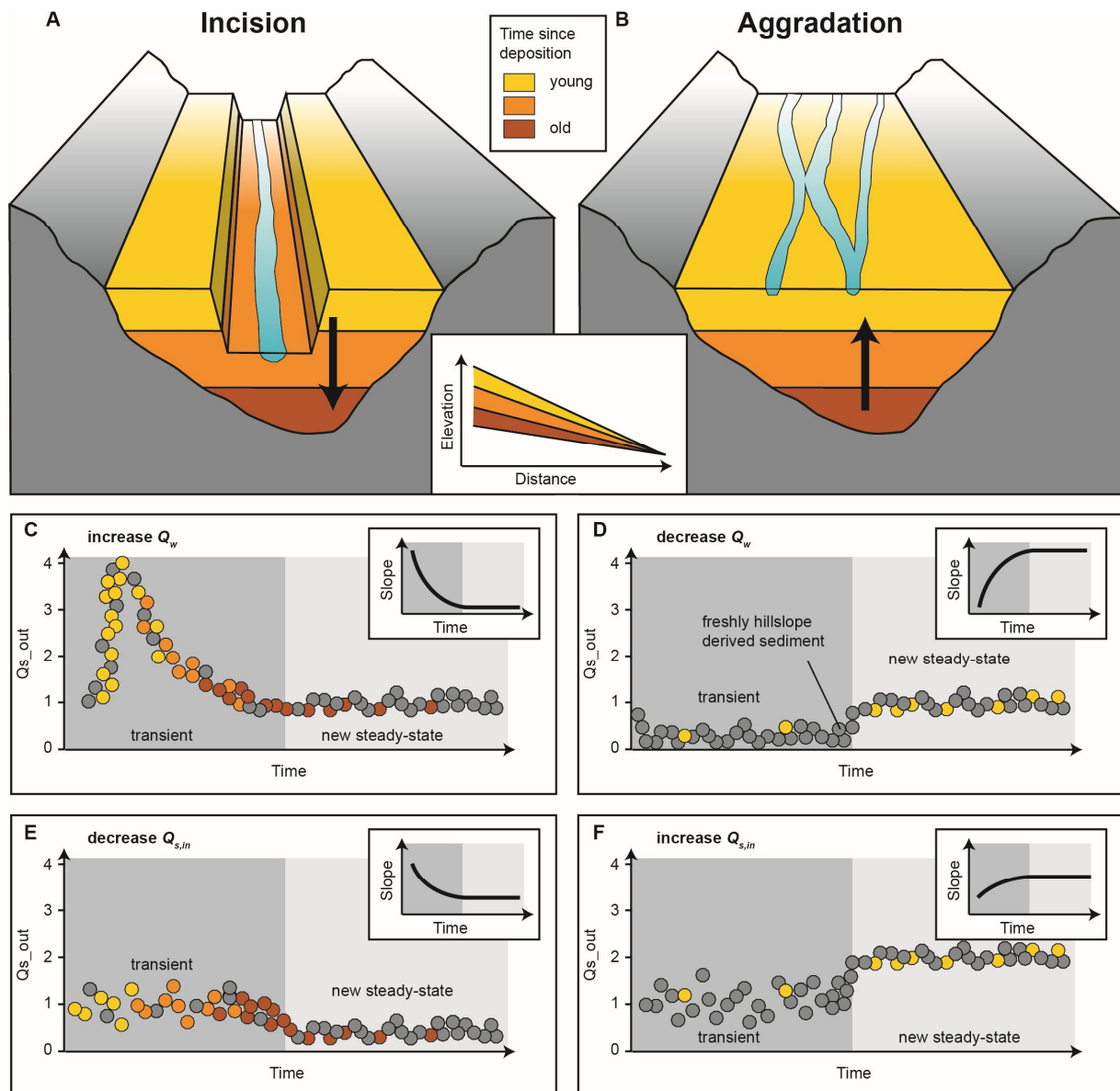


Fig. 3.7 Schematic model of the evolution of signals at the outlet stored in either sediment volume or the chemical composition of the sediment.

A decrease in $Q_{s,in}$ should, following the achievement of a graded channel profile, also produce a reduced $Q_{s,out}$, whereas an increase in $Q_{s,in}$ should result in enhanced sediment discharge at the outlet (Allen and Densmore, 2000; Armitage et al., 2011). According to Eq. 3.4, a reduction in $Q_{s,in}$ will trigger temporary incision, because a lower slope is required to transport less sediment with the same amount of Q_w , whereas an increase in $Q_{s,in}$ will require a steeper slope and thus trigger aggradation. We observed channel incision and slope reduction in the $DQ_{s,in}$ experiments (Fig. 3.4D, H and 3.5D, E) and aggradation and slope increase following an increase in $Q_{s,in}$ (Fig. 3.4F and 3.5E). However, in none of the experiments with

variable Q_s is a clear signal in $Q_{s,out}$ recognizable during the transient phase of slope adjustment (**Fig. 3.5D and E, 3.7E and F**). We consider the negative feedback between $Q_{s,in}$ and the bed-elevation change during the transient channel-adjustment phase as the main reason for this lack of response (Simpson and Castelltort, 2012; van den Berg van Saparoea and Postma, 2008). The additional sediment supplied upstream is deposited within the channel, resulting in aggradation, and is therefore not detectable at the outlet. When less sediment is supplied upstream, the channel incises and complements the supplied upstream sediment with remobilized sediment from within the reach, such that once again, no clear reduction in $Q_{s,out}$ is visible during the adjustment phase. We did not run the experiments long enough to analyze the adjusted steady-state phase, but we would expect that once the channel has adjusted to new equilibrium conditions, the changes in $Q_{s,in}$ will eventually become visible in $Q_{s,out}$ (Allen and Densmore, 2000; Armitage et al., 2011).

Internal dynamics within the channel can lead to variability in $Q_{s,out}$ even without external forcing. In the *Ctrl_1* and *Ctrl_2* experiments, scatter in the $Q_{s,out}$ signal was up to 5 times the value of $Q_{s,in}$ (**Fig. 3.5A**). This variability is due to continuous lateral movement of the channel and subsequent bank collapse, which results in stochastic contributions of additional sediment. Lateral channel mobility of a stream varies with water and sediment discharge (Bufe et al., 2018; Wickert et al., 2013). However, if the volume of sediment mobilized from valley walls due to lateral migration is much larger than the change in $Q_{s,in}$, then no clear signal in $Q_{s,out}$ might be recognizable, even after channel adjustment. The channel instead will continually adjust to the stochastic lateral input of sediment.

Regarding $Q_{s,out}$ signals, we conclude that terraces, floodplains, and the channel itself act as a temporary storage space where sediment can be deposited or remobilized when boundary conditions change (Coulthard et al., 2005; Simpson and Castelltort, 2012; van den Berg van Saparoea and Postma, 2008). Our data support earlier findings by Simpson and Castelltort (2012) and van den Berg van Saparoea and Postma (2008), who concluded from their respective numerical model and physical experiments that signals of Q_w variability create an amplified signal in $Q_{s,out}$, whereas changes in $Q_{s,in}$ create a dampened signal in $Q_{s,out}$ due to the a negative feedback between $Q_{s,in}$ and channel gradient. Our experiments, illustrated schematically in **Fig. 3.7**, also suggest that Q_w -driven $Q_{s,out}$ signals are transient, and that as the channel slope adjusts to the new input Q_w , $Q_{s,out}$ evolves back to its initial steady-state value. In contrast, $Q_{s,out}$ signals driven by changes in $Q_{s,in}$ may not be observable during transient channel adjustment, but will occur and persist once the channel has adjusted to new steady-state conditions.

Our findings also have implications for geochemical signatures of sediment, for example the concentration of cosmogenic ^{10}Be , which is commonly measured to infer catchment mean denudation rates (Bierman and Steig, 1996; Brown et al., 1995; Granger et al., 1996). In cases of channel aggradation, $Q_{s,out}$ is reduced compared to $Q_{s,in}$ due to deposition within the channel (**Fig. 3.7B, D, F**). The exported sediment

could be sourced from incoming sediment that is not deposited (grey circles) and/or mixing with remobilized sediment within the channel (yellow circles). In general, net deposition along the channel leads to the majority of the grains at the outlet being freshly delivered from hillslopes, thus carrying the modern chemical composition at the time of transport. In contrast, during incision, older material stored within the channel, floodplain, and/or terraces is remobilized and contributes to the temporary peak in $Q_{s,out}$ (**Fig. 3.7A, C, E**). Shortly after the perturbation, most of the remobilized sediment will be stratigraphically high and relatively young (yellow circles), but older material from deeper layers (orange and red circles) will progressively be remobilized and mixed with young material from upstream. Cosmogenic nuclide analyses along the eastern Altiplano margin (Hippe et al., 2012) and in the Amazon basin (Wittmann et al., 2011) indicate that sediment can be stored within the fluvial system over thousands to millions of years. Remobilization of formerly deposited material and subsequent mixing with fresh hillslope material (incoming sediment) can temporally buffer signals stored in the geochemical composition of detrital river sediments (e.g., Tofelde et al., 2018; Wittmann et al., 2016, 2011). We conclude that modern chemical signals are more likely to be transmitted through the system during aggradation phases, whereas local sediment that has been transiently stored may strongly overprint the signal of modern sediments during times of incision.

3.6. Summary and Conclusions

We performed seven physical experiments to investigate the effects of changing boundary conditions ($Q_{s,in}$, Q_w , base level) on channel geometry, fill-terrace formation and signal propagation in fluvial sediments. In particular, we recorded the evolution of channel slope and width during adjustment to new boundary conditions. Furthermore, we explored the conditions under which fill terraces form and how well they preserve the channel profile prior to perturbation based on lag-times between the onset of perturbation and terrace cutting, synchronicity of incision along the length of the channel, and the relationship between terrace-surface slopes and terrace-formation mechanisms. In addition, we examined the implications of changing boundary conditions on signal propagation through the sediment-routing system. Our experimental findings can be summarized as follows:

1. An increase in Q_w , a decrease in $Q_{s,in}$, or a drop in base level triggered river incision and terrace cutting, combined with an instantaneous reduction in channel width.
2. The observed reduction of channel width after an increase in Q_w runs contrary to the expected channel widening under equilibrium conditions. This finding indicates that the transient response of the fluvial system – not captured in the equilibrium relationship between channel width (w), discharge (Q_w) and slope (S) from the coupled equations of Wickert and Schildgen (2018) – may be significant. We

suggest that the transient channel-width response may lead to an excess shear stress at bankfull flow (ϵ) that differs from the commonly assumed and encountered value of $\sim 0.2\tau_c$ (Parker, 1978; Phillips and Jerolmack, 2016).

3. The lag-time between an external perturbation and terrace cutting determines (i) how well terraces preserve and record the pre-perturbation channel longitudinal profile, and (ii) the degree of reworking of terrace-surface sediment. We found that rapid incision creates terraces that effectively track external forcing and record the pre-perturbation channel profile, whereas slower incision enables lateral migration of the channel, with terraces cut during the transient phase that lag behind the timing of forcing and do not preserve the pre-perturbation channel profile.
4. In comparison to incision triggered by changes in upstream conditions ($Q_{s,in}$, Q_w), which occurred near synchronously along the entire channel reach, incision triggered by base-level fall created the upstream migration of a knickzone. Consequently, the lag-time between the drop in base level and the cutting of a terrace surface increased with distance upstream. Due to increased surface reworking with distance upstream, the preservation potential of the channel surface prior to perturbation decreases with distance upstream.
5. Terraces related to upstream perturbations ($Q_{s,in}$, Q_w) were always steeper than the active channel at the end of the experiment. In contrast, the final, adjusted channel slope was similar to the initial channel slope in the base-level fall experiment. This difference can help to identify the terrace-formation mechanism in field settings, but complicates the interpretation of terraces as tectonic deformation markers.
6. Changes in Q_w caused a measurable signal in $Q_{s,out}$ during the transient phase of channel adjustment, whereas $Q_{s,out}$ signals related to changes in $Q_{s,in}$ were not detectable during the transient phase due to buffering (sediment storage or release) of $Q_{s,in}$ as the channel adjusted its gradient. Changes in $Q_{s,in}$ are thought to become more recognizable once the channel has adjusted to new steady-state conditions. Because Q_w -driven signals generated an amplified $Q_{s,out}$ signal during the transient channel response phase, they have a higher potential to be preserved in the stratigraphic record than do changes in $Q_{s,in}$ if upstream conditions are changing periodically with a period that is shorter than the channel response time.
7. Signals extracted from the geochemical composition of sediments are more likely to represent modern-day conditions during times of aggradation, whereas the signal will be temporally buffered due to mixing with older, remobilized sediment during times of channel incision.

We experimentally demonstrated that fluvial fill terraces can form due to changes in water discharge (climate), sediment supply (climate or tectonics), or base level (climate or tectonics). We demonstrated major differences in lag-times between the onset of perturbation and terrace cutting, and

consequently in the resulting terrace elevation profiles and slopes. Therefore, information on the initial channel and environmental conditions that existed prior to the time of perturbation are not always well preserved in the terraces. We conclude that identifying the mechanism of fluvial fill terrace formation is necessary to reconstruct past climatic or tectonic forcing accurately and that sediment storage and remobilization of sediment in alluvial channels can influence signals stored in the discharge ($Q_{s,out}$) or chemical composition of sediment.

Acknowledgments

We thank Ben Erickson, Richard Christopher, Chris Ellis, Jim Mullin, and Eric Steen for their help in building the experimental setup and installing equipment. We are also thankful to Jean-Louis Grimaud and Chris Paola for fruitful discussions and suggestions. Financial support for this study was provided by the Emmy-Noether-Programme of the Deutsche Forschungsgemeinschaft (DFG), grant number SCHI 1241/1-1 awarded to T.S. and start-up funds provided to A.W. by the University of Minnesota. S.S. acknowledges support from the Alexander von Humboldt Foundation, grant ITA 1154030 STP.

4. Fluvial fill terraces in the Quebrada del Toro

Published as:

Tofelde, S., Schildgen, T.F., Savi, S., Pingel, H., Wickert, A.D., Bookhagen, B., Wittmann, H., Alonso, R.N., Cottle, J., Strecker, M.R., 2017. 100 kyr fluvial cut-and-fill terrace cycles since the Middle Pleistocene in the southern Central Andes, NW Argentina. *Earth Planet. Sci. Lett.* 473, 141–153.

Keywords:

*¹⁰Be depth-profiles,
surface inflation,
aggradation-incision
cycles, glacial-
interglacial cycles,
landscape response to
climate change, Eastern
Cordillera*

Abstract

Fluvial fill terraces in intermontane basins are valuable geomorphic archives that can record tectonically and/or climatically driven changes of the Earth-surface process system. However, often the preservation of fill terrace sequences is incomplete and/or they may form far away from their source areas, complicating the identification of causal links between forcing mechanisms and landscape response, especially over multi-millennial timescales. The intermontane Toro Basin in the southern Central Andes exhibits at least five generations of fluvial terraces that have been sculpted into several-hundred-meter-thick Quaternary valley-fill conglomerates. New surface-exposure dating using nine cosmogenic ¹⁰Be depth profiles reveals the successive abandonment of these terraces with a 100 kyr cyclicity between 75±7 and 487±34 ka. Depositional ages of the conglomerates, determined by four ²⁶Al/¹⁰Be burial samples and U-Pb zircon ages of three intercalated volcanic ash beds, range from 18±141 to 936±170 ka, indicating that there were multiple cut-and-fill episodes. Although the initial onset of aggradation at ~1 Ma and the overall net incision since ca. 500 ka can be linked to tectonic processes at the narrow basin outlet, the superimposed 100 kyr cycles of aggradation and incision are best explained by eccentricity-driven climate change. Within these cycles, the onset of river incision can be correlated with global cold periods and enhanced humid phases recorded in paleoclimate archives on the adjacent Bolivian Altiplano, whereas deposition occurred mainly during more arid phases on the Altiplano and global interglacial periods. We suggest that enhanced runoff during global cold phases – due to increased regional precipitation rates, reduced evapotranspiration, or both – resulted in an increased sediment-transport capacity in the Toro Basin, which outweighed any possible increases in upstream sediment supply and thus triggered incision. Compared with two nearby basins that record precessional (21-kyr) and long-eccentricity (400-kyr) forcing within sedimentary and geomorphic archives, the recorded cyclicity scales with the square of the drainage basin length.

4.1. Introduction

Mountain belts are continually reshaped by Earth-surface processes that erode, transiently store, and transport sediment to foreland regions and beyond (e.g., Allen, 2008b). This sediment transport system responds to perturbations in climate and tectonics, and thus has varied significantly during the Cenozoic. However, most of our understanding of sediment source-to-sink dynamics in the past is based on sedimentary archives that are often located far from their source areas, such that temporal buffering of the sediment transport complicates a direct correlation with a particular external forcing mechanism (Castelltort and Van Den Driessche, 2003). Despite major advances in understanding the timing of past climatic changes during the Quaternary, our knowledge about how (often cyclic) changes in environmental conditions are reflected and preserved in terrestrial landscapes is still limited (Braun et al., 2015; Castelltort and Van Den Driessche, 2003; Godard et al., 2013).

Fluvial fill terraces offer potential insights into this problem, as they record changes in sediment flux (Q_s) and/or water discharge (Q_w) over time. As early as 1884, A. Penck correlated river terraces in the European Alpine foreland with glacial advance and retreat in the mountains (Penck, 1884). Based on multiple fluvial terrace sequences in the arid interior of Central Asia, Huntington (1907) suggested a close link between increased hillslope erosion, reduced vegetation cover, and aggradation during arid conditions, followed by incision during humid phases. Since then, studies from around the globe have linked fluvial fill terrace formation in glaciated catchments with variability in Q_s and Q_w over glacial-interglacial cycles (e.g. Bridgland and Westaway, 2008; Huang et al., 2014; Pan et al., 2003; Wegmann and Pazzaglia, 2009). Little is known, however, about how variability in global climate may have affected Earth-surface processes on multi-millennial timescales in regions far from major glaciers and ice sheets, and how those changes might be reflected in the landscape.

High-altitude moraines indicate the presence of past glaciers in the Central Andes (Haselton et al., 2002; Zech et al., 2009). Even in areas without extensive past ice cover, multiple levels of fluvial terraces in the Central Andes have been described (e.g., Baker et al., 2009; Farabaugh and Rigsby, 2005; Schildgen et al., 2016; Steffen et al., 2010; Tchilinguirian and Pereyra, 2001). Where dated, the terraces mainly span the last glacial-interglacial cycle (Farabaugh and Rigsby, 2005; Schildgen et al., 2016; Steffen et al., 2010); terraces spanning timescales longer than 120 kyr have only been reported in one study from the Andes – along the Río Diamante (**Fig. 4.1b**; Baker et al., 2009).

The Toro Basin in the Central Andes of NW Argentina (**Fig. 4.1**) contains several hundred meters of sub-horizontal conglomerates deposited after 0.98 Ma (Marrett et al., 1994) that have been incised by the Río Toro to create multiple terrace levels. These terraces are located high in the basin, proximal to the source area, offering a rare opportunity to study the sediment routing system before sediment storage and

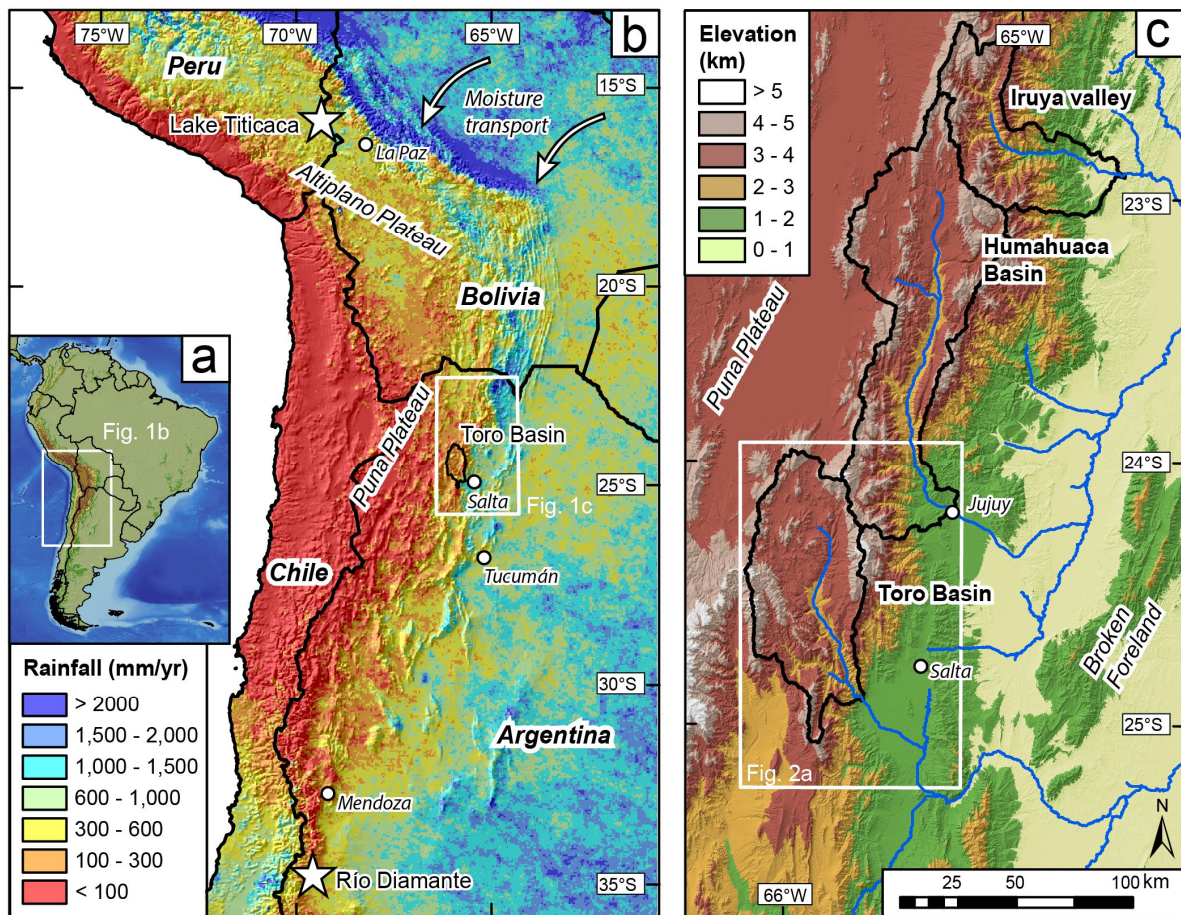


Fig. 4.1 Rainfall of the Central Andes and regional topography of NW Argentina. (a) Map of South America. White box shows outline of (b). (b) Rainfall map calculated from TRMM2B31 product with a 5 km resolution (Bookhagen and Strecker, 2008). Stars mark Lake Titicaca – a paleo climate record site (Fritz et al., 2007) and Río Diamante - a site of dated fluvial fill terraces that cover several glacial-interglacial cycles (Baker et al., 2009). (c) Topography from SRTM dataset (~30 m resolution; data available from the U.S. Geological Survey). Black lines delineate the catchments of the Toro Basin, Humahuaca Basin and Iruya valley.

re-mobilization buffer the signal. To better understand the dynamics of the sediment transport system within this intermontane basin, we determined the onset of river-incision phases by dating the exposure of the three most extensive and best-preserved terrace surfaces (treads) with cosmogenic ^{10}Be depth profiles. The timing of depositional events is based on cosmogenic burial dating and U-Pb zircon dating of volcanic ashes that are incorporated into the fill material. Based on the chronology we derive from these data, we consider the potential impact of autogenic forcing, tectonics, and climate variability on the evolution of the valley fill.

Fluvial fill terraces in the Quebrada del Toro

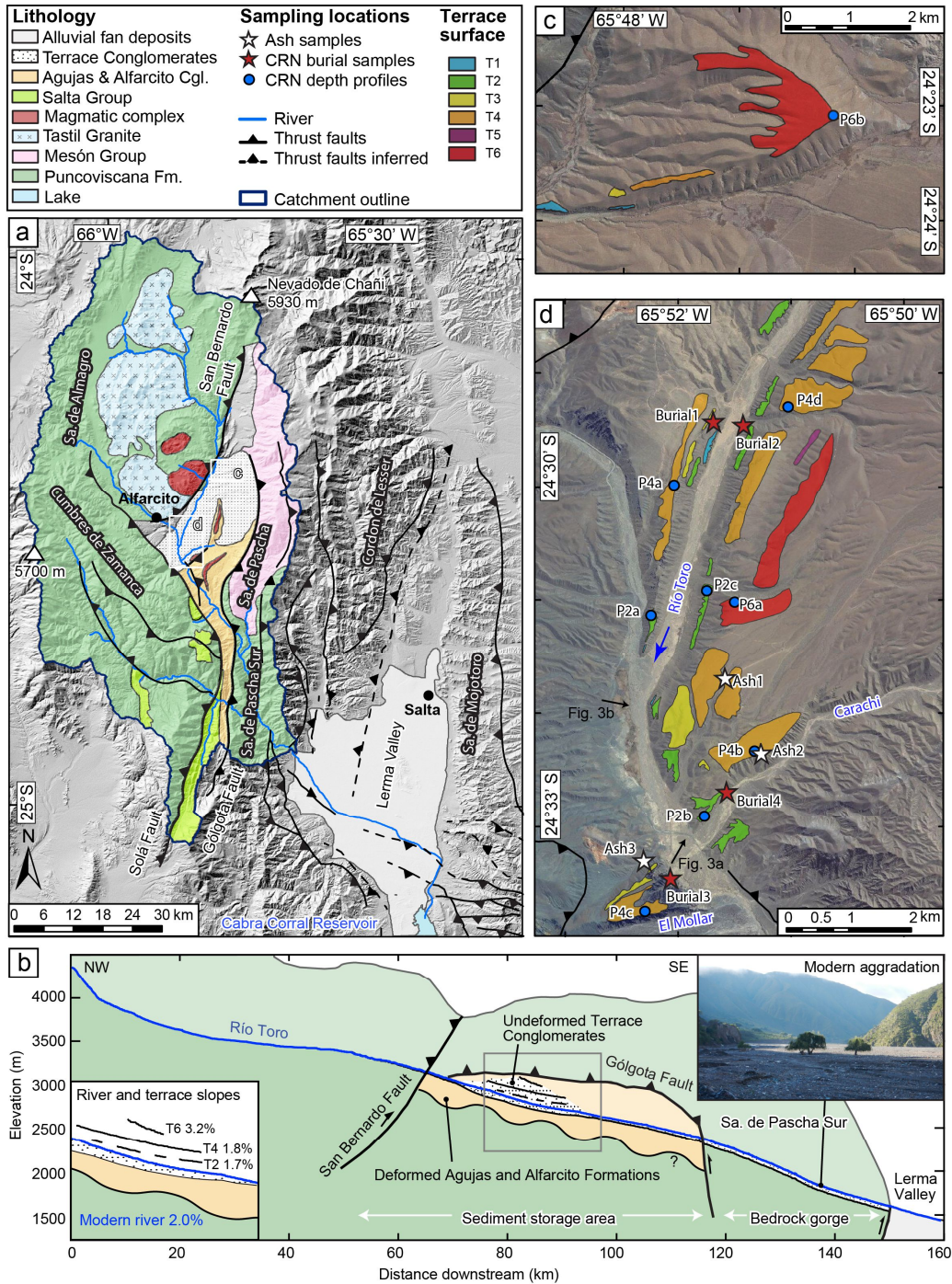


Fig. 4.2 Detailed overview of the Toro Basin and the fill terraces. (a) Geological map of the Toro Basin and northern part of the Lerma Valley based on previous work by García et al. (2013) and Hilley and Strecker (2005). (b) Longitudinal profile of the Río Toro with projected lithological and structural interpretations. Left insert: Slopes of the modern river and of three out of six terraces. The terrace slopes were estimated based on differential GPS measurements and SRTM data. Right insert: Filed photograph showing modern sediment aggradation of the riverbed. Note the buried trees. (c) and (d) ArcGIS Basemap imagery including sample locations and mapped terrace levels. Black arrows in (d) indicate direction of field photos shown in Fig. 4.3a and b. Abbreviations: Cgl. = Conglomerates, Fm. = Formation, Sa. = Sierra.

4.2. Study area

4.2.1. Geological and geomorphic setting

The Central Andean Plateau is subdivided into a northern (Altiplano) and a southern (Puna) sector (**Fig. 4.1b**). The Toro Basin at $\sim 24.5^{\circ}\text{S}$ is one of several intermontane basins located in transition between the high-elevation, arid Puna to the west and the low-elevation, humid foreland to the east (**Fig. 4.1c**).

The basin is confined by reverse-fault bounded basement ranges, namely the Cumbres de Zamanca and Sierra de Almagro to the west and the Sierra de Pascha and the Sierra de Pascha Sur to the east (**Fig. 4.2a**). The main basin-bounding faults are the west-dipping Solá Fault to the west, the northwest-dipping San Bernardo Fault to the north, and the east-dipping Gólgota Fault to the east (Marrett and Strecker, 2000). The Solá Fault has been active at least since the Pliocene, and deformation along the San Bernardo and Gólgota faults extends from the Miocene until at least 0.98 Ma (Marrett and Strecker, 2000), with potential re-activation of the Gólgota Fault after 0.98 Ma (Hilley and Strecker, 2005). Exposed basement rocks mainly comprise quartz-bearing meta-sediments of the Late Proterozoic to Cambrian Puncoviscana Formation and Paleozoic quartzites and shales of the Mesón group (Schwab and Schäfer, 1976).

Whereas the morphology of southern part of the basin is dominated by a narrow bedrock gorge presently experiencing sediment aggradation (**Fig. 4.2b**), the region upstream of the Gólgota Fault is a low-relief landscape, where most of the late Cenozoic sedimentary basin deposits are stored. The Toro Basin is drained by the perennial, braided Río Toro, which flows with a mean gradient of $\sim 1.6\%$ between the upper end of the terrace deposits and the lower end of the bedrock gorge. At the outlet of the gorge, a fraction of the sediment removed from the Toro Basin is re-deposited on an alluvial fan in the Lerma Valley (**Fig. 4.2a**).

Hilley and Strecker (2005) suggested that the oscillatory character of the sediment deposition and excavation in the Toro Basin, comprising at least two periods of filling and excavation since 8 Ma, is related to the interplay between rock uplift, rock type, and climate. The eroded and tilted Alfarcito conglomerates document an initial basin-filling stage. After 0.98 Ma, the Toro Basin was excavated to a base level lower than today. It was subsequently re-filled by a several-hundred-meter thick, sub-horizontal conglomeratic unit (“Terrace Conglomerates”) (**Fig. 4.2a & b**) (Hilley and Strecker, 2005; Marrett and Strecker, 2000). Hilley and Strecker (2005) suggested that this valley fill resulted from reactivated uplift of the Sierra de Pascha Sur after 0.98 Ma, a basement block bounded to the west by the Gólgota Fault and to the east by a less pronounced fault at the basin outlet. The mechanically strong basement rock of the Sierra de Pascha Sur could not be incised as quickly as it was uplifted, which led to aggradation upstream of the Gólgota Fault and channel steepening within the gorge (**Fig. 4.2b**). The resultant post-0.98 Ma Terrace Conglomerates overlie tectonically-deformed and eroded paleo-topography. This conglomerate was then

incised, leaving behind a flight of at least five to six paired terrace levels (one surface is only visible in one location as small remnants) between 20 and 220 m above the present-day river (**Fig. 4.3a and b**) (Hilley and Strecker, 2005; Marrett and Strecker, 2000; Schwab and Schäfer, 1976). The stratigraphy of the unlithified, sub-horizontal Terrace Conglomerates does not reveal distinct units. Therefore, it is unclear whether the Terrace Conglomerates consist of one fill unit followed by stepwise incision or if each terrace is related to one cut-and-fill cycle.

The Terrace Conglomerates are clast-supported, pebble to cobble conglomerates that consist of well-rounded, often imbricated, and partly sorted clasts, commonly up to several decimeters in diameter, with rare boulders. The gently inclined terraces are capped by desert pavements (**Fig. 4.3**), characterized by closely packed, interlocking clasts that overlie a layer of fine sand and silt (e.g., McFadden et al., 1987), which in turn covers the conglomerates. The thickness of these fine sand/silt layers varies among the surfaces from 10 to 50 cm, with the higher terraces generally having a greater thickness.

4.2.2. Climatic setting

The eastern flanks of the southern Central Andes of Argentina (including the intermontane basins of the Eastern Cordillera) are characterized by pronounced orographic rainfall gradients (**Fig. 4.1b**, Bookhagen and Strecker, 2008). Water vapor transport from the Atlantic Ocean and Amazon Basin is mainly governed by the South American Summer Monsoon (SASM) system, in which the South American low-level jet (SALLJ) funnels air masses southward along the Andes into (sub-)tropical South America (Castino et al., 2016; Vera et al., 2006). The Toro Basin, situated at the southern end of the SALLJ conveyor, receives rainfall ranging from ~900 mm/yr at the outlet to <200 mm/yr in the interior of the basin.

Moisture supplied to the Central Andes has varied significantly over the past several tens of thousands of years (see review by Baker and Fritz, 2015). Variability in the intensity of SASM precipitation on precessional timescales (21 kyr) has been documented by paleo-lake studies on the Puna Plateau of Argentina and Chile (Bobst et al., 2001; Godfrey et al., 2003) and the Bolivian Altiplano (Titicaca Basin: Fritz et al., 2010; Uyuni Basin: Fritz et al., 2004; Placzek et al., 2006). During cold periods in the Northern Hemisphere, the Atlantic portion of the intertropical convergence zone (ITCZ) was displaced southward and caused corresponding shifts of the moisture-bearing wind systems (Broccoli et al., 2006). The enhancement of rainfall in the Central Andes during these cold phases provided the necessary moisture for glacier growth and higher lake levels (Haselton et al., 2002; Vizzy and Cook, 2007). An overall increase in moisture supply to the Altiplano during colder phases also occurred on ~100 kyr (eccentricity) cycles. Near Lake Titicaca (**Fig. 4.1b**), increased pollen abundance of aquatic species and green algae (Gosling et

Fluvial fill terraces in the Quebrada del Toro

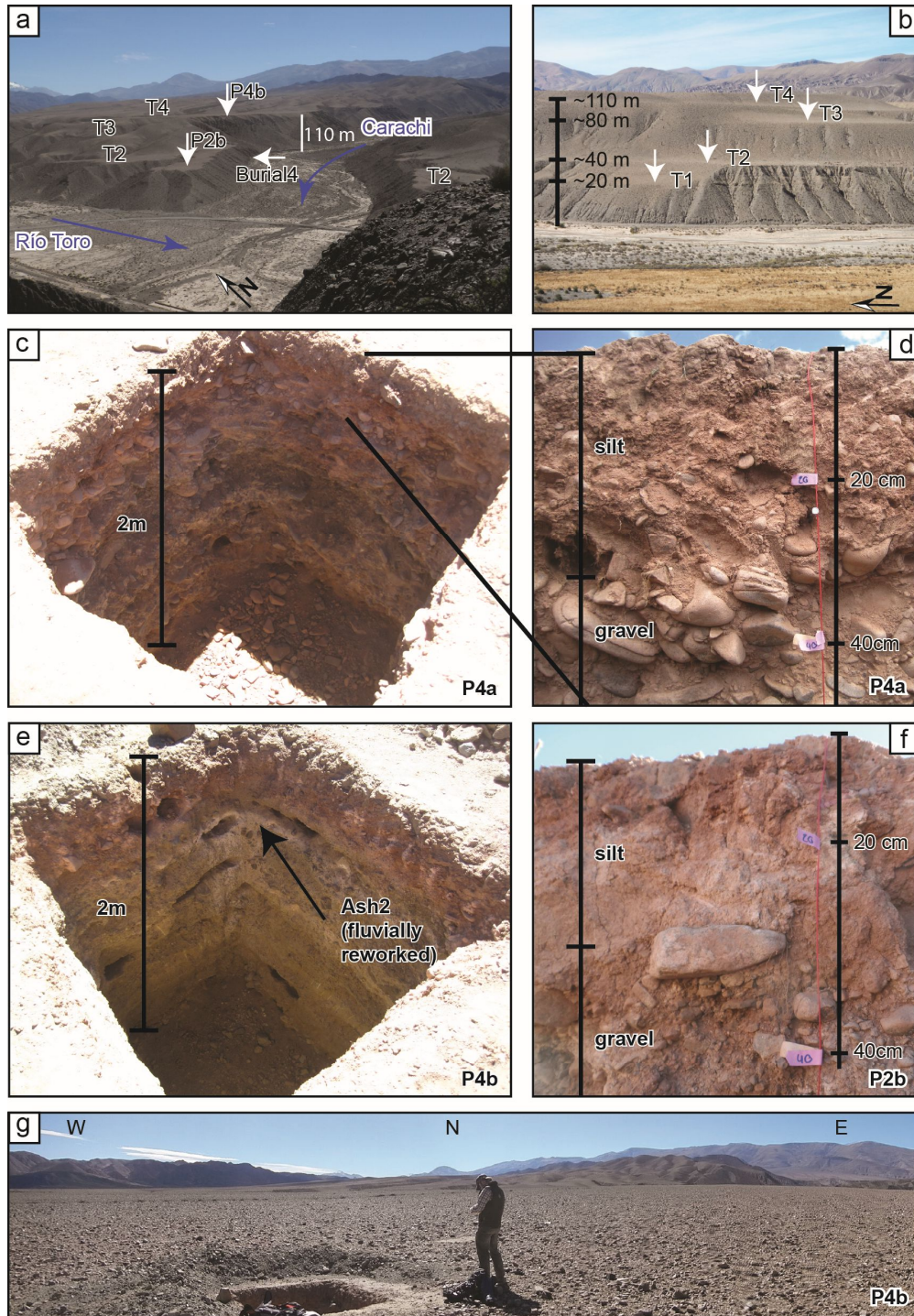


Fig. 4.3 Field pictures of the Terrace Conglomerates. (a) Fluvial fill terraces at a confluence and (b) along the Río Toro main-channel. The locations of the terrace field photos are indicated by arrows in Fig. 4.2d. The pits for ^{10}Be depth profiles (c,e) were excavated on terrace surfaces far from the terrace margins and slopes of nearby terraces to avoid erosion or potential overwash. Within the pits seven to eight samples for ^{10}Be depth profile analysis were collected. Close-ups of the upper 40 cm of P4a (d) and P2b (f). A fine sand to silt layer can be distinguished from underlying gravel – a feature commonly observed in desert pavements (McFadden et al., 1987); same as the layer of closely packed, interlocking clast at the surface. (g) Panorama view of a terrace surface. The fine sand to silt layer in desert pavements is related to aeolian input and causes inflation of the surfaces over time.

al., 2008) as well as lake highstands (Fritz et al., 2007) correlate with regional glacial advances and global glacial stages.

At present, the high ranges surrounding the Toro Basin are not glaciated. However, glacial landforms and multiple generations of moraines above 3,800 m elevation document previous glacial activity in the region, with an estimated cover of less than 5% of the Toro Basin.

4.3. Methods

To determine the onset of incision phases of the Terrace Conglomerates, we applied cosmogenic radionuclide (CRN) exposure dating to the terrace treads. The timing of aggradation was identified based on $^{26}\text{Al}/^{10}\text{Be}$ burial dating and U-Pb zircon dating of intercalated, Puna-derived volcanic ash deposits. Fluvial terraces were mapped in the field with GPS and correlated using aerial and satellite imagery based on their elevation above the modern channel.

4.3.1. Cosmogenic radionuclide dating

Exposure ages of the most prominent terrace treads were derived from *in situ* cosmogenic ^{10}Be depth profiles collected from newly dug pits. The *in situ* production of ^{10}Be is highest at the Earth's surface and decreases approximately exponentially with depth (Lal, 1991). Hence, exponential curve fitting of a suite of measured ^{10}Be concentrations from a vertical profile can reveal the most likely surface and inherited concentrations (Anderson et al., 1996). The latter comprises ^{10}Be accumulated prior to deposition (during exhumation and transport), and is assumed to be uniform with depth. After subtracting the inheritance from the surface concentration, the remaining ^{10}Be concentration is used to calculate a surface-exposure age.

Depth profiles P2a, P2b, P4a, P4b and P4c were sampled in 2014, whereas P2c, P4d, P6a and P6b were sampled in 2003. In the profile names, "P" indicates a depth profile, numbers refer to the corresponding terrace (T1 through T6 from low to high elevation), and the final letter distinguishes multiple profiles from the same terrace (a-d). To ensure a minimal influence of terrace modification (erosion or burial) on calculated ages, the location of each depth profile was chosen several tens of meters from the closest terrace edge (**Fig. 4.3g**). Each depth profile from 2014 consists of seven to eight samples collected over a depth range of 2 to 5 m below the surface, with each sample comprising material collected over a ca. 10 to 20 cm depth interval (**Table C1**). Due to the available material, samples from profiles P2b, P4a and P4c comprise 60-100 amalgamated pebbles (1-3 cm diameter), whereas those from P2a and P4b comprise sand. The depth profiles from 2003 consist of five to seven samples each, collected over a depth

range of 2.5 m (**Table C1**). Each sample comprises 20 to 30 pebbles (3-5 cm diameter) collected over a depth interval of up to 50 cm.

Additionally, we dated the timing of sediment burial based on $^{26}\text{Al}/^{10}\text{Be}$ ratios of sand samples (e.g., Granger and Muzikar, 2001) collected in 2015 (**Fig. 4.2d, Table C2**). Because the decay constant of ^{26}Al ($\lambda_{\text{Al}} = 9.83 \pm 0.25 \times 10^{-7} \text{ yr}^{-1}$) (Nishiizumi, 2004) is nearly twice as high as that of ^{10}Be ($\lambda_{\text{Be}} = 4.99 \pm 0.043 \times 10^{-7} \text{ yr}^{-1}$) (e.g., Chmeleff et al., 2010), the initial surface nuclide ratio of $^{26}\text{Al}/^{10}\text{Be} = 6.75$ (Balco and Shuster, 2009) decreases with time after burial. To minimize effects of post-burial CRN production, we collected the four burial samples at locations that were shielded by at least 10 m of sediment cover (**Fig. C1**). This approach restricted us to sampling only a few feasible sites.

All CRN samples collected in 2003 were processed at the Space Science Laboratory (UC Berkeley, USA), with AMS measurements performed at Lawrence Livermore National Laboratory (USA). The samples collected in 2014 and 2015 were processed both at the University of Potsdam and GeoForschungsZentrum Potsdam (Germany), with AMS measurements performed at the University of Cologne (Germany). The sample preparation followed standard procedures; a detailed description is provided in the supplementary material.

Terrace tread exposure ages were determined using a combination of a Monte Carlo simulator (Hidy et al., 2010) and the CRONUS Earth online calculator v2.2 (Balco et al., 2008). We adjusted the Monte Carlo simulator to allow for this combined approach (see supplementary material). All CRN calculations were performed with the regional reference production rate from Blard et al. (2013, $3.79 \pm 0.23 \text{ atm g}^{-1} \text{ yr}^{-1}$) and the time-dependent (“*Lm*”) (Balco et al., 2008) scaling scheme.

4.3.2. U-Pb zircon geochronology

We dated three intercalated volcanic ashes to support cosmogenic burial dating constrains on the timing of conglomerate deposition. Zircon grains were extracted using standard magnetic and heavy liquid methods, handpicked, mounted in epoxy, and polished for U, Th, and Pb isotope analysis using a Laser Ablation Multi-Collector Inductively Coupled Plasma Mass Spectrometer (LA-MC-ICPMS) at the University of California, Santa Barbara. Due to significant pre-eruption residence times and/or post-eruptive reworking, analyzed samples show a wide distribution of $^{206}\text{Pb}/^{238}\text{U}$ zircon ages. Therefore, we systematically excluded the oldest ages from our calculations of an average zircon crystallization age until near-unity values for the mean square of weighted deviates ($\text{MSWD} < 2$) were achieved. Where no coherent population was found, we selected the youngest $^{206}\text{Pb}/^{238}\text{U}$ zircon ages to represent a maximum depositional

age. All analytical results and further methodological information can be found in the supplementary material (**Appendix C**).

4.4. Results

4.4.1. Terrace tread exposure dating

Out of six observed terrace levels in the Toro Basin (T1-T6), we determined exposure ages of the three most extensive and best-preserved treads (T2, T4 and T6). On each selected terrace, we sampled between two and four depth profiles for cosmogenic ^{10}Be analyses (**Fig. 4.2c and d, Table C1**).

In general, ^{10}Be concentrations from the depth profiles decrease exponentially with depth, except for P2c, which does not show any correlation with depth, and P2a, which appears to have two exponential trends separated by a thin paleosol at ~ 45 cm depth (**Fig. 4.2**). In several cases (P2a, P2b, P4a, P4b, P4c and P6a), the surface samples have a ^{10}Be concentration that falls below the expected exponential pattern (red circles in **Fig. 4.2**); this is also the case for the shallow subsurface sample in P4b. These samples all fall within the layer of fine sand/silt (see **section 4.2.1 and Fig. 4.3**). Although these samples may be outliers, another explanation is dilution of the originally deposited material with aeolian fine sand and silt. During desert pavement formation, aeolian material accumulates beneath and inflates the upper clast layer (e.g., McFadden et al., 1987). To account for potential inflation of desert-pavement surfaces, we pursued three different approaches for each depth profile to calculate the terrace-surface exposure ages. We term these (1) the *Stable-surface* approach, (2) the *Inflation-corrected* approach, and (3) the *Surface-pebbles* approach (for a summary see **Fig. C2**).

In the *Stable-surface* and *Inflation-corrected* approaches, we removed the uppermost low-concentration samples from the profiles (red circles in **Fig. 4.4**) and performed exposure-age calculations based on curve-fitting to the remaining samples. The *Stable-surface* approach assumes no inflation of the terrace surface over time (although total erosion is allowed to vary between ± 1 cm), whereas in the *Inflation-corrected* approach, we simulated the accumulation of the fine sand/silt layer in the upper part of the profiles over time. In the *Surface-pebbles* approach, we subtracted the most-probable inherited ^{10}Be concentration derived from the depth profiles from the surface samples (the ones that were excluded from the first two approaches; red circles in **Fig. 4.4**) and then calculated exposure ages from the remaining ^{10}Be concentration.

Ages derived from the *Stable-surface* and *Inflation-corrected* approaches range from $75^{+4}_{-.7}$ and $732^{+53}_{-.56}$ ka and are reported with 1σ uncertainty (**Table 4.1**; details in **Table C5 and Fig. C3**). When comparing the two sets of results, the *Inflation-corrected* ages are younger by 11% (P2b) to 26% (P4d).

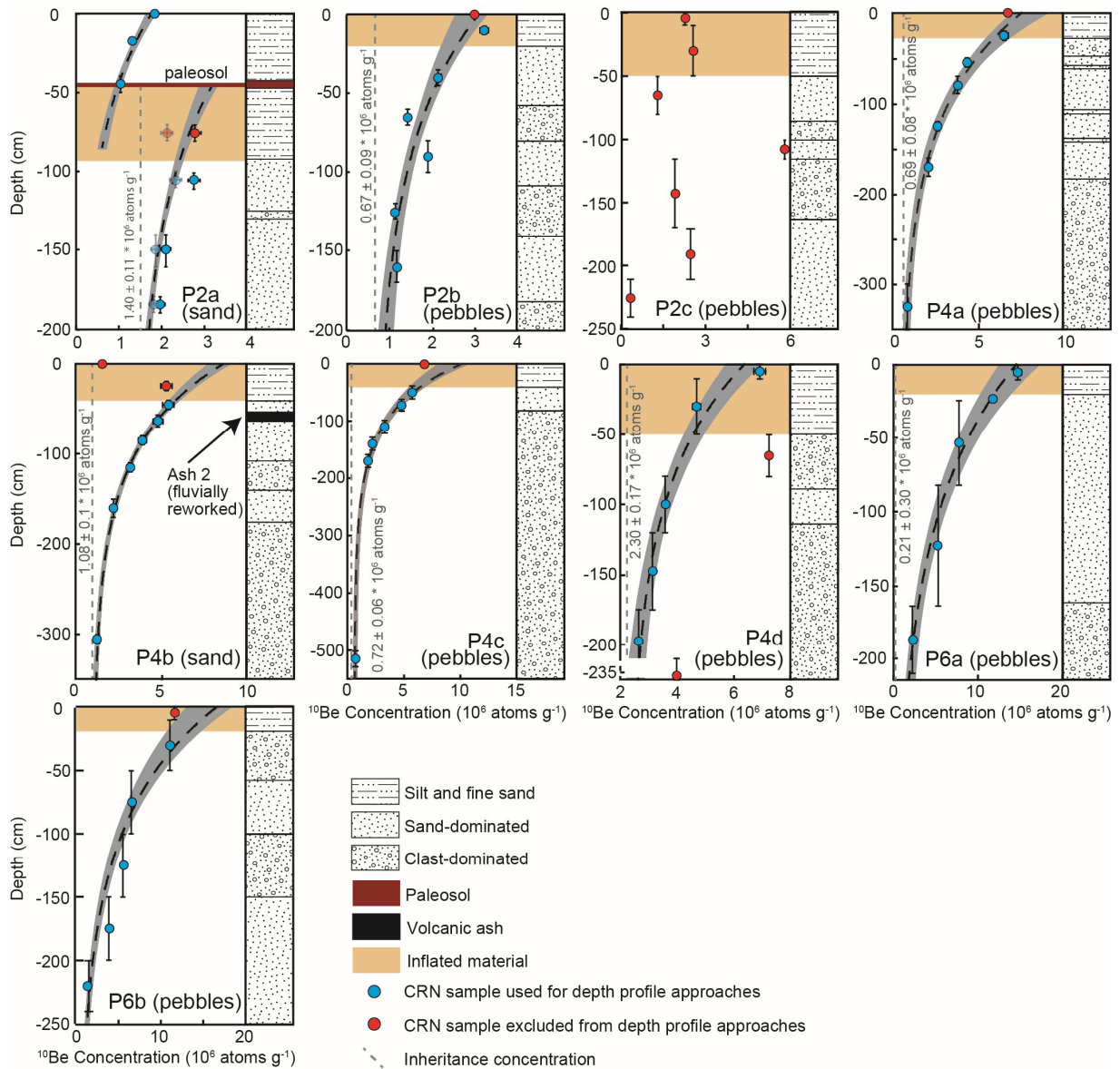


Fig. 4.4 Distribution of ^{10}Be concentration with depth for the nine profiles and sedimentary logs of the sampled pit walls. Areas shaded in light brown indicate the silt/fine sand layer observed at the top of each profile. Within each profile we either sampled exclusively sand or pebbles. Each sample was collected over a vertical depth range indicated by the vertical error bar. The horizontal error bar represent the 1σ analytical uncertainty. Samples marked in blue were included for the Stable-surface approach and the Inflation-corrected approach (Fig. C2), while red samples were excluded. The red surface samples were used for the Surface-pebbles approach instead. For P2a the top and lower part were considered as two individual profiles. For the lower profile we corrected the concentration for the time of burial by the top unit (transparent circles). We used the Monte Carlo simulator (Hidy et al., 2010) to fit 50,000 curves to each profile (grey), resulting in a most-probable fit (black dashed curve).

The *Surface-pebbles* approach was only applied to the pebble profiles. Because the ^{10}Be concentration in the surface-pebble sample is insensitive to dilution by aeolian material, it allows us to test

Table 4.1 Summary of terrace surface exposure ages based on the three different approaches. The standard deviation (1σ) for the depth profiles includes the uncertainty in the surface concentration (outcome of Monte Carlo fits), the uncertainties of the local production rate and of the ^{10}Be decay constant. The standard deviation for the surface pebbles samples is the external uncertainty given by the CRONUS calculator. The CRONUS input included the analytical uncertainty of the surface sample as well as the uncertainty of the predicted inheritance. Ages in bold we consider as most reliable and are plotted in Fig. 4.6d as light blue lines.

Sample name (Inflation in cm)	Terrace level	(1) <i>Stable-surface</i> (ka $\pm 1\sigma$)	(2) <i>Inflation-corrected</i> (ka $\pm 1\sigma$)	(3) <i>Surface-pebbles</i> (ka $\pm 1\sigma$)
P2a (40-45)	T2	153 ⁺¹⁴ / ₋₁₇	133 ⁺¹² / ₋₁₁	
P2a (top only)	T2	75 ⁺⁴ / ₋₇		
P2b (20-22)	T2	104 ⁺¹⁰ / ₋₁₁	93 ⁺⁹ / ₋₉	108 \pm 9
P2c	T2	-	-	85 \pm 8
P4a (20-25)	T4	319 ⁺²³ / ₋₂₂	282 ⁺²⁰ / ₋₂₀	269 \pm 20
P4b (30-40)	T4	327 ⁺²⁵ / ₋₂₂	266 ⁺²⁰ / ₋₂₀	
P4c (30-50)	T4	411 ⁺³² / ₋₃₄	307 ⁺²⁸ / ₋₂₄	284 \pm 26
P4d (45-50)	T4	164 ⁺¹² / ₋₁₇	121 ⁺¹¹ / ₋₁₁	190 \pm 14/ 263 \pm 18
P6a (18-22)	T6	732 ⁺⁵³ / ₋₅₆	644 ⁺⁴³ / ₋₄₉	487 \pm 34
P6b (22-24)	T6	406 ⁺²⁶ / ₋₂₈	358 ⁺²¹ / ₋₂₆	453 \pm 33

the inflation hypothesis. The resulting ages range from 85 \pm 8 ka to 487 \pm 34 ka (**Table 4.1**, details in **Table C7**).

A sub-set of the profiles required modifications in our approaches. When applying the *Stable-surface* and *Inflation-corrected* approaches to profile P2a, we infer that the two exponential trends define two depositional events separated by a period of exposure as indicated by the formation of a paleosol. For the upper fill, we calculated a surface-exposure age of 75 ⁺⁴/₋₇ ka. To calculate the exposure age for the lower fill, we first subtracted the amount of ^{10}Be produced in the samples of the lower fill unit since the deposition by the upper fill unit. Based on the remaining ^{10}Be concentration (**Fig. 4.4**, transparent circles in P2a), we calculated a surface exposure duration for the lower unit. The exposure duration is 78 ⁺¹²/₋₁₅ ka for the *Stable-surface* approach or 58⁺¹¹/₋₈ ka for the *Inflation-corrected* approach. Thus, the addition of the exposure duration of the lower surface to the exposure age of the upper surface implies that the lower surface was exposed at either 153 ⁺¹⁴/₋₁₇ ka (*Stable-surface*) or at 133 ⁺¹²/₋₁₁ ka (*Inflation-corrected*).

For three profiles (P6a, P2c and P4d) we needed to adjust the *Surface-pebbles* approach due to insufficiently constrained ^{10}Be inheritance concentrations. For P6a, the depth-profile fits suggested no inheritance, and for P2c, we could not find any depth profile fits. Therefore, for both profiles, we assumed that the inheritance is equal to the concentration of the lowermost sample in the profile, and thus we obtained ages of 487 \pm 34 ka and 85 \pm 8 ka, respectively. We performed two calculations using the *Surface-pebbles* approach for P4d: one with the calculated inheritance from P4d (*P4d_surf_4d* in **Table C7**) and one with the calculated inheritance from P4a (*P4d_surf_4a*), which is located on the same terrace level and

Table 4.2 Burial ages based on paired ^{10}Be and ^{26}Al measurements. For the calculations we assumed a constant surface production ratio of $^{26}\text{Al}/^{10}\text{Be} = 6.75$, an ^{26}Al decay constant of $\lambda_{\text{Al}} = 9.38 \times 10^{-7}$ (Nishiizumi, 2004) and a ^{10}Be decay constant of $\lambda_{\text{Be}} = 4.987 \times 10^{-7}$ (e.g., Chmeleff et al., 2010). Burial age uncertainties include measurement and decay-constant uncertainties. Ages in bold we consider as most reliable and are plotted in Fig. 4.6e as solid red lines.

Sample name	Calculated ^{10}Be concentration (^{10}Be atm $\text{g}^{-1} \pm 1\sigma$)		Calculated ^{26}Al concentration (^{26}Al atm $\text{g}^{-1} \pm 1\sigma$)		$^{26}\text{Al}/^{10}\text{Be}$ ratio	Burial age (ka $\pm 1\sigma$)	
Burial 1	7.21E+05 \pm	3.86E+04	4.82E+06 \pm	2.04E+05	6.69 \pm 0.07	18 \pm	141
Burial 2	8.05E+05 \pm	2.57E+04	4.69E+06 \pm	2.37E+05	5.82 \pm 0.06	306 \pm	125
Burial 3	1.71E+05 \pm	6.56E+03	7.34E+05 \pm	5.07E+04	4.29 \pm 0.08	936 \pm	170
Burial 4	2.91E+05 \pm	1.02E+04	1.68E+06 \pm	8.72E+04	5.77 \pm 0.06	325 \pm	130

received material from the same catchment. The two resulting exposure ages are 190 ± 14 ka and 263 ± 18 ka, respectively.

4.4.2. Depositional ages

To clarify whether the conglomeratic fill of the Toro Basin was emplaced during a single depositional episode and was later incrementally incised, or if it records multiple cut-and-fill cycles, we determined four CRN burial ages (**Fig. 4.2d, Table C2**). *Burial1* was sampled from the fill unit below T3. *Burial2* and *Burial4* were sampled from material below T2, with *Burial2* containing sands derived from the Toro main stem, whereas *Burial4* sands were transported by the Carachi tributary river (**Fig. 4.2d and Fig. 4.3a**). *Burial3* was located below T4, but sampled at the exposed base of the fill unit. $^{26}\text{Al}/^{10}\text{Be}$ ratios of 6.69 ± 0.07 , 5.82 ± 0.06 , 4.29 ± 0.08 and 5.77 ± 0.06 yield burial ages of 18 ± 141 ka (*Burial1*), 306 ± 125 ka (*Burial2*), 936 ± 170 ka (*Burial3*) and 325 ± 130 ka (*Burial4*) (**Table 4.2**; ages given with 1σ uncertainty).

In addition to the burial ages, we obtained three U-Pb zircon ages from intercalated volcanic ash layers in the Terrace Conglomerates (**Fig. 4.2d, Table C8**). *Ash1* is from a several dm thick, fluvially reworked ash layer that was sampled a few centimeters below the surface of T4 and yielded a maximum depositional age of 269 ± 30 ka ($n = 2/49$; 2σ uncertainty). *Ash2* from within P4b on T4 is also reworked, but much less pronounced than *Ash1*. It was deposited around fluvially transported clasts (**Fig. 4.3e**) and yielded a maximum depositional age of 417 ± 38 ka ($n = 2/60$). Finally, *Ash3* was collected from a prominent ash layer in fill material north of the El Mollar tributary. Although terrace surfaces are not well preserved in this location, the elevation above the current river suggests that the ash-bearing material belongs to the fill material below T3. This sample yielded a consistent age population of 218 ± 14 ka (MSWD = 1.48; $n = 14/60$).

4.5. Discussion

4.5.1. Reliability and interpretation of terrace exposure

A comparison of the three different approaches to calculate terrace-surface exposure ages (**Table 4.1**) reveals that (a) the exposure ages vary significantly depending on the chosen approach (e.g. including inflation or not) and (b) ages from the *Surface-pebbles* approach generally agree better with the *Inflation-corrected* ages than with the *Stable-surface* ages. Because the age distribution suggests that inflation has raised the terrace surfaces by several 10s of cm with respect to the underlying material, with a consequent large influence on exposure-age calculations, we consider the ages derived from the *Surface-pebbles* approach (which is insensitive to surface inflation) to be more reliable. For P4d, two ages with different inheritance concentrations were generated (190 ± 14 ka and 263 ± 18 ka). Because P4d is located on the same terrace level as P4a and P4c with calculated ages of 269 ± 20 ka and 284 ± 26 ka, we consider the calculated age for P4d of 263 ± 18 ka (based on P4a inheritance concentrations) to be more reliable.

For the two sand profiles (P2a, P4b), the age determination is limited to the depth-profile calculations, since we cannot apply the *Surface-pebbles* approach. Because the *Inflation-corrected* approach ages of the pebble profiles correlate better with the *Surface-pebbles* ages, we prefer the *Inflation-corrected* age for P4b. For the upper surface of P2a, we could only calculate an age using the *Stable-surface* approach, because no obvious sand/silt layer is visible. Following these choices (bold ages in **Table 4.1**), we obtain preferred exposure ages of ca. 75 to 110 ka for the lowermost dated terrace surface (T2), ca. 260 to 285 ka for T4, and ca. 450 to 490 ka for T6 (**Fig. 4.5a**).

We assume that the exposure ages of the terrace treads are equivalent to the time of terrace abandonment associated with the onset of incision. The three dated terraces (T2, T4, and T6) are separated by ca. 200 kyr and the presence of two terraces of unknown age in between (T3 and T5) suggests the formation of one terrace every ~100 kyr. Consequently, we infer an abandonment age of ca. 170 ka for T3 and ca. 370 ka for T5.

4.5.2. Cut-and-fill cycles within the Toro Basin

Sometime after 0.98 Ma, the Toro Basin experienced incision to a base-level similar to today, followed by a major phase of aggradation related to basement block uplift in the lower part of the Basin (see **section 4.2.1** and **Fig. 4.2b**, Hilley and Strecker, 2005). The age constraint is based on a 0.98 Ma ash (Marrett et al., 1994) that is incorporated into the deformed uppermost Alfarcito conglomerate, which is unconformably overlain by the undeformed Terrace Conglomerates (**Fig. 4.5b**). Although Hilley and Strecker (2005) suggested that this aggradation was followed by episodic incision with no intervening

Fluvial fill terraces in the Quebrada del Toro

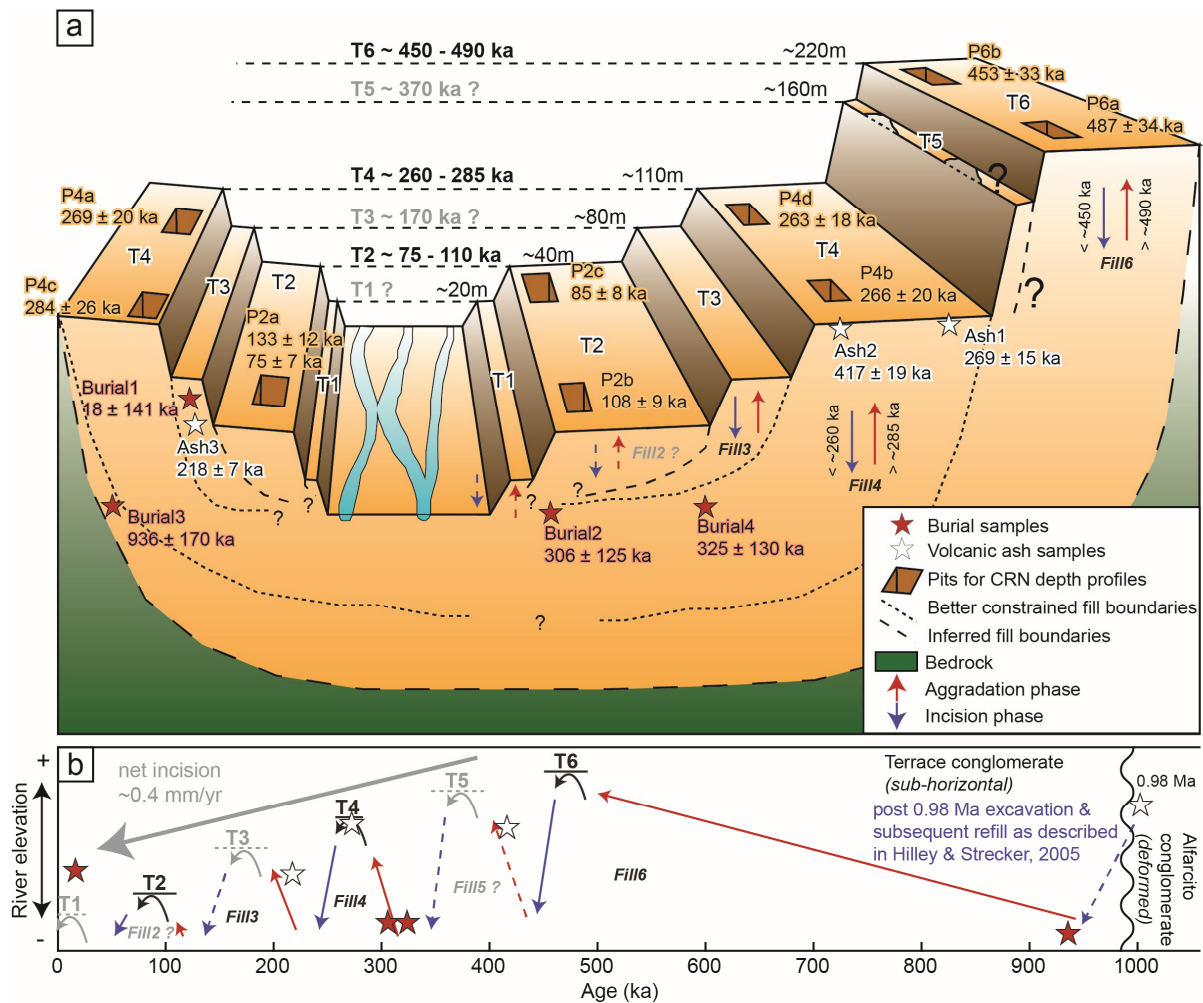


Fig. 4.5 Simplified overview of the spatial sample distribution and the temporal evolution of the fill terraces. (a) Schematic block diagram across the Toro Basin illustrating the relative locations of Pleistocene fluvial terraces and our samples. Ages on the dashed lines in the back indicate terrace age ranges based on the depth profiles (black) and predicted ages for undated terraces (grey). Height numbers give the approximate elevation of the terrace treads above the modern channel. (b) Temporal evolution of the Toro Basin and relative locations of our samples. Solid red and blue lines indicates better constrained aggradation and incision phases, while dashed lines indicate inferred phases of river elevation change. The equivalent fill units are numbered in accordance and distinguished between better constrained (black) and inferred (grey). 0.98 Ma volcanic ash in the upper Alfarcito conglomerate from Marrett et al. (1994).

filling phases to create the terraces, the position of our samples in the stratigraphy and our $^{26}\text{Al}/^{10}\text{Be}$ burial and U-Pb zircon ages (ranging from 18 ± 141 ka to 936 ± 170 ka) preclude the possibility of a single fill unit that was episodically incised. Instead, our results imply several cut-and-fill events. We do not have age constraints for the fill beneath each terrace tread. Fill units are named according to the terrace tread that lies above it (e.g., *Fill6* lies beneath T6) and based on their ages, we assign each CRN burial and ash sample to one fill unit.

The oldest fill unit (*Fill6*) is defined by the age of *Burial3* (936 ± 170 ka), which was collected from an undeformed conglomerate ~ 15 m above the current main channel (**Fig. 4.5b**). Hence, at around 940 ka, the elevation of the upper reaches of the Río Toro was locally almost as deep as today, and more than 200 m of net aggradation occurred before the formation of the highest dated terrace (T6) at ca. 450 to 490 ka. We have no time constraints on the abandonment of T5 (although we predict it to be around 370 ka), nor do we know if a separate fill unit (*Fill5*) underlies it.

The next aggradation phase (*Fill4*) is dated by the CRN burial samples *Burial2* (306 ± 125 ka) and *Burial4* (325 ± 130 ka), which were collected ~ 15 to 20 m above the current river level, implying that the river elevation at ~ 300 ka, between the abandonment of T5 and aggradation to T4, was at least as low as it is today. These sites were recently exposed due to undercutting by the Río Toro, and thus time for post-depositional CRN production has been short. Similarities in elevation and age imply that both conglomerates belong to a single aggradation phase shortly before the abandonment of T4 (260-285 ka).

The ash layer *Ash1* (269 ± 15 ka), sampled from *Fill4* 30 cm below the T4 tread, corresponds closely to the surface-abandonment age of T4 (ca. 260-285 ka), indicating that the ash was deposited on the floodplain shortly before the river system switched from aggradation to incision. *Ash2* was sampled within P4b at ~ 50 -60 cm below the T4 tread and yielded an age of 417 ± 38 ka, which is considerably older than the terrace tread above it (260-285 ka) and also older than *Ash1*, which was deposited at a similar stratigraphic level. Because we interpret *Ash2* to be reworked and less pronounced than *Ash1*, its age only provides an upper limit to the depositional age of *Fill4*.

The next aggradation phase (*Fill3*) is constrained by *Ash3* (218 ± 14 ka), which we correlate with the fill deposit below T3 based on its elevation. This ash limits the abandonment age of terrace T3 to < 218 ka (undated, but inferred to be ~ 170 ka). Stratigraphically, *Burial1*, which yielded an age of 18 ± 141 ka, belongs to the same fill unit as *Ash2* and should therefore be older than the surface-abandonment age of the T3 terrace (estimated to be ca. 170 ka). *Burial1* was collected from a vertical wall (**Fig. C1**) 60 m above the current channel. As such, some post-depositional nuclide production may have occurred since the river first exposed the outcrop, which would reduce the burial age and may explain why it overlaps with the present day within uncertainty. Although the 2σ age uncertainty also overlaps with the inferred abandonment age of T3, to avoid confusion, we omit this sample from further discussion.

We find no younger depositional ages documenting another fill unit (a hypothetical *Fill2*). However, an additional incision phase is marked by the abandonment of terrace T2 between ca. 75 and 110 ka based on the depth profiles P2a, P2b and P2c (bold ages in **Table 4.1**).

Together, the CRN burial ages, the volcanic-ash ages, and the terrace-abandonment ages suggest that the terraces formed as a result of multiple cut-and-fill cycles. Based on the limited number of burial and ash ages obtained, we suggest a minimum of three principal phases of aggradation (solid red arrows in **Fig. 4.5b**); however, more filling phases – potentially one related to each terrace – are possible. Currently, we cannot determine whether there was (a) an overall reduction of the cut-and-fill amplitude (**Fig. 4.5b**), or if (b) younger incision events have cut deeper below the present river level. Nevertheless, we observe net incision at a rate of about 0.4 mm/yr based on the decreasing tread heights since the formation of the T6 surface (**Fig. 4.5b** and **Fig. C1**).

4.5.3. Potential causes of terrace formation

The formation of fluvial terraces associated with ~100 kyr cut-and-fill cycles indicates significant changes in sediment supply and/or runoff within the Toro Basin. Below, we discuss the potential roles of (a) autogenic forcing, (b) tectonics, and (c) climate as potential drivers of sediment filling and excavation within the Toro Basin.

4.5.3.1. Autogenic forcing

External perturbation of a fluvial system does not necessarily result in the formation of a single terrace, but rather can lead to autogenic terrace formation, in which several waves of bed-elevation change form a flight of terraces (e.g., Schumm and Parker, 1973). In this case, the highest terrace is created by the initial perturbation, while subsequent feedback mechanisms between the main channel and tributaries induce alternations between aggradation and incision and thus generate additional, lower fill terraces. In the field, we did not find any evidence for such major perturbations related to river capture or landslides voluminous enough to explain hundreds of meters of aggradation over timescales of 10^4 to 10^5 years. However, a perturbation at the outlet of the Río Toro could have been possible. After exiting the basin, the Río Toro crosses the alluvial fan in the Lerma Valley and today drains into the Cabra Corral reservoir (~1030 m asl) at the southeastern border of the basin (**Fig. 4.2a**). Lacustrine deposits in the Lerma Valley indicate the existence of the Pleistocene ‘Lake Lerma’ (most likely between 0.78-0.1 Ma) with a highstand ≤ 170 m above the current Cabra Corral level (Malamud et al., 1996). However, a single major lake-level drop of 170 m can still not explain multiple fill thicknesses of at least 220 m in the upper sectors of the Toro Basin.

4.5.3.2. Tectonic forcing

Hilley and Strecker (2005) related the onset of deposition of the Terrace Conglomerates within the Toro Basin (<0.98 Ma) to the reactivated uplift of the Sierra de Pascha Sur, which would have caused steepening of the river channel within the gorge and deposition upstream of the Gólgota Fault (**Fig. 4.2b**).

Since the formation of T6 (ca. 450 to 490 ka), we observe net fluvial incision of the Terrace Conglomerates with multiple superimposed cut-and-fill cycles. A purely local tectonic explanation for this landscape would require a cyclically changing uplift rate of the Sierra de Pascha Sur. Although such changes are difficult to envisage, the terrace region could also be influenced by changes in base-level in the Lerma Valley, assuming that these signals can propagate upstream. There is evidence for tectonically induced long-term rock uplift as well as base-level rise in the region (García et al., 2013; Hilley and Strecker, 2005) both of which should affect river incision and aggradation.

Uplift of the Mojotoro range, which bounds the Lerma Valley to the east (**Fig. 4.2a**), started at 10 to 5 Ma, and contributed to several hundred meters of surface uplift during the Quaternary (García et al., 2013; Hain et al., 2011). This enhancement of orographic shielding likely reduced precipitation and fluvial-transport capacity within the hinterland basins (Hain et al., 2011). Although no evidence was found for sustained internal drainage of the Lerma Valley on longer timescales (Hain et al., 2011), the reduced fluvial connectivity to the foreland and associated transient sediment storage is expressed in a 300 m elevation difference between the Lerma Valley and the lower, adjacent basin to the east (Hain et al., 2011). Thus, the overall rise in base-level elevation in the Lerma Valley could also have promoted sediment aggradation in the Toro Basin, but its timing is poorly constrained.

We cannot differentiate whether the onset of net incision of the Terrace Conglomerates at ca. 500 ka was related to changes in tectonic uplift rates or a decrease in the Q_s/Q_w ratio in the Toro Basin. The net incision rate of ~ 0.4 mm/yr in the terrace region (**Fig. 4.5b** and **Fig. C1**) correlates well with reported long-term uplift rates of the eastern bounding and adjacent ranges, which range from 0.4 to 0.6 mm/yr (Sierra de Pascha, Hilley and Strecker, 2005) and from 0.3 to 1.0 mm/yr (Cordon de Lesser, García et al., 2013). This correspondence could mean that the region of the river terraces has experienced a similar uplift rate, and that net river incision is keeping pace with that uplift. Alternatively, a slowing of the uplift rate of the Sierra de Pascha Sur could have driven net incision in the terrace region, but at a rate that is difficult to predict. Through either mechanism, the tectonic activity of the region could explain the net incision of the Toro Basin since at least ca. 500 ka. However, the cyclical alternations between aggradation and incision on ~ 100 kyr timescales likely requires an additional driver.

4.5.3.3. Climatic forcing

Another mechanism to trigger fluvial incision or aggradation is by changing the incoming Q_s/Q_w ratio (Parker, 1998). Because the Toro Basin has a virtually unlimited supply of sediment in the form of unlithified fluvial conglomerate, the influence of climate on terrace formation and fluvial long-profile

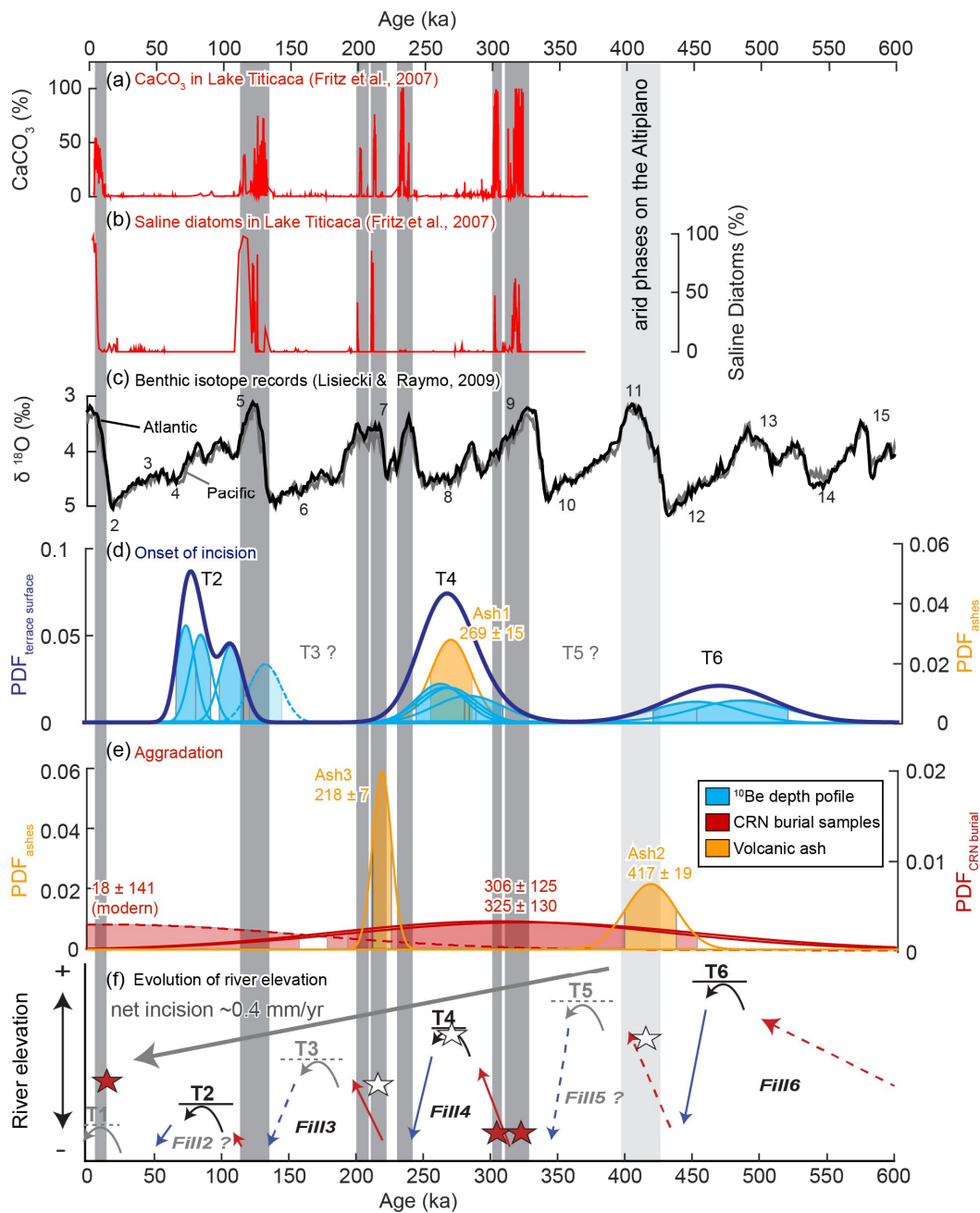


Fig. 4.6 Comparison of aggradation and incision phases in the Toro Basin with regional and global climate proxies. CaCO_3 concentrations (a) and saline diatom abundance (b) in a Lake Titicaca sediment core (Fritz et al., 2007). High values of both indicate arid phases, which are marked by the grey bars. (c) Average benthic isotope records for the Atlantic (black) and Pacific (grey) oceans (Lisiecki and Raymo, 2009). Numbers indicate Marine Isotope Stages (MIS). (d) Probability density functions (PDF) of the nine terrace surface abandonment ages (light blue) based on the ^{10}Be depth profiles as indicated in bold in Table 4.1 and a stacked PDF to show the overall trend of onset of incision (dark blue). Dashed line represents the lower, buried unit of P2a and is not included in the stacked PDF. Based on its location close to a confluence, we consider this lower unit as a period of no deposition and later re-occupation rather than the onset of a major incision phase. Additionally, the PDF of Ash1, which was deposited on the floodplain shortly before incision must have started, is plotted in orange. (e) PDFs of the CRN burial (red) and volcanic ash (orange) ages that represent times of deposition. Note the different y-axis for the CRN burial and volcanic ash ages for better visibility. The shaded areas in (d) and (e) represent the 1σ uncertainty ranges. (f) Approximate evolution of river elevation (same as Fig. 4.5b).

evolution may be primarily associated with past variability in Q_w . Unfortunately, there is no paleoclimate record from the nearby Puna that is sufficiently old to compare with our terrace sequence. However, there is one terrestrial paleo-climate record from the Altiplano based on a drill core from Lake Titicaca (**Fig. 4.1b**), whose CaCO_3 content (**Fig. 4.6a**) and diatoms with saline affinity (**Fig. 4.6b**) show a dominant 100 kyr cyclicity in humidity (Fritz et al., 2007). A comparison of our terrace exposure, $^{26}\text{Al}/^{10}\text{Be}$ burial, and volcanic ash ages to temporal trends in the Lake Titicaca records shows that the onsets of the three dated incision phases (i.e., terrace-abandonment ages; **Fig. 4.6d**) correlate with wetter phases in the Lake Titicaca region. We plotted *Ash1* together with the terrace surface abandonment ages (**Fig. 4.6d**) because that sample was collected a few cm below the surface of T4, and must have been deposited on the floodplain shortly before incision started. Conversely, the episodes of deposition (**Fig. 4.6e**) occur during arid phases (~218 ka, ~306-325 ka, and ~417 ka). Aggradation of the Rio Toro today, during the present arid interglacial, corroborates this pattern (**Fig. 4.2b**). Furthermore, a comparison with global benthic oxygen isotope records (**Fig. 4.6c**, Lisiecki and Raymo, 2009) implies that the onset of terrace abandonment phases correlates with transitions into global glacial stages. Wetter conditions in the Central Andes due to increased precipitation and/or reduced evapotranspiration during glacial times have commonly been inferred from field studies (Baker and Fritz, 2015; Fritz et al., 2007; Haselton et al., 2002) and modelling studies (Vizy and Cook, 2007). As a result, the fluvial transport capacity in the Toro Basin may have increased during glacial phases more than the sediment flux did. In contrast, during the warm, arid phases, the transport capacity would have been reduced, resulting in an increase in the Q_s/Q_w ratio and aggradation (e.g., Hanson et al., 2006). Overall, we suggest that while post-500-ka net incision of the Toro Basin is likely controlled by regional tectonic activity, the superimposed 100 kyr aggradation-incision cycles are climate-driven and have been caused by changes in the Q_s/Q_w ratio.

4.5.4. Impacts of global climate change on sedimentary systems

Although fluvial terraces in the Central Andes have commonly been linked to moisture fluctuations within the past ~100 kyr (e.g. Farabaugh and Rigsby, 2005; Schildgen et al., 2016; Steffen et al., 2010; Tchilinguirian and Pereyra, 2001), the only other record of Andean fluvial terraces that span multiple 100 kyr glacial cycles is from the southernmost Central Andes (Río Diamante, **Fig. 4.1b**), where Baker et al. (2009) correlated the deposition of fluvial fill units with glacial advances. Globally, the formation of fluvial terraces related to 100 kyr glacial-interglacial cycles has also been shown in the Tian Shan (Huang et al., 2014), on the NE Tibetan Plateau (Pan et al., 2003), in the Apennines (Wegmann and Pazzaglia, 2009), and in several locations within Europe (Bridgland and Westaway, 2008).

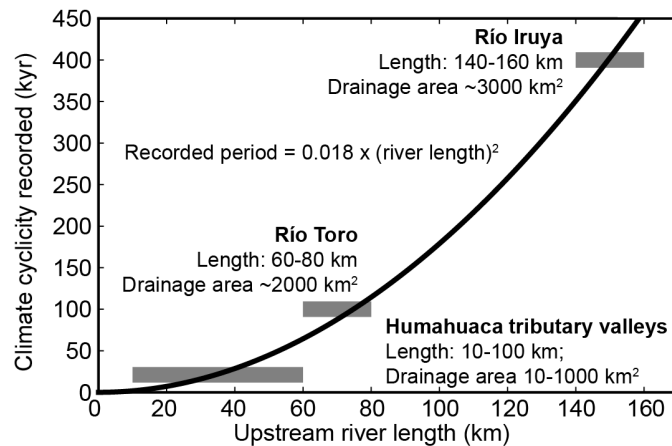


Fig. 4.7 Correlation of recorded climate cyclicity and river length. Three sedimentary records from the eastern flank of the southern Central Andes (Fisher et al., 2016; Schildgen et al., 2016; this study) preserve paleoclimate cycle periodicities that are proportional to the square of river length upstream of their depositional area, consistent with the linear-diffusional model of Castellort and Van Den Driessche (2003).

But why have 100 kyr cycles in terrace formation only been reported in one other location in the Andes (Río Diamante), despite the large number of existing terrace studies? Our knowledge of how periodic forcing signals are preserved in sedimentary records is limited and mainly based on numerical models (e.g. Braun et al., 2015; Castellort and Van Den Driessche, 2003; Godard et al., 2013). It has been suggested that if the response time of the alluvial long profile is longer than the periodicity of the forcing, changes in sediment export efficiency will be buffered and will not lead to a morphological response (Allen, 2008a). Castellort and Van Den Driessche (2003) proposed that diffusive waves of sediments in alluvial systems lead to a perturbation response time that is proportional to a representative transport distance squared, following the linear diffusive model of Paola et al. (1992a). This result contrasts with the length scale-independent response to climate change described by Braun et al. (2015), whose landscape evolution model includes stream power based channel erosion and hillslope diffusion, but does not explicitly model sediment transport through the river system.

Although we cannot explain with certainty why the geomorphic record in Toro Basin is dominated by 100 kyr climate cyclicity, a correlation between catchment length scales and recorded climate periodicity exists throughout the southern Central Andes. For example, late Quaternary fluvial deposits in tributary valleys within the Humahuaca Basin (**Fig. 4.1c**) record changes associated with precessional (21 kyr) cyclicity from catchments ranging in length from 10 to 100 km (Schildgen et al., 2016), whereas Pliocene to late Pleistocene deposits in the ~140-160 km long Río Iruya (**Fig. 4.1c**) record long-eccentricity (400 kyr) cyclicity (Fisher et al., 2016). For comparison, the river length upstream from the terraces in the Toro

Basin is ~60-80 km. A simple curve-fit, albeit with only three river systems (**Fig. 4.7**), provides empirical support for the length-scale-dependent fluvial response time in alluvial rivers (e.g. Castelltort and Van Den Driessche, 2003). Hence, although river length is likely not the only factor affecting fluvial response times, these three drainage systems in NW Argentina offer compelling evidence of how different periodicities of climate forcing can be preserved in geomorphic archives at differing distances from their source areas.

4.6. Conclusions

Three terrace abandonment ages in the Toro Basin of NW Argentina calculated from nine *in situ* ^{10}Be depth profiles range from 75 ± 7 to 487 ± 34 ka and reveal an apparent 100 kyr cyclicality in the formation of six terraces. Additional dating of sediment deposition, based on cosmogenic burial samples and volcanic ashes, suggest the terraces result from multiple cut-and-fill cycles. The initial filling of the extensive Terrace Conglomerate within the Toro Basin is most likely linked to basement uplift near the catchment outlet, beginning at ~1 Ma. Either (1) changes in uplift rate of this basement block or (2) regional rock uplift could explain the net incision of the Río Toro since ca. 500 ka. However, the superimposed 100 kyr aggradation and incision cycles are best explained by climate forcing. Preservation of these cycles likely results from a fortuitous combination of enhanced preservation potential in a region of long-term net incision together with river response times (potentially linked to channel length) that are appropriate for recording 100 kyr cyclic forcing. The times of river incision onset correlate with wetter phases recorded in a Lake Titicaca sediment core, whereas depositional phases mainly fall within arid periods. Increased moisture availability in the southern Central Andes has been previously shown to coincide with global glacial cycles. We suggest that enhanced precipitation and/or reduced evapotranspiration during global cold phases resulted in increased water discharge and sediment transport capacity in the Río Toro and its tributaries, which outweighed any increases in sediment flux in this transport-limited system and thus triggered river incision.

Acknowledgments

This study was funded by the Emmy-Noether-Programme of the Deutsche Forschungsgemeinschaft (DFG) grant number SCHI 1241/1-1 awarded to T. Schildgen. M. Strecker acknowledges DFG funding (grant number STR 373/32-1, StRATEGy). We thank George Hilley for providing data from the sampling campaign he performed in 2003, and Walter Düsing for field assistance. Jan Schüürmann, Lilian Pollozek, David Käter, Martin Lang, and Cathrin Schulz are thanked for their help during sample processing and Steve Binnie and Stefan Heinze for performing the AMS measurements. We

Fluvial fill terraces in the Quebrada del Toro

thank Luca Malatesta and one anonymous reviewer for their very detailed and constructive reviews that helped to improve the manuscript.

5. Discussion and Synthesis

Within this thesis I would like to address additional questions to those already discussed within chapters 2 to 4. As a reminder, I repeat all four topics and questions that were raised in the introduction:

Topic 1) Signals in the geochemical composition of sediment: (A) Do hillslope processes create a distinct and traceable ^{10}Be signal in clastic sediments with differing grain-sizes? (B) How is a potential hillslope-process signal stored in the [^{10}Be] difference between grain sizes altered during propagation along the sediment routing system?

Topic 2) Signals in the sediment discharge amount (Q_s): Does variability in $Q_{s,in}$ and Q_w create a distinct signal in $Q_{s,out}$, and how do these signals differ from one another?

Topic 3) From boundary conditions to channel responses and terrace formation: (A) How does an alluvial-channel reach adjust its morphology (longitudinal profile, width) in response to changes in boundary conditions? (B) Under which conditions are fill terraces formed? (C) And how do the resulting terraces differ from one another with regards to lag-times compared to the onset of forcing and surface slopes?

Topic 4) Reconstructions of boundary conditions from fill terraces: (A) When were the terraces in the Quebrada del Toro formed (individual aggradation and incision times)? (B) By which mechanism were the terraces formed (Q_s , Q_w , base level or autogenic/ complex response)? (C) What information regarding paleo- Q_s and paleo- Q_w can be extracted from those terraces?

In the following, I will shortly summarize the main findings of chapters 2 to 4. Then, I will address the questions that have not been discussed so far, however, in a mixed order. I subdivided the discussion into two parts. First, I will discuss fluvial fill terraces as particular sedimentary features within the transfer zone (topic 3 and 4). I will discuss in particular, based on data from previous chapters and new analysis, how the fill terraces in the Quebrada del Toro were formed (question 4B) and what can be learned about paleo environmental conditions from those terraces (question 4C). In the second part, I will broaden my scope and address the more general implications of the findings of this work on signal propagation in sedimentary systems (topics 1 and 2). In particular, I will focus on how the *NSGI* is potentially altered

during transport along the sediment routing system (question 1B) and I will discuss signals in Q_s in more detail (question 2).

5.1. Summary of key findings

In **chapter 2** I compared the ^{10}Be concentrations (denoted $[^{10}\text{Be}]$) in fluvial sand and gravel with a detailed hillslope process inventory from the entire Quebrada del Toro, NW Argentina. I found that the often observed non-linear increase in catchment-mean denudation rate with catchment-median slope, which has commonly been explained by an adjustment in landslide-frequency (e.g., Bennett et al., 2016; Larsen and Montgomery, 2012), coincides with a shift in the type of hillslope processes. To test whether a signal of hillslope-processes active within the catchment are reflected in a comparison of the $[^{10}\text{Be}]$ of sand and gravel, we define the normalized sand-gravel index (*NSGI*) as the $[^{10}\text{Be}]$ difference between sand and gravel divided by their summed concentrations. I observed a positive, linear relationship between *NSGI* and catchment-average slope. The increase in *NSGI* also coincided with a shift in hillslope-process type from low-slope gully and scree production to steep-slope gully and landsliding, suggesting that it might be possible to track hillslope processes through time from geochemical signals stored in sedimentary archives.

In **chapter 3** I presented experimental work to test how an alluvial-channel reach responds to changes in $Q_{s,in}$, Q_w and base-level. I investigated in particular the formation of fluvial fill terraces and the effects of changing boundary conditions on sediment discharge at the basin outlet ($Q_{s,out}$). River incision, channel-width narrowing and terrace cutting were initiated by either an increase in Q_w , a decrease in $Q_{s,in}$ or a drop in base level. The lag-time between the external perturbation and the terrace cutting determined (1) how well a terrace surface preserved the channel profile prior to perturbation and (2) the degree of reworking of terrace-surface material. Short lag-times and well preserved profiles were observed in cases with a rapid onset of incision. Also, lag-times were more synchronous along the entire channel after upstream perturbations (Q_w , $Q_{s,in}$), whereas base-level fall triggered an upstream migrating knickzone, such that lag-times increased with distance upstream. I also observed that terraces formed after upstream perturbations (Q_w , $Q_{s,in}$) were always steeper when compared to the active channel in new equilibrium conditions. In the base-level fall experiment, the slope of the terrace-surfaces and the modern channel were similar. Hence, comparisons between the slopes of the terrace surface and the modern channel can give insights into the mechanism of terrace formation. Furthermore, changes in Q_w caused a discernable signal in $Q_{s,out}$ during the transient channel response phase, whereas $Q_{s,out}$ signals related to changes in $Q_{s,in}$ were at least temporarily buffered within the channel reach. I inferred from this result that signals extracted from the geochemical composition of sediments (e.g., $[^{10}\text{Be}]$) are more likely to represent modern-day conditions

during times of aggradation, whereas the signal will be temporally buffered due to mixing with older, remobilized sediment during times of channel incision.

In **chapter 4** I established the chronology of the cut-and-fill terrace sequence in the Quebrada del Toro, NW Argentina. By combining ^{10}Be depth-profile dating, cosmogenic burial dating and U-Pb dating of zircons within volcanic ashes, I dated times of sediment deposition as well as the onset of river incision and terrace-surface abandonment. The terrace chronology revealed an apparent 100 kyr cyclicality, with the oldest terraces surfaces being ~ 470 kyr old. Times of sediment deposition within the sequence correlated with regional dry phases and local interglacials, whereas the onset of river incision correlated with wetter conditions and the transitions into global glacial phases. Although the temporal correlation between aggradation/incision times with paleo-climate records suggest that changes in Q_w have largely controlled aggradational and incision cycles in the Quebrada del Toro, additional analyses are required to identify the specific driver of the terrace formation within the Quebrada del Toro.

5.2. Fluvial fill terraces

Fluvial fill terraces form due to alternating phases of river aggradation and incision, and thus, indicate unsteadiness in the system (Bull, 1990). As variability in river-bed elevation can be triggered by changes in the tectonic or climatic boundary conditions, fluvial fill terraces have the potential to record information on environmental conditions of the past (e.g., Bridgland and Westaway, 2008; Bull, 1990; Merritts et al., 1994). But as the type of information that can be extracted from fluvial terraces depends on the local environmental conditions and on the terrace-formation mechanism itself, the essential first step is to identify the mechanism of formation. In this chapter, I will transfer the findings from the laboratory terrace experiments to the field. First, I will discuss in general what the comparison of experimental and field data reveals about the terrace-formation mechanism(s) in the Quebrada del Toro. However, when considering upstream perturbations (Q_s , Q_w) as potential drivers, the comparison with paleo-climate records only indicates how Q_w might have changed over time. As the switch between aggradation and incision is controlled by the ratio of Q_s and Q_w , I will perform new analyses to investigate the roles of both Q_w and Q_s in terrace formation in the Quebrada del Toro.

5.2.1. First insights on terrace formation in the Quebrada del Toro

From my laboratory experiments (chapter 3), I documented that fluvial fill terraces can be cut by (i) an increase in water discharge (Q_w), (ii) a decrease in sediment supply ($Q_{s,in}$) or (iii) a drop in base-level (**Fig. 3.3**). Although I did not observe channel incision due to autogenic processes or complex response in

my experiments, I cannot rule out the formation of fluvial-fill terraces due to internal feedback mechanisms (Schumm, 1979, 1973) or the exceedance of internal thresholds (Schumm, 1979). Consequently, I will discuss all four possibilities as potential driving mechanisms of terrace formation in the Quebrada del Toro.

Non-linear sediment transport due to internal feedback mechanisms between the main stem and tributaries despite a linear external change (complex response) have been observed in the field (Faulkner et al., 2016; Schumm, 1979, 1973; Womack and Schumm, 1977). But those internal feedback mechanisms have been related to terraces up to a few meters in height, and never to terraces several hundred meters in height. As an alluvial channel adjusts its slope to transport the incoming sediment downstream with the available water (S scales with Q_s/Q_w ; Blom et al., 2016; Lane, 1955; Mackin, 1948), bed-elevation changes of hundreds of meters would have a major impact on the channel slope. Such a change is unlikely in cases of constant Q_s and Q_w . Autogenic-terrace formation (purely internal dynamics with constant boundary conditions) have been described in the case of a meander-bend cutoff. However, meander-bend cutoff can be ruled out in the Quebrada del Toro, because the Río Toro is a braided river system with a mean gradient of 1.6 % (chapter 4.2.1). Another form of autogenic terrace formation is related to the local storage and release of sediment, such that each section of a channel effects the local boundary conditions ($Q_{s,in}/Q_w$) of the downstream channel segment. As a consequence, sediment deposition, channel incision, and terrace formation have been described simultaneously in different parts of the channel (Lewis, 1944; Patton and Schumm, 1981). These feedback-mechanisms might explain some bed-elevation variability on the scale of a few meters, but not the formation of a terrace sequence several hundred meters in height. Consequently, I rule out complex response and autogenic processes as the main driver of terrace formation in the Quebrada del Toro.

Alternating phases of base-level fall and rise can also be excluded as a terrace-formation mechanism in the Quebrada del Toro. The base level of the alluvial reach, where fill terraces occur, is controlled by the Gólgota Fault (Hilley and Strecker, 2005). The Gólgota Fault crosses the main-stem Río Toro river about ~ 20 km downstream of the terraces (**Fig. 4.2b**). This thrust fault uplifts the Sierra Pasha Sur basement block and can therefore only cause a local rise in base-level, but not a base-level drop (**Fig. 4.2**). Cyclicity in base-level fall and rise has mainly been invoked in settings in which the base-level is controlled by a lake or the sea (e.g., Farabaugh and Rigsby, 2005; Merritts et al., 1994). By exclusion, this leaves upstream perturbations in either water discharge (Q_w) and/or sediment supply ($Q_{s,in}$) as potential drivers for the formation of the terraces in the Quebrada del Toro.

This conclusion is supported by the reduction in terrace-surface slopes over time. The experimental results have shown that terraces formed from upstream perturbations differ from those formed from downstream perturbations in that the surface slopes of the former differ from that of the alluvial channel

following incision (**Fig. 3.6A-D**). In contrast, terraces related to base-level change maintain the same surface slope as the incised channel (**Fig. 3.6E**). These experimental results are in agreement with earlier observations from the field (Faulkner et al., 2016; Poisson and Avouac, 2004). The fluvial terraces in the Quebrada del Toro show a successive lowering in slope (measured parallel to the modern trunk stream) from 3.2% (T6), to 1.8% (T4), to 1.7% (T2) (**Fig. 4.2b insert**). As terrace surfaces mark the time of a switch from aggradation to incision, the terraces-surface slopes cannot be compared with the slope of the modern channel (2%), which is currently in a phase of aggradation. But the decrease in surface slope from older to younger terraces qualitatively supports upstream perturbation (in Q_w , $Q_{s,in}$ or both) as the driver of terrace formation in the Quebrada del Toro.

The aggradation phases of the Río Toro have been shown to correlate with dry phases around Lake Titicaca and global interstadials, whereas the onset of incision coincides with the transition into regionally wetter and global stadial phases (**Fig. 5.1 and Fig 4.6**; Fritz et al., 2007; Lisiecki and Raymo, 2009). The evolution of the Río Toro channel-bed elevation thus agrees well with the experimental results, in which a decrease in discharge triggered channel aggradation, and an increase in discharge triggered channel incision and terrace cutting (**Fig. 3.4**). The temporal correlation between the Río Toro channel-bed evolution inferred from the terrace record and the paleo-climate record therefore suggests that changes in Q_w play an important role in terrace formation. However, variability in precipitation can also drive changes in $Q_{s,in}$, for example through enhanced landsliding (Anderson and Sitar, 1995; Chen et al., 2006; Iverson, 2000). Changes in the ratio of Q_s/Q_w ultimately control whether alluvial rivers aggrade or incise. Therefore, to better understand the relative contribution of $Q_{s,in}$ and Q_w to terrace formation in the Quebrada del Toro, I will provide new data and analyses to quantify the effect of variability in $Q_{s,in}$ and eventually Q_w over time. This additional analysis will provide quantitative estimates on paleo-discharge, information that is rarely recovered from paleo-climate proxies.

5.2.2. Reconstruction of paleo sediment supply ($Q_{s,in}$)

I performed new analyses to estimate paleo- $Q_{s,in}$ variations based on paleo-denudation rates. Paleo-denudation rates can be calculated from ^{10}Be concentrations of terrace sediments if the age of the deposited material is known and if the samples have been well shielded from further ^{10}Be production (e.g., Schaller et al., 2004, 2002). Post-depositional ^{10}Be production would raise the ^{10}Be concentration within the sediment and consequently decrease calculated paleo-denudation rates. I calculated paleo-denudation rates for the cosmogenic burial samples (**Table 4.2**), for the calculated inheritance values of depth profiles (**Fig. 4.4**) and for additional unpublished data (summarized in **Table 5.1**). Paleo-denudation rates calculated from depth profiles were limited to those profiles for which an inheritance value could be reconstructed. I

Table 5.1 Cosmogenic nuclide samples for calculation of paleo-denudation rates. Calculations were performed using the 07KNSTD ^{10}Be standard unless indicated differently. P (μm) = muon production rate, P (sp) = spallation production rate. Paleo-denudation rate uncertainties include analytical uncertainties, decay-rate uncertainties and production-rate uncertainties. CC = class sample, CS = sand sample.

Sample	Latitude (°S)	Longitude (°W)	Age \pm 1 σ (ka)	^{10}Be \pm 1 σ (atoms/g)	decay corrected ^{10}Be \pm 1 σ (atoms/g)	Topo. shielding *** (-)	P (μm) (atoms/g yr)	P (sp) (atoms/g yr)	Paleo denudation rate \pm 1 σ (mm/yr)
Main channel									
P4a *	24.50001	65.86240	269 \pm 20	698600 \pm 78200	798894 \pm 89786	0.99	0.237	43.80	0.035 \pm 0.0051
ST14_13_300	24.50001	65.86240	269 \pm 20	1128956 \pm 34461	1291034 \pm 41485	0.99	0.237	43.80	0.021 \pm 0.0021
P4d ***	24.48647	65.85588	263 \pm 18	698600 \pm 78200	796507 \pm 89450	0.99	0.238	43.52	0.040 \pm 0.0058
P6a ***	24.51435	65.86596	487 \pm 34	1173548 \pm 22982	1496155 \pm 38883	0.99	0.237	42.75	0.021 \pm 0.0020
Burial_2 *	24.49123	65.85794	306 \pm 125	805142 \pm 25727	937879 \pm 65710	0.99	0.237	43.69	0.028 \pm 0.0032
Burial_3 *	24.55496	65.86765	936 \pm 170	171038 \pm 6555	272781 \pm 25403	0.99	0.570	40.22	0.096 \pm 0.0105
Carachi									
P2b *	24.55100	65.86200	108 \pm 9	671200 \pm 88150	708342 \pm 93083	0.99	0.218	37.27	0.035 \pm 0.0056
P4b *	24.54200	65.85280	266 \pm 20	1075300 \pm 102700	1227837 \pm 117915	0.99	0.219	37.60	0.019 \pm 0.0026
Burial_4 *	24.55100	65.86200	325 \pm 130	291096 \pm 10180	342314 \pm 25220	0.99	0.218	37.05	0.064 \pm 0.0074
ST14_76_CC	24.55100	65.86200	325 \pm 130	533976 \pm 16697	627930 \pm 45206	0.99	0.218	37.05	0.033 \pm 0.0038
ST14_05_CS	24.55100	65.86200	325 \pm 130	336912 \pm 10552	396192 \pm 28531	0.99	0.218	37.05	0.054 \pm 0.0063
El Mollar									
P4c *	24.56590	65.86406	284 \pm 26	716400 \pm 57300	825401 \pm 66888	0.97	0.232	41.54	0.031 \pm 0.0038

* Depth profiles and burial samples published in Tofelde et al. (2017).

** Samples were normalized to the isotope ratio standards of (Nishiizumi, 2004).

*** Topographic shielding calculated with 30m SRTM data.

excluded profile P2a due to its subdivision into two events with a limited number of samples per event, which results in less reliable inheritance estimations. Initially, I performed two fits to profile P4d with two different inheritance values. To calculate paleo-denudation rates, I chose the values related to the resulting surface age of 263 ± 18 ka, which agreed well with the other ages from the same surface (269 – 284 ka) (**Table 4.1**). Also, due to possible post-depositional ^{10}Be production, sample “Burial 1” was excluded from the analysis.

The depositional ages of the burial samples are known, as their burial ages were calculated based on their $^{26}\text{Al}/^{10}\text{Be}$ ratio. For the depth profiles and new samples, I used the surface age of the overlying terrace, which is a minimum age because the sampled material was deposited some time before the cutting of the associated surface (**assumed ages listed in Table 5.1**). Before calculating paleo-denudation rates, ^{10}Be concentrations were corrected for nuclide decay based on their depositional age and assuming a nuclide decay rate of $4.99 \pm 0.043 \times 10^{-7} \text{ yr}^{-1}$ (Chmeleff et al., 2010; Korschinek et al., 2010). Denudation-rate calculations were performed as described in chapter 2.3.1. Catchment outlines were determined from the nearby active channel. As such, I assume that the paleo-topography and catchment shapes during sediment deposition were similar to today. For the samples close to stream confluences, the source catchment was identified based on clast-imbrication.

In total, I calculated 12 paleo denudation rates distributed along the main stem (n=6), the Carachi tributary (n=5), and the El Mollar tributary (n=1) (**Table 5.1, Fig. 5.1**). Paleo-denudation rates vary from 0.021 to 0.096 mm/yr for the main stem, 0.019 to 0.064 mm/yr in Carachi, and 0.031 mm/yr for the sample in El Mollar. Modern equivalent denudation rates are 0.035 mm/yr (main stem), 0.05-0.112 mm/yr (Carachi), and 0.025 mm/yr (El Mollar) (**Table 2.1**). It may be important that modern denudation rates were calculated from sand samples only (**Fig. 5.1C, D**), whereas paleo-denudation rates were calculated from sand (circles) and gravel (diamonds) samples. However, ^{10}Be concentrations in the sand and gravel fractions of the modern samples in this part of the Quebrada del Toro are very similar to each other (**Table 2.1**). Consequently, modern denudation rates derived from gravel would be similar to those derived from sand shown in **Fig. 5.1**.

^{10}Be derived denudation rates average over a certain time range, which is defined as the required time to erode ~60 cm of surface material with the prevailing denudation rate. That relationship results in an integration time for the lowest measured denudation rates (0.019 mm/yr) of about 31.6 ka. As such, although denudation rates are overall low, their integration times are still shorter than the 100-kyr-forcing period and thus are likely to reflect adjusted denudation rates.

When compared to the entire Quebrada del Toro, which experiences a range of modern denudation rates spanning two orders of magnitude (0.01 – 1.3 mm/yr) (**Fig. 2.4**), the denudation rates in the terrace

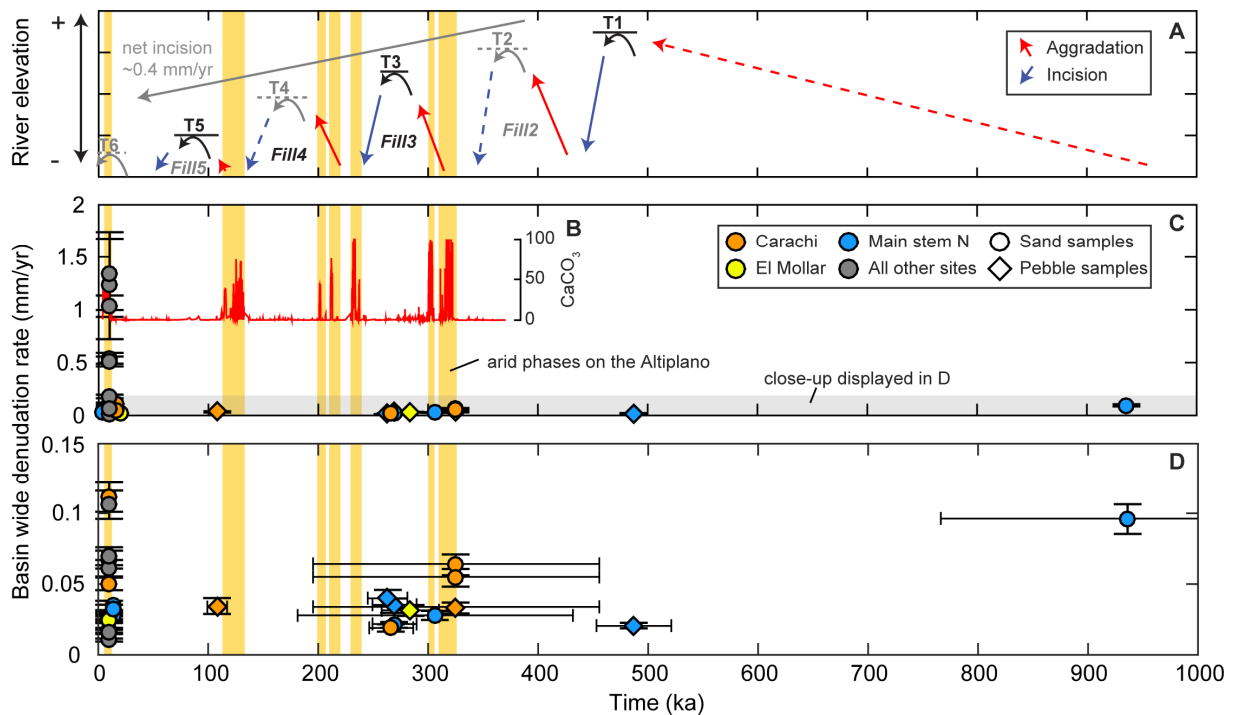


Fig. 5.1 Modern versus paleo-denudation rates in the Quebrada del Toro. (A) Temporal evolution of river-bed elevation of the Río Toro. Solid red and blue lines indicate better constrained aggradation and incision phases, while dashed lines indicate inferred phases of bed-elevation change. The equivalent fill units are numbered in accordance and distinguished between those better constrained (black) and inferred (grey; same as Fig. 4.5b). (B) CaCO₃ concentrations in a Lake Titicaca sediment core located on the Altiplano (Fritz et al., 2007). Peaks indicate arid conditions, which are marked as yellow bars (same as Fig. 4.6a). (C) Modern catchment-mean denudation rates (grey) compared to paleo-denudation rates calculated from ¹⁰Be inheritance concentrations (depth profiles), burial samples, and new data. Modern denudation rates were calculated from the sand fraction (circles) only, whereas paleo-denudation rates are based on sand and pebble (diamond) samples. Paleo-denudation rates calculated from the terraces show little variability over time compared to the spread in denudation rates in the entire Quebrada del Toro today. (D) Close-up of denudation rates from the terrace region only (indicated by grey bar in C). Denudation rates vary over time by a factor of 2 along the main stem and a factor of 3.4 in the Carachi tributary.

region have shown surprisingly little variation over the last ~1 Ma (**Fig. 5.1C**). Nevertheless, some variability is apparent (**Fig. 5.1D**). Denudation rates along the main stem vary by a factor of 2 during the last ~500 kyr (time of terrace formation) with a minimum denudation rate of 0.019 mm/yr and a maximum rate of 0.040 mm/yr. In the Carachi tributary, the ratio between the minimum and maximum denudation rate is 3.4. The temporal resolution of the data is not high enough to investigate changes in rates during individual climatic phases. Although the data indicates some variability in denudation rates over time, the fluctuation is minor compared to the neighboring Quebrada de Humahuaca, where denudation rates in some tributaries have been shown to vary by more than an order of magnitude over time (Schildgen et al., 2016). Similar to the temporal variability in denudation rates in the Quebrada del Toro, fairly constant paleo-denudation rates (differing by a maximum factor of 4) have also been reconstructed from sediments in Central European terraces (Schaller et al., 2004, 2002) and from an alluvial-fan sequence in Death Valley,

USA (Mason et al., 2018). Although the magnitude of paleo-denudation rate variability varies among those studies, it cannot be clearly stated whether or not those terraces have been formed purely by changes in $Q_{s,in}$, because the stratigraphic records from which paleo-denudation rates were reconstructed are incomplete. In fact, in my experiments I found that sediment mobilized during times of incision are typically not preserved in the terrace stratigraphy. Consequently, the reconstructed paleo-denudation rates only capture a sub-set of the conditions likely to have affected the region, and not necessarily the full range of paleo-denudation rates (Mason et al., 2018).

Based on the proposed relationship between S , $Q_{s,in}$ and Q_w by Wickert and Schildgen (2018) (eq. 3.4), changes in sediment supply by a factor of 2, or even 3.4 in the case of Carachi, in theory would be able to explain the majority of terrace-slope changes, if there is sufficient time for the alluvial channels to adjust their slopes. However, the incompleteness of the stratigraphic record combined with relatively large uncertainties in ages (especially the burial samples), precludes investigation of whether the individual aggradation and incision events were purely driven by changes in $Q_{s,in}$. Moreover, changes in $Q_{s,in}$ could be purely tectonically driven (e.g., Keefer, 1994; Marc et al., 2015; McPhillips et al., 2014; Meunier et al., 2007), but are often related to climatic changes as well (e.g., Bookhagen and Strecker, 2012; DiBiase and Whipple, 2011; Lague et al., 2005; Moon et al., 2011). For example, soil production, and thus sediment supply to the channel, has been shown to be also controlled by rainfall (Norton et al., 2014). As several previous studies have suggested that fluvial fill terraces form due to coupled changes in $Q_{s,in}$ and Q_w (Bookhagen et al., 2006; Dey et al., 2016; Steffen et al., 2010, 2009), I will use the new dataset on paleo-denudation rates to quantify variability in Q_w over the past ~500 kyr.

5.2.3. Reconstruction of paleo water discharge (Q_w)

To investigate whether water discharge (Q_w) in the Quebrada del Toro has varied during the times of terrace formation, the times of sediment deposition and river incision can be compared to a paleo-climate record (Fig. 4.6), or Q_w can be reconstructed directly from the terraces. My physical experiments have demonstrated that changes in either $Q_{s,in}$ or Q_w trigger an adjustment of channel slope (Fig. 3.5). As $Q_{s,in}$, Q_w and S are dependent on one another, Q_w can theoretically be calculated if S and $Q_{s,in}$ are known, under the assumption that the terrace surfaces have not been tectonically deformed since abandonment.

Paleo-hydrological variability in the Central Andes on millennial timescales has been reconstructed using proxies including pollen assemblages and plant fossils (Chepstow-Lusty et al., 2005; Gosling et al., 2008; Torres et al., 2016), stable isotopes in lipid biomarkers (Fornace et al., 2016), ice-cores (Ramirez et al., 2003; Thompson et al., 1998, 1995) and speleothems (Cruz et al., 2005; Kanner et al., 2013, 2012; Wang et al., 2007), and by studying geomorphic archives including glacial moraines (Haselton et al., 2002;

Luna et al., 2018; Martini et al., 2017; Smith et al., 2005a, 2005b; Ward et al., 2015; Zech et al., 2009, 2008), lake cores and lake shore lines (Baker et al., 2001; Baker and Fritz, 2015; Bookhagen et al., 2001; Fritz et al., 2007; Placzek et al., 2009, 2006; Trauth et al., 2003b) and sedimentary deposits (Bekaddour et al., 2014; Litty et al., 2016; Nester et al., 2007; Savi et al., 2016; Schildgen et al., 2016; Steffen et al., 2010, 2009). While most of those proxies and archive analyses allow for a qualitative reconstruction on whether the climate has been drier or wetter, few provide quantitative paleo-hydrological information. Quantitative rainfall reconstructions for the Central Andes are primarily limited to modeling studies reconstructing (1) the extent of a paleo-lake in NW Argentina (Bookhagen et al., 2001) and the Bolivian Altiplano (Placzek et al., 2013), (2) the extent of glaciers in the Eastern Bolivian Andes (Kull et al., 2008), and (3) combined studies of a paleo-lake level and glacial moraines of a similar age on the Bolivian Altiplano (Blard et al., 2009; Martin et al., 2018; Placzek et al., 2013). Also, Litty et al. (2016) reconstructed paleo-discharge for the Pisco valley in Peru from a ~40 kyr terrace deposit. They proposed ca. 7 – 8 times greater discharge at 40 ka compared to today. Their reconstruction is based on a physical model that requires information on channel gradient, channel width, and grain-size distribution (Litty et al., 2016). While channel gradient (terrace surface gradient) and grain-size distribution can be extracted from the terrace deposits (e.g., Guerit et al., 2018), paleo-channel width can rarely be measured in the field, and its reconstruction is often based on broad assumptions. Litty et al. (2016), for example, assumed a constant ratio between the width of the river channel and the width of the entire valley over time.

To overcome the problem of constraining paleo-channel width, I use a newly proposed relationship among Q_w , Q_s and slope (S). Wickert and Schildgen (2018) derived an equation for the long-profile evolution of transport-limited gravel-bed rivers that allows for a self-adjusting channel width – a factor that has often been neglected in past formulations. They suggest that Q_w , Q_s and S in gravel-bed rivers scale as follows:

$$Q_w = \frac{1}{k_{Q_s} I} \frac{Q_s}{S^{7/6}} \quad (\text{eq. 5.1})$$

with k_{Q_s} (sediment discharge coefficient) being the product of the threshold river-width coefficient (k_b) and the specific sediment-discharge coefficient (k_{qs}) and I being intermittency, defined as the fraction of the total time during which geomorphically-effective flow conditions persist (Paola et al., 1992a). As the aim is to compare paleo Q_w to modern Q_w , but neither I nor k_{Q_s} are known for the Quebrada del Toro, I use modern data of Q_w , Q_s and slope for a calibration. In theory, k_{Q_s} is known for gravel-bed rivers with a rectangular cross-section (0.041; Wickert and Schildgen, 2018). However, the Río Toro is a braided channel, such that it is more efficient in transporting sediment than the equivalent rectangular channel (Paola et al., 1999); consequently its k_{Q_s} would be > 0.041 . In a second step, discharge can be reconstructed

Table 5.2 Calculation of paleo-discharge from terraces in the Quebrada del Toro based on calibration with modern data (see text for details).

	Denudation rate $\pm 1\sigma$ (mm/yr)	Slope $\pm 10\%$ (m/m)	Catchment area $\pm 1\%$ (km ²)	$Q_s \pm 1\sigma$ (m ³ /yr)	Q_w estimated (m ³ /yr)
Modern data for calibration					
M08_CS	0.028 \pm 0.0027	0.013 \pm 0.0013	2196 \pm 22.0	61178 \pm 5877	13484247
M15_CS	0.035 \pm 0.0033	0.019 \pm 0.0019	1665 \pm 16.6	58141 \pm 5567	10155343
T11_CS	0.112 \pm 0.0105	0.038 \pm 0.0038	130 \pm 1.3	14500 \pm 1368	674363
T69_CS	0.025 \pm 0.0024	0.051 \pm 0.0051	79 \pm 0.8	1962 \pm 190	387556
T68_CS	0.017 \pm 0.0017	0.030 \pm 0.0030	474 \pm 4.7	8286 \pm 804	2862165
M48_CS	0.067 \pm 0.0064	0.034 \pm 0.0034	2962 \pm 29.6	199481 \pm 18920	17776482
M60_CS	0.026 \pm 0.0025	0.024 \pm 0.0024	1495 \pm 15.0	39350 \pm 3788	9194442
T26_CS	1.232 \pm 0.5100	0.054 \pm 0.0054	33 \pm 0.3	40679 \pm 16852	625952
T27_CS	1.337 \pm 0.3398	0.109 \pm 0.0109	9 \pm 0.1	12513 \pm 3183	193458
T28_CS	0.106 \pm 0.0100	0.058 \pm 0.0058	114 \pm 1.1	12106 \pm 1152	517621
T32_CS	0.181 \pm 0.0174	0.107 \pm 0.0107	11 \pm 0.1	1899 \pm 184	44144
T35_CS	0.061 \pm 0.0058	0.056 \pm 0.0056	100 \pm 1.0	6101 \pm 583	710578
T43_CS	0.541 \pm 0.0513	0.028 \pm 0.0028	770 \pm 7.7	416559 \pm 39743	5391447
T44_CS	1.033 \pm 0.1009	0.056 \pm 0.0056	176 \pm 1.8	181511 \pm 17824	1083711
T59_CS	0.010 \pm 0.0010	0.076 \pm 0.0076	99 \pm 1.0	1038 \pm 102	623945
Paleo samples for Q_w reconstruction					Q_w calculated
P2b	0.035 \pm 0.0056	0.031 \pm 0.0031	130 \pm 1.3	4490 \pm 731	910121.305
P4b	0.019 \pm 0.0026	0.029 \pm 0.0029	127 \pm 1.3	2425 \pm 327	744992.26
P4a	0.035 \pm 0.0051	0.014 \pm 0.0014	1671 \pm 16.7	58169 \pm 8530	13580495.3
P4c	0.031 \pm 0.0038	0.034 \pm 0.0034	79 \pm 0.8	2479 \pm 304	712686.177

if paleo-slope and paleo- Q_s are known. This approach, however, assumes that both I and k_{Q_s} have been constant over time. This assumption I consider reasonable for k_{Q_s} , as long as I am only comparing depositional conditions with each other, during which the braided channel form likely persisted. Paleo-channel slope (or terrace-surface slope) can be measured with a differential GPS (dGPS) or from a DEM. Paleo- Q_s can be reconstructed from cosmogenic nuclide derived paleo-denudation rates (**Fig. 5.1**).

For the calibration with modern data, information on local channel slope, Q_s and Q_w were required. Slope data was acquired from TanDEM-X DEMs (~11-m resolution). First, a profile between the sampling location of cosmogenic nuclide samples and the closest upstream confluence was drawn in Google Earth; second, the associated elevation profile was extracted from TanDEM-X data. Slope values were calculated based on a linear fit to the extracted profiles with an assumed uncertainty of 10% (**Table 5.2**). Q_s for each catchment was calculated as the product of the ¹⁰Be derived denudation rate and the associated catchment area. Only sand derived denudation rates were used for the Q_s analysis of modern data, and denudation rates were taken from **Table 2.1**. For error propagation, I assumed an uncertainty in catchment area of 1%. Modern Q_w measurements were only available at one gauging station at the outlet of the Quebrada del Toro in Campo Quijano (data from: <https://back.argentina.gob.ar/interior/secretaria-de-infraestructura-y-politica-hidrica/base-de-datos-hidrologica-integrada>). Consequently, the local discharge at each sampling location must be estimated. To be comparable to the ¹⁰Be derived total annual sediment supply (Q_s), discharge (Q_w) is needed as the total annual water discharge. Discharge measurements in Campo Quijano

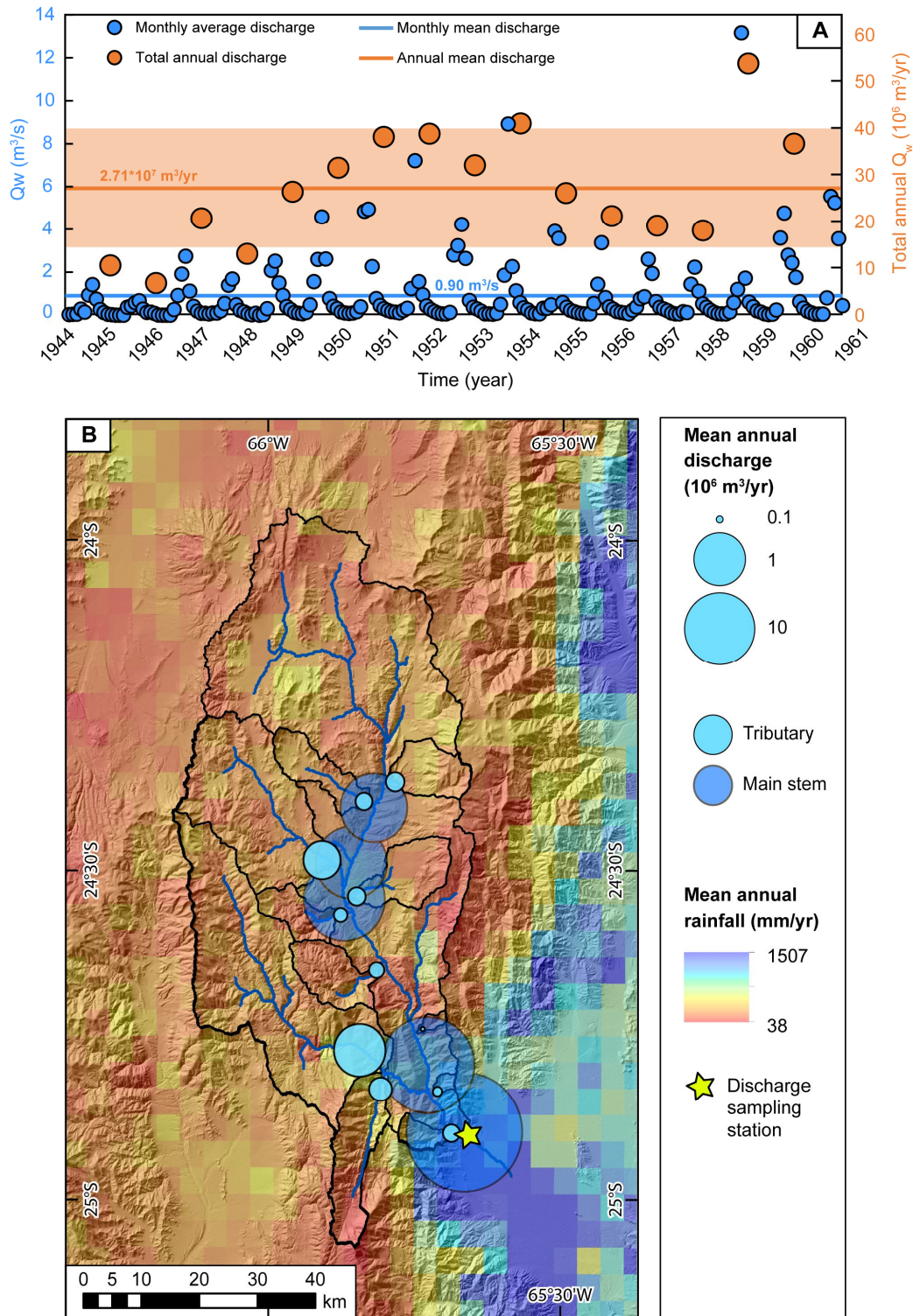


Fig. 5.2 Discharge measurements at Campo Quijano and estimated annual mean discharge for the CRN sampling locations. (A) Measured monthly-average discharge (blue) and calculated total annual discharge (orange) between 1944 and 1961 from the outlet of the Quebrada del Toro (yellow star in B). A 16-year mean of the total annual discharge (orange line) was used to estimate discharge for individual sampling locations within the Quebrada del Toro (B). Discharge was scaled to each location based on satellite-derived mean annual rainfall distribution (Bookhagen and Strecker, 2008).

were available as monthly mean discharge rates from September 1944 to August 1961 (**Fig. 5.2A blue circles**). From the monthly mean values, I estimated the total annual discharge for each year by multiplying the monthly mean discharge rate with the time of the month and summing up all 12 months of the year (**orange circles**). Next, I calculated the mean total annual discharge of the 16 years, which is $2.71 \pm 1.27 * 10^7$ m³/yr (**orange line; orange shadow represent 1 σ**). I scaled the mean total annual discharge from the entire Quebrada del Toro to each location based on the distribution of TRMM derived annual rainfall in each catchment (Bookhagen and Strecker, 2008). For example, if catchment T59 only receives 2.31% of the total annual rainfall in the entire Quebrada del Toro, I estimated the local discharge to be 2.31% of $2.71 * 10^7$ m³/yr, which is $0.06 * 10^7$ m³/yr (**Fig. 5.2B, Table 5.2**).

Based on the above calculations, Q_w tends to increase with the ratio of Q_s over S (**Fig. 5.3A**). Two samples however, T43 and T44, plot far off the linear relationship. While all other samples sites are either located on the main stem or are direct tributaries to the main stem, the two outlier samples are sub-catchments of a tributary. They also show differences in lithology compared to the other catchments, with greater exposure of weak Cretaceous/ Paleogene sandstones (**Fig. A2**), which might erode more easily and thus explain enhanced Q_s . Hence, I consider them as outliers and do not include them in the calibration step. The remaining data is linearly correlated at a significance level of 5%, and the regression line is described by $y = 1.58x + 0.51 * 10^6$. For better visibility, the same correlation is shown in semi-log space (**Fig. 5.3B**).

With this linear model, it is possible to reconstruct past Q_w if paleo- Q_s and paleo- S are known and if we assume that intermittency (I) and the sediment discharge coefficient (k_{Q_s}) have been constant over time. I restricted the paleo-discharge reconstructions to the location of the depth profiles P2b, P4a, P4b and P4c. I excluded the profiles P4d and P6a, although paleo-denudation rates have been reconstructed (**Table 5.1**). Those two depth profiles were sampled in 2003, and the sampling protocol at that time resulted in high uncertainties on estimated inheritance and calculated paleo-denudation rates. Paleo- Q_s was calculated in a manner equivalent to modern Q_s , thereby assuming a paleo-topography similar to the modern topography (**Table 5.2**). Paleo-slope was reconstructed from the terrace surface remnants. By doing so, I assumed that the terrace slope in the channel-parallel direction has not significantly changed since its formation.

Reconstructed paleo-discharges for the four sampling sites fall between $0.71 * 10^6$ and $13.58 * 10^6$ m³/yr (**Fig. 5.3B red circles, Table 5.2**), all of which exceed modern discharge (**Fig. 5.3B insert**). According to the analysis, the annual discharge in the Carachi tributary was 1.35 times the modern discharge at ca. 108 ka, when the channel bed now associated with the T2 terrace was incised. During the incision event that formed the T4 terrace (~270 ka), discharge along the main stem, Carachi and El Mollar were 1.34, 1.10 and 1.84 times the modern equivalents, respectively.

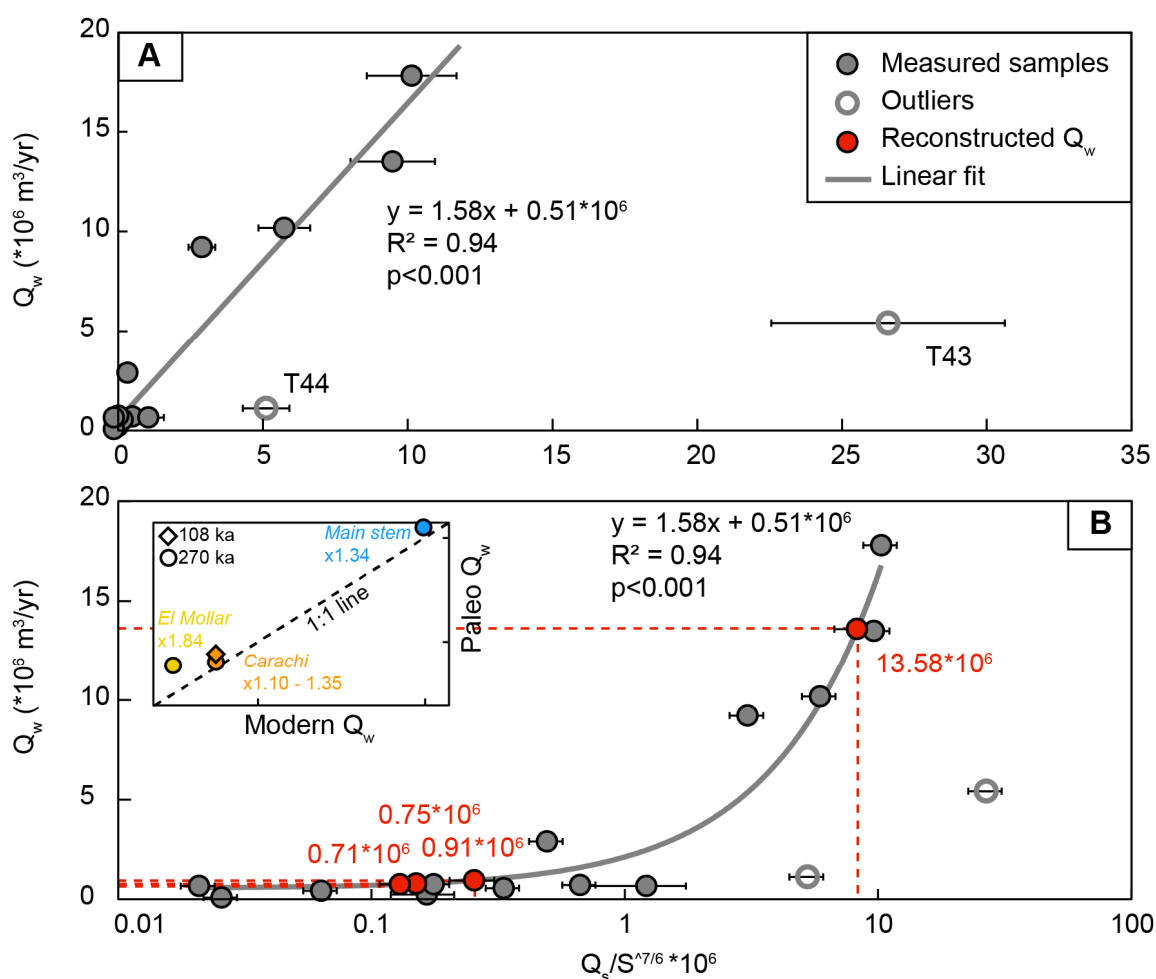


Fig. 5.3 Paleo Q_w reconstructions from terrace surface slopes and CRN-derived paleo- Q_s estimates. (A) Calibration of the Q_s , Q_w and S relationship in the Quebrada del Toro based on modern conditions. Q_w estimates were derived from a 16-year discharge record at the outlet of the Quebrada del Toro (Fig. 5.2), Q_s was estimated from ^{10}Be derived denudation rates and slopes were extracted from TanDEM-X satellite imagery. A linear regression indicates a significant relationship between the Q_s/S ratio and Q_w . (B) Same data as in A, shown in semi-log space. Based on the linear regression, paleo- Q_w can be reconstructed for sites of known paleo- Q_s and terrace surface slope. All 4 sites indicate higher discharge values for times shortly before river incision started compared to today (insert).

Despite some variability, all four data points suggest increased discharge compared to today during the final stages of sediment deposition in the channel, shortly before river incision started. As climatic changes associated with variations in solar insolation tend to be gradual and not instantaneous, I assume that discharge increased even more to eventually initiate river incision, but the conditions shortly before and shortly after the onset of incision probably do not differ substantially. The concept of a switch from aggradation to incision near the mid-point of a climate cycles has been demonstrated for aggradation-incision cycles of alluvial fans in NW Argentina (D’Arcy et al., 2017), and for the fill terraces in the neighboring Humahuaca valley (Schildgen et al., 2016).

The calculation of those paleo- Q_w values was based on the assumption that intermittency (I) and the sediment discharge coefficient (k_{Q_s}) stayed constant over time; an assumption that seemed reasonable in the case of k_{Q_s} . Regarding I , equation 5.1 reveals that Q_s scales linearly with both Q_w and I . Therefore, the alternative explanation for changes in the ratio of Q_s and S (eq. 5.1) would be that Q_w (bankfull discharge) stayed constant over time, but instead I (frequency of channel-forming discharge events) varied. In that case, increases in the Q_s/S ratio would result in reduced I values, which imply that bankfull floods were more frequent and conditions also overall wetter. As such, the observed changes in the ratio of Q_s and S (Fig. 5.3) could either affect Q_w or I , but the result would be overall wetter conditions in both cases.

Although the data indicates more discharge during times of regional wetter conditions (Baker and Fritz, 2015 and references therein; Fritz et al., 2007), the reconstructed discharge rates need to be considered with care, because the analysis is built on several assumptions. First, the modern Q_w and Q_s data were averaged over different timescales. While the ^{10}Be derived denudation rates, and thus Q_s , average over 10^3 - 10^5 years, Q_w estimates are based on only a 16-year record. Previous studies have shown that millennial average denudation rates based on cosmogenic nuclide can differ substantially from short term (few decades) measured stream sediment yields (e.g., Bierman et al., 2005; Kirchner et al., 2001). Whereas short-term sediment yield would be more comparable to the short-term discharge data, ^{10}Be derived denudation rates can be applied to modern and paleo-rivers. Second, the equation used to model paleo- Q_w (eq. 5.1; Wickert and Schildgen, 2018) represents equilibrium channel conditions, but has been shown to work less well during transient channel adjustment phases (chapter 3). Along the eastern flank of the southern Central Andes, however, 80% of the annual precipitation falls between November and February (Bianchi and Yañez, 1992; Garreaud et al., 2003). Hence, the local conditions vary throughout the year, and total annual discharge values used in the analysis are not necessarily representative for the channel forming discharge conditions, including flashfloods (Cencetti and Rivelli, 2011). On the other hand, due to the 1:1 relationship between Q_w and I , as discussed above, the results might have limited sensitivity to the timing and variability of discharge. Due to those restrictions, the calculated absolute paleo-discharge values should be taken with care. However, the relative differences between modern and paleo-discharge (factor 1.10 to 1.84) are independent of absolute modern Q_w values that are used in the calibration, and hence, they should be more reliable.

An increase in discharge in the Quebrada del Toro between ca. 10% and 84% during wetter times at ~108 and 270 ka is significantly less compared to the 7 to 8x increased discharge reconstructed for the Pisco river, Peru during the pluvial Minchin period at ~40 ka (Litty et al., 2016). However, for the same pluvial wet phase, Bookhagen et al. (2001) reconstructed an increase of only 10-15% of mean annual rainfall compared to today to maintain a paleo-lake in the Santa Maria Basin, located about 200 km south

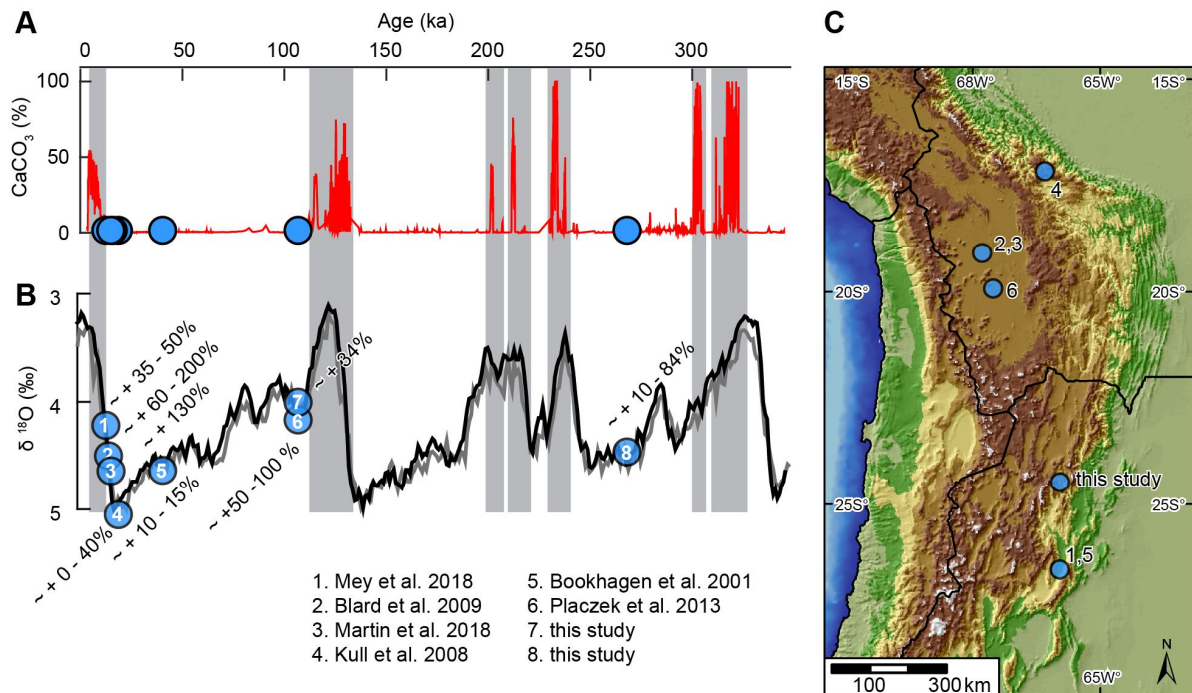


Fig. 5.4 Quantitative paleo-hydrological reconstructions from the Central and Eastern Andes. Quantitative paleo-hydrological reconstructions compared to (A) a regional paleo-climate record based on CaCO₃ concentrations from Lake Titicaca (Fritz et al., 2007) and (B) a global paleo-climate record based on benthic oxygen isotopes in the Atlantic (black) and Pacific (grey) (Lisiecki and Raymo, 2009). (C) Study sites for which reconstructions were performed. All studies indicate wetter conditions (more rainfall or higher discharge) than today for specific times at the according study sites.

of the Quebrada del Toro (**Fig. 5.4**). A higher estimate of ca. 35-50% has been derived from more recent modelling that combined the reconstruction of the extent of the same lake (which was later re-dated to Younger Dryas age; Hermanns et al., 2004) together with the extent of glaciers of the Younger Dryas (Mey et al., 2018). The reconstruction of rainfall from maximum glacier extents along the eastern Andean margin of Bolivia at ~ 20 ka suggested increased precipitation between 1 and 1.4 times of modern rainfall (Kull et al., 2008). Furthermore, Placzek et al. (2013) reconstructed rainfall for the last 130 kyr from shoreline deposits of paleo-lakes on the southern Bolivian Altiplano. They suggest no increase in rainfall during the pluvial phase at 46-47 ka, but 1.5 to 2 times more rainfall during the Ouki lake phase, which temporally overlaps with the exposure age of the T2 terrace. Also on the Bolivian Altiplano, modelling studies combining glacial mass-balances and lake-level high stands reconstructed a mean increase in precipitation during the Lake Tauca Highstand (~14.5-16.5 ka) of 60-200 % (Blard et al., 2009) and 130 % (Martin et al., 2018). These values are higher compared to most other paleo-hydrological reconstructions. However, the anomalously high precipitation rates were suggested to be partly driven by local moisture recycling

from the greatly expanded lake surface itself (Blard et al., 2009; Martin et al., 2018). Despite temporal and spatial differences, enhanced discharge between 10 and 84% in the Quebrada del Toro during globally cooler and regionally wetter phases (**Fig. 5.4B**) is in agreement with other paleo-hydrological studies from the Eastern Andes (Bookhagen et al., 2001; Kull et al., 2008; Mey et al., 2018) and the southern Altiplano Plateau (Blard et al., 2009; Martin et al., 2018; Placzek et al., 2013). Although absolute numbers differ among those studies, they all predict wetter conditions during more humid conditions inferred from Lake Titicaca sediment cores (**Fig. 5.4A**). Remarkably higher rainfall rates in the Pisco valley compared to all other studies (Litty et al., 2016; outside of the shown map extent in **Fig. 5.4C**) might be related to its location along the western margin of the Andes, a region that experiences different climate dynamics compared to the eastern margin of the Central Andes (Baker and Fritz, 2015). In addition, the assumption about a constant ratio of channel to valley width used for the reconstruction by Litty et al. (2016) might not hold true in all cases, and could have led to an overestimation of paleo-rainfall.

The newly presented approach of reconstructing discharge based on a combination of slope analysis and cosmogenic nuclide derived denudation rates provides comparable results to the few existing paleo-hydrological studies from the Eastern and Central Andes, and particularly those nearest to the Quebrada del Toro. As the studied fluvial terrace sequence is older than any paleo-lake deposit and most of the moraines in the Central Andes, this approach offers a new opportunity for quantitative reconstructions of sediment supply and discharge further back in time.

5.2.4. Concluding remarks on terrace formation in the Quebrada del Toro

Reconstructed variability in paleo- Q_s in the Quebrada del Toro during the last 500 kyr ranged between a factor of 2 and 4, while calculated variability in Q_w only ranged between a factor of 1.1 and 1.84. These results suggest, according to equation 5.1, that sediment supply variability has played a greater role than variability in discharge in driving bed-elevation changes of the Río Toro, although the variability in Q_s is still substantially lower compared to the neighboring Humahuaca valley (Schildgen et al., 2016). However, it should be noted that reconstructions of Q_s integrate conditions over 10s of kyr, while Q_w was only reconstructed for two snapshots in time. Also, the terraces only preserve the aggradation phases of the history of channel evolution (Mason et al., 2018). Hence, it is possible that the full range of variability in Q_w and Q_s were not captured. Independently of the paleo-discharge reconstructions from the terraces themselves, a range of paleo-hydrological studies from the Central Andes have all suggested higher precipitation rates during times inferred to have been wetter phases according to a sediment core from Lake Titicaca (Fritz et al., 2007). The studies vary in their estimates of Q_w variability over time, which can either be related to differences in local climate conditions of each study area, or to simplifications and assumptions

incorporated in the individual methods of reconstruction. The physical experiments also showed that increases in Q_w initiated channel incision and terrace cutting faster than a reduction in $Q_{s,in}$, such that terraces incised following an increase in Q_w were always paired. Terraces in the Quebrada del Toro are also paired, which does not prove, but at least qualitatively suggests that changes in Q_w were also of importance. As such, I conclude that the fill terraces in the Quebrada del Toro were formed in response to upstream perturbations, most likely by a combination of variability in $Q_{s,in}$ and Q_w . Because Q_s was reconstructed for the times of sediment deposition, and Q_w based on the final slope before incision, it cannot be resolved whether a further increase in Q_w or a decrease in Q_s eventually changed the Q_s/Q_w ratio sufficiently to trigger incision.

5.3. Signal propagation in fluvial sediments

The reconstructions of environmental conditions based on sedimentary signal inversion requires a detailed understanding of the generation of signals as well as the alteration of signals during transport and after deposition. Signals can be stored in sediment in the form of sediment discharge volume (Q_s), grain size distribution (GSD) and the sediment composition. In my thesis, I focused on the ^{10}Be concentrations in detrital fluvial sediment (chemical composition) and on the volume of sediment discharge (Q_s). In the following, I will first discuss what we have learned about the generation as well as the transfer of ^{10}Be signals with a particular focus on the *NSGI* – a potential geochemical tracer of hillslope processes. Second, I will discuss whether or not changes in boundary conditions ($Q_{s,in}$, Q_w) create distinct signals in $Q_{s,out}$, with a particular focus on the timing and location of signal generation.

5.3.1. Chemical composition (^{10}Be) signals

The ^{10}Be concentration (denoted [^{10}Be]) in detrital sediments has been commonly utilized over the last decades to estimate catchment-mean denudation rates (e.g., Bierman and Steig, 1996; Brown et al., 1995; Granger et al., 1996). During the last few years, several studies have reported particularly low [^{10}Be] in regions downstream of deep-excavation events, for example landslides or debris-flows (Kober et al., 2012; Niemi et al., 2005; Puchol et al., 2014; West et al., 2014; Yanites et al., 2009). Other studies reported differences in [^{10}Be] for different detrital grain sizes (e.g., Aguilar et al., 2014; Carretier et al., 2015; Codilean et al., 2014; Palumbo et al., 2009; Puchol et al., 2014; Savi et al., 2016; Schildgen et al., 2016; Wittmann et al., 2007). This variability of [^{10}Be] among different grain-size fractions has mainly been linked to the activity of deep-excavation events within the catchment, which can mobilize material up to several meters depth instantly, thereby contributing lower [^{10}Be] and coarser GSDs compared to other

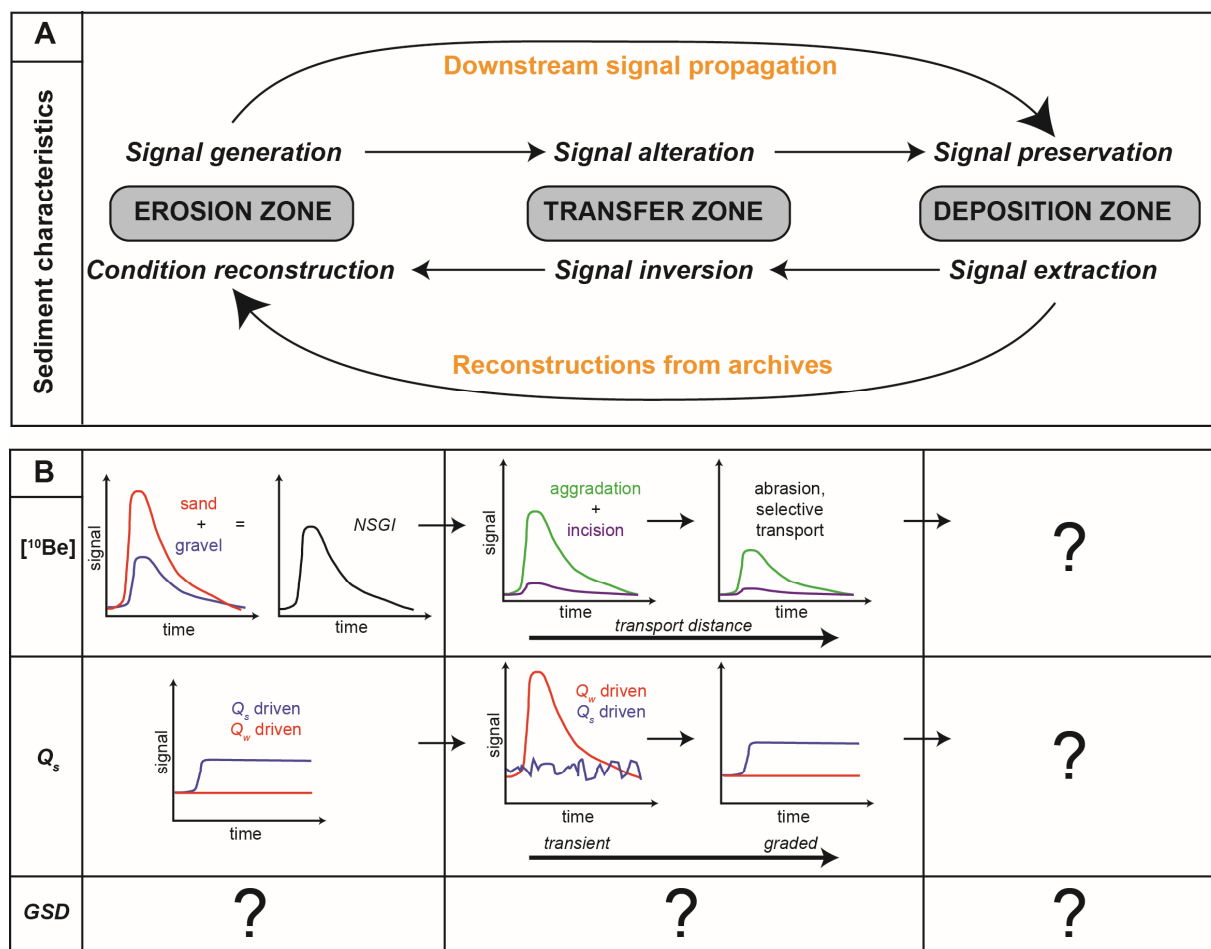


Fig. 5.5 Summary on new insights into signal propagation. (A) Overview of the three zones of the sediment routing systems and their functions within the signal propagation and signal inversion cascade. (B, upper panel) Geochemical (¹⁰Be) signals produced in the erosion zone vary with grain size and can be interpreted as a signal of hillslope processes active in the catchment. When moved along the transfer zone, NSGI signals are more likely representative of modern conditions during aggradation phases compared to incision phases, when formerly deposited sediment is mixed in. However, with increasing transport distance, the signal will weaken due to abrasion and/or selective transport. (B, lower panel) Sediment-discharge signals driven by enhanced Q_w are generated within the transfer zone shortly after perturbation. The peak in sediment-discharge is related to the adjustment of the channel to new equilibrium conditions. To lower the channel slope, the river remobilizes sediment from within its bed. In contrast, increases in sediment supply from the erosion zone will trigger a steepening of the channel by depositing the extra sediment within the channel bed. As such, only a fraction of the excess sediment reaches the outlet. Hence, sediment signals at the outlet can be strongly obscured until the channel bed has reached equilibrium conditions. Once in equilibrium, all the sediment supplied from the hillslopes will be transported to the outlet such that Q_{s,in} = Q_{s,out}.

hillslope processes (Aguilar et al., 2014; Belmont et al., 2007; Carretier et al., 2015; Puchol et al., 2014; Schildgen et al., 2016). I found that [¹⁰Be] in fluvial sand and fluvial gravel in the Quebrada del Toro also differed from each other (**Fig. A3**). As such, the ¹⁰Be signal generated in the erosion zone, from which catchment-mean denudation rates are normally inferred, varies with grain size (**Fig. 5.5B** upper left panel). However, my comparison of the [¹⁰Be] from two different grain sizes (expressed as the NSGI) with a detailed hillslope-process inventory from the whole Quebrada del Toro revealed that a shift in NSGI

coincided with a shift in the distribution of hillslope-processes in the contributing catchment (**Fig. 2.4C**). This finding suggests that [^{10}Be] in fluvial sediment cannot only be used to infer denudation rates, but that additional information on hillslope processes are stored in the [^{10}Be] difference between the sand and gravel fraction. In the following, I will discuss how the *NSGI* can potentially be altered during transfer along the sediment routing system. In chapter 2.5.2, I described how transient storage on an alluvial fan may alter the *NSGI*, a process for which I reported empirical evidence in the Quebrada del Toro. Here, I consider how additional processes, such as lateral sediment inputs, aggradation and incision phases, size-selective transport and abrasion may affect the *NSGI*.

A major influence on the *NSGI* along the main stem will be local input of sand and gravel from tributaries and adjacent hillslopes. If the *NSGI* of locally contributed material differs from the *NSGI* in the main stem, the downstream *NSGI* signal will be a mixture of the different input *NSGI* values. Reasons for spatial variability in sand and gravel [^{10}Be] and thus *NSGI* can include stochastic sediment release, different evacuation timescales of sediment for different parts of the catchment, and differences in ^{10}Be production rates due to differences in elevation distributions of the contributing catchment (Dingle et al., 2018; Lupker et al., 2012; Schildgen et al., 2016). Potentially opposite trends in *NSGI* values for distinct parts of the catchment might neutralize each other.

The experimental work described in chapter 3 showed that channel incision driven by a change in Q_w resulted in a peak in $Q_{s,out}$ of up to 20 times the amount of $Q_{s,in}$ (**Fig. 3.5**). Peaks in $Q_{s,out}$ after increased rainfall have also been observed and predicted by other experimental and numerical studies (Allen and Densmore, 2000; Armitage et al., 2013; Braun et al., 2015; Godard et al., 2013; Simpson and Castelltort, 2012; van den Berg van Saparoea and Postma, 2008). The excess sediment was remobilized from within the channel bed; accordingly, the age of the remobilized sediment increased with depth of channel incision. In such scenarios, the remobilization of formerly deposited sediment would alter the *NSGI* of freshly derived hillslope material following a mixture of the two sources within the transfer zone. In turn, during times of channel aggradation, $Q_{s,out}$ is only a fraction of $Q_{s,in}$. Due to sediment deposition along the channel reach, minimal amounts of the formerly deposited sediment are remobilized, and the sediment –fraction that reaches the outlet has most likely only recently been eroded from the hillslopes. Hence, the *NSGI* in modern channel sediment is more likely to reflect current hillslope processes during times of overall aggradation, whereas during times of incision, modern [^{10}Be] in sand and gravel are likely to be mixed with remobilized, older material, which will alter the *NSGI* signal (**Fig. 5.5B** upper middle panel).

The *NSGI* is calculated based on the [^{10}Be] difference between the fluvial sand and gravel fraction. As such, another possible alteration of the *NSGI* will be related to differences in the evolution of the sand and gravel fraction in the downstream direction, which can result from different mechanisms. First, fluvial

GSDs tend to fine in the downstream direction (Sternberg, 1875), which is attributed to the combination of size-selective transport and gravel abrasion (Attal and Lavé, 2009, 2006; Ferguson et al., 1996; Paola et al., 1992b). Grain-size selective transport describes grain-size sorting due to selective entrainment, transport and deposition, which normally results in longer transport times for gravel compared to sand (Ferguson et al., 1996; Hoey and Ferguson, 1994; Menting et al., 2015; Miller et al., 2014; Paola et al., 1992b). Hence, after a change in hillslope processes, different transport times of signals in the gravel and sand fraction can cause gradual shifts in the *NSGI* signal, and a delay in time by which the *NSGI* at the outlet reflects the *NSGI* of recently mobilized hillslope material. Second, the importance of gravel-abrasion, which reduces gravel to sand and silt, increases with downstream transport distance (Attal and Lavé, 2009, 2006; Dingle et al., 2017; Lupker et al., 2017). Abrasion rates for Himalayan quartzites, quartzitic sandstones, and granites have been experimentally determined to range from 0.15 to 0.4 %/km (Attal and Lavé, 2009, 2006). These values imply that most gravel has been turned into sand after a few hundred kilometers of transport through the fluvial system. The sudden disappearance of coarse gravel in alluvial rivers is called the gravel-sand transition (Paola et al., 1992b; Parker and Cui, 1998). Dingle et al. (2017) mapped the gravel-sand transition for Himalayan rivers within 10 to 40 km after entering the Ganga Plain. Consequently, no *NSGI* analyses are possible downstream of the gravel-sand transition. But even upstream of the gravel-sand transition, abrasion can affect the *NSGI* by diluting the $[^{10}\text{Be}]_{\text{sand}}$ fraction with sand abraded from low- $[^{10}\text{Be}]$ gravel. Lupker et al. (2017) observed a dilution of $[^{10}\text{Be}]_{\text{sand}}$ in the downstream direction of the Tsangpo-Brahmaputra catchment. They suggested that dilution by mixing with abrasion material of landslide-derived, low- $[^{10}\text{Be}]$ gravel and in their model, they found that abrasion becomes apparent after 50 to 150 km of transport distance. Hence, the longer the transport distances, the larger the contribution of the abraded gravel to the sand fraction, such that differences in $[^{10}\text{Be}]$ between the sand and gravel fraction will be reduced. Therefore, both size-selective transport and abrasion are likely to affect the *NSGI* value with increasing transport distances (**Fig. 5.5B** upper middle panel).

Within the Quebrada del Toro, I found larger scatter in the *NSGI* values in the northern part of the catchment, where larger amounts of sediments are transiently stored and potentially remobilized within the catchments, resulting in a mix of younger and older sediment. But overall, the continuous burial of large trees (still in life position) within the main channel (**Fig. 4.2b insert**) and the ongoing avulsion (sudden changes in channel position) of channels I observed in the field both suggest ongoing aggradation in the Río Toro today. This interpretation is in agreement with the long-term evolution of the channel-bed elevation derived from the terrace chronology, which suggests channel aggradation during interglacials. In addition, the channel length of the tributaries ranges from ~4 to ~75 km. As such, selective transport and abrasion might play a role for the farthest traveled gravel, but not for the majority of gravel. Hence, I conclude that modern river sediments in the Quebrada del Toro analyzed for *NSGI* calculations faithfully

represent the modern conditions on hillslopes. In summary, I conclude that obtaining *NSGI* values to track hillslope processes works best in aggrading systems with a uniform distribution of processes in the sampled sub-catchment (stable *NSGI* values from lateral input), with relatively short transport distances and flow-conditions that regularly move both sampled grain sizes.

5.3.2. Sediment discharge (Q_s) signals

In the sand-box experiments, I observed a distinct change in $Q_{s,out}$ following a perturbation in Q_w , whereas perturbations in $Q_{s,in}$ resulted in no visible signal in $Q_{s,out}$ (**Fig. 3.5**). However, when tracing $Q_{s,out}$ at a basin outlet, it is important to distinguish between the two zones that affect the amount of sediment discharge – the erosion zone with hillslopes that initially supply sediment ($Q_{s,in}$) and the channel system itself (transfer zone). Changes in conditions within the erosion zone, that is the amount of sediment supplied from surrounding hillslopes ($Q_{s,in}$) and the amount of rainfall on those hillslopes (Q_w), automatically also affect the transfer zone, because modified Q_s/Q_w ratios require an adjustment of the channel until the profile reaches equilibrium again (Blom et al., 2016; Lane, 1955; Mackin, 1948; Wickert and Schildgen, 2018). The channel adjustment is achieved by either deposition (channel steepening) or excavation (slope reduction) of sediment within the channel bed (**Fig. 3.4**), which, in turn, affects the total amount of sediment reaching the channel outlet. Whereas changes in boundary conditions within the erosion zone, and consequently Q_w and Q_s delivered to the channel, persist at least as long as the forcing conditions persist, the influence on $Q_{s,out}$ from within the transfer zone is temporary, and defined by the response time for the channel to reach equilibrium conditions again (Howard, 1982; Paola et al., 1992a).

In the Q_w experiments, I held $Q_{s,in}$ constant, such that no variability in the Q_s signal was generated within the erosion zone (**Fig. 5.5B** middle left panel). Consequently, any variation in the signal observed at the basin outlet has been generated within the transfer zone due to the adjustment of the channel profile. An increase in Q_w requires a lower slope to transport a constant amount of incoming sediment (Lane, 1955; Mackin, 1948; Wickert and Schildgen, 2018), such that the river incises into its bed and thereby temporarily mobilizes sediment. In my experiments, this phenomenon can be seen as a distinct peak with $Q_{s,out}$ up to more than 20 times $Q_{s,in}$ (**Fig. 3.5B**). Following that perturbation, the channel approaches equilibrium, where $Q_{s,out}$ equals $Q_{s,in}$. A peak in $Q_{s,out}$ that is relatively amplified compared to an increase in discharge has been shown by other physical experiments (van den Berg van Saparoea and Postma, 2008) as well as by a range of different numerical models including alluvial and bedrock channel systems (Allen and Densmore, 2000; Armitage et al., 2013; Braun et al., 2015; Simpson and Castelltort, 2012).

In the experiments in which I varied $Q_{s,in}$, changes in $Q_{s,in}$ did not generate visible signals in $Q_{s,out}$ (**Fig. 3.5D, E**). Similar experiments carried out by van den Berg van Saparoea and Postma (2008) also

indicated that changes in $Q_{s,in}$ are less recognizable in $Q_{s,out}$ compared to changes in Q_w . Numerical model results from Simpson and Castelltort (2012) show a dampened response in $Q_{s,out}$ to perturbation in $Q_{s,in}$, whereas perturbations in Q_w were amplified and generated a clearer signal. Compared to the Q_w experiments, in which all changes in $Q_{s,out}$ were realized within the transfer zone, in the Q_s experiments, $Q_{s,out}$ is affected by the amount of sediment supplied from the erosion zone and by sediment deposition or remobilization within the transfer zone. A permanent or long-lasting increase of sediment discharge from the erosion zone (**Fig. 5.5B** blue line in middle left panel) changes the local Q_s/Q_w ratio within the channel and therefore triggers temporary aggradation within the channel bed (**Fig. 3.5**). As such, the two subsystems (erosion zone and transfer zone) behave in opposite ways. An increase in $Q_{s,in}$ with Q_w held constant requires a steeper channel slope, which will be archived by sediment deposition within the channel (negative feedback between S and $Q_{s,in}$; (Simpson and Castelltort, 2012; van den Berg van Saparoea and Postma, 2008). Hence, the extra sediment supply from upstream diminishes in the downstream direction due to enhanced sediment deposition within the channel during the transient adjustment phase. In contrast, a reduction in $Q_{s,in}$ should eventually result in a reduction in $Q_{s,out}$. But as a lowering of Q_s/Q_w requires a lower channel slope, river incision and sediment remobilization from the channel bed counteracts the expected decrease in $Q_{s,out}$ during the transient adjustment phase.

In the longer-term $Q_{s,in}$ perturbation experiment by van den Berg van Saparoea and Postma (2008), however, slight changes in $Q_{s,out}$ became apparent. This response is comparable to the long-term changes in $Q_{s,out}$ after perturbations in $Q_{s,in}$ predicted by the numerical model of Allen and Densmore (2000). They modeled a simple catchment-fan system separated by a normal fault with a landscape evolution model, and saw an eventual decrease in the catchment's $Q_{s,out}$ following a relative reduction in $Q_{s,in}$ (indirectly modelled through a decrease in fault slip rate; Fig. 7 in Allen and Densmore, 2000), but only after a certain lag-time (channel response time). Also, the numerical model by Armitage et al. (2011) predicted a clear increase in $Q_{s,out}$ following an increase in $Q_{s,in}$ (indirectly modelled through an increase in the catchment uplift rate; Fig. 2f in Armitage et al., 2011). This model was run over million-year timescales and thus does not resolve the times of channel adjustment. As such, $Q_{s,in}$ -driven changes in $Q_{s,out}$ become detectable once the system has achieved new equilibrium conditions, that is if the perturbation lasts longer than the response time of the channel. The negative feedback between $Q_{s,in}$ and the channel gradient during the transient phase might explain why neither in my experiments, nor in those short-term perturbations from van den Berg van Saparoea and Postma (2008) a clear signal in $Q_{s,out}$ was detectable.

Because $Q_{s,out}$ -signals driven by changes in Q_w are generated during the transient channel adjustment phase and $Q_{s,in}$ -driven signals in $Q_{s,out}$ only become apparent after the transient phase, the response time of a channel system to reach new equilibrium conditions (Howard, 1982; Paola et al., 1992a)

is of particular importance for sequence stratigraphy. The duration of a river's response time has been proposed to be a function of the system length and its diffusivity (Howard, 1982; Paola et al., 1992a), with the diffusivity scaling with $Q_{s,out}$, channel width (w) and slope (S) (Métivier and Gaudemer, 1999). Later, however, Simpson and Castellort (2012) suggested that the channel response time also depends on the sign of forcing, that is response times differ in aggradational settings compared to incision settings. Simpson and Castellort (2012) proposed that the response time for aggradation depends on the volume of sediment that needs to be deposited in the channel to reach new equilibrium conditions (a triangular shaped volume defined by the system length, magnitude of required slope change and system width) and the amount of provided sediment per time ($Q_{s,in}$). In contrast, the response time in incisional settings depends only on the period of perturbation (Simpson and Castellort, 2012). Indeed, the experimental results imply that the channel-response time in incisional settings is shorter compared to aggradational settings (**Fig. 3.5C, E**). However, the differences in response times can be related to differences in the parameters setting the maximum incision or aggradation rate, geometrical differences, or both. Regarding aggradation, the amount of supplied sediment limits the rate of sediment deposition along the channel, as suggested by Simpson and Castellort (2012). But as the perturbation in the experiments was applied instantly and not periodically, the response time of channel adjustment during incision must be defined differently than proposed by Simpson and Castellort (2012). I suggest that the response time in a down-cutting alluvial system depends on the maximum incision rate (rate of slope change in **Fig 3.5**) and the magnitude of change (initial slope versus new equilibrium slope). The maximum incision rate should be a function of the excess-transport capacity, which is related to the amount of discharge (Q_w), upstream sediment supply ($Q_{s,in}$) and slope (S). In addition to different parameters driving the maximum rates of aggradation and incision, the absolute volume of moved sediment within the channel reach differs between aggradation and incision. Because I performed the aggradation experiments first, the channel needed to deposit sediment within the entire valley width during aggradation. In the subsequent incision state, the river only incised about half a valley width (**Fig. 3.3**), such that the amount of sediment removed from within the channel is less compared to the amount of sediment deposited during prior aggradation. Because I did not perform experiments with repeated cyclicality in input parameters and because the experiments did not always completely reach new equilibrium conditions, no final conclusions whether the maximum incision/aggradation rates or differences in channel geometry are the dominant parameter setting the channel response time are possible.

Both the physical experiments presented here and numerical models (Armitage et al., 2011; Simpson and Castellort, 2012) support the inference that an increase in Q_w results in a peak in $Q_{s,out}$, but it is important to note that reality is more complex. Variability in Q_w is often climate related, such that $Q_{s,in}$ might also be affected simultaneously. In semi-arid settings, it has been proposed that increased rainfall due to wetter climate conditions might initially supply additional sediment to the channel, at least until increased

vegetation cover leads to greater protection of hillslopes from erosion (Garcin et al., 2017; Langbein and Schumm, 1958; Olen et al., 2016; Torres Acosta et al., 2015). Sediment production rates on hillslopes might also change due to changes in the rates of chemical weathering (Dixon et al., 2009; Maher and Chamberlain, 2014; Riebe et al., 2004) or frost cracking (Walder and Hallet, 1985). Increased rainfall has also the potential to increase pore pressure and initiate landsliding (Anderson and Sitar, 1995; Chen et al., 2006; Iverson, 2000). A more realistic picture than the flat line shown in the middle left panel in **Fig. 5.5B** is that described by Steffen et al. (2010, 2009). Those authors suggest that an increase in rainfall triggers a pulse of sediment removal from the hillslopes to the channel, which causes aggradation within the channel. Once the hillslopes are depleted of sediment, the Q_s/Q_w ratio in the channel decreases (without any further changes in boundary conditions) and the river incises into its bed.

In conclusion, both changes in Q_w or changes in $Q_{s,in}$ can trigger signals in $Q_{s,out}$ (**Fig. 5.5B** middle panel). However, the major difference is that signals in $Q_{s,out}$ driven by changes in Q_w are generated during the transient phase of channel adjustment, while changes in $Q_{s,in}$ are only transmitted once the channel has reached new equilibrium conditions. Hence, $Q_{s,in}$ signals are only transmitted after a lag-time and thus can only be expected in a down-system stratigraphic record if the perturbation lasted substantially longer than the response time of the channel. As many environmental perturbations are of cyclic origin (Milankovitch, 1941) and only persist for a certain time, the generation of signals in $Q_{s,out}$ driven by changes in Q_w is more likely than those generated by perturbations in $Q_{s,in}$. However in this study, I only investigated the generation of signals at the basin outlet, but not any further evolution of the signal along the sediment routing system.

In the Quebrada del Toro, the majority of the sediment exiting the basin will be deposited within the alluvial fan in the Lerma valley (**Fig. 4.2a**). Therefore, the sequence stratigraphy of the alluvial fan might preserve signals that were created in the Quebrada del Toro as responses to changes in $Q_{s,in}$ and Q_w . The reconstructions from the fill terrace archive in the upstream part of the basin suggested variability in $Q_{s,in}$ and Q_w over the last ~500 ka. However, the terrace archive is incomplete, as only conditions during times of sediment deposition (aggradation) and the onset of incision could be reconstructed. Because incision driven by increased Q_w has been shown to generate a distinct signal in $Q_{s,out}$, the combination of reconstructions from the terraces with signal extraction from the alluvial fan in the Lerma valley would potentially provide a more complete picture of past conditions.

5.4. Emerging research questions

The results obtained from this work raise new research questions, some of which will be briefly elaborated on below:

The presented calibration of *NSGI* with the hillslope-process inventory suggests that the *NSGI*, measured in dated stratigraphic sections, might potentially track hillslope processes through time. But to quantify the contribution of the different hillslope processes to the fluvial sand and gravel fraction, we would need to know (1) the average depth per hillslope process and average recurrence, and (2) the vertical distribution of grain sizes on hillslopes. Currently, our knowledge on grain-size distribution on hillslopes is limited due to a restricted number of field measurements (Attal et al., 2015; Attal and Lavé, 2006; Marshall and Sklar, 2012; Roda-Boluda et al., 2018; Sklar et al., 2017; Whittaker et al., 2010). A detailed analysis of GSD on hillslopes within the Quebrada del Toro and also within the sedimentary deposits of the different hillslope-process types (e.g. landslide deposits) would improve our understanding of sediment contributions associated with the different hillslope processes.

In addition, I expect the *NSGI* to alter in the downstream direction due to gravel abrasion (Attal and Lavé, 2009, 2006; Dingle et al., 2017) and selective transport (Ferguson et al., 1996; Paola et al., 1992b). Lupker et al. (2017) explained a reduction of $[^{10}\text{Be}]_{\text{sand}}$ in the downstream direction of the Tsangpo-Brahmaputra catchment by abrasion of landslide-derived, low $[^{10}\text{Be}]$ gravel and the consequent dilution of the $[^{10}\text{Be}]_{\text{sand}}$. In addition to the *NSGI* values obtained from several tributaries, a systematic sampling of *NSGI* at several locations along the main stem, including downstream of the Quebrada del Toro, would provide insight into the alteration of the *NSGI* signal during transport. Only when the degree of alteration is known the *NSGI* can be applied to reconstruct hillslope-processes in the past from sedimentary deposits.

The *NSGI* presented in chapter 2 is calibrated for the Quebrada del Toro. And as transport distances in the northern catchments in the Quebrada del Toro are short, and the similar $[^{10}\text{Be}]$ in the sand and gravel fractions indicate little abrasion, the *NSGI* could be measured in fill-terrace deposits of known age to understand whether hillslope-processes in the past have been stable, or might have varied with the proposed variability in discharge (and thus climate) over time.

The reconstruction of Q_w from the fill terraces in the Quebrada del Toro indicates wetter conditions at the onset of river incision compared to today. The bed-elevation changes of the Río Toro, recorded within the cut-and-fill terrace sequence, also coincided with wetter and drier conditions inferred from a sediment core from Lake Titicaca. Lake Titicaca, however, is located about 1000 km to the north of the Quebrada del Toro, such that local paleo-climate conditions in Toro might have differed. An independent paleo-hydrology proxy applied to the Quebrada del Toro would provide an independent dataset to evaluate the

terrace-based paleo-hydrological reconstruction. Lipid biomarkers, as for example long-chain *n*-alkanes, may provide such an opportunity. Long-chain *n*-alkanes are embedded in the leaf-wax layer of higher terrestrial plants (Collister et al., 1994; Eglinton and Hamilton, 1967; Rieley et al., 1991), and have been shown to be stable in sedimentary deposits over geological timescales (Eglinton and Eglinton, 2008). The hydrogen isotopic composition of *n*-alkanes correlates with the hydrogen isotopic composition of the local rainfall (Garcin et al., 2012; Sachse et al., 2012; Smith and Freeman, 2006), which in turn is a function of the amount of rainfall and air temperature (Dansgaard, 1964; Gat, 1996; Poage and Chamberlain, 2001). As such, the hydrogen isotopic composition of these *n*-alkanes from sedimentary deposits in the Quebrada del Toro can be measured to test for variability in temperature and rainfall amount over time, which can be compared to the water discharge reconstruction from the terraces.

Finally, terrace formation has been investigated in the field and in physical experiments. These datasets could be useful for improving numerical models of terrace evolution. As already discussed, the width reduction following an increase in water discharge in the experiments, which differed from the long-term prediction by the equation proposed by Wickert and Schildgen (2018), suggests variability in the excess-shear stress at bankfull flow (ϵ). Comparing the field data or experimental data to numerical models can help to identify important parameters or processes that may be neglected in the models so far, which may be important, in this case, for better understanding and predicting alluvial channel behavior during transient adjustments to external forcing.

6. Bibliography

- Aguilar, G., Carretier, S., Regard, V., Vassallo, R., Riquelme, R., Martinod, J., 2014. Grain size-dependent ^{10}Be concentrations in alluvial stream sediment of the Huasco Valley, a semi-arid Andes region. *Quat. Geochronol.* 19, 163–172.
- Ahnert, F., 1998. *Introduction to geomorphology*. John Wiley & Sons Inc.
- Ahnert, F., 1970. Functional relationship between denudation, relief and uplift in large mid-latitude drainage basins. *Am. J. Sci.* 268, 243–263.
- Allen, P.A., 2008a. Time scales of tectonic landscapes and their sediment routing systems. *Landscape Evol. Denudation, Clim. Tectonics Over Differ. Time Sp. Scales* 296, 7–28.
- Allen, P.A., 2008b. From landscapes into geological history. *Nature* 451, 274–276.
- Allen, P.A., 2017. *Sediment routing systems: The fate of sediment from source to sink*. Cambridge University Press.
- Allen, P.A., Armitage, J.J., Carter, A., Duller, R.A., Whittaker, A.C., 2013. The Q_s problem: Sediment volumetric balance of proximal foreland basin systems. *Sedimentology* 60, 102–130.
- Allen, P. A., Densmore, A. L., 2000. Sediment flux from an uplifting fault block. *Basin Res.* 12, 367–380.
- Alloway, B. V., Lowe, D.J., Barrell, D.J.A., Newnham, R.M., Almond, P.C., Augustinus, P.C., Bertler, N.A.N., Carter, L., Litchfield, N.J., Mcglone, M.S., Shulmeister, J., Vandergoes, M.J., Williams, P.W., Members, N.-I., 2007. Towards a climate event stratigraphy for New Zealand over the past 30,000 years (NZ-INTIMATE project). *J. Quat. Sci.* 22, 9–35.
- Alonso, R.N., Bookhagen, B., Carrapa, B., Coutand, I., Haschke, M., Hilley, G.E., Schoenbohm, L., Sobel, E.R., Strecker, M.R., Trauth, M.H., 2006. Tectonics, climate, and landscape evolution of the southern central Andes: the Argentine Puna Plateau and adjacent regions between 22° and 30° S, in: *The Andes*. Springer, pp. 265–283.
- Andersen, T., 2002. Correction of common lead in U-Pb analyses that do not report ^{204}Pb . *Chem. Geol.* 192, 59–79.
- Anderson, R.S., Repka, J.L., Dick, G.S., 1996. Explicit treatment of inheritance in dating depositional surfaces using in situ ^{10}Be and ^{26}Al . *Geology* 24, 47–51.
- Anderson, S.A., Sitar, N., 1995. Analysis of rainfall-induced debris flows. *J. Geotech. Eng.* 121, 544–552.
- Armitage, J.J., Duller, R.A., Whittaker, A.C., Allen, P.A., 2011. Transformation of tectonic and climatic signals from source to sedimentary archive. *Nat. Geosci.* 4, 231–235.
- Armitage, J.J., Dunkley Jones, T., Duller, R.A., Whittaker, A.C., Allen, P.A., 2013. Temporal buffering of climate-driven sediment flux cycles by transient catchment response. *Earth Planet. Sci. Lett.* 369–370, 200–210.
- Atkinson, D.A., 2004. *Weathering, slopes and landforms*. Hodder & Stoughton.
- Attal, M., Lavé, J., 2009. Pebble abrasion during fluvial transport: Experimental results and implications for the evolution of the sediment load along rivers. *J. Geophys. Res. Earth Surf.* 114.
- Attal, M., Lavé, J., 2006. Changes of bedload characteristics along the Marsyandi River (central Nepal): Implications for understanding hillslope sediment supply, sediment load evolution along fluvial networks, and denudation in active orogenic belts. *Tectonics, Clim. Landsc. Evol.* 398, 143–171.

Bibliography

- Attal, M., Mudd, S.M., Hurst, M.D., Weinman, B., Yoo, K., Naylor, M., 2015. Impact of change in erosion rate and landscape steepness on hillslope and fluvial sediments grain size in the Feather River basin (Sierra Nevada, California). *Earth Surf. Dyn.* 3, 201–222.
- Bagnold, R.A., 1977. Bed load transport by natural rivers. *Water Resour. Res.* 13, 303–312.
- Baker, P.A., Rigsby, C.A., Seltzer, G.O., Fritz, S.C., Lowenstein, T.K., Bacher, N.P., Veliz, C., 2001. Tropical climate changes at millennial and orbital timescales on the Bolivian Altiplano. *Nature* 409, 698–701.
- Baker, P. A., Seltzer, G.O., Fritz, S.C., Dunbar, R.B., Grove, M.J., Tapia, P.M., Cross, S.L., Rowe, H.D., Broda, J.P., 2001. The history of South American tropical precipitation for the past 25,000 years. *Science* 291, 640–643.
- Baker, P.A., Fritz, S.C., 2015. Nature and causes of Quaternary climate variation of tropical South America. *Quat. Sci. Rev.* 124, 31–47.
- Baker, S.E., Gosse, J.C., McDonald, E. V., Evenson, E.B., Martínez, O., 2009. Quaternary history of the piedmont reach of Río Diamante, Argentina. *J. South Am. Earth Sci.* 28, 54–73.
- Balco, G., Shuster, D.L., 2009. ^{26}Al - ^{10}Be - ^{21}Ne burial dating. *Earth Planet. Sci. Lett.* 286, 570–575.
- Balco, G., Stone, J.O., Lifton, N.A., Dunai, T.J., 2008. A complete and easily accessible means of calculating surface exposure ages or erosion rates from ^{10}Be and ^{26}Al measurements. *Quat. Geochronol.* 3, 174–195.
- Balco, G., Stone, J.O.H., 2005. Measuring middle Pleistocene erosion rates with cosmic-ray-produced nuclides in buried alluvial sediment, Fisher Valley, southeastern Utah. *Earth Surf. Process. Landforms* 30, 1051–1067.
- Baynes, E.R.C., Lague, D., Kermarrec, J., 2018. Supercritical river terraces generated by hydraulic and geomorphic interactions. *Geology* 46, 499–502.
- Begin, Z.B., Meyer, D.F., Schumm, S.A., 1981. Development of longitudinal profiles of alluvial channels in response to base-level lowering. *Earth Surf. Process. Landforms* 6, 49–68.
- Bekaddour, T., Schlunegger, F., Vogel, H., Delunel, R., Norton, K.P., Akçar, N., Kubik, P., 2014. Paleo-erosion rates and climate shifts recorded by Quaternary cut-and-fill sequences in the Pisco valley, central Peru. *Earth Planet. Sci. Lett.* 390, 103–115.
- Belmont, P., Pazzaglia, F.J., Gosse, J.C., 2007. Cosmogenic ^{10}Be as a tracer for hillslope and channel sediment dynamics in the Clearwater River, western Washington State. *Earth Planet. Sci. Lett.* 264, 123–135.
- Bennett, G.L., Miller, S.R., Roering, J.J., Schmidt, D.A., 2016. Landslides, threshold slopes, and the survival of relict terrain in the wake of the Mendocino Triple Junction. *Geology* 44, 363–366.
- Bianchi, A.R., Yañez, C.E., 1992. Las precipitaciones en el noroeste argentino. *Inst. Nac. Tecnol. Agropecu.*
- Bierman, P., Steig, E.J., 1996. Estimating rates of denudation using cosmogenic isotope abundances in sediment. *Earth Surf. Process. Landforms* 21, 125–139.
- Bierman, P.R., Reuter, J.M., Pavich, M., Gellis, A.C., Caffee, M.W., Larsen, J., 2005. Using cosmogenic nuclides to contrast rates of erosion and sediment yield in a semi-arid, arroyo-dominated landscape, Rio Puerco Basin, New Mexico. *Earth Surf. Process. Landforms* 30, 935–953.
- Binnie, S.A., Phillips, W.M., Summerfield, M.A., Fifield, L.K., 2007. Tectonic uplift, threshold hillslopes, and denudation rates in a developing mountain range. *Geology* 35, 743–746.

Bibliography

- Blard, P.-H., Braucher, R., Lavé, J., Bourlès, D.L., 2013. Cosmogenic ^{10}Be production rate calibrated against ^3He in the high Tropical Andes (3800–4900 m, 20–22° S). *Earth Planet. Sci. Lett.* 382, 140–149.
- Blard, P.H., Lavé, J., Farley, K.A., Fornari, M., Jiménez, N., Ramirez, V., 2009. Late local glacial maximum in the Central Altiplano triggered by cold and locally-wet conditions during the paleolake Tauca episode (17–15 ka, Heinrich 1). *Quat. Sci. Rev.* 28, 3414–3427.
- Blom, A., Arkesteijn, L., Chavarrias, V., Viparelli, E., 2017. The equilibrium alluvial river under variable flow and its channel-forming discharge. *J. Geophys. Res. Earth Surf.* 122, 1924–1948.
- Blom, A., Viparelli, E., Chavarrias, V., 2016. The graded alluvial river: Profile concavity and downstream fining. *Geophys. Res. Lett.* 43, 6285–6293.
- Blöthe, J.H., Korup, O., 2013. Millennial lag times in the Himalayan sediment routing system. *Earth Planet. Sci. Lett.* 382, 38–46.
- Blum, M.D., Tornqvist, T.E., 2000. Fluvial responses to climate and sea-level change: a review and look forward. *Sedimentology* 47, 2–48.
- Bobst, A.L., Lowenstein, T.K., Jordan, T.E., Godfrey, L. V, Ku, T.-L., Luo, S., 2001. A 106 ka paleoclimate record from drill core of the Salar de Atacama, northern Chile. *Palaeogeogr. Palaeoclimatol. Palaeoecol.* 173, 21–42.
- Bogaart, P.W., van Balen, R.T., 2000. Numerical modeling of the response of alluvial rivers to Quaternary climate change. *Glob. Planet. Change* 27, 147–163.
- Boll, J., Thewessen, T.J.M., Meijer, E.L., Kroonenberg, S.B., 1988. A simulation of the development of river terraces. *Zeitschrift für Geomorphol.* 32, 31–45.
- Bookhagen, B., Fleitmann, D., Nishiizumi, K., Strecker, M.R., Thiede, R.C., 2006. Holocene monsoonal dynamics and fluvial terrace formation in the northwest Himalaya, India. *Geology* 34, 601–604.
- Bookhagen, B., Haselton, K., Trauth, M.H., 2001. Hydrological modelling of a Pleistocene landslide-dammed lake in the Santa Maria Basin, NW Argentina. *Palaeogeogr. Palaeoclimatol. Palaeoecol.* 169, 113–127.
- Bookhagen, B., Strecker, M.R., 2012. Spatiotemporal trends in erosion rates across a pronounced rainfall gradient: Examples from the southern Central Andes. *Earth Planet. Sci. Lett.* 327, 97–110.
- Bookhagen, B., Strecker, M.R., 2008. Orographic barriers, high-resolution TRMM rainfall, and relief variations along the eastern Andes. *Geophys. Res. Lett.* 35.6.
- Borchers, B., Marrero, S., Balco, G., Caffee, M., Goehring, B., Lifton, N., Nishiizumi, K., Phillips, F., Schaefer, J., Stone, J., 2016. Geological calibration of spallation production rates in the CRONUS-Earth project. *Quat. Geochronol.* 31, 188–198.
- Bradley, W.C., 1970. Effect of weathering on abrasion of granitic gravel, Colorado River (Texas). *Geol. Soc. Am. Bull.* 81, 61–80.
- Braun, J., Voisin, C., Gurlan, A.T., Chauvel, C., 2015. Erosional response of an actively uplifting mountain belt to cyclic rainfall variations. *Earth Surf. Dyn.* 3, 1–14.
- Bridgland, D., Westaway, R., 2008. Climatically controlled river terrace staircases: a worldwide Quaternary phenomenon. *Geomorphology* 98, 285–315.
- Broccoli, A.J., Dahl, K.A., Stouffer, R.J., 2006. Response of the ITCZ to Northern Hemisphere cooling. *Geophys. Res. Lett.* 33.

Bibliography

- Brown, E.T., Stallard, R.F., Larsen, M.C., Raisbeck, G.M., Yiou, F., 1995. Denudation rates determined from the accumulation of in situ-produced ^{10}Be in the Luquillo Experimental Forest, Puerto Rico. *Earth Planet. Sci. Lett.* 129, 193–202.
- Bufe, A., Turowski, J.M., Burbank, D.W., Paola, C., Wickert, A.D., Tofelde, S., 2018. Controls on lateral channel mobility and the reworked area of active alluvial surfaces, in: EGU General Assembly Conference Abstracts. p. 13437.
- Buffington, J.M., 2012. Changes in channel morphology over human time scales [Chapter 32]. *Gravel-Bed Rivers Process. Tools, Environ.* 435–463.
- Bull, W.B., 1991. Geomorphic responses to climatic change.
- Bull, W.B., 1990. Stream-terrace genesis: implications for soil development. *Geomorphology* 3, 351–367.
- Burbank, D.W., Anderson, R.S., 2011. *Tectonic geomorphology*. John Wiley & Sons.
- Burbank, D.W., Leland, J., Fielding, E., Anderson, R.S., Brozovic, N., Reid, M.R., Duncan, C., 1996. Bedrock incision, rock uplift and threshold hillslopes in the northwestern Himalayas. *Nature* 379, 505–510.
- Carretier, S., Regard, V., Vassallo, R., Aguilar, G., Martinod, J., Riquelme, R., Christophoul, F., Charrier, R., Gayer, E., Fariás, M., Audin, L., Lagane, C., 2015. Differences in ^{10}Be concentrations between river sand, gravel and pebbles along the western side of the central Andes. *Quat. Geochronol.* 27, 33–51.
- Carretier, S., Regard, V., Vassallo, R., Aguilar, G., Martinod, J., Riquelme, R., Pepin, E., Charrier, R., Hérail, G., Fariás, M., Guyot, J.L., Vargas, G., Lagane, C., 2013. Slope and climate variability control of erosion in the Andes of central Chile. *Geology* 41, 195–198.
- Castelltort, S., Van Den Driessche, J., 2003. How plausible are high-frequency sediment supply-driven cycles in the stratigraphic record? *Sediment. Geol.* 157, 3–13.
- Castino, F., Bookhagen, B., Strecker, M.R., 2016. Rainfall variability and trends of the past six decades (1950–2014) in the subtropical NW Argentine Andes. *Clim. Dyn.* 48, 1049–1067.
- Cencetti, C., Rivelli, F.R., 2011. Landslides dams induced by debris flows in Quebrada Del Toro (Province of Salta, Argentina). In *5th International Conference on Debris-Flow Hazards Mitigation: Mechanics, Prediction and Assessment*, pp. 645–650.
- Chen, H., Dadson, S., Chi, Y.-G., 2006. Recent rainfall-induced landslides and debris flow in northern Taiwan. *Geomorphology* 77, 112–125.
- Chepstow-Lusty, A., Bush, M.B., Frogley, M.R., Baker, P.A., Fritz, S.C., Aronson, J., 2005. Vegetation and climate change on the Bolivian Altiplano between 108,000 and 18,000 yr ago. *Quat. Res.* 63, 90–98.
- Chmeleff, J., von Blanckenburg, F., Kossert, K., Jakob, D., 2010. Determination of the ^{10}Be half-life by multicollector ICP-MS and liquid scintillation counting. *Nucl. Instruments Methods Phys. Res. Sect. B Beam Interact. with Mater. Atoms* 268, 192–199.
- Church, M., 2006. Bed Material Transport and the Morphology of Alluvial River Channels. *Annu. Rev. Earth Planet. Sci.* 34, 325–354.
- Church, M., 1995. Geomorphic response to river flow regulation: Case studies and time-scales. *River Res. Appl.* 11, 3–22.
- Clapp, E.M., Bierman, P.R., Caffee, M., 2002. Using ^{10}Be and ^{26}Al to determine sediment generation rates and identify sediment source areas in an arid region drainage basin. *Geomorphology* 45, 89–104.

Bibliography

- Codilean, A.T., Fenton, C.R., Fabel, D., Bishop, P., Xu, S., 2014. Discordance between cosmogenic nuclide concentrations in amalgamated sands and individual fluvial pebbles in an arid zone catchment. *Quat. Geochronol.* 19, 173–180.
- Codilean, A.T., Munack, H., Cohen, T.J., Saktura, W.M., Gray, A., Mudd, S.M., 2018. OCTOPUS: An Open Cosmogenic Isotope and Luminescence Database. *Earth Syst. Sci. Data Discuss* 1–23.
- Collister, J.W., Rieley, G., Stern, B., Eglinton, G., Fry, B., 1994. Compound-specific $\delta^{13}\text{C}$ analyses of leaf lipids from plants with differing carbon dioxide metabolisms. *Org. Geochem.* 21, 619–627.
- Cottle, J.M., 2014. In-situ U-Th/Pb geochronology of (urano)thorite. *Am. Mineral.* 99, 1985–1995.
- Cottle, J.M., Burrows, A.J., Kylander-Clark, A., Freedman, P. a., Cohen, R.S., 2013. Enhanced sensitivity in laser ablation multi-collector inductively coupled plasma mass spectrometry. *J. Anal. At. Spectrom.* 28, 1700.
- Coulthard, T.J., Van de Wiel, M.J., 2017. Modelling long term basin scale sediment connectivity, driven by spatial land use changes. *Geomorphology* 277, 265–281.
- Coulthard, T.J., Van de Wiel, M.J., 2013. Climate, tectonics or morphology: what signals can we see in drainage basin sediment yields? *Earth Surf. Dyn.* 1, 13–27.
- Coulthard, T.J., Wiel, M.J. Van De, 2007. Quantifying fluvial non linearity and finding self-organized criticality? Insights from simulations of river basin evolution 91, 216–235.
- Coulthard, T.J.T., Lewin, J., Macklin, M.G., 2005. Modelling differential catchment response to environmental change. *Geomorphology* 69, 222–241.
- Crowley, J.L., Schoene, B., Bowring, S.A., 2007. U-Pb dating of zircon in the Bishop Tuff at the millennial scale. *Geology* 35, 1123–1126.
- Cruz, F.W., Burns, S.J., Karmann, I., Sharp, W.D., Vuille, M., Cardoso, A.O., Ferrari, J.A., Dias, P.L.S., Viana Jr, O., 2005. Insolation-driven changes in atmospheric circulation over the past 116,000 years in subtropical Brazil. *Nature* 434, 63.
- Curtis, K.E., Renshaw, C.E., Magilligan, F.J., Dade, W.B., 2010. Temporal and spatial scales of geomorphic adjustments to reduced competency following flow regulation in bedload-dominated systems. *Geomorphology* 118, 105–117.
- Cyr, A.J., Granger, D.E., Olivetti, V., Molin, P., 2010. Quantifying rock uplift rates using channel steepness and cosmogenic nuclide-determined erosion rates: Examples from northern and southern Italy. *Lithosphere* 2, 188–198.
- D’Arcy, M., Whittaker, A.C., Roda-Boluda, D.C., 2016. Measuring alluvial fan sensitivity to past climate changes using a self-similarity approach to grain-size fining, Death Valley, California. *Sedimentology* 64.2, 388–424.
- D’Arcy, M.K., Schildgen, T.F., Tofelde, S., Strecker, M.R., Wittmann, H., Duesing, W., Weissmann, P., Roda-Boluda, D.C., 2017. Sensitivity of Catchment-Alluvial Fan Systems to Millennial-Scale Climate Change in the Southern Central Andes (27°S), in: AGU Fall Meeting Abstracts. p. EP32A-06.
- Dade, W.B., Renshaw, C.E., Magilligan, F.J., 2011. Sediment transport constraints on river response to regulation. *Geomorphology* 126, 245–251.
- Dansgaard, W., 1964. Stable isotopes in precipitation. *Tellus* 16, 436–468.
- Datta, D.K., Gupta, L.P., Subramanian, V., 1999. Distribution of C, N and P in the sediments of the Ganges–Brahmaputra–Meghna river system in the Bengal basin. *Org. Geochem.* 30, 75–82.

Bibliography

- Davis, W.M., 1899. The geographical cycle. *Geogr. J.* 14, 481–504.
- Delunel, R., van der Beek, P.A., Bourlès, D.L., Carcaillet, J., Schlunegger, F., 2014. Transient sediment supply in a high-altitude Alpine environment evidenced through a ^{10}Be budget of the Etages catchment (French Western Alps). *Earth Surf. Process. Landforms* 39, 890–899.
- Desilets, D., Zreda, M., Prabu, T., 2006. Extended scaling factors for in situ cosmogenic nuclides: new measurements at low latitude. *Earth Planet. Sci. Lett.* 246, 265–276.
- Dey, S., Thiede, R.C., Schildgen, T.F., Wittmann, H., Bookhagen, B., Scherler, D., Jain, V., Strecker, M.R., 2016. Climate-driven sediment aggradation and incision since the late Pleistocene in the NW Himalaya, India. *Earth Planet. Sci. Lett.* 449, 321–331.
- DiBiase, R.A., Whipple, K.X., 2011. The influence of erosion thresholds and runoff variability on the relationships among topography, climate, and erosion rate. *J. Geophys. Res. Earth Surf.* 116, 1–17.
- DiBiase, R.A., Whipple, K.X., Heimsath, A.M., Ouimet, W.B., 2010. Landscape form and millennial erosion rates in the San Gabriel Mountains, CA. *Earth Planet. Sci. Lett.* 289, 134–144.
- Didan, K., 2009. MOD13A1. 6. NASA EOSDIS Land Processes DAAC [WWW Document]. USGS Earth Resour. Obs. Sci. Center, Sioux Falls, South Dakota.
- Dingle, E.H., Attal, M., Sinclair, H.D., 2017. Abrasion-set limits on Himalayan gravel flux. *Nature* 544, 471–474.
- Dingle, E.H., Sinclair, H.D., Attal, M., Rodés, Á., Singh, V., 2018. Temporal variability in detrital ^{10}Be concentrations in large Himalayan catchments. *Earth Surf. Dyn. Diss.*
- Dixon, J.L., Heimsath, A.M., Kaste, J., Amundson, R., 2009. Climate-driven processes of hillslope weathering. *Geology* 37, 975–978.
- Duller, R.A., Whittaker, A.C., Fedele, J.J., Whitchurch, A.L., Springett, J., Smithells, R., Fordyce, S., Allen, P.A., 2010. From grain size to tectonics. *J. Geophys. Res. Earth Surf.* 115(F3).
- Dunai, T., 2010. *Cosmogenic Nuclides: Principles, Concepts and Applications in the Earth Surface Sciences*, Annals of Physics.
- Dunai, T.J., 2001. Influence of secular variation of the geomagnetic field on production rates of in-situ produced cosmogenic nuclides. *Earth Planet. Sci. Lett.* 193, 197–212.
- Dunai, T.J., 2000. Scaling factors for production rates of in situ produced cosmogenic nuclides: a critical reevaluation. *Earth Planet. Sci. Lett.* 176, 157–169.
- Eglinton, G., Hamilton, R.J., 1967. Leaf epicuticular waxes. *Science* 156, 1322–1335.
- Eglinton, T.I., Eglinton, G., 2008. Molecular proxies for paleoclimatology. *Earth Planet. Sci. Lett.* 275, 1–16.
- Einsele, G., Ratschbacher, L., Wetzel, A., 1996. The Himalaya-Bengal Fan denudation-accumulation system during the past 20 Ma. *J. Geol.* 104, 163–184.
- Erkens, G., Dambeck, R., Volleberg, K.P., Bouman, M.T.I.J., Bos, J. a a, Cohen, K.M., Wallinga, J., Hoek, W.Z., 2009. Fluvial terrace formation in the northern Upper Rhine Graben during the last 20,000 years as a result of allogenic controls and autogenic evolution. *Geomorphology* 103, 476–495.
- Farabaugh, R.L., Rigsby, C.A., 2005. Climatic influence on sedimentology and geomorphology of the Rio Ramis valley, Peru. *J. Sediment. Res.* 75, 12–28.
- Faulkner, D.J., Larson, P.H., Jol, H.M., Running, G.L., Loope, H.M., Goble, R.J., 2016. Autogenic incision and terrace formation resulting from abrupt late-glacial base-level fall, lower Chippewa River, Wisconsin, USA. *Geomorphology* 266, 75–95.

Bibliography

- Ferguson, R., Hoey, T., Wathen, S., Werritty, A., 1996. Field evidence for rapid downstream fining of river gravels through selective transport. *Geology* 24, 179–182.
- Fisher, G.B., Amidon, W.H., Burbank, D.W., Luna, L. V., 2016. Late Miocene to Early Pleistocene paleo-erosion rates and provenance change in the NE Argentinian Andes: apparent coupling of sediment fluxes with 400-kyr eccentricity cycles. *EGU Gen. Assem. Conf. Abstr.* 18, 5310.
- Fisk, N.H., 1944. Geological Investigation of the Alluvial Valley of the Lower Mississippi River. Mississippi River Com. Vicksbg.
- Fornace, K.L., Whitney, B.S., Galy, V., Hughen, K.A., Mayle, F.E., 2016. Late Quaternary environmental change in the interior South American tropics: new insight from leaf wax stable isotopes. *Earth Planet. Sci. Lett.* 438, 75–85.
- France-Lanord, C., Derry, L.A., 1997. Organic carbon burial forcing of the carbon cycle from Himalayan erosion. *Nature* 390, 65–67.
- Frankel, K.L., Pazzaglia, F.J., Vaughn, J.D., 2007. Knickpoint evolution in a vertically bedded substrate, upstream-dipping terraces, and Atlantic slope bedrock channels. *GSA Bull.* 119, 476–486.
- Fritz, S.C., Baker, P.A., Ekdahl, E., Seltzer, G.O., Stevens, L.R., 2010. Millennial-scale climate variability during the Last Glacial period in the tropical Andes. *Quat. Sci. Rev.* 29, 1017–1024.
- Fritz, S.C., Baker, P.A., Lowenstein, T.K., Seltzer, G.O., Rigsby, C.A., Dwyer, G.S., Tapia, P.M., Arnold, K.K., Ku, T.-L., Luo, S., 2004. Hydrologic variation during the last 170,000 years in the southern hemisphere tropics of South America. *Quat. Res.* 61, 95–104.
- Fritz, S.C., Baker, P.A., Seltzer, G.O., Ballantyne, A., Tapia, P., Cheng, H., Edwards, R.L., 2007. Quaternary glaciation and hydrologic variation in the South American tropics as reconstructed from the Lake Titicaca drilling project. *Quat. Res.* 68, 410–420.
- Fryirs, K.A., 2017. River sensitivity: a lost foundation concept in fluvial geomorphology. *Earth Surf. Process. Landforms* 42, 55–70.
- Fuller, I.C., Macklin, M.G., Lewin, J., Passmore, D.G., Wintle, A.G., 1998. River response to high-frequency climate oscillations in southern Europe over the past 200 k.y. *Geology* 26, 275–278.
- Galy, V., France-Lanord, C., Lartiges, B., 2008. Loading and fate of particulate organic carbon from the Himalaya to the Ganga-Brahmaputra delta. *Geochim. Cosmochim. Acta* 72, 1767–1787.
- García, V.H., Hongn, F., Cristallini, E.O., 2013. Late Miocene to recent morphotectonic evolution and potential seismic hazard of the northern Lerma valley: Clues from Lomas de Medeiros, Cordillera Oriental, NW Argentina. *Tectonophysics* 608, 1238–1253.
- Garcin, Y., Schildgen, T.F., Torres Acosta, V., Melnick, D., Guillemoteau, J., Willenbring, J., Strecker, M.R., 2017. Short-lived increase in erosion during the African Humid Period: Evidence from the northern Kenya Rift. *Earth Planet. Sci. Lett.* 459, 58–69.
- Garcin, Y., Schwab, V.F., Gleixner, G., Kahmen, A., Todou, G., Séné, O., Onana, J.-M., Achoundong, G., Sachse, D., 2012. Hydrogen isotope ratios of lacustrine sedimentary *n*-alkanes as proxies of tropical African hydrology: Insights from a calibration transect across Cameroon. *Geochim. Cosmochim. Acta* 79, 106–126.
- Gardner, T.W., 1983. Experimental study of knickpoint and longitudinal profile evolution in cohesive, homogeneous material. *Geol. Soc. Am. Bull.* 94, 664–572.
- Garreaud, R., Vuille, M., Clement, A.C., 2003. The climate of the Altiplano: observed current conditions and mechanisms of past changes. *Palaeogeogr. Palaeoclimatol. Palaeoecol.* 194, 5–22.

Bibliography

- Gat, J.R., 1996. Oxygen and hydrogen isotopes in the hydrologic cycle. *Annu. Rev. Earth Planet. Sci.* 24, 225–262.
- Gilbert, G.K., 1877. Report on the Geology of the Henry Mountains. US Gov. Print. Off.
- Godard, V., Tucker, G.E., Burch Fisher, G., Burbank, D.W., Bookhagen, B., 2013. Frequency-dependent landscape response to climatic forcing. *Geophys. Res. Lett.* 40, 859–863.
- Godfrey, L. V., Jordan, T.E., Lowenstein, T.K., Alonso, R.L., 2003. Stable isotope constraints on the transport of water to the Andes between 22° and 26° S during the last glacial cycle. *Palaeogeogr. Palaeoclimatol. Palaeoecol.* 194, 299–317.
- Gonzalez, M.A., 2001. Recent formation of arroyos in the Little Missouri Badlands of southwestern North Dakota. *Geomorphology* 38, 63–84.
- Gosling, W.D., Bush, M.B., Hanselman, J.A., Chepstow-Lusty, A., 2008. Glacial-interglacial changes in moisture balance and the impact on vegetation in the southern hemisphere tropical Andes (Bolivia/Peru). *Palaeogeogr. Palaeoclimatol. Palaeoecol.* 259, 35–50.
- Gosse, J.C., Phillips, F.M., 2001. Terrestrial in situ cosmogenic nuclides: theory and application. *Quat. Sci. Rev.* 20, 1475–1560.
- Granger, D.E., Kirchner, J.W., Finkel, R., 1996. Spatially averaged long-term erosion rates measured from in situ-produced cosmogenic nuclides in alluvial sediment. *J. Geol.* 104, 249–257.
- Granger, D.E., Muzikar, P.F., 2001. Dating sediment burial with in situ-produced cosmogenic nuclides: Theory, techniques, and limitations. *Earth Planet. Sci. Lett.* 188, 269–281.
- Grimaud, J.-L., Paola, C., Voller, V., 2015. Experimental migration of knickpoints: influence of style of base-level fall and bed lithology. *Earth Surf. Dyn. Discuss.* 3, 773–805.
- Guerit, L., Barrier, L., Liu, Y., Narteau, C., Lajeunesse, E., Gayer, E., Métivier, F., 2018. Uniform grain-size distribution in the active layer of a shallow, gravel-bedded, braided river (the Urumqi River, China) and implications for paleo-hydrology. *Earth Surf. Dyn.* 6, 1011–1021.
- Hack, J.T., 1973. Stream-profile analysis and stream gradient index. *J. Res. U.S. Geol. Surv.* 1, 421–429.
- Hain, M.P., Strecker, M.R., Bookhagen, B., Alonso, R.N., Pingel, H., Schmitt, a. K., 2011. Neogene to Quaternary broken foreland formation and sedimentation dynamics in the Andes of NW Argentina (25°S). *Tectonics* 30.2.
- Hancock, G.S., Anderson, R.S., 2002. Numerical modeling of fluvial strath-terrace formation in response to oscillating climate. *Geol. Soc. Am. Bull.* 114, 1131–1142.
- Hanson, P.R., Mason, J.A., Goble, R.J., 2006. Fluvial terrace formation along Wyoming's Laramie Range as a response to increased late Pleistocene flood magnitudes. *Geomorphology* 76, 12–25.
- Haselton, K., Hilley, G., Strecker, M.R., 2002. Average Pleistocene Climatic Patterns in the Southern Central Andes: Controls on Mountain Glaciation and Paleoclimate Implications. *J. Geol.* 110, 211–226.
- Heimsath, A.M., Chappell, J., Fifield, K., 2010. Eroding Australia: rates and processes from Bega Valley to Arnhem Land. *Geol. Soc. London, Spec. Publ.* 346, 225–241.
- Heller, P.L., Paola, C., 1992. The large-scale dynamics of grain-size variation in alluvial basins, 2: Application to syntectonic conglomerate. *Basin Res.* 4, 91–102.
- Hermanns, R.L., Niedermann, S., Ivy-Ochs, S., Kubik, P.W., 2004. Rock avalanching into a landslide-dammed lake causing multiple dam failure in las conchas valley (NW argentina) - Evidence from surface exposure dating and stratigraphic analyses. *Landslides* 1, 113–122.

Bibliography

- Hermanns, R.L., Trauth, M.H., Niedermann, S., McWilliams, M., Strecker, M.R., The, S., January, N., Hermanns, R.L., Trauth, M.H., Niedermann, S., McWilliams, M., Strecker, M.R., 2000. Tephrochronologic constraints on temporal distribution of large landslides in northwest Argentina. *J. Geol.* 108, 35–52.
- Hewawasam, T., von Blanckenburg, F., Schaller, M., Kubik, P., 2003. Increase of human over natural erosion rates in tropical highlands constrained by cosmogenic nuclides. *Geology* 31, 597–600.
- Hidy, A.J., Gosse, J.C., Pederson, J.L., Mattern, J.P., Finkel, R.C., 2010. A geologically constrained Monte Carlo approach to modeling exposure ages from profiles of cosmogenic nuclides: An example from Lees Ferry, Arizona. *Geochemistry, Geophys. Geosystems* 11.
- Hilley, G.E., Strecker, M.R., 2005. Processes of oscillatory basin filling and excavation in a tectonically active orogen: Quebrada del Toro Basin, NW Argentina. *Bull. Geol. Soc. Am.* 117, 887–901.
- Hinderer, M., Einsele, G., 2001. The world's large lake basins as denudation-accumulation systems and implications for their lifetimes. *J. Paleolimnol.* 26, 355–372.
- Hippe, K., Gordijn, T., Picotti, V., Hajdas, I., Jansen, J.D., Christl, M., Vockenhuber, C., Maden, C., Akcar, N., Ivy-Ochs, S., 2018. Fluvial dynamics and ^{14}C - ^{10}Be disequilibrium on the Bolivian Altiplano. *Earth Surf. Process. Landforms*.
- Hippe, K., Kober, F., Zeilinger, G., Ivy-ochs, S., Maden, C., Wacker, L., Kubik, P.W., Wieler, R., 2012. Quantifying denudation rates and sediment storage on the eastern Altiplano, Bolivia, using cosmogenic ^{10}Be , ^{26}Al , and in situ ^{14}C . *Geomorphology* 179, 58–70.
- Hoey, T.B., Ferguson, R., 1994. Numerical simulation of downstream fining by selective transport in gravel-bed rivers: Model development and illustration. *Water Resour. Res.* 30, 2251–2260.
- Hoffmann, T., 2015. Sediment residence time and connectivity in non-equilibrium and transient geomorphic systems. *Earth-Science Rev.* 150, 609–627.
- Hovius, N., Meunier, P., Lin, C.-W., Chen, H., Chen, Y.-G., Dadson, S., Horng, M.-J., Lines, M., 2011. Prolonged seismically induced erosion and the mass balance of a large earthquake. *Earth Planet. Sci. Lett.* 304, 347–355.
- Hovius, N., Stark, C.P., Hao-Tsu, C., Jiun-Chuan, L., 2000. Supply and Removal of Sediment in a Landslide-Dominated Mountain Belt: Central Range, Taiwan. *J. Geol.* 108, 73–89.
- Howard, A.D., 1982. Equilibrium and time scales in geomorphology: Application to sand-bed alluvial streams. *Earth Surf. Process. Landforms* 7, 303–325.
- Howard, A.D., Dietrich, W.E., Seidl, M.A., 1994. Modeling fluvial erosion on regional to continental scales. *J. Geophys. Res. Solid Earth* 99, 13971–13986.
- Hu, X., Pan, B., Fan, Y., Wang, J., Hu, Z., Cao, B., Li, Q., Geng, H., 2017. Folded fluvial terraces in a young, actively deforming intramontane basin between the Yumu Shan and the Qilian Shan mountains, NE Tibet. *Lithosphere* 9, 545–560.
- Huang, W.L., Yang, X.P., Li, A., Thompson, J. A., Zhang, L., 2014. Climatically controlled formation of river terraces in a tectonically active region along the southern piedmont of the Tian Shan, NW China. *Geomorphology* 220, 15–29.
- Huete, A., Didan, K., Miura, T., Rodriguez, E.P., Gao, X., Ferreira, L.G., 2002. Overview of the radiometric and biophysical performance of the MODIS vegetation indices. *Remote Sens. Environ.* 83, 195–213.
- Huntington, E., 1907. Some characteristics of the glacial period in non-glaciated region. *Bull. Geol. Soc. Am.* 18, 351–388.

Bibliography

- Iverson, R.M., 2000. Landslide triggering by rain infiltration. *Water Resour. Res.* 36, 1897–1910.
- Jackson, J.A., Austrheim, H., McKenzie, D., Priestley, K., 2004. Metastability, mechanical strength, and the support of mountain belts. *Geology* 32, 625–628.
- Jerolmack, D.J., Paola, C., 2010. Shredding of environmental signals by sediment transport. *Geophys. Res. Lett.* 37.
- Kanner, L.C., Burns, S.J., Cheng, H., Edwards, R.L., 2012. High-Latitude Forcing of the South American Summer Monsoon During the Last Glacial. *Science*, 1213397.
- Kanner, L.C., Burns, S.J., Cheng, H., Edwards, R.L., Vuille, M., 2013. High-resolution variability of the South American summer monsoon over the last seven millennia: Insights from a speleothem record from the central Peruvian Andes. *Quat. Sci. Rev.* 75, 1–10.
- Keefer, D.K., 1994. The importance of earthquake-induced landslides to long-term slope erosion and slope-failure hazards in seismically active regions, in: *Geomorphology and Natural Hazards*. Elsevier, pp. 265–284.
- Kirby, E., Whipple, K., 2001. Quantifying differential rock-uplift rates via stream profile analysis. *Geology* 29, 415–418.
- Kirchner, J.W., Finkel, R.C., Riebe, C.S., Granger, D.E., Clayton, J.L., King, J.G., Megahan, W.F., 2001. Mountain erosion over 10 yr, 10 ky, and 10 my time scales. *Geology* 29, 591–594.
- Kober, F., Hippe, K., Salcher, B., Ivy-Ochs, S., Kubik, P.W., Wacker, L., Hählen, N., 2012. Debris-flow-dependent variation of cosmogenically derived catchment-wide denudation rates. *Geology* 40, 935–938.
- Kodama, Y., 1994. Experimental study of abrasion and its role in producing downstream fining in gravel-bed rivers. *J. Sediment. Res.* 64, 76–85.
- Koppes, M.N., Montgomery, D.R., 2009. The relative efficacy of fluvial and glacial erosion over modern to orogenic timescales. *Nat. Geosci.* 2, 644–647.
- Korschinek, G., Bergmaier, A., Faestermann, T., Gerstmann, U.C., Knie, K., Rugel, G., Wallner, A., Dillmann, I., Dollinger, G., von Gostomski, C.L., Kossert, K., Maiti, M., Poutivtsev, M., Remmert, A., 2010. A new value for the half-life of ^{10}Be by heavy-ion elastic recoil detection and liquid scintillation counting. *Nucl. Instruments Methods Phys. Res. Sect. B Beam Interact. with Mater. Atoms* 268, 187–191.
- Kuehl, S.A., DeMaster, D.J., Nittrouer, C.A., 1986. Nature of sediment accumulation on the Amazon continental shelf. *Cont. Shelf Res.* 6, 209–225.
- Kuenen, P.H., 1956. Experimental Abrasion of Pebbles: 2. Rolling by Current. *J. Geol.* 64, 336–368.
- Kull, C., Imhof, S., Grosjean, M., Zech, R., Veit, H., 2008. Late Pleistocene glaciation in the Central Andes: Temperature versus humidity control — A case study from the eastern Bolivian Andes (17° S) and regional synthesis. *Global and Planetary Change*, 60, 148–164.
- Lague, D., Hovius, N., Davy, P., 2005. Discharge, discharge variability, and the bedrock channel profile. *J. Geophys. Res. Earth Surf.* 110 (F4).
- Lal, D., 1991. Cosmic ray labeling of erosion surfaces: in situ nuclide production rates and erosion models. *Earth Planet. Sci. Lett.* 104, 424–439.
- Lane, E.W., 1955. Importance of fluvial morphology in hydraulic engineering. *Proc. American Soc. Civ. Eng.* 81.

Bibliography

- Langbein, W.B., Schumm, S.A., 1958. Yield of Sediment in Relation to Mean Annual Precipitation. *Trans. Am. Geophys. Union* 39, 1076–1084.
- Larsen, I.J., Montgomery, D.R., 2012. Landslide erosion coupled to tectonics and river incision. *Nat. Geosci.* 5, 468–473.
- Lavé, J., Avouac, J.-P., 2000. Active folding of fluvial terraces across the Siwaliks Hills, Himalayas of central Nepal. *J. Geophys. Res.* 105, 5735–5770.
- Leopold, B.L.B., Miller, J.P., 1954. A postglacial chronology for some alluvial valleys in Wyoming. Washington, DC: US Government Printing Office.
- Leopold, L.B., Bull, W.B., 1979. Base level, aggradation, and grade. *Proc. Am. Philos. Soc.* 123, 168–202.
- Lewis, W. V., 1944. Stream Trough Experiments and Terrace Formation. *Geol. Mag.* 81, 241–253.
- Lifton, N.A., Bieber, J.W., Clem, J.M., Duldig, M.L., Evenson, P., Humble, J.E., Pyle, R., 2005. Addressing solar modulation and long-term uncertainties in scaling secondary cosmic rays for in situ cosmogenic nuclide applications. *Earth Planet. Sci. Lett.* 239, 140–161.
- Lifton, N., Sato, T., Dunai, T.J., 2014. Scaling in situ cosmogenic nuclide production rates using analytical approximations to atmospheric cosmic-ray fluxes. *Earth Planet. Sci. Lett.* 386, 149–160.
- Limaye, A.B.S., Lamb, M.P., 2016. Numerical model predictions of autogenic fluvial terraces and comparison to climate change expectations. *J. Geophys. Res. F Earth Surf.* 121, 512–544.
- Lisiecki, L.E., Raymo, M.E., 2009. Diachronous benthic $\delta^{18}\text{O}$ responses during late Pleistocene terminations. *Paleoceanography* 24.
- Litchfield, N., Berryman, K., 2006. Relations between postglacial fluvial incision rates and uplift rates in the North Island, New Zealand. *J. Geophys. Res.* 111 (F2).
- Litty, C., Duller, R., Schlunegger, F., 2016. Paleohydraulic reconstruction of a 40 ka-old terrace sequence implies that water discharge was larger than today. *Earth Surf. Process. Landforms* 41, 884–898.
- Litty, C., Schlunegger, F., Viveen, W., 2017. Possible threshold controls on sediment grain properties of Peruvian coastal river basins. *Earth Surf. Dyn.* 571–583.
- Luna, L. V., Bookhagen, B., Niedermann, S., Rugel, G., Scharf, A., Merchel, S., 2018. Glacial chronology and production rate cross-calibration of five cosmogenic nuclide and mineral systems from the southern Central Andean Plateau. *Earth Planet. Sci. Lett.* 500, 242–253.
- Lupker, M., Blard, P.-H., Lave, J., France-Lanord, C., Leanni, L., Puchol, N., Charreau, J., Bourlès, D., 2012. ^{10}Be -derived Himalayan denudation rates and sediment budgets in the Ganga basin. *Earth Planet. Sci. Lett.* 333, 146–156.
- Lupker, M., Lavé, J., France-Lanord, C., Christl, M., Bourlès, D., Carcaillet, J., Maden, C., Wieler, R., Rahman, M., Bezbaruah, D., Xiaohan, L., 2017. ^{10}Be systematics in the Tsangpo-Brahmaputra catchment: the cosmogenic nuclide legacy of the eastern Himalayan syntaxis. *Earth Surf. Dyn.* 5, 429–449.
- Lyell, C., 1830. *Principles of geology*. Murray, London 3.
- Lynn, D.C., Bonatti, E., 1965. Mobility of manganese in diagenesis of deep-sea sediments. *Mar. Geol.* 3, 457–474.
- Mackin, J.H., 1948. Concept of the graded river. *Bull. Geol. Soc. Am.* 59, 463–512.
- Macklin, M.G., Lewin, J., 2003. River sediments, great floods and centennial-scale Holocene climate change. *J. Quat. Sci.* 18, 101–105.

Bibliography

- Maher, K., Chamberlain, C.P., 2014. Hydrologic regulation of chemical weathering and the geologic carbon cycle. *Science* 343, 1502–1504.
- Malamud, B.D., Jordan, T.E., Alonso, R.A., Gallardo, E.F., González, R.E., Kelley, S.A., 1996. Pleistocene Lake Lerma, Salta Province, NW Argentina. *Present. theXIII Congr. Geológico Argentino* 103–116.
- Malatesta, L., Avouac, J.-P., Brown, N.D., Breitenbach, S.F.M., Pan, J., Chevalier, M.-L., Rhodes, E., Saint-Carlier, D., Zhang, W., Charreau, J., Lavé, J., Blard, P.-H., 2018. Lag and mixing during sediment transfer across the Tian Shan piedmont caused by climate- driven aggradation-incision cycles. *Basin Res.* 30, 613–635.
- Malatesta, L.C., Avouac, J., 2018. Contrasting river incision in north and south Tian Shan piedmonts due to variable glacial imprint in mountain valleys. *Geology* 46, 659–662.
- Malatesta, L.C., Prancevic, J.P., Avouac, J., 2017. Autogenic entrenchment patterns and terraces due to coupling with lateral erosion in incising alluvial channels. *J. Geophys. Res. Earth Surf.* 122, 335–355.
- Marc, O., Hovius, N., Meunier, P., Uchida, T., Hayashi, S., 2015. Transient changes of landslide rates after earthquakes. *Geology* 43, 883–886.
- Marrett, R.A., Allmendinger, R.W., Alonso, R.N., Drake, R.E., 1994. Late Cenozoic tectonic evolution of the Puna Plateau and adjacent foreland, northwestern Argentine Andes. *J. South Am. Earth Sci.* 7, 179–207.
- Marrett, R.A., Strecker, M.R., 2000. Response of intracontinental deformation in the central Andes to late Cenozoic reorganization of South American Plate motions. *Tectonics* 19, 452–467.
- Marshall, J.A., Sklar, L.S., 2012. Mining soil databases for landscape-scale patterns in the abundance and size distribution of hillslope rock fragments. *Earth Surf. Process. Landforms* 37, 287–300.
- Martin, L.C.P., Blard, P.-H., Balco, G., Lavé, J., Delunel, R., Lifton, N., Laurent, V., 2016. The CREp program and the ICE-D production rate calibration database: A fully parameterizable and updated online tool to compute cosmic-ray exposure ages. *Quat. Geochronol.* 38.
- Martin, L.C.P., Blard, P.-H., Lavé, J., Condom, T., Prémaillon, M., Jomelli, V., Brunstein, D., Lupker, M., Charreau, J., Mariotti, V., 2018. Lake Tauca highstand (Heinrich Stadial 1a) driven by a southward shift of the Bolivian High. *Sci. Adv.* 4, eaar2514.
- Martini, M.A., Kaplan, M.R., Strelin, J.A., Astini, R.A., Schaefer, J.M., Caffee, M.W., Schwartz, R., 2017. Late Pleistocene glacial fluctuations in Cordillera Oriental, subtropical Andes. *Quat. Sci. Rev.* 171, 245–259.
- Mason, C.C., Romans, B., Mason, C.C., Romans, B.W., 2018. Climate-driven unsteady denudation and sediment flux in a high-relief unglaciated catchment – fan using ^{26}Al and ^{10}Be : Panamint Valley, California. *Earth Planet. Sci. Lett.* 492, 130–143.
- Matmon, A., Bierman, P.R., Larsen, J., Southworth, S., Pavich, M., Finkel, R., Caffee, M., 2003. Erosion of an ancient mountain range, the Great Smoky Mountains, North Carolina and Tennessee. *Am. J. Sci.* 303, 817–855.
- Matmon, A., Schwartz, D.P., Finkel, R., Clemmens, S., Hanks, T., 2005. Dating offset fans along the Mojave section of the San Andreas Fault using cosmogenic ^{26}Al and ^{10}Be . *GSA Bull.* 117, 795–807.
- McFadden, L.D., Wells, S.G., Jercinovich, M.J., 1987. Influences of eolian and pedogenic processes on the origin and evolution of desert pavements. *Geology* 15, 504–508.

Bibliography

- McPhillips, D., Bierman, P.R., Rood, D.H., 2014. Millennial-scale record of landslides in the Andes consistent with earthquake trigger. *Nat. Geosci.* 7, 925–930.
- Meade, R.H., 1982. Sources, sinks, and storage of river sediment in the Atlantic drainage of the United States. *J. Geol.* 90, 235–252.
- Meade, R.H.R., Dunne, T., Richey, J.E., Santos, U. de M., Salati, E., 1985. Storage and remobilization of suspended sediment in the lower Amazon River of Brazil. *Science* 228, 488–490.
- Menting, F., Langston, A.L., Temme, A.J.A.M., 2015. Downstream fining, selective transport, and hillslope influence on channel bed sediment in mountain streams, Colorado Front Range, USA. *Geomorphology* 239, 91–105.
- Merritts, D.J., Vincent, K.R., Wohl, E.E., 1994. Long-river profiles, tectonism, and eustasy: A guide to interpreting fluvial terraces. *J. Geophys. Res.* 99, 14031–14050.
- Métivier, F., Gaudemer, Y., 1999. Stability of output fluxes of large rivers in South and East Asia during the last 2 million years: implications on floodplain processes. *Basin Res.* 11, 293–303.
- Meunier, P., Hovius, N., Haines, A.J., 2007. Regional patterns of earthquake-triggered landslides and their relation to ground motion. *Geophys. Res. Lett.* 34.
- Mey, J., D’Arcy, M.K., Egholm, D.L., Schildgen, T.F., 2018. Constraints on the Younger Dryas climate from glacial moraines and a landslide-dammed paleolake in the southern Central Andes, NW Argentina, in: Abstract EGU General Assembly. p. 7318.
- Mikuz, T., 2003. Tectonic and climatic controls on mountain-front collapse in Sierra Pasha, Cordillera Oriental; Salta Province; northwest Argentina. unpubl. Diploma thesis, Univ. Vienna 87–97.
- Milankovitch, M.K., 1941. Kanon der Erdbestrahlung und seine Anwendung auf das Eiszeitenproblem. *R. Serbian Acad. Spec. Publ.* 133, 1–633.
- Miller, K.L., Szabó, T., Jerolmack, D.J., Domsos, G., 2014. Quantifying the significance of abrasion and selective transport for downstream fluvial grain size evolution. *J. Geophys. Res. Earth Surf.* 119, 2412–2429.
- Milliman, J.D., Syvitski, J.P.M., 1992. Geomorphic/tectonic control of sediment discharge to the ocean: the importance of small mountainous rivers. *J. Geol.* 100, 525–544.
- Milliman, J.D., Yun-Shan, Q., Mei-e, R., Saito, Y., 1987. Man’s Influence on the Erosion and Transport of Sediment by Asian Rivers: The Yellow River (Huanghe) Example. *J. Geol.* 95, 751–762.
- Mizutani, T., 1998. Laboratory experiment and digital simulation of multiple fill-cut terrace formation. *Geomorphology* 24, 353–361.
- Montgomery, D.R., Brandon, M.T., 2002. Topographic controls on erosion rates in tectonically active mountain ranges. *Earth Planet. Sci. Lett.* 201, 481–489.
- Moon, S., Page Chamberlain, C., Blisniuk, K., Levine, N., Rood, D.H., Hilley, G.E., 2011. Climatic control of denudation in the deglaciated landscape of the Washington Cascades. *Nat. Geosci.* 4, 469–473.
- Mortimer, E., Carrapa, B., Coutand, I., Schoenbohm, L., Sobel, E.R., Sosa Gomez, J., Strecker, M.R., 2007. Fragmentation of a foreland basin in response to out-of-sequence basement uplifts and structural reactivation: El Cajon-Campo del Arenal basin, NW Argentina. *Geol. Soc. Am. Bull.* 119, 637–653.
- Nester, P.L., Gayo, E., Latorre, C., Jordan, T.E., Blanco, N., 2007. Perennial stream discharge in the hyperarid Atacama Desert of northern Chile during the latest Pleistocene. *Proc. Natl. Acad. Sci.* 104, 19724–19729.

Bibliography

- Niemi, N. A., Oskin, M., Burbank, D.W., Heimsath, A.M., Gabet, E.J., 2005. Effects of bedrock landslides on cosmogenically determined erosion rates. *Earth Planet. Sci. Lett.* 237, 480–498.
- Nishiizumi, K., 2004. Preparation of ^{26}Al AMS standards. *Nucl. Instruments Methods Phys. Res. Sect. B Beam Interact. with Mater. Atoms* 223, 388–392.
- Nishiizumi, K., Imamura, M., Caffee, M.W., Southon, J.R., Finkel, R.C., McAninch, J., 2007. Absolute calibration of ^{10}Be AMS standards. *Nucl. Instruments Methods Phys. Res. Sect. B Beam Interact. with Mater. Atoms* 258, 403–413.
- Nishiizumi, K., Kohl, C.P., Winterer, E.L., Klein, J., Middleton, R., 1989. Cosmic ray production rates of ^{10}Be and ^{26}Al in quartz from glacially polished rocks. *J. Geophys. Res.* 94, 907–917.
- Norton, K.P., Molnar, P., Schlunegger, F., 2014. The role of climate-driven chemical weathering on soil production. *Geomorphology* 204, 510–517.
- Norton, K.P., Schlunegger, F., Litty, C., 2015. On the potential for regolith control of fluvial terrace formation in semi-arid escarpments. *Earth Surf. Dyn. Discuss.* 3, 715–738.
- Olen, S.M., Bookhagen, B., Hoffmann, B., Sachse, D., Adhikari, D.P., Strecker, M.R., 2015. Understanding erosion rates in the Himalayan orogen: A case study from the Arun Valley. *J. Geophys. Res. Earth Surf.* 120, 2080–2102.
- Olen, S.M., Bookhagen, B., Strecker, M.R., 2016. Role of climate and vegetation density in modulating denudation rates in the Himalaya. *Earth Planet. Sci. Lett.* 445, 57–67.
- Omarini, R.H., Sureda, R.J., Götze, H.-J., Seilacher, A., Pflüger, F., 1999. Puncoviscana folded belt in northwestern Argentina: testimony of Late Proterozoic Rodinia fragmentation and pre-Gondwana collisional episodes. *Int. J. Earth Sci.* 88, 76–97.
- Oskin, M., Perg, L., Shelef, E., Strane, M., Gurney, E., Singer, B., Zhang, X., 2008. Elevated shear zone loading rate during an earthquake cluster in eastern California. *Geology* 36, 507–510.
- Ouimet, W.B., Whipple, K.X., Granger, D.E., 2009. Beyond threshold hillslopes: Channel adjustment to base-level fall in tectonically active mountain ranges. *Geology* 37, 579–582.
- Paasche, Ø., Strømsøe, J.R., Dahl, S.O., Linge, H., 2006. Weathering characteristics of arctic islands in northern Norway. *Geomorphology* 82, 430–452.
- Palumbo, L., Hetzel, R., Tao, M., Li, X., 2009. Topographic and lithologic control on catchment-wide denudation rates derived from cosmogenic ^{10}Be in two mountain ranges at the margin of NE Tibet. *Geomorphology* 117, 130–142.
- Pan, B., Burbank, D., Wang, Y., Wu, G., Li, J., Guan, Q., 2003. A 900 ky record of strath terrace formation during glacial-interglacial transitions in northwest China. *Geology* 31, 957–960.
- Paola, C., Heller, P.L., Angevine, C.L., 1992a. The large-scale dynamics of grain-size variation in alluvial basins, 1: Theory. *Basin Res.* 4, 73–90.
- Paola, C., Parker, G., Mohrig, D.C., Whipple, K.X., 1999. The influence of transport fluctuations on spatially averaged topography on a sandy, braided fluvial fan. *SEPM* 62.
- Paola, C., Parker, G., Seal, R., Sinha, S.K., Southard, J.B., Wilcock, P.R., 1992b. Downstream Fining by Selective Deposition in a Laboratory Flume. *Science* 258, 1757–1760.
- Parker, G., 1998. Alluvial fans formed by channelized fluvial and sheet flow. I: Theory. *J. Hydraul. Eng.* 985–995.
- Parker, G., 1979. Hydraulic geometry of active gravel rivers. *J. Hydraul. Div.* 105, 1185–1201.

Bibliography

- Parker, G., 1978. Self-formed straight rivers with equilibrium banks and mobile bed. Part 2. The gravel river. *J. Fluid Mech.* 89, 127–146.
- Parker, G., Cui, Y., 1998. The arrested gravel front: Stable gravel-sand transitions in Rivers Part 1: Simplified analytical solution. *J. Hydraul. Res.* 36, 75–100.
- Paton, C., Woodhead, J.D., Hellstrom, J.C., Hergt, J.M., Greig, A., Maas, R., 2010. Improved laser ablation U-Pb zircon geochronology through robust downhole fractionation correction. *Geochemistry, Geophys. Geosystems* 11.
- Patton, P.C., Schumm, S.A., 1981. Ephemeral-Stream Processes: Implications for Studies of Quaternary Valley Fills. *Quat. Res.* 15, 24–43.
- Pazzaglia, F.J., 2013. Fluvial terraces. *Treatise Geomorphol.* 379–412.
- Pederson, J.L., Anders, M.D., Rittenhour, T.M., Sharp, W.D., Gosse, J.C., Karlstrom, K.E., 2006. Using fill terraces to understand incision rates and evolution of the Colorado River in eastern Grand Canyon, Arizona. *J. Geophys. Res.* 111.
- Penck, A., 1884. Über Periodicität der Thalbildung. *Verhandlung der Gesellschaft für Erdkd. zu Berlin* 39–59.
- Penck, A., Brückner, E., 1909. *Die Alpen im Eiszeitalter*. Tauchnitz.
- Peters, G., van Balen, R.T., 2007. Pleistocene tectonics inferred from fluvial terraces of the northern Upper Rhine Graben, Germany. *Tectonophysics* 430, 41–65.
- Pfeiffer, A.M., Finnegan, N.J., Willenbring, J.K., 2017. Sediment supply controls equilibrium channel geometry in gravel rivers. *Proc. Natl. Acad. Sci.* 114, 3346–3351.
- Phillips, C.B., Jerolmack, D.J., 2016. Self-organization of river channels as a critical filter on climate signals. *Science* 352, 694–697.
- Placzek, C., Quade, J., Betancourt, J.L., Jonathan, P., Rech, J. A., Latorre, C., Matmon, A., Holmgren, C., English, N.B., Patchett, P.J., Rech, J. A., Latorre, C., Matmon, A., Holmgren, C., English, N.B., 2009. Climate in the dry Central Andes over geologic, millennial, and interannual timescales 1. *Ann. Missouri Bot. Gard.* 96, 386–397.
- Placzek, C., Quade, J., Patchett, P.J., 2006. Geochronology and stratigraphy of late Pleistocene lake cycles on the southern Bolivian Altiplano: implications for causes of tropical climate change. *Geol. Soc. Am. Bull.* 118, 515–532.
- Placzek, C.J., Quade, J., Patchett, P.J., 2013. A 130ka reconstruction of rainfall on the Bolivian Altiplano. *Earth Planet. Sci. Lett.* 363, 97–108.
- Poage, M.A., Chamberlain, C.P., 2001. Empirical relationships between elevation and the stable isotope composition of precipitation and surface waters: Considerations for studies of paleoelevation change. *Am. J. Sci.* 301, 1–15.
- Poisson, B., Avouac, J.P., 2004. Holocene Hydrological Changes Inferred from Alluvial Stream Entrenchment in North Tian Shan (Northwestern China). *J. Geol.* 112, 231–249.
- Portenga, E.W., Bierman, P.R., 2011. Understanding earth's eroding surface with ¹⁰Be. *GSA Today* 21, 4–10.
- Puchol, N., Lavé, J., Lupker, M., Blard, P., Gallo, F., France-Lanord, C., Team, A., 2014. Grain-size dependent concentration of cosmogenic ¹⁰Be and erosion dynamics in a landslide-dominated Himalayan watershed. *Geomorphology* 224, 55–68.

Bibliography

- Ramirez, E., Hoffmann, G., Taupin, J.-D., Francou, B., Ribstein, P., Caillon, N., Ferron, F.A., Landais, A., Petit, J.R., Pouyaud, B., 2003. A new Andean deep ice core from Nevado Illimani (6350 m), Bolivia. *Earth Planet. Sci. Lett.* 212, 337–350.
- Reinhardt, L.J., Hoey, T.B., Barrows, T.T., Dempster, T.J., Bishop, P., Fifield, L.K., 2007. Interpreting erosion rates from cosmogenic radionuclide concentrations measured in rapidly eroding terrain. *Earth Surf. Process. Landforms* 32, 390–406.
- Reyes, F.C., Salfity, J.A., 1973. Stratigraphy considerations about the Cretaceous (Pirgua Subgroup) in Northwestern Argentina. *Quinto Congr. Geológico Argentino* 3.
- Riebe, C.S., Granger, D.E., 2013. Quantifying effects of deep and near-surface chemical erosion on cosmogenic nuclides in soils, saprolite, and sediment. *Earth Surf. Process. Landforms* 38, 523–533.
- Riebe, C.S., Kirchner, J.W., Finkel, R.C., 2004. Erosional and climatic effects on long-term chemical weathering rates in granitic landscapes spanning diverse climate regimes. *Earth Planet. Sci. Lett.* 224, 547–562.
- Riebe, C.S., Sklar, L.S., Lukens, C.E., Shuster, D.L., 2015. Climate and topography control the size and flux of sediment produced on steep mountain slopes. *Proc. Natl. Acad. Sci.* 112, 15574–15579.
- Rieley, G., Collier, R.J., Jones, D.M., Eglinton, G., Eakin, P.A., Fallick, A.E., 1991. Sources of sedimentary lipids deduced from stable carbon-isotope analyses of individual compounds. *Lett. to Nat.* 352, 425–427.
- Robinson, R.A.J., Spencer, J.Q.G., Strecker, M.R., Richter, A., Alonso, R.N., 2005. Luminescence dating of alluvial fans in intramontane basins of NW Argentina. *Geol. Soc. London, Spec. Publ.* 251, 153–168.
- Roda-Boluda, D.C., D’Arcy, M., McDonald, J., Whittaker, A.C., 2018. Lithological controls on hillslope sediment supply: insights from landslide activity and grain size distributions. *Earth Surf. Process. Landforms* 43, 956–977.
- Roe, G.H., Whipple, K.X., Fletcher, J.K., 2008. Feedbacks among climate, erosion, and tectonics in a critical wedge orogen. *Am. J. Sci.* 308, 815–842.
- Romans, B.W., Castelltort, S., Covault, J. a., Fildani, A., Walsh, J.P., 2016. Environmental signal propagation in sedimentary systems across timescales. *Earth-Science Rev.* 153, 7–29.
- Ruxton, B.P., Beery, L., 1957. Weathering of granite and associated erosional features in Hong Kong. *Geol. Soc. Am. Bull.* 68, 1263–1292.
- Sachse, D., Billault, I., Bowen, G.J., Chikaraishi, Y., Dawson, T.E., Feakins, S.J., Freeman, K.H., Magill, C.R., McInerney, F. a., van der Meer, M.T.J.J., Polissar, P., Robins, R.J., Sachs, J.P., Schmidt, H.-L., Sessions, A.L., White, J.W.C., West, J.B., Kahmen, A., 2012. Molecular paleohydrology: interpreting the hydrogen-isotopic composition of lipid biomarkers from photosynthesizing organisms. *Annu. Rev. Earth Planet. Sci.* 40, 221–249.
- Sancho, C., Luis, J., Rivelli, F., Rhodes, E., Muñoz, A., 2008. Geomorphological evolution of the Tilcara alluvial fan (Jujuy Province, NW Argentina): Tectonic implications and paleo-environmental considerations. *J. South Am. Earth Sci.* 26, 68–77.
- Savi, S., Delunel, R., Schlunegger, F., 2015. Efficiency of frost-cracking processes through space and time: An example from the eastern Italian Alps. *Geomorphology* 232, 248–260.
- Savi, S., Norton, K.P., Picotti, V., Akçar, N., Delunel, R., Brardinoni, F., Kubik, P., Schlunegger, F., 2014. Quantifying sediment supply at the end of the last glaciation: Dynamic reconstruction of an alpine debris-flow fan. *GSA Bull.* 126, 773–790.

Bibliography

- Savi, S., Schildgen, T.F., Tofelde, S., Wittmann, H., Scherler, D., Mey, J., Alonso, R.N., Strecker, M.R., 2016. Climatic controls on debris-flow activity and sediment aggradation: The Del Medio fan, NW Argentina. *J. Geophys. Res. Earth Surf.* 2424–2445.
- Schaller, M., von Blanckenburg, F., Hovius, N., Veldkamp, A., van den Berg, M.W., Kubik, P.W., 2004. Paleo-erosion rates from cosmogenic ^{10}Be in a 1.3 Ma terrace sequence: Response of the River Meuse to changes in climate and rock uplift. *J. Geol.* 112, 127–144.
- Schaller, M., Von Blanckenburg, F., Veldkamp, A., Tebbens, L.A., Hovius, N., Kubik, P.W., 2002. A 30,000 yr record of erosion rates from cosmogenic ^{10}Be in Middle European river terraces. *Earth Planet. Sci. Lett.* 204, 307–320.
- Scherler, D., Bookhagen, B., Strecker, M.R., 2014. Tectonic control on ^{10}Be -derived erosion rates in the Garhwal Himalaya, India. *J. Geophys. Res. Earth Surf.* 119, 83–105.
- Scherler, D., Bookhagen, B., Wulf, H., Preusser, F., Strecker, M.R., 2015. Increased late Pleistocene erosion rates during fluvial aggradation in the Garhwal Himalaya, northern India. *Earth Planet. Sci. Lett.* 428, 255–266.
- Scherler, D., Lamb, M.P., Rhodes, E.J., Avouac, J.P., 2016. Climate-change versus landslide origin of fill terraces in a rapidly eroding bedrock landscape: San Gabriel River, California. *Bull. Geol. Soc. Am.* 128, 1228–1248.
- Schildgen, T., Dethier, D.P., Bierman, P., Caffee, M., 2002. ^{26}Al and ^{10}Be dating of Late Pleistocene and Holocene fill terraces: A record of fluvial deposition and incision, Colorado Front Range. *Earth Surf. Process. Landforms* 27, 773–787.
- Schildgen, T.F., Robinson, R.A.J., Savi, S., Phillips, W.M., Spencer, J.Q.G., Bookhagen, B., Scherler, D., Tofelde, S., Alonso, R.N., Kubik, P.W., Binnie, S.A., Strecker, M.R., 2016. Landscape response to late Pleistocene climate change in NW Argentina: Sediment flux modulated by basin geometry and connectivity. *J. Geophys. Res. Earth Surf.* 121, 392–414.
- Schumm, S.A., 1979. Geomorphic thresholds: the concept and its applications. *R. Geogr. Soc.* 4, 485–515.
- Schumm, S.A., 1977. *The fluvial system*. Wiley New York.
- Schumm, S.A., 1973. Geomorphic thresholds and complex response of drainage systems. *Fluv. Geomorphol.* 6, 69–85.
- Schumm, S.A., Parker, R.S., 1973. Implication of complex response of drainage systems for Quaternary alluvial stratigraphy. *Nat. Phys. Sci.* 243, 99–100.
- Schwab, K., Schäfer, A., 1976. Sedimentation und Tektonik im mittleren Abschnitt des Rio Toro in der Ostkordillere NW-Argentiniens. *Geol. Rundschau* 65, 175–194.
- Schwanghart, W., Kuhn, N.J., 2010. TopoToolbox: A set of Matlab functions for topographic analysis. *Environ. Model. Softw.* 25, 770–781.
- Schwanghart, W., Scherler, D., 2014. TopoToolbox 2 – MATLAB-based software for topographic analysis and modeling in Earth surface sciences. *Earth Surf. Dyn.* 2, 1–7.
- Shen, Z., Törnqvist, T.E., Autin, W.J., Mateo, Z.R.P., Straub, K.M., Mauz, B., 2012. Rapid and widespread response of the Lower Mississippi River to eustatic forcing during the last glacial-interglacial cycle. *GSA Bull.* 124, 690–704.
- Shields, A., 1936. *Anwendung der Aehnlichkeitsmechanik und der Turbulenzforschung auf die Geschiebebewegung*. PhD Thesis Tech. Univ. Berlin.
- Simpson, G., Castellort, S., 2012. Model shows that rivers transmit high-frequency climate cycles to the sedimentary record. *Geology* 40, 1131–1134.

Bibliography

- Sinha, R., Friend, P.F., 1994. River systems and their sediment flux, Indo-Gangetic plains, Northern Bihar, India. *Sedimentology* 41, 825–845.
- Sklar, L.S., Riebe, C.S., Marshall, J.A., Genetti, J., Leclere, S., Lukens, C.L., Mercus, V., 2017. The problem of predicting the size distribution of sediment supplied by hillslopes to rivers. *Geomorphology* 277, 31–49.
- Slingerland, R.L., Snow, R.S., 1988. Stability analysis of a rejuvenated fluvial system. *Zeitschrift für Geomorphol.* 67, 93–102.
- Smith, F.A., Freeman, K.H., 2006. Influence of physiology and climate on δD of leaf wax *n*-alkanes from C₃ and C₄ grasses. *Geochim. Cosmochim. Acta* 70, 1172–1187.
- Smith, J., Finkel, R.C., Farber, D.L., Rodbell, D.T., Seltzer, G.O., 2005a. Moraine preservation and boulder erosion in the tropical Andes: Interpreting old surface exposure ages in glaciated valleys. *J. Quat. Sci.* 20, 735–758.
- Smith, J., Seltzer, G.O., Farber, D.L., Rodbell, D.T., Finkel, R.C., 2005b. Early local last glacial maximum in the tropical Andes. *Science* 308, 678–681.
- Spencer, J.Q.G., Robinson, R.A.J., 2008. Dating intramontane alluvial deposits from NW Argentina using luminescence techniques: Problems and potential. *Geomorphology* 93, 144–155.
- Steffen, D., Schlunegger, F., Preusser, F., 2010. Late Pleistocene fans and terraces in the Majes valley, southern Peru, and their relation to climatic variations. *Int. J. Earth Sci.* 99, 1975–1989.
- Steffen, D., Schlunegger, F., Preusser, F., 2009. Drainage basin response to climate change in the Pisco valley, Peru. *Geology* 37, 491–494.
- Sternberg, H., 1875. Untersuchungen über Langen- und Querprofil geschiebeführender Flüsse. *Zeitschrift für Bauwes.* 25, 483–506.
- Stone, J.O., 2000. Air pressure and cosmogenic isotope production. *J. Geophys. Res. Solid Earth* 105, 23753–23759.
- Strecker, M.R., Alonso, R., Bookhagen, B., Carrapa, B., Coutand, I., Hain, M.P., Hilley, G.E., Mortimer, E., Schoenbohm, L., Sobel, E.R., 2009. Does the topographic distribution of the central Andean Puna Plateau result from climatic or geodynamic processes? *Geology* 37, 643–646.
- Strecker, M.R., Marrett, R., 1999. Kinematic evolution of fault ramps and its role in development of landslides and lakes in the northwestern Argentine Andes. *Geology* 27, 307–310.
- Suess, E., 1875. Die Entstehung der Alpen.
- Tchilinguirian, P., Pereyra, F.X., 2001. Geomorfología del sector Salinas Grandes-Quebrada de Humahuaca, provincia de Jujuy. *Rev. la Asoc. Geol. Argentina* 56.1, 3–15.
- Tebbens, L.A., Veldkamp, A., Dijke, J.J. Van, Schoorl, J.M., 2000. Modeling longitudinal-profile development in response to Late Quaternary tectonics, climate and sea-level changes: the River Meuse. *Glob. Planet. Change* 165–186.
- Thompson, L.G., Davis, M.E., Mosley-Thompson, E., Sowers, T.A., Henderson, K.A., Zagorodnov, V.S., Lin, P.-N., Mikhalenko, V.N., Campen, R.K., Bolzan, J.F., 1998. A 25,000-year tropical climate history from Bolivian ice cores. *Science* 282, 1858–1864.
- Thompson, L.G., Mosley-Thompson, E., Davis, M.E., Lin, P.-N., Henderson, K.A., Cole-Dai, J., Bolzan, J.F., Liu, K.-B., 1995. Late glacial stage and Holocene tropical ice core records from Huascaran, Peru. *Science* 269, 46–50.

Bibliography

- Tofelde, S., Duesing, W., Schildgen, T.F., Wickert, A.D., Wittmann, H., Alonso, R.N., Strecker, M.R., 2018. Effects of deep-seated versus shallow hillslope processes on cosmogenic ^{10}Be concentrations in fluvial sand and gravel. *Earth Surf. Process. Landforms*.
- Tofelde, S., Schildgen, T.F., Savi, S., Pingel, H., Wickert, A.D., Bookhagen, B., Wittmann, H., Alonso, R.N., Cottle, J., Strecker, M.R., 2017. 100 kyr fluvial cut-and-fill terrace cycles since the Middle Pleistocene in the southern Central Andes, NW Argentina. *Earth Planet. Sci. Lett.* 473, 141–153.
- Torres, G.R., Lupo, L.C., Kulemeyer, J.J., Perez, C.F., 2016. Palynological evidence of the geocological belts dynamics from Eastern Cordillera of NW Argentina (23 S) during the Pre-Last Glacial Maximum. *Andean Geol.* 43, 151–165.
- Torres Acosta, V., Schildgen, T.F., Clarke, B.A., Scherler, D., Bookhagen, B., Wittmann, H., von Blanckenburg, F., Strecker, M.R., 2015. Effect of vegetation cover on millennial-scale landscape denudation rates in East Africa. *Lithosphere* 7, 408–420.
- Trauth, M.H., Alonso, R.A., Haselton, K.R., Hermanns, R.L., Strecker, M.R., 2000. Climate change and mass movements in the NW Argentine Andes. *Earth Planet. Sci. Lett.* 179, 243–256.
- Trauth, M.H., Bookhagen, B., Marwan, N., Strecker, M.R., 2003a. Multiple landslide clusters record Quaternary climate changes in the northwestern Argentine Andes. *Palaeogeogr. Palaeoclimatol. Palaeoecol.* 194, 109–121.
- Trauth, M.H., Strecker, M.R., 1999. Formation of landslide-dammed lakes during a wet period between 40,000 and 25,000 yr B.P. in northwestern Argentina. *Palaeogeogr. Palaeoclimatol. Palaeoecol.* 153, 277–287.
- Trauth, M.H.M., Bookhagen, B., Mueller, A.B., Strecker, M.R., 2003b. Late Pleistocene climate change and erosion in the Santa Maria basin, NW Argentina. *J. Sediment. Res.* 73, 82–90.
- Tucker, G.E., 2004. Drainage basin sensitivity to tectonic and climatic forcing: Implications of a stochastic model for the role of entrainment and erosion thresholds. *Earth Surf. Process. Landforms* 205, 185–205.
- Tucker, G.E., Slingerland, R., 1997. Drainage basin responses to climate change. *Water Resour. Res.* 33, 2031–2047.
- Uppala, S.M., Kallberg, P.W., Simmons, A.J., Andrae, U., Bechtold, V.D., Fiorino, M., Gibson, J.K., Haseler, J., Hernandez, A., Kelly, G.A., Li, X., Onogi, K., Saarinen, S., Sokka, N., Allan, R.P., Andersson, E., Arpe, K., Balmaseda, M.A., Beljaars, A.C.M., Van De Berg, L., Bidlot, J., Bormann, N., Caires, S., Chevallier, F., Dethof, A., Dragosavac, M., Fisher, M., Fuentes, M., Hagemann, S., Holm, E., Hoskins, B.J., Isaksen, I., Janssen, P.A.E.M., Jenne, R., McNally, A.P., Mahfouf, J.F., Morcrette, J.J., Rayner, N.A., Saunders, R.W., Simon, P., Sterl, A., Trenberth, K.E., Untch, A., Vasiljevic, D., Viterbo, P., Woollen, J., 2005. The ERA-40 re-analysis. *Q. J. R. Meteorol. Soc.* 131, 2961–3012.
- van de Wiel, M.J., Coulthard, T.J., 2010. Self-organized criticality in river basins: Challenging sedimentary records of environmental change. *Geology* 38, 87–90.
- van den Berg van Saparoea, A.-P.H., Postma, G., 2008. Control of climate change on the yield of river systems. *Recent Adv. Model. Siliciclastic Shallow-Marine Stratigr. SEPM Spec. Publ.* 90, 15–33.
- Vandenbergh, J., 2003. Climate forcing of fluvial system development: An evolution of ideas. *Quat. Sci. Rev.* 22, 2053–2060.
- Vandenbergh, J., 1995. Timescales, climate and river development. *Quat. Sci. Rev.* 14, 631–638.

Bibliography

- Veldkamp, A., 1992. A 3/D model of quaternary terrace development, simulations of terrace stratigraphy and valley asymmetry: A case study for the Allier terraces (Limagne, France). *Earth Surf. Process. Landforms* 17, 487–500.
- Veldkamp, A., Tebbens, L.A., 2001. Registration of abrupt climate changes within fluvial systems: insights from numerical modelling experiments. *Glob. Planet. Change* 28, 129–144.
- Veldkamp, A., Van Dijke, J.J., 2000. Simulating internal and external controls on fluvial terrace stratigraphy: a qualitative comparison with the Maas record. *Geomorphology* 33, 225–236.
- Veldkamp, A., Vermeulen, S.E.J.W., 1989. River terrace formation, modelling, and 3-d graphical simulation. *Earth Surf. Process. Landforms* 14, 641–654.
- Veldkamp, T., Van Dijke, J.J., 1998. Modelling long-term erosion and sedimentation processes in fluvial systems: a case study for the Allier/ Loire system. *Paleohydrology Environ. Chang.*
- Vera, C., Higgins, W., Amador, J., Ambrizzi, T., Garreaud, R., Gochis, D., Gutzler, D., Lettenmaier, D., Marengo, J., Mechoso, C.R., Nogues-Paegle, J., Silva Dias, P.L., Zhang, C., 2006. Toward a unified view of the American monsoon systems. *J. Clim.* 19, 4977 – 5000.
- Vizy, E.K., Cook, K.H., 2007. Relationship between Amazon and high Andes rainfall. *J. Geophys. Res. Atmos.* 112, 1–14.
- von Blanckenburg, F., 2005. The control mechanisms of erosion and weathering at basin scale from cosmogenic nuclides in river sediment. *Earth Planet. Sci. Lett.* 237, 462–479.
- von Blanckenburg, F., Hewawasam, T., Kubik, P.W., 2004. Cosmogenic nuclide evidence for low weathering and denudation in the wet, tropical highlands of Sri Lanka. *J. Geophys. Res. Earth Surf.* 109.
- Walder, J., Hallet, B., 1985. A theoretical model of the fracture of rock during freezing. *Geol. Soc. Am. Bull.* 96, 336–346.
- Wang, X., Auler, A.S., Edwards, R.L., Cheng, H., Ito, E., Wang, Y., Kong, X., Solheid, M., 2007. Millennial-scale precipitation changes in southern Brazil over the past 90,000 years. *Geophys. Res. Lett.* 34.
- Ward, D.J., Cesta, J.M., Galewsky, J., Sagredo, E., 2015. Late Pleistocene glaciations of the arid subtropical Andes and new results from the. *Quat. Sci. Rev.* 128, 98–116.
- Wegmann, K.W., Pazzaglia, F.J., 2009. Late Quaternary fluvial terraces of the Romagna and Marche Apennines, Italy: Climatic, lithologic, and tectonic controls on terrace genesis in an active orogen. *Quat. Sci. Rev.* 28, 137–165.
- West, A.J., Hetzel, R., Li, G., Jin, Z., Zhang, F., Hilton, R.G., Densmore, A.L., 2014. Dilution of ^{10}Be in detrital quartz by earthquake-induced landslides: Implications for determining denudation rates and potential to provide insights into landslide sediment dynamics. *Earth Planet. Sci. Lett.* 396, 143–153.
- Wetzel, A., 1984. Bioturbation in deep-sea fine-grained sediments: influence of sediment texture, turbidite frequency and rates of environmental change. *Geol. Soc. London, Spec. Publ.* 15, 595–608.
- Whipple, K.X., Tucker, G.E., 1999. Dynamics of the stream-power river incision model: Implications for height limits of mountain ranges, landscape response timescales, and research needs. *J. Geop* 104, 17661–17674.
- Whittaker, A.C., 2012. How do landscapes record tectonics and climate? *Lithosphere* 4, 160–164.
- Whittaker, A.C., Attal, M., Allen, P.A., 2010. Characterizing the origin, nature and fate of sediment exported from catchments perturbed by active tectonics. *Basin Research* 22, 809–828.

Bibliography

- Wickert, A.D., Martin, J.M., Tal, M., Kim, W., Sheets, B., Paola, C., 2013. River channel lateral mobility: Metrics, time scales, and controls. *J. Geophys. Res. Earth Surf.* 118, 396–412.
- Wickert, A.D., Schildgen, T.F., 2018. Long-Profile Evolution of Transport-Limited Gravel-Bed Rivers. *Earth Surf. Dyn.*
- Wiedenbeck, M., Allé, P., Corfu, F., Griffin, W.L., Meier, M., Oberli, F., von Quadt, A., Roddick, J.C., Spiegel, W., 1995. Three natural zircon standards for U-Th-Pb, Lu-Hf, trace element and REE analyses. *Geostand. Newsl.* 19, 1–23.
- Willenbring, J.K., Codilean, A.T., McElroy, B., 2013. Earth is (mostly) flat: Apportionment of the flux of continental sediment over millennial time scales. *Geology* 41, 343–346.
- Wilson, J.T., 1968. Static or Mobile Earth: The Current Scientific Revolution. *Proc. Am. Philos. Soc.* 112, 309–320.
- Wittmann, H., Malusà, M.G., Resentini, A., Garzanti, E., Niedermann, S., 2016. The cosmogenic record of mountain erosion transmitted across a foreland basin: source-to-sink analysis of in situ ^{10}Be , ^{26}Al and ^{21}Ne in sediment of the Po river catchment. *Earth Planet. Sci. Lett.* 452, 258–271.
- Wittmann, H., von Blanckenburg, F., 2009. Cosmogenic nuclide budgeting of floodplain sediment transfer. *Geomorphology* 109, 246–256.
- Wittmann, H., von Blanckenburg, F., Kruesmann, T., Norton, K.P., Kubik, P.W., 2007. Relation between rock uplift and denudation from cosmogenic nuclides in river sediment in the Central Alps of Switzerland. *J. Geophys. Res.* 112, F04010.
- Wittmann, H., von Blanckenburg, F., Maurice, L., Guyot, J.L., Kubik, P.W., 2011. Recycling of Amazon floodplain sediment quantified by cosmogenic ^{26}Al and ^{10}Be . *Geology* 39, 467–470.
- Wobus, C., Whipple, K.X., Kirby, E., Snyder, N., Johnson, J., Spyropoulou, K., Crosby, B., Sheehan, D., 2006. Tectonics from topography: procedures, promise, and pitfalls. *Geol. Soc. Am. Spec. Pap.* 398, 55–74.
- Wohl, E., Ikeda, H., 1997. Experimental simulation of channel incision into a cohesive substrate at varying gradients. *Geology* 25, 295–298.
- Womack, W.R., Schumm, S.A., 1977. Terraces of Douglas Creek, northwestern Colorado: An example of episodic erosion. *Geology* 5, 72–76.
- Yanites, B.J., Tucker, G.E., Anderson, R.S., 2009. Numerical and analytical models of cosmogenic radionuclide dynamics in landslide-dominated drainage basins. *J. Geophys. Res. Earth Surf.* 114.
- Young, W.J., Olley, J.M., Prosser, I.P., Warner, R.F., 2001. Relative changes in sediment supply and sediment transport capacity in a bedrock-controlled river. *Water Resour. Res.* 37, 3307–3320.
- Zech, J., Zech, R., Kubik, P.W., Veit, H., 2009. Glacier and climate reconstruction at Tres Lagunas, NW Argentina, based on ^{10}Be surface exposure dating and lake sediment analyses. *Palaeogeogr. Palaeoclimatol. Palaeoecol.* 284, 180–190.
- Zech, R., May, J., Kull, C., Ilgner, J., Kubik, P.W., Veit, H., 2008. Timing of the late Quaternary glaciation in the Andes from ~ 15 to 40°S. *Journal of Quaternary Science: Published for the Quaternary Research Association* 23, 635–647.
- Zhang, P., Molnar, P., Downs, W.R., 2001. Increased sedimentation rates and grain sizes 2–4 Myr ago due to the influence of climate change on erosion rates. *Nature* 410, 891–897.

Appendix A

Hillslope process inventory

To create the erosion-process inventory, we mapped the four main types of hillslope erosion processes within our study area. The four types include 1) *low-slope gullying*, 2) *scree production*, 3) *steep-slope gullying*, and 4) *deep-seated landsliding*. The areas affected by any of those processes were mapped as a shapefile in Google Earth and later imported in ArcGIS. The total area for each process was calculated (**Table A1**). However, to calculate the areas covered by any of those polygons, the total polygon area is reduced, because the 3D view in which the mapping took place is simplified to a 2D map view. Consequently, steep polygons are reduced more in surface area than are gently-sloping polygons. Therefore, the *steep-slope gully erosion* and *deep-seated landslides*, which often occur on the steeper slopes, are probably underestimated in size compared to *low-slope gullying*, which dominantly occurs on more gentle slopes. However, if we were able to correct for this effect, it would only make our observations of a change in processes with increasing slopes and erosion rates more pronounced.

We most likely overestimate the area covered by diffusion, which we define as the remaining area that is not affected by any of the four previously mentioned processes. The remaining area, however, also includes the river channel system itself, for which we do not correct. Because we focus our analysis on the few percent area covered by those four processes, and not on the diffusive part, a slight decrease in those numbers would not affect our results.

Table A1 Surface area affected by each of the mapped hillslope processes in absolute and relative values.

Sample site	Land-slide (m2)	Steep-slope gully (m2)	Scree (m2)	Low-slope gully (m2)	Diffusion (m2)	Total (m2)	Land-slide (%)	Steep-slope gully (%)	Scree (%)	Low-slope gully (%)	Diffusion (%)
M08	0	1787137	4695915	26044859	2156452732	2188980643	0.00	0.08	0.21	1.19	98.51
T11	0	26670	612651	23733376	105212358	129585054	0.00	0.02	0.47	18.31	81.19
M15	0	1512998	3355033	19496086	1636942340	1661306457	0.00	0.09	0.20	1.17	98.53
M48	47596	12006126	11601206	101322570	2826979557	2951957055	0.00	0.41	0.39	3.43	95.77
M60	0	1512998	2591408	6826561	1477472738	1488403705	0.00	0.10	0.17	0.46	99.27
T68	0	108809	1231931	2283230	469877317	473501287	0.00	0.02	0.26	0.48	99.23
T69	0	589313	1021581	466598	74892137	76969629	0.00	0.77	1.33	0.61	97.30
T26	11337	614388	0	0	32344068	32969793	0.03	1.86	0.00	0.00	98.10
T27	42972	127004	0	0	9312056	9482033	0.45	1.34	0.00	0.00	98.21
T28	0	2138976	1750263	1385814	108041227	113316281	0.00	1.89	1.54	1.22	95.34
T32	25271	262907	42505	0	10124189	10454872	0.24	2.51	0.41	0.00	96.84
T35	0	250865	585928	747772	99183860	100768425	0.00	0.25	0.58	0.74	98.43
T43	4876	9123614	2589246	8417986	747404261	767539983	0.00	1.19	0.34	1.10	97.38
T44	22689	5345148	1285179	245287	167740806	174639109	0.01	3.06	0.74	0.14	96.05
T59	0	572447	434474	940392	96464304	98411617	0.00	0.58	0.44	0.96	98.02
C1*	0	1512998	3355033	19711302	1639521600	1664100933	0.00	0.09	0.20	1.18	98.52
C2*	0	108811	1341989	3646528	488132815	493230143	0.00	0.02	0.27	0.74	98.97
C3*	0	26670	612651	23743239	105502291	129884851	0.00	0.02	0.47	18.28	81.23
C5*	4604	1876183	621441	4290367	170108080	176900674	0.00	1.06	0.35	2.43	96.16
C6*	100160	17863470	4026998	9993932	975915978	1007900538	0.01	1.77	0.40	0.99	96.83

Remote sensing analysis

Topographic and climatic data for all catchments are summarized in **Table A2**. The correlation between the different parameters and sand-derived basin mean denudation rates are shown in **Fig. A1**.

Slope

Our slope analysis is based on the ~30 m resolution SRTM digital elevation model (DEM) (data available from the U.S. Geological Survey). The slope is calculated for each pixel as the maximum rate of change in elevation between that pixel cell and its neighbouring 8 cells. Then, a median slope value for the entire catchment is calculated. Previous studies have shown, that the standard deviation of the slope value depends on the resolution of the DEM (Ouimet et al., 2009), making it less meaningful. We therefore report no standard deviation, but only the mean and median values (**Table A2**) and the slope distributions (**Fig. 2.6**).

Channel steepness index

From the SRTM DEM, we extract the longitudinal river profiles for each catchment. Typical river profiles have a concave up shape, and empirical data have shown a power-law relationship between channel slope (S) and drainage area (A), known as Flint's law:

$$S = k_s A^{-\theta} \quad (\text{A1})$$

where k_s is the steepness index and θ the concavity (Kirby and Whipple, 2001). However, to be able to compare several catchment areas, Wobus et al. (2006) suggested to calculate a normalized steepness index, k_{sn} , by using a reference concavity value, θ_{ref} . The reference concavity used is typically 0.45.

To calculate the k_{sn} values for the drainage system in the Quebrada del Toro, we used tools within Topotoolbox (Schwanghart and Kuhn, 2010). k_{sn} values were calculated for streams with a minimum drainage area of 1 km² and values were averaged over stream segments of 1 km. Finally, we calculated the average k_{sn} value of all stream segments within each catchment. Ouimet et al., 2009 suggested to use k_{sn} as a metric for erosion rate instead of mean basin slope, because plots of erosion rate versus mean slope reach a saturation when the hillslopes reach threshold slopes. However, in the Quebrada del Toro, the k_{sn} values also seem to reach a saturation value (**Fig. A1B**). Similar behavior can be observed in the Apennines, Italy (Cyr et al., 2010) and the San Gabriel Mountains, USA (DiBiase et al., 2010), where k_{sn} values never exceed

200. We thus prefer to compare our erosion rates with mean hillslope angles, considering that we later investigate erosion processes on those hillslopes.

Relief

Basin relief is defined as the difference between maximum and minimum elevation within a defined radius. Because some of our catchment areas are as small as 9 km², we calculated basin relief using focal statistics in ArcGIS with a 2-km radius around each pixel (equivalent to 68 cells in our ~30 m resolution DEM). Then we calculated the basin mean value.

Rainfall

Mean annual rainfall (MAR) was calculated from the TRMM2B31 product with a 5 km resolution, calibrated for our study region by Bookhagen and Strecker (2008). The TRMM product only includes rainfall, and does not include snowfall. However, in our study region, there are virtually no glaciated peaks. As such, the contribution from snow-and icemelt to streamflow is negligible, instead the vast majority of precipitation falls as rain. The basin mean denudation rates show no clear trend with mean annual rainfall (**Fig. A1D**), contrary to previous findings in NW Argentina (Bookhagen and Strecker, 2012). However, Bookhagen and Strecker (2012) investigated a large region with a pronounced gradient in rainfall, whereas the rainfall gradient in the Quebrada del Toro (MAR = 130 to 626 mm/yr) may not be strong enough to dominate the denudation signal.

Vegetation cover

We determined the relative difference in vegetation cover between the catchment using the Enhanced Vegetation Index (EVI). EVI is calculated using the following equation (Huete et al., 2002):

$$EVI = G * \frac{(NIR-RED)}{(NIR+C1*RED-C2*BLUE+L)} \quad (A2)$$

We used a pre-processed EVI map, calculated from the MODIS product MOD13A1, which has a 500 m resolution and a 16 day compositing period (Didan, 2009). However, because we are not interested in temporal but rather spatial changes in vegetation cover, we used a single product recorded in January 2014 that represents summer vegetation. Although no clear trend is obvious, in general, we observe higher EVI values (indicating denser vegetation) in regions with higher denudation rates (**Fig. A1E**). This is different from previous observation, for instance in East Africa, where Acosta et al. (2015) observed

Appendix

significant differences in denudation rates for the same slopes between densely and sparsely vegetated areas. One important difference compared to East Africa is that in the Quebrada del Toro, the densely vegetated parts are exclusively found close to the basin outlet and coincide with the steepest slopes. Thus, the slopes might be too steep for vegetation cover to have a protective and erosion-reducing effect.

Table A2 Topographic and climatic characteristics of the catchments.

Sample site	Mean elevation (m)	Median elevation (m)	Mean basin slope (°)	Median basin slope (°)	Mean ksn	Median ksn	Mean relief 2 km (m)	Median relief 2 km (m)	Mean annual rainfall (mm)	Median annual rainfall (mm)	Mean EVI	Median EVI	D ₅₀ (mm)	NSGI
M08	3801	3724	15.9	15.6	83	66	668	637	189	179	0.08	0.08	25	-0.04
T11	3497	3395	13.5	11.6	93	86	645	568	161	124	0.06	0.06	31	-0.18
M15	3825	3736	15.5	14.9	78	60	654	625	188	176	0.08	0.08	19	-0.14
T26	2712	2630	30.8	32.2	174	170	1309	1291	584	534	0.44	0.47	50	0.77
T27	2433	2427	27.9	28.9	132	130	1021	1042	628	624	0.42	0.42	31	0.77
T28	3642	3748	24.5	25.4	121	116	914	943	141	121	0.07	0.07	20	-0.03
T32	3096	3064	29.1	30.0	172	196	1286	1322	130	90	0.20	0.21	28.5	0.49
T35	4128	3932	17.6	16.8	136	129	867	891	217	178	0.08	0.08	25	-0.22
T43	3741	3648	23.5	23.9	155	147	990	977	216	206	0.09	0.09		0.65
T44	3674	3657	26.8	28.2	191	188	1258	1236	191	184	0.17	0.17		0.79
M48	3701	3668	17.1	16.7	97	76	723	676	185	176	0.08	0.08	33	
T59	3615	3571	14.9	14.4	59	42	610	615	195	180	0.09	0.09	20.5	0.48
M60	3876	3771	15.7	15.2	75	59	665	638	190	176	0.09	0.08		
T68	3788	3719	17.6	17.9	98	85	719	673	186	185	0.09	0.09	30.5	0.18
T69	3745	3777	23.6	23.8	126	116	883	906	155	135	0.08	0.08	26	0.02
C1*	3824	3735	15.5	14.9	78	60	653	625	188	176	0.08	0.08	19	
C2*	3764	3705	17.5	17.7	99	86	715	673	189	185	0.09	0.08	30.5	
C3*	3495	3393	13.5	11.5	93	86	645	567	161	124	0.06	0.06	31	
C5*	3703	3591	19.3	18.8	149	135	872	866	163	83	0.09	0.08	27.5	
C6*	3666	3588	24.5	25.1	165	154	1055	1043	215	206	0.11	0.09	26	

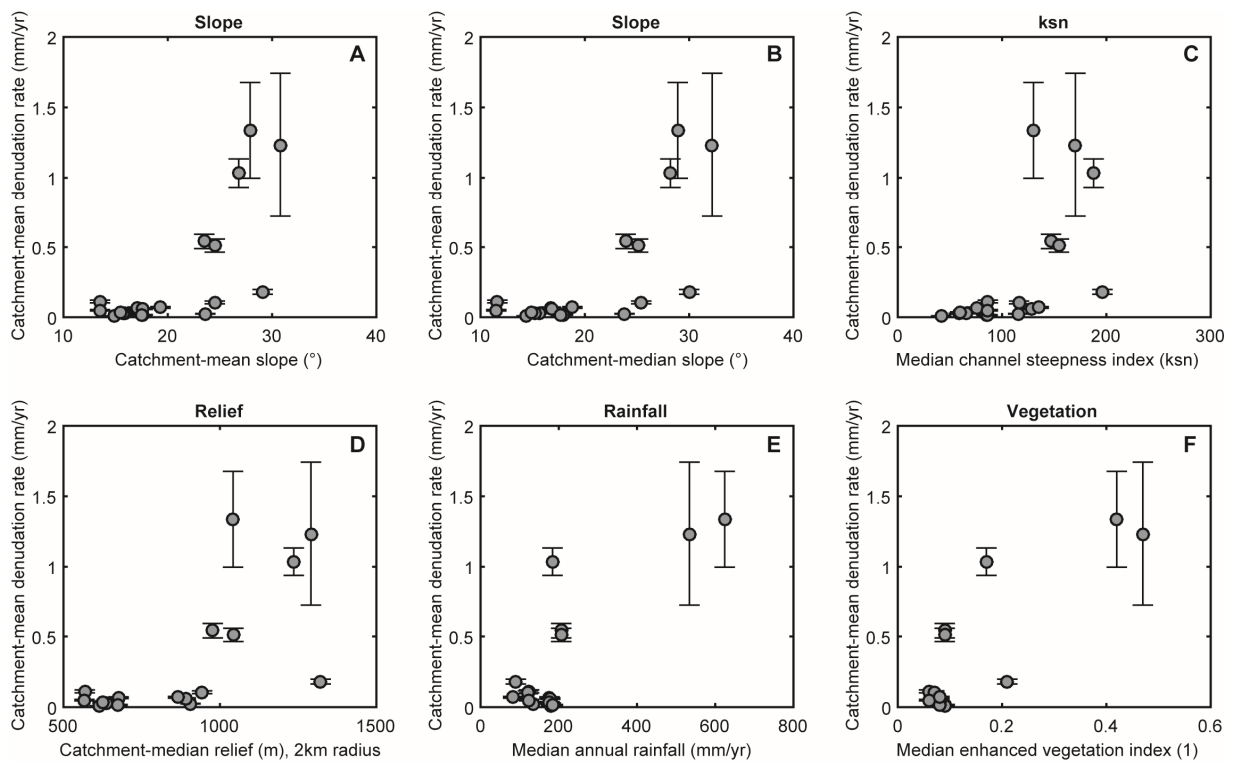


Fig. A1 Basin mean denudation rates compared to topographic (A, B, C, D) and climatic (E, F) parameters.

Previous studies of ^{10}Be in different grain sizes

Table A3 Detailed list of cosmogenic nuclide studies that have measured ^{10}Be concentrations in a sand and a gravel fraction for the same location. The list is an update of the compilation by Codilean et al., (2014), which was itself updated by Carretier et al., (2015).

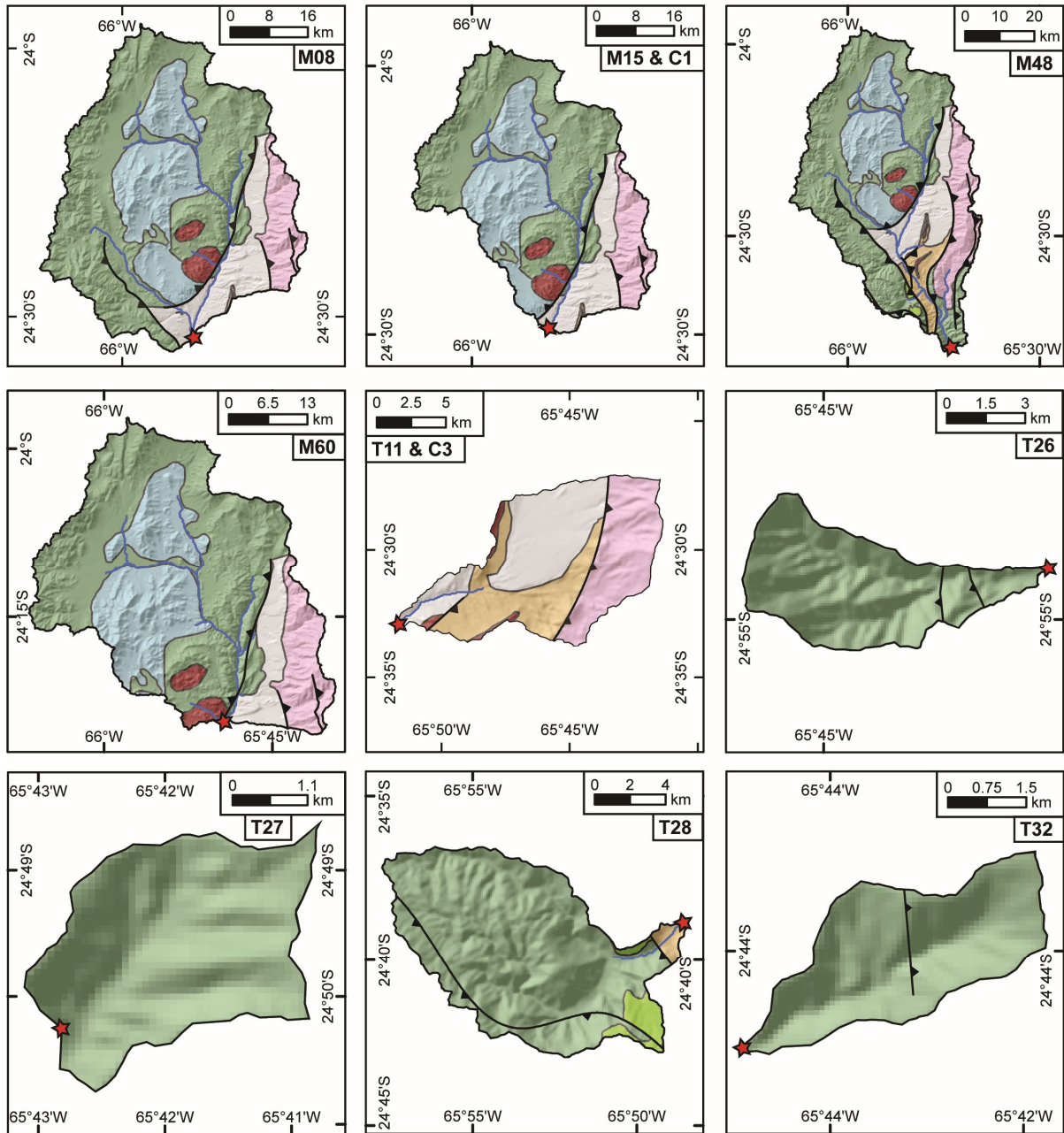
Reference	Title	Grain sizes (mm) sand and pebbles
(Aguilar et al., 2014)	Grain size-dependent ^{10}Be concentrations in alluvial stream sediment of the Huasco Valley, a semi-arid Andes region	0.5 – 1 10 – 30 50 - 100
(Belmont et al., 2007)	Cosmogenic ^{10}Be as a tracer for hillslope and channel sediment dynamics in the Clearwater River, western Washington State	0.25 – 0.5 22.6 - 90
(Brown et al., 1995)	Denudation rates determined from the accumulation of in situ-produced ^{10}Be in the Luquillo experimental forest, Puerto Rico	0.25 – 0.5 gravel
(Carretier et al., 2015)	Differences in ^{10}Be concentrations between river sand, gravel and pebbles along the western side of the central Andes	0.5 – 1 10 - 30 50 - 100
(Clapp et al., 2002)	Using ^{10}Be and ^{26}Al to determine sediment generation rates and identify sediment source areas in an arid region drainage basin	0.25 – 0.5 0.5 – 1 – 2 – 4 4 – 12.7 > 12.7
(Codilean et al., 2014)	Discordance between cosmogenic nuclide concentrations in amalgamated sands and individual fluvial pebbles in an arid zone catchment	0.25 – 0.5 16-21
(Delunel et al., 2014)	Transient sediment supply in a high-altitude Alpine environment evidenced through a ^{10}Be budget of the Etages catchment (French Western Alps)	0.125 – 0.25 0.25 – 0.5 1 – 4 4 - 10 10 – 20 (1 sample) 50 - 100
(Heimsath et al., 2010)	Eroding Australia: rates and processes from Bega Valley to Arnhem Land	sand and gravel
(Hewawasam et al., 2003)	Increase of human over natural erosion rates in tropical highlands constrained by cosmogenic nuclides	0.25 – 0.5 1 – 2 2 – 3 3 – 6 12 - 20
(Matmon et al., 2003)	Erosion of an ancient mountain range, the Great Smoky Mountains, North Carolina and Tennessee	0.25 – 0.85 0.85 – 2 2 – 10 10 - 20
(Matmon et al., 2005)	Dating offset fans along the Mojave section of the San Andreas fault using	0.25 – 0.85 0.85 – 2 2 – 10 > 10

Appendix

(Oskin et al., 2008)	Elevated shear zone loading rate during an earthquake cluster in eastern California	sand and pebble
(Reinhardt et al., 2007)	Interpreting erosion rates from cosmogenic radionuclide concentrations measured in rapidly eroding terrain	0.25 – 0.5 8 – 16
(Palumbo et al., 2009)	Topographic and lithologic control on catchment-wide denudation rates derived from cosmogenic ¹⁰ Be in two mountain ranges at the margin of NE Tibet	0.2 – 0.71 20 - 200
(Puchol et al., 2014)	Grain-size dependent concentration of cosmogenic ¹⁰ Be and erosion dynamics in a landslide-dominated Himalayan watershed	0.075 - 0.25 0.25 - 0.5 0.5 – 1 1 - 2 2 – 4.7 4.7 – 40
(Savi et al., 2016)	Climatic controls on debris-flow activity and sediment aggradation: The Del Medio fan, NW Argentina	0.25 – 0.71 10 – 40
(Schildgen et al., 2016)	Landscape response to late Pleistocene climate change in NW Argentina: Sediment flux modulated by basin geometry and connectivity	0.25 – 0.71 10 – 30

Geological maps

Fig. A2 shows the geological maps for each catchment (main stem and tributary) for which we collected cosmogenic radionuclide samples.



Appendix

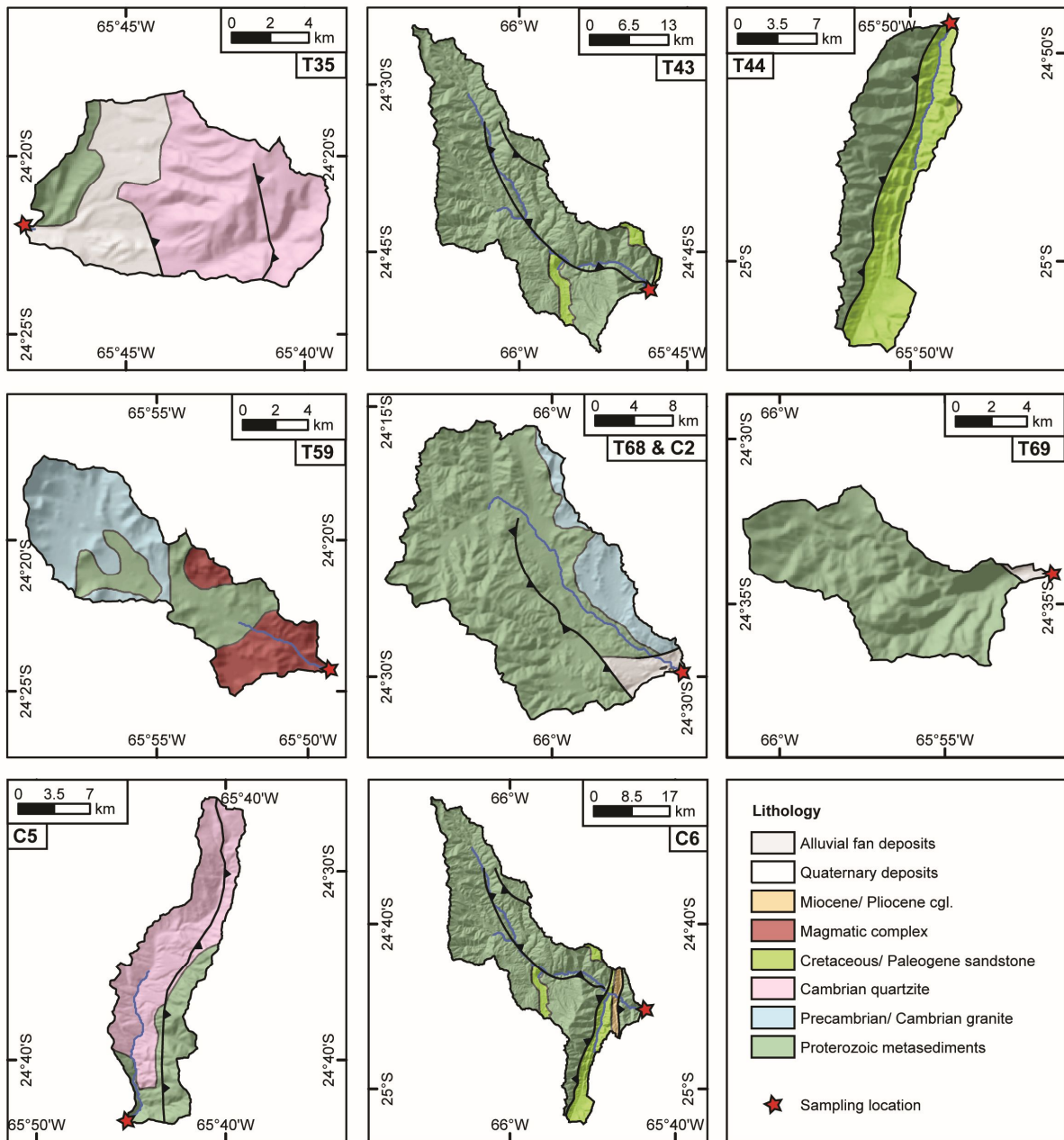


Fig. A2 Geological maps of all sampled catchments.

^{10}Be concentration differences in sand and gravel

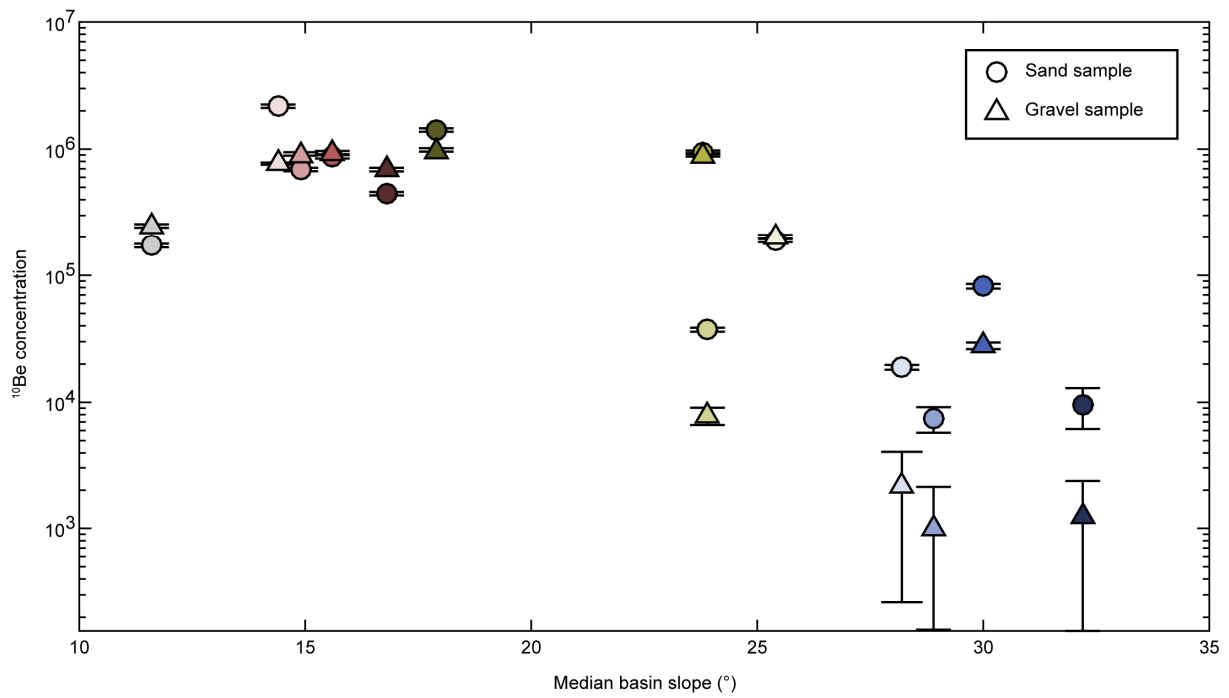


Fig. A3 ^{10}Be concentration of the sand and gravel pairs compared to median basin slope. Each pair is represented by one color. Circles represent sand samples, triangles the gravel samples. Note that the y-axis is logarithmic. In steeper areas ($> 25^\circ$) the ^{10}Be concentration in gravel is significantly lower than in the sand samples.

Appendix B

Table B1 Evolution of height, slope and sediment discharge at the outlet in the Ctrl_1 experiment.

Ctrl_1

Runtime (min)	Height inlet (cm)	Height outlet (min)	Calculated slope (m/m)	$O_{s,out}$ (ml/s)	Runtime (min)	Height inlet (cm)	Height outlet (min)	Calculated slope (m/m)	$O_{s,out}$ (ml/s)
Setting: $Q_w = 94.6$ ml/s; $Q_{s,in} = 1.29$ ml/s									
0	35.0	13.0	0.055		400	30.5	2.0	0.071	
20				15.0	403				2.3
30	34.0	4.0	0.075		408	30.5	2.0		
32				12.5	411				1.8
48	33.5	3.0	0.076	10.0	418	30.5	2.0	0.071	
60	33.5	2.5	0.078		420	30.0	2.0	0.070	
73				14.0	426	30.0	2.0	0.070	4.3
90	33.5	3.0	0.076		435	30.0	2.0	0.070	1.7
95				4.4	448				1.6
107	33.5	2.5	0.078		450				
113				9.0	455	30.5	2.0	0.071	
117				5.0	465				2.6
120	32.5	2.5	0.075		474	30.5	2.0	0.071	2.2
125				4.9	480				
133	32.5	2.5	0.075	4.9	488	30.5	2.0	0.071	1.7
150	32.5	2.5	0.075		497	30.5	2.0	0.071	1.6
154				4.5	510	30.0	2.0	0.070	
160	32.0	2.5	0.074	4.3	513				1.4
180	32.0	2.5	0.074	4.5	524				2.0
187	32.0	2.5	0.074	2.4	530	30.0	2.0	0.070	
197				4.8	533				1.5
210	32.0	2.5	0.074		540	29.5	2.0	0.069	
212				4.3	543				1.0
231				4.3	546				3.8
240	32.0	2.5	0.074		550	29.5	2.0	0.069	
252				3.2	555				7.0
270	32.0	2.5	0.074		564				5.8
280				2.0	567	29.5	1.5	0.070	
288	32.0	2.5		2.1	568				2.7
300	32.0	2.5	0.074		570				
310	32.0	2.0	0.075	3.2	573				1.6
319				3.5	579				4.3
330	32.0	2.0	0.075		591	29.5	1.5	0.070	1.7
337	32.0	2.0	0.075	2.2	600	29.5	1.5	0.070	
343				2.7	604	29.5	1.5	0.070	2.4
347	32.0	2.0	0.075		615				1.6
350				1.3	625				3.8
354				2.5	630				
360	31.5	2.0	0.074		645	29.5	1.5	0.070	2.7
365				2.3	657				3.9
375				2.3	660	29.5	1.5	0.070	
388				2.6	668				2.3
390	31.0	2.0	0.073		687				3.2
394				4.0	690	29.5	1.5	0.070	

Appendix

Table B2 Evolution of height, slope and sediment discharge at the outlet in the Ctrl_2 experiment.

Ctrl_2

Runtime (min)	Height inlet (cm)	Height outlet (min)	Calculated slope (m/m)	$O_{s,out}$ (ml/s)	Runtime (min)	Height inlet (cm)	Height outlet (min)	Calculated slope (m/m)	$O_{s,out}$ (ml/s)
Setting: $Q_w = 94.6$ ml/s; $Q_{s,in} = 1.29$ ml/s									
0	34.0	13.0	0.053		350	30.5	2.0	0.071	5.7
10	33.0	4.0	0.073	27.5	360	30.3	2.0	0.071	4.6
20	32.8	4.0	0.072	21.5	370	30.0	2.0	0.070	2.6
30	32.5	3.5	0.073	9.0	380	30.5	2.3	0.071	4.0
40	33.0	3.5	0.074	12.5	390	30.0	2.3	0.069	6.0
50	33.0	2.5	0.076	13.0	400	30.5	2.3	0.071	3.0
60	32.8	2.8	0.075	12.6	410	30.3	2.0	0.071	3.0
70	33.0	2.5	0.076	8.2	420	30.3	2.3	0.070	4.1
80	33.0	2.3	0.077	11.8	430	29.8	2.0	0.069	3.6
90	33.0	2.0	0.078	6.6	440	30.0	2.0	0.070	4.7
100	33.0	2.3	0.077	13.0	450	30.0	2.3	0.069	5.4
110	32.5	2.0	0.076	5.5	460	30.0	2.3	0.069	1.8
120	32.0	2.5	0.074	11.6	470	30.3	2.0	0.071	3.6
130	32.5	2.3	0.076	4.6	480	30.0	2.0	0.070	3.1
140	32.3	2.5	0.074	4.6	490	30.0	2.0	0.070	2.5
150	32.0	2.3	0.074	5.6	500	30.0	2.3	0.069	1.7
160	31.8	2.3	0.074	7.6	510	29.5	2.0	0.069	4.0
170	32.5	2.3	0.076	10.6	520	30.0	2.3	0.069	2.6
180	32.0	2.5	0.074	5.1	530	30.0	2.3	0.069	2.2
190	31.8	2.0	0.074	5.4	540	29.8	1.8	0.070	1.8
200	32.0	2.0	0.075	5.0	550	29.5	2.5	0.068	2.6
210	31.3	2.0	0.073	4.4	560	30.0	2.3	0.069	3.0
220	31.0	2.3	0.072	3.8	570	29.8	2.3	0.069	3.8
230	31.5	2.5	0.073	4.7	580	30.0	2.0	0.070	2.7
240	31.0	2.8	0.071	3.8	590	29.8	2.0	0.069	2.9
250	30.8	2.5	0.071	3.0	600	29.5	2.3	0.068	2.4
260	30.5	2.0	0.071	4.6	610	30.0	2.0	0.070	6.0
270	31.0	2.5	0.071	3.4	620	30.0	2.0	0.070	1.8
280	31.0	2.3	0.072	7.2	630	29.3	2.3	0.068	2.0
290	31.3	2.3	0.073	4.2	640	29.8	2.5	0.068	3.8
300	30.5	2.5	0.070	7.0	650	29.5	2.0	0.069	3.0
310	30.8	2.5	0.071	3.6	660	29.3	2.3	0.068	2.8
320	31.0	2.5	0.071	6.7	670	30.0	1.8	0.071	2.4
330	30.5	2.5	0.070	5.2	680	29.0	2.3	0.067	1.6
340	30.8	2.5	0.071	3.9	690	29.0	2.3	0.067	3.2

Appendix

Table B3 Evolution of height, slope and sediment discharge at the outlet in the IQ_w experiment.

IQ_w

Runtime (min)	Height inlet (cm)	Height outlet (min)	Calculated slope (m/m)	$O_{s,out}$ (ml/s)	Runtime (min)	Height inlet (cm)	Height outlet (min)	Calculated slope (m/m)	$O_{s,out}$ (ml/s)
Setting: $Q_w = 94.6$ ml/s; $Q_{s,in} = 1.29$ ml/s									
0	36.0	14.0	0.055		250	29.0	2.0	0.068	20.7
4	31.5	5.0	0.066		260	28.0	2.5	0.064	29.0
11	31.5	5.0	0.066	30.0	270	26.0	2.0	0.060	16.8
20	31.5	5.0	0.066	18.0	280	25.0	2.0	0.058	26.3
30	32.0	4.0	0.070	18.5	290	24.0	2.0	0.055	17.3
40				17.9	300	23.0	2.0	0.053	9.6
42	32.0	4.0	0.070		310	23.0	2.0	0.053	10.9
50	32.5	3.5	0.073	20.5	320	23.0	2.5	0.051	13.0
60	32.0	2.5	0.074	13.0	330	21.0	2.0	0.048	11.3
70	32.0	3.0	0.073	9.3	340	22.0	2.0	0.050	17.5
80	32.0	3.0	0.073	11.9	350	21.0	2.0	0.048	11.3
90	32.0	2.5	0.074	8.0	360	21.0	2.0	0.048	7.7
100	32.0	2.5	0.074	7.9	370	20.5	1.5	0.048	8.1
110	32.0	2.5	0.074	7.7	380	20.5	2.0	0.046	9.8
120	32.0	2.5	0.074	6.7	390	20.0	1.5	0.046	5.6
130	32.0	3.0	0.073	6.0	400	20.0	1.5	0.046	7.6
138	32.5	2.0	0.076		410	20.0	2.0	0.045	8.8
140				9.3	420	20.0	1.5	0.046	5.1
150	32.5	2.0	0.076	5.1	430	20.0	2.0	0.045	11.6
158	32.5	2.0	0.076		440	20.0	1.0	0.048	10.6
160				8.1	450	19.0	1.5	0.044	8.6
170	32.5	2.0	0.076	7.9	460	19.0	1.0	0.045	9.9
181	32.0	2.5	0.074	7.9	470	19.0	1.0	0.045	6.7
190	32.0	2.0	0.075	4.5	480	19.0	2.0	0.043	4.1
200	31.5	2.0	0.074	6.8	490	19.0	2.0	0.043	8.3
210	31.0	2.0	0.073	3.3	500	19.0	2.0	0.043	10.3
220	31.0	2.0	0.073	6.0	510	19.0	2.0	0.043	2.9
230	31.0	2.0	0.073	5.3	520	19.0	1.5	0.044	3.8
240	31.0	2.0	0.073	10.9	530	19.0	1.0	0.045	5.0
$Q_w = 189.2$ ml/s; $Q_{s,in} = 1.29$ ml/s					534	18.5	1.5	0.043	
240	31.0	2.0	0.073		540	18.5	1.0	0.044	4.6
245	30.0	2.0	0.070						

Appendix

Table B4 Evolution of height, slope and sediment discharge at the outlet in the DQ_w - IQ_w experiment.

DQ_w - IQ_w

Runtime (min)	Height inlet (cm)	Height outlet (min)	Calculated slope (m/m)	$Q_{s,out}$ (ml/s)	Runtime (min)	Height inlet (cm)	Height outlet (min)	Calculated slope (m/m)	$Q_{s,out}$ (ml/s)
Setting: $Q_w = 94.6$ ml/s; $Q_{s,in} = 1.29$ ml/s									
0	33.5	13.0	0.051		350	34.5	2.0	0.081	1.4
10	31.5	4.5	0.068	31.0	360	34.5	2.0	0.081	1.0
20	31.8	3.5	0.071	30.0	370	34.5	2.0	0.081	0.7
30	32.0	3.5	0.071	18.0	380	34.8	1.5	0.083	1.2
40	33.0	3.0	0.075	14.0	390	34.8	2.0	0.082	1.9
50	32.5	2.5	0.075	15.0	400	34.8	1.5	0.083	1.0
60	32.8	2.0	0.077	12.0	410	34.8	1.5	0.083	0.9
70	32.5	2.0	0.076	9.5	420	34.8	1.8	0.083	1.3
80	32.5	2.0	0.076	13.5	430	34.8	2.0	0.082	1.1
90	32.5	2.0	0.076	15.4	440	34.8	1.5	0.083	1.0
100	32.5	2.0	0.076	11.1	450	34.8	1.5	0.083	1.5
110	32.5	2.5	0.075	9.5	460	35.0	1.5	0.084	2.5
120	32.5	2.5	0.075	11.0	470	35.0	1.5	0.084	0.9
130	32.0	2.0	0.075	8.7	480	35.3	1.5	0.084	1.0
140	32.0	2.5	0.074	8.7	$Q_w = 94.6$ ml/s; $Q_{s,in} = 1.29$ ml/s				
150	31.8	2.0	0.074	4.5	490	32.8	2.0	0.077	4.6
160	31.5	2.0	0.074	10.0	500	31.8	2.0	0.074	3.3
170	31.5	2.0	0.074	8.6	510	31.0	2.0	0.073	12.0
180	30.5	1.5	0.073	8.8	520	30.8	1.5	0.073	2.2
190	30.5	2.0	0.071	4.7	530	30.8	2.0	0.072	5.2
200	31.0	1.5	0.074	5.2	540	30.8	2.0	0.072	3.2
210	31.0	2.0	0.073	10.6	550	30.5	2.0	0.071	5.8
220	31.0	2.0	0.073	5.6	560	30.3	2.0	0.071	5.1
230	30.8	1.5	0.073	6.2	570	30.3	2.0	0.071	5.2
240	30.8	2.0	0.072	3.7	580	30.0	2.0	0.070	5.4
$Q_w = 47.2$ ml/s; $Q_{s,in} = 1.29$ ml/s					590	30.3	2.0	0.071	3.8
250	32.0	2.0	0.075	1.7	600	30.3	2.0	0.071	4.6
260	32.5	1.5	0.078	2.0	610	30.3	2.0	0.071	6.9
270	33.0	2.0	0.078	2.3	620	30.5	2.5	0.070	5.1
280	33.0	2.0	0.078	1.9	630	30.0	2.0	0.070	9.4
290	33.3	2.0	0.078	2.8	640	29.5	2.0	0.069	3.0
300	33.5	2.0	0.079	1.4	650	29.8	2.5	0.068	4.6
310	33.8	2.0	0.079	1.2	660	30.0	2.0	0.070	5.3
320	34.0	2.0	0.080	2.1	670	30.3	1.5	0.072	5.0
330	34.0	2.0	0.080	1.9	680	29.8	1.8	0.070	3.3
340	34.3	2.0	0.081	0.9	690	29.8	2.0	0.069	

Appendix

Table B5 Evolution of height, slope and sediment discharge at the outlet in the $DQ_{s,in}$ experiment.

$DQ_{s,in}$									
Runtime (min)	Height inlet (cm)	Height outlet (min)	Calculated slope (m/m)	$Q_{s,out}$ (ml/s)	Runtime (min)	Height inlet (cm)	Height outlet (min)	Calculated slope (m/m)	$Q_{s,out}$ (ml/s)
Setting: $Q_w = 94.6$ ml/s; $Q_{s,in} = 1.29$ ml/s									
0	34.0	12.0	0.055		280	31.0	2.0	0.073	7.3
10				29.3	290	30.5	2.5	0.070	5.5
12	34.0	4.0	0.075		298	30.5	2.0	0.071	
20	34.0	3.0	0.078	19.0	300				8.3
29	33.0	4.0	0.073	18.0	310	30.5	2.0	0.071	7.0
30					320	30.0	2.0	0.070	7.5
40	33.0	3.0	0.075	20.0	330	30.0	2.0	0.070	5.8
50	33.0	3.0	0.075	16.3	332	30.0	2.0	0.070	
60	33.0	3.0	0.075	19.8	340	29.8	2.0	0.069	6.5
66	33.0	3.0	0.075		348	29.8	2.0	0.069	
70				13.5	350				9.8
76	33.0	3.0	0.075		352	29.5	1.5	0.070	
80				7.8	360	29.0	1.5	0.069	5.8
85	33.0	3.0	0.075		370	29.0	1.5	0.069	3.5
90				7.0	380	28.8	2.0	0.067	4.0
100	33.0	3.0	0.075	5.8	389	28.8	2.0	0.067	
110	33.0	2.5	0.076	10.5	390				2.8
120	33.0	2.5	0.076		400	28.5	2.0	0.066	4.7
130	33.0	2.0	0.078	7.5	410	28.5	2.0	0.066	5.3
140	33.0	2.0	0.078	6.0	420	28.5	2.0	0.066	3.7
150	33.5	2.5	0.078	10.0	430	28.0	1.5	0.066	5.8
160	33.5	2.0	0.079	7.5	438	28.0	1.5	0.066	
167	33.5	2.0	0.079		440				4.3
170	33.5	2.0	0.079	5.5	450	28.0	2.0	0.065	5.0
180	33.5	2.0	0.079	8.2	460	28.0	2.0	0.065	4.3
186	33.5	2.0	0.079		470	27.8	2.0	0.064	6.8
190	33.5	2.5	0.078	5.0	480	27.5	2.0	0.064	5.5
200	33.5	2.0	0.079	9.3	490	27.5	2.0	0.064	2.6
210	33.5	2.0	0.079	4.0	500	27.0	2.5	0.061	4.0
218	33.5	2.0	0.079		510	27.0	1.5	0.064	3.0
220				6.8	520	27.0	2.0	0.063	8.0
230	33.5	2.0	0.079	9.0	522				4.5
240	33.5	2.0	0.079	6.0	530	26.8	2.0	0.062	7.0
$Q_w = 94.6$ ml/s; $Q_{s,in} = 0.22$ ml/s					540	26.8	2.0	0.062	3.4
244	33.0	2.0	0.078		550	26.8	2.0	0.062	3.1
250	32.5	2.0	0.076	4.5	560	26.8	2.0	0.062	7.1
260	32.0	2.0	0.075	6.5	570	26.8	2.0	0.062	2.2
268	31.0	2.0	0.073		580	26.8	2.0	0.062	2.8
270				6.0	590	26.5	2.0	0.061	3.8
273	31.0	2.0	0.073		600	26.0	2.0	0.060	4.5

Appendix

Table B6 Evolution of height, slope and sediment discharge at the outlet in the $IQ_{s,in} \text{ } _DQ_{s,in}$ experiment.

$IQ_{s,in} \text{ } _DQ_{s,in}$									
Runtime (min)	Height inlet (cm)	Height outlet (min)	Calculated slope (m/m)	$Q_{s,out}$ (ml/s)	Runtime (min)	Height inlet (cm)	Height outlet (min)	Calculated slope (m/m)	$Q_{s,out}$ (ml/s)
Setting: $Q_w = 94.6 \text{ ml/s}$; $Q_{s,in} = 1.29 \text{ ml/s}$									
0	34.0	14.0	0.050		370	32.5	2.3	0.076	7.2
10	30.0	3.0	0.068	20.4	380	32.8	2.0	0.077	4.3
20	29.8	2.5	0.068	13.5	390	32.8	2.0	0.077	2.9
30	30.0	3.0	0.068		400	32.8	2.3	0.076	2.4
40	30.0	2.5	0.069	20.3	410	32.8	1.5	0.078	2.5
50	30.0	2.5	0.069	11.4	420	33.0	2.0	0.078	5.0
60	30.2	2.5	0.069	9.4	430	33.3	2.0	0.078	3.7
70	30.5	2.5	0.070	11.6	440	33.0	2.3	0.077	2.3
80	31.0	2.0	0.073	7.0	450	32.8	2.3	0.076	2.2
90	30.8	2.0	0.072	16.1	460	33.0	2.5	0.076	4.5
100	31.0	2.0	0.073	7.0	470	33.0	2.0	0.078	4.8
110	31.0	2.0	0.073	7.1	480	33.0	2.0	0.078	6.5
120	31.0	2.0	0.073	3.9	$Q_w = 94.6 \text{ ml/s}$; $Q_{s,in} = 1.29 \text{ ml/s}$				
130	31.0	2.5	0.071	8.1	490	31.8	1.8	0.075	2.6
140	31.0	2.5	0.071	8.0	500	31.0	2.0	0.073	5.9
150	31.0	2.5	0.071	5.9	510	30.8	2.3	0.071	3.6
160	31.3	2.5	0.072	6.8	520	30.8	2.0	0.072	14.0
170	31.0	2.5	0.071	4.9	530	30.0	2.0	0.070	11.4
180	31.0	2.5	0.071	5.4	540	30.1	2.0	0.070	5.5
190	30.5	2.5	0.070	3.5	550	30.5	1.8	0.072	4.2
200	30.0	2.5	0.069	7.6	560	30.8	1.8	0.073	6.4
210	29.8	2.3	0.069	8.2	570	30.5	2.3	0.071	5.5
220	30.3	2.0	0.071	3.7	570	30.0	2.0	0.070	
230	30.0	2.0	0.070	10.2	580	30.0	2.0	0.070	3.0
240	30.0	2.0	0.070	4.2	590	30.0	2.0	0.070	6.0
$Q_w = 94.6 \text{ ml/s}$; $Q_{s,in} = 2.6 \text{ ml/s}$					600	30.3	2.3	0.070	3.0
250	30.8	2.0	0.072	14.1	610	30.5	2.0	0.071	2.3
260	31.0	2.0	0.073	5.5	620	30.8	2.3	0.071	2.8
270	31.0	2.0	0.073	5.6	630	30.3	2.5	0.069	3.3
280	31.8	2.0	0.074	5.1	640	30.0	2.3	0.069	3.3
290	32.0	2.0	0.075	5.6	650	29.8	2.5	0.068	3.9
300	32.0	2.3	0.074	3.8	660	29.8	2.5	0.068	3.2
310	32.3	2.3	0.075	5.2	670	30.0	2.5	0.069	4.2
320	32.5	2.3	0.076	3.2	680	30.0	2.0	0.070	4.5
330	32.5	2.3	0.076	5.4	690	29.8	2.0	0.069	8.6
340	31.8	2.0	0.074	3.8	700	30.3	2.0	0.071	4.4
350	31.9	2.0	0.075	6.4	710	30.5	2.0	0.071	4.1
360	32.0	2.3	0.074	4.6	720	29.8	2.0	0.069	4.0

Appendix

Table B7 Evolution of height, slope and sediment discharge at the outlet in the BLF experiment.

BLF

Runtime (min)	Height inlet (cm)	Height outlet (min)	Calculated slope (m/m)	$O_{s,out}$ (ml/s)	Runtime (min)	Height inlet (cm)	Height outlet (min)	Calculated slope (m/m)	$O_{s,out}$ (ml/s)
Setting: $Q_w = 94.6$ ml/s; $Q_{s,in} = 1.29$ ml/s					225	32.8	14.0	0.047	
0	34.0	13.8	0.051		230	32.9	14.0	0.047	
13	30.5	13.8	0.042		240	32.9	14.0	0.047	
20	30.3	13.8	0.041		Onset of base-level fall: 0.5 cm/min				
30	30.3	14.0	0.041		250	33.0	9.0	0.060	
40	30.8	14.0	0.042		260	33.0	4.0	0.073	
45	30.5	14.0	0.041		270	33.1	3.5	0.074	
50	30.8	14.0	0.042		280	33.0	3.0	0.075	11.8
60	30.8	14.0	0.042		290	33.0	3.0	0.075	18.0
70	30.8	14.0	0.042		300	32.9	2.5	0.076	14.4
75	31.0	14.0	0.043		310	33.0	2.5	0.076	11.7
80	31.0	14.0	0.043		320	33.2	2.5	0.077	12.3
90	31.0	14.0	0.043		330	33.2	2.0	0.078	14.6
100	31.5	14.0	0.044		340	33.2	2.0	0.078	10.4
108	31.5	14.0	0.044		350	33.5	2.0	0.079	12.7
110	31.5	14.0	0.044		360	32.8	2.0	0.077	7.4
120	31.8	14.0	0.044		370	32.0	2.0	0.075	7.7
130	31.8	14.0	0.044		380	31.9	2.0	0.075	11.5
135	31.8	14.0	0.044		390	32.0	2.0	0.075	11.0
140	32.0	14.0	0.045		400	32.0	2.0	0.075	7.2
150	32.0	14.0	0.045		410	32.0	2.0	0.075	8.2
160	32.3	14.0	0.046		420	32.0	2.0	0.075	6.5
165	32.3	14.0	0.046		430	32.0	2.5	0.074	10.7
170	32.5	14.0	0.046		440	32.0	2.0	0.075	6.9
180	32.5	14.0	0.046		450	32.0	2.3	0.074	3.7
190	32.8	14.0	0.047		460	32.0	2.5	0.074	5.0
195	32.8	14.0	0.047		470	32.0	2.5	0.074	3.9
200	32.8	14.0	0.047		480	31.8	2.5	0.073	13.2
210	32.8	14.0	0.047						
220	32.8	14.0	0.047						

Appendix C

CRN sample preparation

The preparation of all cosmogenic radionuclide (CRN) samples was performed following standard procedures (Nishiizumi et al., 1989; von Blanckenburg et al., 2004; Wittmann et al., 2016). For the 2014 and 2015 samples, mineral separation and quartz purification was carried out at the University of Potsdam. For sand samples, we processed grain sizes between 250 and 500 μm , whereas for crushed pebble samples, we processed grain sizes between 250 and 1000 μm . Quartz was concentrated by removing the magnetic fraction, followed HCl and H₂O₂ treatment to dissolve carbonates and organics. Next, samples were leached in a 1%HF/1%HNO₃ solution a minimum of three times for 12 h each in an ultrasonic bath to dissolve non-quartz minerals and to remove meteoric ¹⁰Be prior to column chemistry.

Column chemistry and target preparation followed procedures described by von Blanckenburg et al. (2004) and Wittmann et al. (2016) and was carried out at the GeoForschungsZentrum (GFZ) Potsdam. A carrier of 150 μg of ⁹Be was added to each sample prior to quartz digestion and isolation of Be(OH)₂ via column chemistry. Be was then oxidized to BeO and prepared as targets for analysis by accelerator mass spectrometer (AMS). AMS measurements were performed at the Department of Geology and Mineralogy, University of Cologne, Germany. Measured Be isotope values were normalized to the standards KN01-6-2 and KN01-5-3 with a nominal ¹⁰Be/⁹Be ratio of $5.35 \cdot 10^{-13}$ and $6.32 \cdot 10^{-12}$, respectively. Concentration corrections were performed for each sample based on several blank ratios processed with the same batches. All blank measurements used for corrections are listed in **Table C3**.

The samples collected in 2003 were processed at UC Berkeley Space Science Laboratory following standard procedures described in Nishiizumi et al. (1989). A carrier of 300 μg of ⁹Be was added and Be(OH)₂ was isolated via ion-exchange column chemistry, oxidized to BeO and loaded into targets for AMS measurements at the Lawrence Livermore National Laboratory (LLNL) and normalized to the standard from K. Nishiizumi (2004).

Terrace surface age analysis

For the *Stable-surface* and *Inflation-corrected* approaches (**Fig. C2**) we used a combination of a Monte Carlo simulator (Hidy et al., 2010) and the CRONUS Earth online calculator v2.2 (Balco et al., 2008). To account for differences in pressure-elevation-conversions, we incorporated the NCEP atmospheric reanalysis data product (http://www.esrl.noaa.gov/psd/data/ncep_reanalysis/) into the Monte Carlo script to be consistent with the one used in the CRONUS Earth calculator v2.2. All depth profiles

Appendix

were run with an assumed sample density of 1.6 to 1.8 g cm⁻³, a neutron attenuation length of 160±5 g cm⁻² and a depth of muon fit of 5 m. We computed 50,000 fitted curves for each run, approaching a nearly normal distribution of fits. We did not perform any depth profile analysis for P2c due to the non-exponential distribution of the data.

It is important to note that the Monte Carlo model of Hidy et al. (2010) simulates inflation simply by imposing constant negative erosion rates for the surfaces. However, it is likely that the surface inflation is instead event-based (McFadden et al., 1987). To gain more insight into these processes, a more detailed approach (e.g. OSL dating) for the aeolian top layer may ultimately reveal the timing of discrete inflation events (e.g., Schildgen et al., 2016).

The Monte Carlo simulator includes only the time-independent Lal/Stone scaling scheme (*St*) (Lal, 1991; Stone, 2000). Thus, it does not account for temporal variability in ¹⁰Be production rates. To overcome this limitation, we performed a first run with the Monte Carlo simulator to estimate the surface-exposure ages (**Table C4; Fig. C3**- *St*-scaling scheme). The most probable ages were then converted into a most probable ¹⁰Be concentration at the surface (C_{surf} , atm g⁻¹) based on eq. C1 and by using a ¹⁰Be decay constant (λ) of $4.987 \pm 0.043 \times 10^{-7}$ atm g⁻¹ yr⁻¹ (Chmeleff et al., 2010; Korschinek et al., 2010).

$$C_{surf} = \frac{P_{0,total}}{\lambda} (1 - e^{-t\lambda}) \quad (C1)$$

where $P_{0,total}$ is the total local production rate at the surface (spallogenic and muogenic, atm g⁻¹ yr⁻¹) and t is the calculated exposure age (yr). Next, the calculated ¹⁰Be surface concentrations were used to perform exposure age calculations with the CRONUS Earth calculator v2.2 (Balco et al., 2008) and the production rate calibration data set from Blard et al. (2013). The resulting time-dependent production rate (Lm) (Balco et al., 2008) based ages were then turned back into time-dependent production rates by solving equation C1 for $P(0)$. As a last step, we re-ran the Monte Carlo simulation by incorporating the time-dependent production rates based on the *Lm*-scaling scheme (**Table C5; Fig. C3**- *Lm*-scaling scheme).

This calibration site for the reference production rate is located in the high tropical Andes (3800-4900 m, 20- 22 ° S), which is the closest one available to our study site (Blard et al., 2013). The original spallation rate published by Blard et al. (2013) (3.63 ± 0.17 atoms g⁻¹ yr⁻¹) was recalculated to adjust it to the different scripts used by the CRONUS Earth calculator (see <https://cosmognosis.wordpress.com/2014/01/07/high-altitude-low-latitude-calibration-sites-ii/> for discussion). Reference spallation production rates are 4.06 ± 0.21 and 3.79 ± 0.23 atm g⁻¹ yr⁻¹ for the time-independent *St* (Lal, 1991; Stone, 2000) and the time-dependent *Lm* (Balco et al., 2008) scaling schemes, respectively. Thus, we also applied the adjusted spallation production rate of 4.06 atm g⁻¹ yr⁻¹ to the Monte

Carlo simulator in the first run. All local production rates are summarized in **Table C6**. We also listed local spallation production rates obtained with the CREP calculator (Martin et al., 2016) based on the LSD scaling scheme (Lifton et al., 2014), the ERA 40 atmospheric model (Uppala et al., 2005) and the LSD geomagnetic database (Lifton et al., 2014) for comparison based on a reference spallation production rate of a regional mean of northern South America ($4.03 \pm 0.14 \text{ atm g}^{-1} \text{ yr}^{-1}$; <http://crep.crpq.cnrs-nancy.fr/#/init>). The larger differences in production rates for the profiles P2c, P4d, P6a and P6b (samples collected in 2003) is probably related to the different Be standardization. For ^{10}Be measurements at the LLNL-CAMS that were performed before 2007, a different nominal isotope ratio was assumed for the standards. While the Monte Carlo simulator does not incorporate a correction for the different nominal isotope ratios, the CRONUS calculator does.

For the third approach (*Surface-pebbles* approach) (**Fig. C2**), we subtracted the most-probable inherited ^{10}Be concentration derived from the depth profiles from the surface samples (red circles in **Fig. 4.4**) and then calculated abandonment ages from the remaining ^{10}Be concentration (**Table C7**).

Zircon analysis

Zircons were separated using standard crushing, heavy liquid, and magnetic separation techniques. When possible, 100 to 150 zircon grains per sample were handpicked, mounted in epoxy, and polished for U, Th, and Pb isotope analysis using a Laser Ablation Multi-Collector Inductively Coupled Plasma Mass Spectrometer (LA-MC-ICPMS) at the University of California, Santa Barbara. Zircons were mapped using a cathodo-luminescence (CL) imaging system attached to a FEI Q400 FEG scanning electron microscope (SEM) at the University of California, Santa Barbara, operated at 10 kV accelerating voltage and a beam current of 0.5 nA. CL images revealed simple concentric zonation in the majority of zircons. Instrumentation for radiometric analyses consists of a Nu Plasma MC-ICPMS and a 193 nm ArF laser ablation system. The analytical protocol is similar to that described by (Cottle, 2014; Cottle et al., 2013). U-Th-Pb analyses were conducted for 15 sec using a spot diameter of 24 μm , a frequency of 4 Hz and 1.2 J/cm² fluence. The 91500-reference zircon ($1065.4 \pm 0.6 \text{ Ma}$ $^{207}\text{Pb}/^{206}\text{Pb}$ ID-TIMS and $1062.4 \pm 0.8 \text{ Ma}$ $^{206}\text{Pb}/^{238}\text{U}$ ID-TIMS) (Wiedenbeck et al., 1995) was used to monitor and correct for mass bias as well as Pb/U and fractionation. To monitor data accuracy, a secondary reference zircon ‘GJ-1’ ($601.7 \pm 1.3 \text{ Ma}$ $^{206}\text{Pb}/^{238}\text{U}$ ID-TIMS age, $608.5 \pm 0.4 \text{ Ma}$ $^{207}\text{Pb}/^{206}\text{Pb}$ ID-TIMS age) (Jackson et al., 2004) was analyzed once every ~7 unknowns and mass bias- and fractionation-corrected based on measured isotopic ratios of the primary reference zircon. Repeat analyses of GJ-1 yield a weighted mean $^{206}\text{Pb}/^{238}\text{U}$ age of 602.7 ± 3.1 , MSWD = 0.44 (n = 7). Data reduction, including corrections for baseline, instrumental drift, mass bias,

Appendix

down-hole fractionation and uncorrected age calculations was carried out using Iolite version 2.5 (Paton et al., 2010). Data were corrected for common lead using the method of (Andersen, 2002). The uncertainty on the ^{207}Pb corrected age incorporates uncertainties on the measured $^{206}\text{Pb}/^{238}\text{U}$ and $^{207}\text{Pb}/^{206}\text{Pb}$ ratios as well as a 2% uncertainty on the assumed common lead composition. Correction for excess ^{230}Th follows the method of (Crowley et al., 2007) assuming $\text{Th}/\text{U}[\text{magma}] = 4.0 \pm 1.0$. All uncertainties are quoted at the 1σ level and include contributions from the external reproducibility of the primary reference material for the $^{207}\text{Pb}/^{206}\text{Pb}$ and $^{206}\text{Pb}/^{238}\text{U}$ ratios.

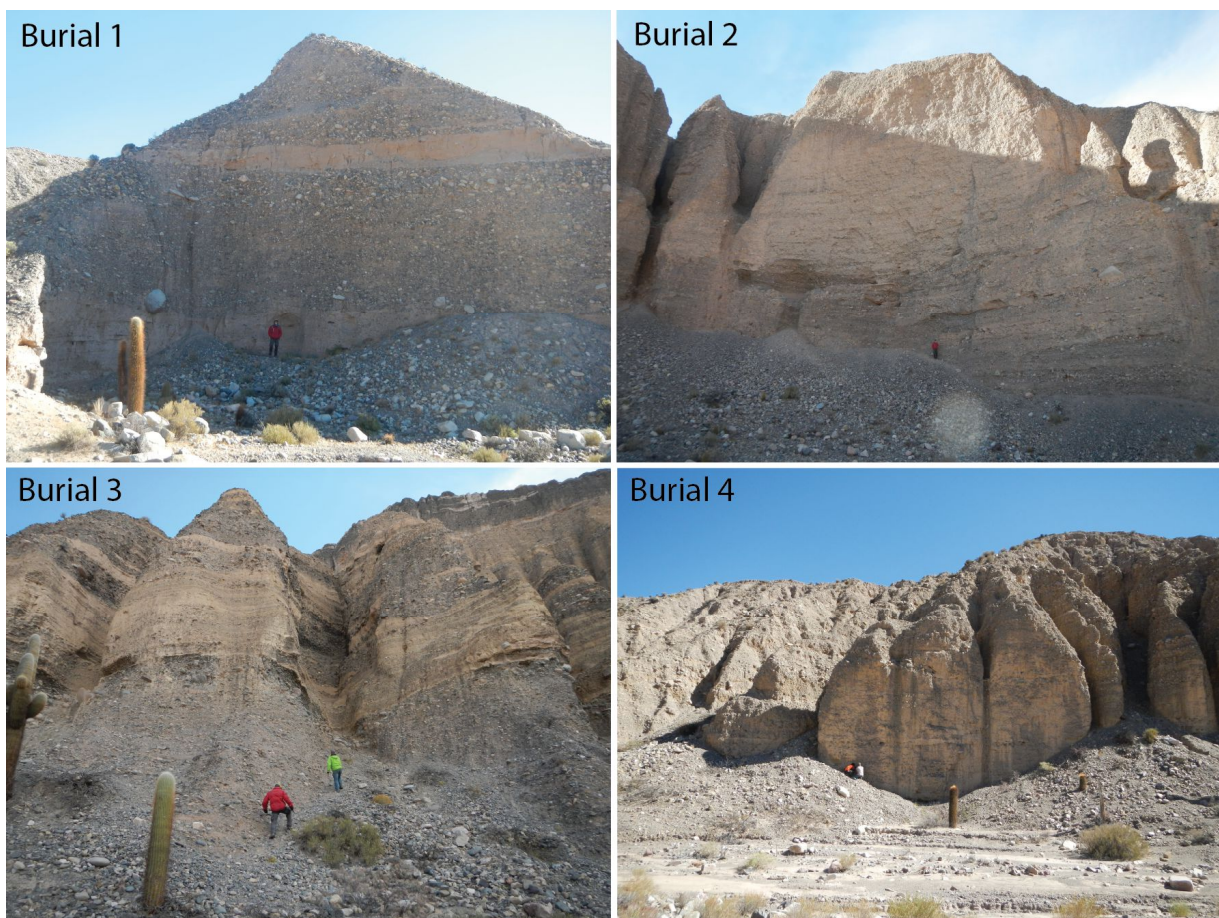


Fig. C1 Field photos of the four $^{26}\text{Al}/^{10}\text{Be}$ burial sites. Samples were only taken at locations with a minimum of 10 m shielding from above to avoid post-depositional production of ^{10}Be and ^{26}Al .

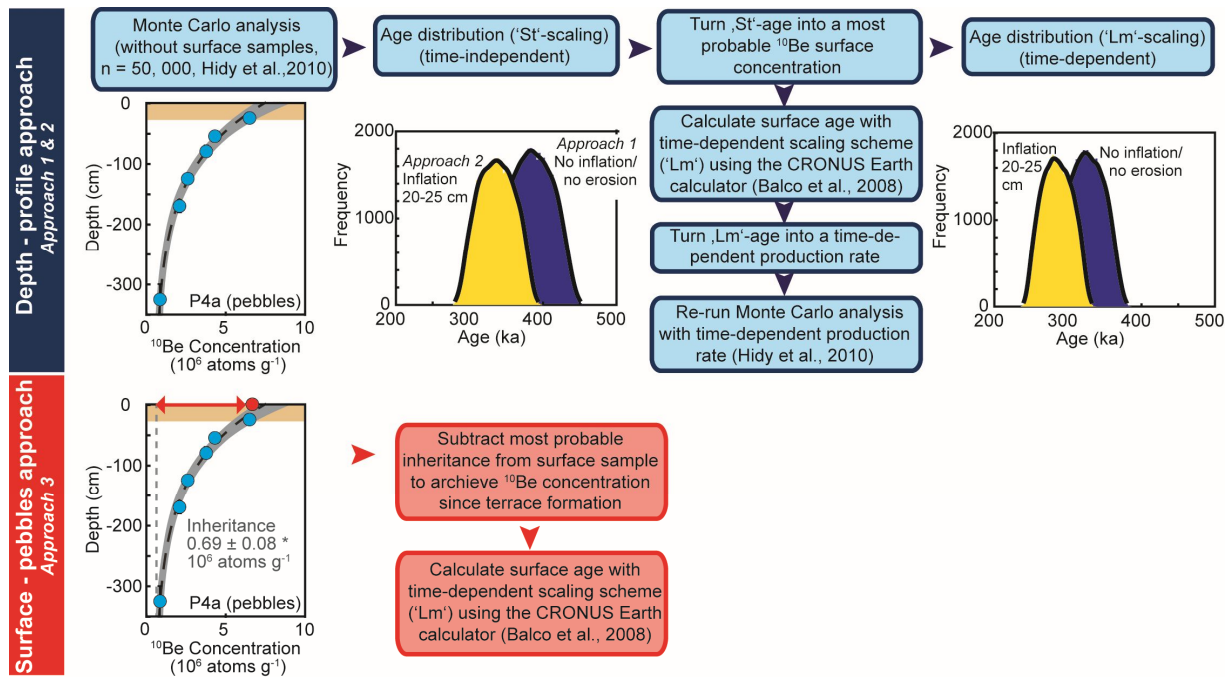


Fig. C2 Overview of the three different approaches for the terrace surface age estimations. Top panel: Approach 1 and 2 use the complete profile excluding the top low-concentration samples (red circles in Fig. 4.4). Approach 1 assumes a stable surface (blue), while Approach 2 corrects for inflation (yellow). The age frequency distributions are calculated with the Monte Carlo depth profile simulator (Hidy et al., 2010) and are based on $n = 50,000$ fits for each run. The Monte Carlo simulator has only the Lal/Stone time-independent ('St') scaling scheme (Lal, 1991; Stone, 2000) built in. To correct for the temporal variability in local production rates, we turned the most probable resulting age into a ^{10}Be surface concentration, which we fed into the CRONUS Earth calculator (Balco et al., 2008) to receive an age based on the time-dependent production rate ('Lm') (Balco et al., 2008). This age was used to calculate a local time-dependent production rate which then was fed into the Monte Carlo simulator to re-run the analyses. Bottom panel: For Approach 3 we only used the surface sample of each pebble-profile and subtracted the most probable inheritance (based on the fit from Approach 1). Surfaces ages were then calculated with the CRONUS Earth calculator based on the remaining ^{10}Be concentration.

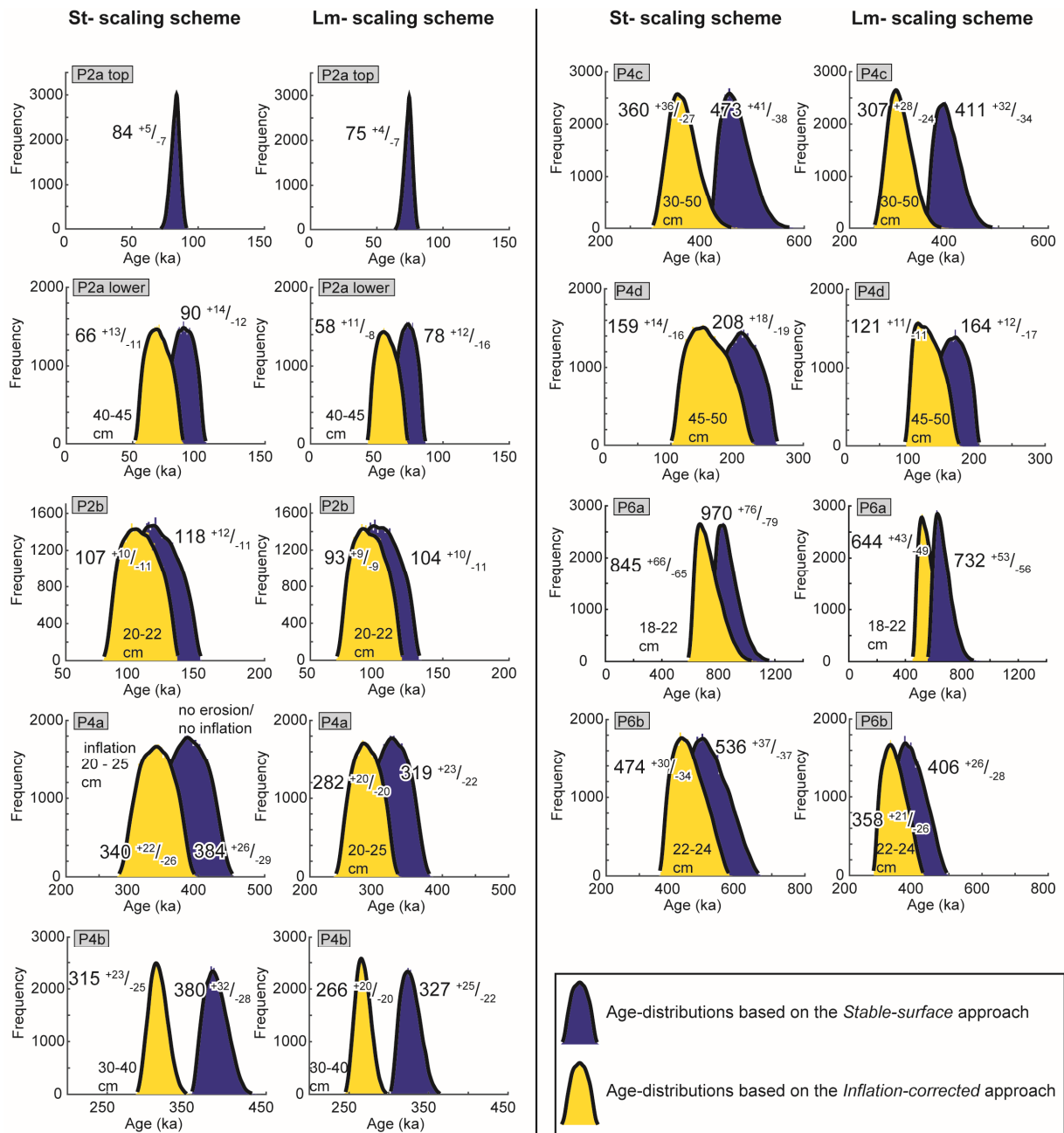


Fig. C3 Age-frequency plots of the ^{10}Be depth-profiles (excluding P2c). P2 is divided into a top part analysis and a lower part analysis. Each samples is analyzed with a local production rate based on the Lal/Stone time-independent scaling scheme ('St', left column) and the Lal/Stone time-dependent scaling scheme ('Lm', right column). Analyses are taken out with the assuming either a stable surface (blue, Approach 1) or including an inflation correction (yellow, Approach 2). The age-frequency distributions are based on $n = 50,000$ fits to the sample distribution and the resulting ages are given with 1σ uncertainty.

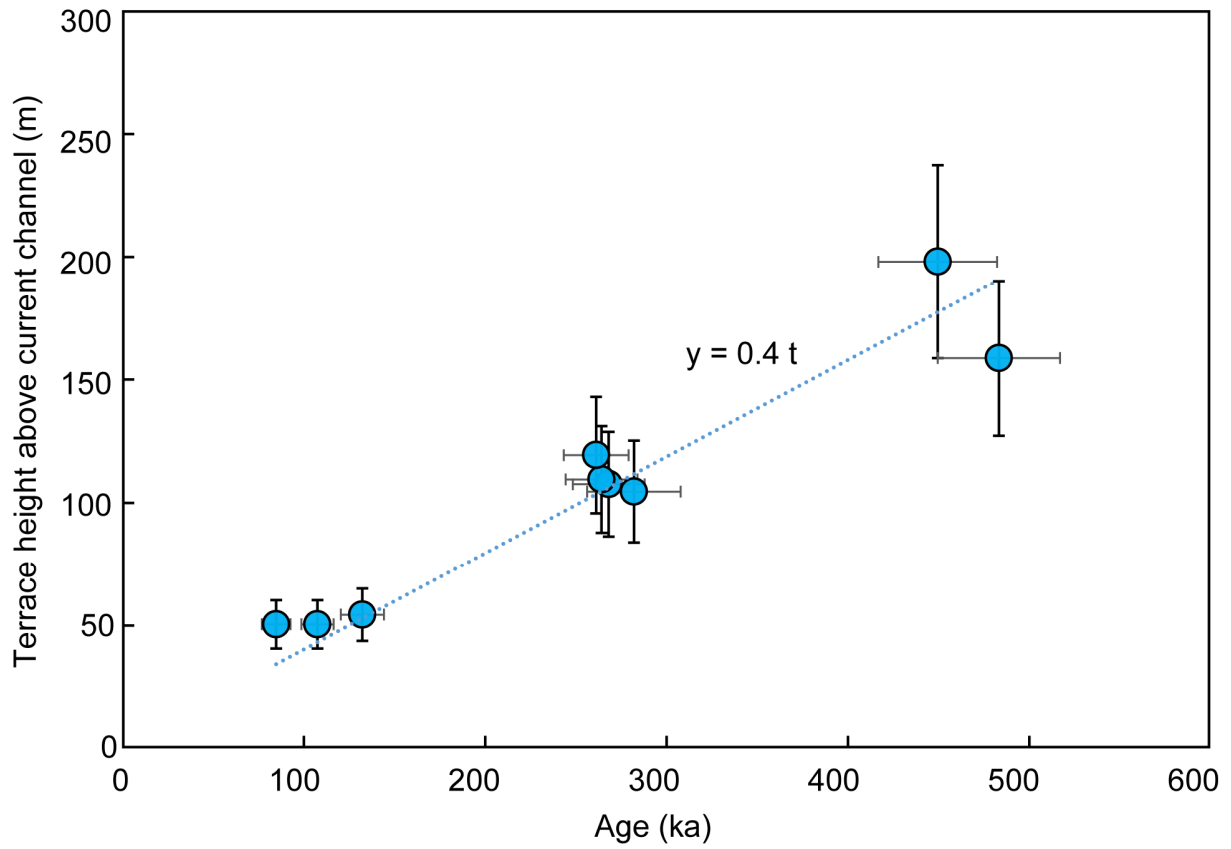


Fig. C4 Height of the terrace surfaces above the current channel compared to their exposure age. An overall net incision rate of ~ 0.4 mm/yr can be observed within the upper Toro Basin.

Table C1 Depth profile samples. Measured $^{10}\text{Be}/^9\text{Be}$ and ratios and resulting ^{10}Be and concentration for the cosmogenic depth profile samples.

Sample name	Latitude (°S)	Longitude (°W)	Elevation (m)	Topogra- phic shielding***	Number of clasts	Mean depth below surface (cm)	Sampled depth range (cm)	Measured $^{10}\text{Be}/^9\text{Be}$ ratio $\pm 1\sigma$ (analytical uncertainty)	Calculated ^{10}Be concentration (^{10}Be atm $\text{g}^{-1} \pm 1\sigma$)
Profile 2a* (P2a)									
ST14_30_CS_0	-24.51922	-65.87083	2761	0.992	sand	0	2	3.58E-12 \pm 1.10E-13	1.84E+06 \pm 5.7E+04
ST14_30_CS_15/20					sand	17.5	5	2.51E-12 \pm 7.84E-14	1.32E+06 \pm 4.1E+04
ST14_30_CS_40/50					sand	45	10	2.98E-12 \pm 9.24E-14	1.06E+06 \pm 3.3E+04
ST14_30_CS_70/80					sand	75	10	1.34E-11 \pm 4.12E-13	2.77E+06 \pm 8.5E+04
ST14_30_CS_100/110					sand	105	10	1.31E-11 \pm 3.98E-13	2.74E+06 \pm 8.3E+04
ST14_30_CS_140/160					sand	150	20	9.96E-12 \pm 3.04E-13	2.09E+06 \pm 6.4E+04
ST14_30_CS >180					sand	185	10	9.49E-12 \pm 2.90E-13	1.96E+06 \pm 6.0E+04
Profile 2b* (P2b)									
ST14_10_CC_0	-24.5488	-65.86298	2713	0.994	92	0	2	5.82E-12 \pm 1.78E-13	2.99E+06 \pm 9.1E+04
ST14_10_CC_10					60	10	5	6.23E-12 \pm 1.90E-13	3.21E+06 \pm 9.8E+04
ST14_10_CC_35/45					65	40	10	6.21E-12 \pm 1.89E-13	2.13E+06 \pm 6.5E+04
ST14_10_CC_60/70					70	65	10	6.83E-12 \pm 2.09E-13	1.43E+06 \pm 4.4E+04
ST14_10_CC_80/100					63	90	20	8.88E-12 \pm 2.71E-13	1.90E+06 \pm 5.8E+04
ST14_10_CC_120/130					100	125	10	5.47E-12 \pm 1.68E-13	1.14E+06 \pm 3.5E+04
ST14_10_CC_150/170					72	160	30	5.86E-12 \pm 1.82E-13	1.17E+06 \pm 3.6E+04
Profile 2c** (P2c)									
BBA-1	-24.51496	-65.85931	2736	0.994	NA	5	10	2.79E-12 \pm 6.03E-14	2.27E+06 \pm 1.2E+05
BBA-2					NA	30	40	3.07E-12 \pm 6.63E-14	2.54E+06 \pm 5.5E+04
BBA-3					NA	107.5	15	7.21E-12 \pm 1.23E-13	5.81E+06 \pm 9.9E+04
BBA-4					NA	190	40	3.10E-12 \pm 5.52E-14	2.48E+06 \pm 4.5E+04
BBA-5					NA	142.5	55	2.48E-12 \pm 5.34E-14	1.95E+06 \pm 4.2E+04
BBA-6					NA	225	30	5.22E-13 \pm 1.17E-14	3.93E+05 \pm 9.2E+03
BBA-7					NA	65	30	1.62E-12 \pm 3.50E-14	1.37E+06 \pm 3.0E+04
Profile 4a* (P4a)									
ST14_13_CC_0	-24.50001	-65.86746	2835	0.996	75	0	1	8.77E-12 \pm 2.67E-13	6.72E+06 \pm 2.1E+05
ST14_13_CC_20/30					65	25	10	8.01E-12 \pm 2.44E-13	6.52E+06 \pm 2.0E+05
ST14_13_CC_50/60					60	55	10	6.72E-12 \pm 2.05E-13	4.34E+06 \pm 1.3E+05
ST14_13_CC_70/90					65	80	20	8.45E-12 \pm 2.58E-13	3.79E+06 \pm 1.2E+05
ST14_13_CC_120/130					65	125	10	8.53E-12 \pm 2.60E-13	2.65E+06 \pm 8.0E+04
ST14_13_CC_160/180					60	170	20	8.99E-12 \pm 2.74E-13	2.11E+06 \pm 6.5E+04
ST14_13_CC_300/350					65	325	50	4.56E-12 \pm 1.40E-13	8.86E+05 \pm 2.7E+04
Profile 4b* (P4b)									
ST14_04_CS_0	-24.5392	-65.85562	2824	0.990	sand	0	1	2.43E-12 \pm 7.62E-14	1.65E+06 \pm 5.2E+04
ST14_04_CS_20/30					sand	25	10	7.63E-12 \pm 2.33E-13	5.24E+06 \pm 1.6E+05
ST14_04_CS_40/50					sand	42.5	10	1.05E-11 \pm 3.19E-13	5.36E+06 \pm 1.6E+05
ST14_04_CS_57/70					sand	62.5	13	9.61E-12 \pm 2.93E-13	4.76E+06 \pm 1.5E+05
ST14_04_CS_80/90					sand	85	10	1.15E-11 \pm 3.49E-13	3.86E+06 \pm 1.2E+05
ST14_04_CS_110/120					sand	115	10	1.10E-11 \pm 3.36E-13	3.16E+06 \pm 9.6E+04
ST14_04_CS_150/170					sand	160	20	1.06E-11 \pm 3.22E-13	2.18E+06 \pm 6.7E+04
ST14_04_CS_300					sand	300	10	6.05E-12 \pm 1.85E-13	1.27E+06 \pm 3.9E+04
Profile 4c* (P4c)									
ST14_22_CC_0	-24.56282	-65.87173	2820	0.971	65	0	1	5.65E-12 \pm 1.73E-13	6.86E+06 \pm 3.67E+05

Appendix

Table C3 ^{10}Be and ^{26}Al blanks processed during sample preparation.

Blank name	Time of measurement	Measured $^{10}\text{Be}/^9\text{Be}$ ratio $\pm 1\sigma$ (analytical uncertainty)		AMS	Samples corrected with these blanks*
Be- blanks					
ST_Blkl	Mar 15	6.84E-15 \pm	1.09E-15	Cologne	P2a, P2b, P4a, P4b, P4c (surface samples only)
SS_Blkl6	Mar 15	6.90E-16 \pm	3.09E-16	Cologne	
ST_Blkl2	Apr 15	3.06E-15 \pm	5.96E-16	Cologne	
ST_Blkl3	Apr 15	1.95E-15 \pm	4.52E-16	Cologne	
ST_Blkl4	Apr 15	9.65E-15 \pm	1.12E-15	Cologne	
ST_Blkl5	May 16	5.11E-15 \pm	1.10E-15	Cologne	P4c (apart from surface samples), four Al-Be burial samples
SS_Blkl10	May 16	7.94E-16 \pm	3.98E-16	Cologne	
SS_Blkl11	May 16	9.25E-16 \pm	4.64E-16	Cologne	
Blank_2003	2004/ 2005	2.00E-14 \pm	5.0E-15	LLNL**	P2c, P4d, P6a, P6b

Blank name	Time of measurement	Measured $^{26}\text{Al}/^{27}\text{Al}$ ratio $\pm 1\sigma$ (analytical uncertainty)		AMS	Samples corrected with these blanks
Al-blank					
ST_Blkl5	May 16	1.23E-15 \pm	9.99E-16	Cologne	four Al-Be burial samples

* Samples were each corrected with a mean blank value of the according group.

** Lawrence Livermore National Laboratory

Table C4 Terrace surface ages calculated with the Monte Carlo depth profile simulator (Hidy et al., 2010) based on the 'St'-scaling-scheme. Gray shaded columns give chosen parameters, non-shaded columns are the model-run outcomes. Number of fits for each run $n = 50,000$. Each profile was run with and without taking inflation into account. *inf* = inflation corrected analysis.

'St'-scaling scheme										
Sample name	Confidence level	Total erosion threshold (cm)	Mean age (ka)	Minimum age (ka)	Maximum age (ka)	Bayesian most probable age (ka)	2 σ upper	2 σ lower	most probable inheritance ($10^4 \text{ atm} \cdot \text{g}^{-1}$)	Erosion rate (cm * ka)
P2a_top	chi 15	1- to 1	82.8	69.7	93.1	84.2	88.7	72	0.68	0
P2a_low	sigma 2	1- to 1	89.2	74	106.7	90.4	118.5	56.6	139.73	0
P2a_low_inf	chi 5	-40 to -45	69.5	51.3	88.7	65.8	90.5	44.3	142.47	-0.63
P2b	chi 60	-1 to 1	119.4	89.1	152.6	117.8	138.8	99	68.77	0
P2b_inf	chi 60	-22 to -20	116.5	85.6	150.9	115.1	134.9	95.2	67.26	-0.02
P4a	chi 20	-1 to 1	384.6	311	458.8	383.6	414.1	344.6	69.86	0
P4a_inf	chi 20	-20 to -25	336.8	277.5	398.8	339.7	362.8	303.6	69.86	-0.07
P4b	sigma 2	-1 to +1	386.7	355.5	443	380.1	427.3	342.3	108.9	0
P4b_inf	sigma 2	-40 to -30	314.3	286.3	359.6	315.1	346.5	278.3	107.53	-0.1
P4c	chi 15	1- to 1	464.4	409.9	597	473.3	533.7	419.1	71.64	0
P4c_inf	chi 20	30-50	356.6	292.8	480.3	359.6	420.2	322.8	69.86	-0.11
P4d	chi 25	-1 to +1	209	160.6	259.3	208.2	236.5	176.9	230.14	0
P4d_inf	chi 40	-40 to -30	156.1	100.4	227.1	158.9	180.1	132.4	224.66	-0.29
P6a	chi 60	-1 to +1	869.6	726.7	1197.5	969.9	1053.1	875.8	0	0
P6a_inf	chi 60	-40 to -30	734.5	583.3	1096.4	845.2	921.6	772.2	0	-0.02
P6b	chi 60	-1 to +1	516.3	417.9	670.8	535.6	574.7	496.2	27.4	0
P6b_inf	chi 60	-40 to -30	450.9	360.4	581.9	474	500	433.8	34.25	-0.05

Appendix

Table C5 Terrace surface ages based on the depth profiles. Ages were calculated with the Monte Carlo simulator (Hidy et al., 2010) based on the calculated 'Lm'-scaling-scheme. Settings are the same as for the 'St' scaling-scheme runs. Number of fits for each run $n = 50,000$. Each profile was run with and without taking inflation into account. *inf* = inflation corrected analysis.

'Lm'-scaling scheme								
Sample name	Mean age (ka)	Minimum age (ka)	Maximum age (ka)	Bayesian most probable age (ka)	2 σ upper	2 σ lower	most probable inheritance ($10^4 \text{ atm} \cdot \text{g}^{-1}$)	Erosion rate ($\text{cm} \cdot \text{kyr}$)
P2a_top	73.7	61.6	82.2	75.3	78.9	64	0	0
P2a_low	76.9	62.8	92	78.1	102.6	47.5	139.73	0
P2a_low_inf	60.1	44.5	77.6	57.5	79.5	41.4	142.47	-0.63
P2b	104.3	77.9	134	104.1	120.4	85.9	67.12	0.01
P2b_inf	94.5	69.6	119.1	93.2	109.3	77.3	67.53	-0.22
P4a	325.3	264.4	386.2	318.5	349.3	291.7	69.86	0
P4a_inf	285.4	236	338.2	282.2	306.6	257.6	69.86	-0.07
P4b	327.3	301.3	375.4	326.7	361.9	300.5	107.53	0
P4b_inf	267.7	243.4	307.2	265.8	294.6	237	106.16	-0.12
P4c	398.8	352.8	500	411	454	360.4	71.67	0
P4c_inf	301.7	249.4	408.8	306.8	352.7	272.7	69.86	-0.1
P4d	161.9	123.4	199.2	164.4	181.6	135.9	230.14	0
P4d_inf	125.3	90.2	174.8	120.5	138.2	101.8	230.14	-0.39
P6a	659.7	552.5	932.3	731.5	787	664	0	0
P6a_inf	556.3	445.9	842.5	643.8	680.5	582.8	0	-0.04
P6b	390.7	318.4	500.6	405.5	431.7	373.7	20.55	0
P6b_inf	336.7	273.8	426.3	357.5	371.9	323.6	27.4	-0.07

Appendix

Table C6 Comparison of muogenic and spallogenic production rates. Muogenic surface production rates are calculated by the Monte Carlo simulator (Hidy et al., 2010). Spallation production rates are compared for the St, Lm and LSD scaling schemes and are calculated based on the Monte Carlo simulator, the CRONUS Earth calculator V2.2 (Balco et al., 2008) and the CREp calculator (Martin et al., 2016). The site-specific production rates based on the St-scaling scheme differ slightly between the Monte Carlo simulator and the CRONUS Earth Calculator due to rounding errors. We implemented the NCEP atmospheric reanalysis data product (http://www.esrl.noaa.gov/psd/data/ncep_reanalysis/) used in the CRONUS Earth calculator in the Monte Carlo simulator to allow back-and-forth calculations of production rates. For the final age calculations the Lm-scaling scheme based production rates (highlighted in gray) were used. The CREp based calculations are only displayed for comparison. These calculations are based on the LSD scaling scheme (Lifton et al., 2014), the ERA 40 atmospheric model (Uppala et al., 2005) and the LSD geomagnetic database (Lifton et al., 2014). For a reference production rate we used the regional average of northern South America ($4.03 \pm 0.14 \text{ atm} \cdot \text{g}^{-1} \cdot \text{yr}^{-1}$; <http://crep.cprg.cnrs-nancy.fr/#/init>). inf = inflation corrected analysis. For P4d, P6a and P6b we used the KNSTD, for all other samples the 07KNSTD Be AMS standard.

Sample name	Muonic production ($\text{atm} \cdot \text{g}^{-1} \cdot \text{yr}^{-1}$)	Spallation production				scaling factor	spallation production rate ($\text{atm} \cdot \text{g}^{-1} \cdot \text{yr}^{-1}$)
		Monte Carlo simulator 'St' scaling scheme* NCEP atm. model ($\text{atm} \cdot \text{g}^{-1} \cdot \text{yr}^{-1}$)	CRONUS calculator 'St' scaling scheme NCEP atm. model ($\text{atm} \cdot \text{g}^{-1} \cdot \text{yr}^{-1}$)	CRONUS calculator 'Lm' scaling scheme** NCEP atm. model ($\text{atm} \cdot \text{g}^{-1} \cdot \text{yr}^{-1}$)	CREp calculator LSD scaling scheme*** ERA 40 atm. model LSD geomagnetic database		
P2a_top	0.437	20.52	20.6	24.05	5.74	23.13	
P2a_low	0.437	20.52	20.6	24.03	5.78	23.29	
P2a_low_inf	0.428	19.57	19.73	22.18	5.41	21.80	
P2b	0.422	19.09	19.2	21.92	5.31	21.40	
P2b_inf	0.422	19.09	19.2	21.57	5.23	21.08	
P4a	0.437	20.52	20.6	24.05	5.74	23.13	
P4a_inf	0.437	20.52	20.6	24.03	5.78	23.29	
P4b	0.436	20.29	20.49	23.91	5.72	23.05	
P4b_inf	0.436	20.29	20.49	23.80	5.71	23.01	
P4c	0.435	19.86	20.45	23.49	5.56	22.41	
P4c_inf	0.435	19.86	20.45	23.89	5.73	23.09	
P4d	0.444	20.91	20.96	26.98	5.84	23.54	
P4d_inf	0.444	20.91	20.96	27.25	5.89	23.74	
P6a	0.435	20.55	20.68	26.12	5.60	22.57	
P6a_inf	0.435	20.55	20.68	26.31	5.50	22.17	
P6b	0.537	30.07	30.78	39.63	8.56	34.50	
P6b_inf	0.537	30.07	30.78	40.14	8.71	35.10	

* Time-independent scaling-scheme by (Lal, 1991), modified by (Stone, 2000)

** Lal/Stone scaling scheme including paleomagnetic corrections described by (Nishiizumi et al., 1989)

*** Scaling-scheme correcting for variability in geomagnetic strength and solar input (Lifton et al., 2014)

Table C7 Terrace surface ages based on the surface-pebbles samples. Ages were calculated using the CRONUS Earth calculator v2.2. Sample thickness varies between 2 cm (P2b, P4a, P4c) and 10 cm (P4d, P6a, P6b), depending on the original sampling strategy. We assumed a sample density of the quartz clasts of $2.6 \text{ g} \cdot \text{cm}^{-3}$ and an erosion rate of $0 \text{ cm} \cdot \text{yr}^{-1}$. Be AMS standards are 07KNSTD for P2b, P4a and P4c and KNSTD for P4d, P6a, P6b, respectively. The reference production rate was obtained from Blard et al., 2013. We performed two calculations for the surface sample derived from P4d; one with the calculated inheritance from P4d (P4d_surf_4d) and one with the calculated inheritance from P4a (P4d_surf_4a), which is located on the same terrace level and received material from the same catchment.

Sample name	Surface sample conc. ($\text{atm} \cdot \text{g}^{-1}$)	Most probable inheritance ($\text{atm} \cdot \text{g}^{-1}$)	^{10}Be atoms accumulated since exposure ($\text{atm} \cdot \text{g}^{-1}$)	Thickness scaling factor	Shielding factor	Production rate muons ($\text{atm} \cdot \text{g}^{-1} \cdot \text{yr}^{-1}$)	Internal uncertainty (ka)	Lm – time-dep. exposure age (ka)	External uncertainty (ka)
P2b_surf	6.86E+06	7.16E+05	6.14E+06	0.9839	0.9714	0.431	21.96	283.72	26.11
P2c_surf	2.27E+06	3.93E+05	1.87E+06	0.923	0.9942	0.41	6.32	84.77	7.69
P4a_surf	6.72E+06	6.99E+05	6.02E+06	0.9839	0.9963	0.432	12.47	269.13	20.39
P4c_surf	2.99E+06	6.71E+05	2.31E+06	0.9839	0.9944	0.418	7.04	107.88	9.07
P4d_surf_4d	6.91E+06	2.30E+06	4.61E+06	0.923	0.9976	0.425	9.19	190.19	14.38
P4d_surf_4a	6.91E+06	6.99E+05	6.21E+06	0.923	0.9976	0.425	5.73	262.61	17.70
P6a_surf	1.16E+07	1.17E+06	1.05E+07	0.923	0.994	0.422	5.83	487.45	33.86
P6b_surf	1.47E+07	2.06E+05	1.45E+07	0.923	0.9769	0.512	14.64	452.78	33.20

Table C8 Raw data of volcanic ash zircon grains.

Sample / grain	Concentrations (ppm)				Isotope ratios						Isotopic age (Ma)						
	Pb	U	Th	Th/U	$^{207}\text{Pb}/^{206}\text{Pb}$	^{26}Th (%)	$^{238}\text{U}/^{206}\text{Pb}$	^{26}Th (%)	$^{207}\text{Pb}/^{235}\text{U}$	^{26}Th (%)	$^{206}\text{Pb}/^{238}\text{U}$	^{26}Th (%)		Rho	^{207}Pb and $^{206}\text{Pb}/^{238}\text{U}$ corrected age	^{26}Th abs.	
Ash1 (QT020314-1): 24.52790 σ_8 ; 65.85910 σ_W ; z = 2865m																	
MIQAA_47	0.1	606	603	0.989	0.11	40.58	31948.88	0.47	0.0004	41.18	0.0000	7.03	0.17	0.262	0.024		w.m.
MIQAA_36	0.0	151	97	0.638	0.26	46.16	20161.29	1.96	0.0015	48.26	0.0000	14.07	0.29	0.299	0.048		$\pm 1\sigma$
MIQAA_3	0.3	1730	525	0.303	0.06	7.54	7788.16	0.06	0.0010	8.08	0.0001	2.92	0.36	0.913	0.045		$\pm 2\sigma$
MIQAA_45	0.4	760	346	0.456	0.10	14.74	5324.81	0.07	0.0028	15.07	0.0002	3.15	0.21	1.214	0.062		MISWD
MIQAA_31	0.6	1126	803	0.717	0.06	9.71	4875.67	0.05	0.0017	10.10	0.0002	2.80	0.28	1.384	0.066		n
MIQAA_27	0.6	1013	500	0.498	0.05	6.02	2787.07	0.04	0.0026	6.57	0.0004	2.62	0.40	2.388	0.110		
MIQAA_17	1.2	707	1038	1.474	0.06	7.01	2678.81	0.05	0.0029	7.56	0.0004	2.83	0.37	2.442	0.118		
MIQAA_13	0.4	291	198	0.679	0.06	10.30	1730.10	0.08	0.0047	10.79	0.0006	3.21	0.30	3.749	0.195		
MIQAA_16	0.4	250	115	0.464	0.10	9.08	1602.56	0.06	0.0091	9.55	0.0006	2.96	0.31	3.813	0.189		
MIQAA_5	0.4	274	136	0.498	0.05	8.23	1216.55	0.06	0.0057	8.72	0.0008	2.86	0.33	5.354	0.260		
MIQAA_2	0.6	283	154	0.542	0.07	7.81	1121.08	0.04	0.0084	8.24	0.0009	2.62	0.32	5.665	0.262		
MIQAA_25	0.7	409	234	0.576	0.05	5.63	1038.42	0.03	0.0066	6.16	0.0010	2.50	0.41	6.261	0.282		
MIQAA_7	0.6	510	112	0.220	0.05	4.95	675.68	0.05	0.0105	5.63	0.0015	2.70	0.48	9.567	0.449		
MIQAA_38	0.8	393	176	0.448	0.05	5.53	668.45	0.04	0.0094	6.09	0.0015	2.56	0.42	9.732	0.444		
MIQAA_4	0.6	350	128	0.366	0.05	5.45	662.69	0.05	0.0100	6.09	0.0015	2.72	0.45	9.787	0.462		
MIQAA_11	1.5	509	334	0.658	0.05	2.30	662.69	0.05	0.0096	3.56	0.0015	2.72	0.76	9.793	0.462		
MIQAA_12	0.8	415	151	0.367	0.05	3.64	659.20	0.03	0.0102	4.42	0.0015	2.52	0.57	9.837	0.444		
MIQAA_23	1.1	345	144	0.421	0.08	4.19	627.35	0.03	0.0179	4.84	0.0016	2.41	0.50	9.903	0.437		
MIQAA_48	1.1	566	237	0.415	0.05	3.53	649.35	0.03	0.0101	4.29	0.0015	2.44	0.57	9.999	0.444		
MIQAA_18	1.1	451	254	0.566	0.05	3.15	645.99	0.03	0.0107	4.02	0.0015	2.50	0.62	10.009	0.450		
MIQAA_20	0.7	362	138	0.382	0.05	5.54	645.99	0.04	0.0101	6.11	0.0015	2.57	0.42	10.047	0.459		
MIQAA_32	0.8	433	184	0.428	0.05	4.24	630.91	0.03	0.0108	4.85	0.0016	2.36	0.49	10.273	0.448		
MIQAA_21	2.8	580	347	0.602	0.09	4.62	595.59	0.03	0.0203	5.24	0.0017	2.48	0.47	10.316	0.462		
MIQAA_14	1.1	459	224	0.492	0.05	4.48	627.35	0.05	0.0105	5.29	0.0016	2.82	0.53	10.334	0.498		
MIQAA_29	0.4	180	68	0.381	0.05	8.43	613.12	0.04	0.0116	8.83	0.0016	2.64	0.30	10.530	0.488		
MIQAA_41	1.3	593	212	0.360	0.05	5.17	610.50	0.04	0.0121	5.80	0.0016	2.63	0.45	10.551	0.489		
MIQAA_37	1.5	641	279	0.435	0.05	3.14	566.57	0.03	0.0114	3.96	0.0018	2.41	0.61	11.448	0.505		
MIQAA_6	1.0	283	102	0.361	0.06	3.84	547.95	0.07	0.0139	4.97	0.0018	3.16	0.64	11.691	0.603		
MIQAA_10	0.8	444	140	0.320	0.05	4.01	547.05	0.03	0.0116	4.71	0.0018	2.48	0.53	11.866	0.531		
MIQAA_35	1.5	541	251	0.466	0.06	2.90	507.61	0.03	0.0150	3.80	0.0020	2.45	0.65	12.637	0.563		
MIQAA_50	1.8	371	309	0.831	0.05	4.04	510.20	0.04	0.0134	4.82	0.0020	2.63	0.55	12.666	0.586		
MIQAA_8	2.1	1338	321	0.243	0.05	1.87	481.46	0.06	0.0138	3.49	0.0021	2.95	0.85	13.427	0.665		
MIQAA_26	1.0	526	158	0.303	0.05	3.75	479.16	0.03	0.0135	4.50	0.0021	2.49	0.55	13.522	0.607		
MIQAA_30	0.7	210	109	0.521	0.05	5.78	467.29	0.03	0.0145	6.27	0.0021	2.43	0.39	13.818	0.612		
MIQAA_42	1.7	646	255	0.395	0.05	2.59	444.44	0.03	0.0144	3.53	0.0023	2.40	0.68	14.584	0.641		
MIQAA_33	1.7	697	256	0.369	0.05	2.71	437.64	0.03	0.0151	3.69	0.0023	2.50	0.68	14.782	0.665		

M1QA4_34	1.6	738	169	0.230	0.05	2.29	333.22	0.05	0.0203	3.58	0.0030	2.74	0.77	19.360	0.918	+
M1QA4_24	4.9	229	234	1.035	0.05	3.55	149.93	0.04	0.0428	4.44	0.0067	2.67	0.60	42.910	2.004	+
M1QA4_15	10.5	346	106	0.311	0.13	1.06	22.43	0.04	0.7740	2.77	0.0446	2.56	0.92	255.239	11.631	+
M1QA4_43	14.8	204	64	0.314	0.06	1.19	13.07	0.04	0.6040	2.88	0.0765	2.62	0.91	474.772	21.942	+
M1QA4_44	7.2	430	29	0.067	0.06	1.14	12.76	0.03	0.6220	2.71	0.0784	2.46	0.91	486.122	21.668	+
M1QA4_9	21.9	114	88	0.773	0.06	1.36	12.24	0.03	0.6476	2.74	0.0817	2.37	0.87	505.328	22.093	+
M1QA4_40	15.7	218	66	0.302	0.06	1.17	12.15	0.04	0.6631	2.81	0.0823	2.56	0.91	509.190	23.203	+
M1QA4_1	8.1	100	32	0.322	0.06	1.23	11.88	0.04	0.6650	2.95	0.0842	2.68	0.91	520.590	24.358	+
M1QA4_49	52.1	332	200	0.602	0.06	1.13	11.78	0.04	0.6800	2.84	0.0849	2.60	0.92	524.972	24.145	+
M1QA4_46	15.1	138	53	0.379	0.06	1.41	11.74	0.04	0.6760	2.95	0.0852	2.60	0.88	527.104	24.226	+
M1QA4_39	19.0	305	62	0.204	0.06	1.09	11.53	0.04	0.7330	2.80	0.0867	2.58	0.92	533.886	24.456	+
M1QA4_19	45.2	324	163	0.508	0.06	1.08	11.15	0.04	0.7100	2.83	0.0897	2.62	0.92	554.016	25.578	+
M1QA4_28	51.4	394	190	0.485	0.06	1.08	10.59	0.05	0.7590	3.03	0.0944	2.84	0.94	582.273	28.163	+
M1QA4_22	11.9	229	22	0.098	0.07	1.08	6.42	0.03	1.5290	2.72	0.1557	2.50	0.92	931.112	41.864	+

<i>ASh2 (ST14_05_Ash): 24.53920 °S; 65.85562 °W; Elevation = 2824 m</i>																
	0.076	374	172	0.4539	0.1540	18.20	17730.50	3.24	0.0012	18.48	0.0001	3.24	0.18	0.41	0.04	Max. age
	0.132	670	473	0.7117	0.0880	11.39	17699.12	3.40	0.0007	11.88	0.0001	3.40	0.29	0.43	0.04	±1s
	0.195	2980	573	0.1904	0.0714	5.23	12953.37	1.96	0.0008	5.59	0.0001	1.96	0.35	0.58	0.04	±2s
	0.126	269	195	0.7294	0.1180	17.81	9487.67	4.43	0.0018	18.35	0.0001	4.43	0.24	0.70	0.05	MISWD
	0.079	233	151	0.6390	0.0640	25.01	9115.77	4.10	0.0010	25.34	0.0001	4.10	0.16	0.78	0.05	n
	0.270	434	287	0.6662	0.1208	7.32	6045.95	2.59	0.0027	7.76	0.0002	2.59	0.33	1.05	0.04	2/60
	0.516	1153	549	0.4836	0.0690	4.69	4486.32	1.64	0.0021	4.97	0.0002	1.64	0.33	1.49	0.04	
	0.196	272	132	0.4762	0.0940	18.10	3367.00	4.21	0.0038	18.58	0.0003	4.21	0.23	1.89	0.09	
	0.609	1195	598	0.3965	0.0519	5.06	3314.94	1.77	0.0021	5.36	0.0003	1.77	0.33	1.91	0.05	
	0.167	222	104	0.4721	0.0528	13.65	2361.83	1.82	0.0031	13.78	0.0004	1.82	0.13	2.80	0.07	
	0.540	361	175	0.4888	0.0781	5.71	1647.45	2.45	0.0043	6.21	0.0006	2.45	0.40	3.98	0.10	
	0.211	234	91	0.3908	0.0512	5.30	1544.64	1.80	0.0070	5.59	0.0006	1.80	0.32	4.09	0.08	
	1.712	470	612	1.3172	0.0915	10.52	1445.09	2.35	0.0088	10.78	0.0007	2.35	0.22	4.26	0.12	
	0.651	416	268	0.6468	0.0564	7.48	1483.68	2.27	0.0052	7.82	0.0007	2.27	0.29	4.37	0.11	
	0.417	307	149													
	0.176	4730	69	0.0142	0.0507	1.51	1421.26	1.67	0.0049	2.26	0.0007	1.67	0.74	4.62	0.08	
	0.852	692	316	0.4505	0.0476	3.23	1394.70	2.17	0.0047	3.89	0.0007	2.17	0.56	4.70	0.11	
	1.773	948	572	0.6046	0.0483	3.18	1146.39	1.64	0.0058	3.58	0.0009	1.64	0.46	5.69	0.10	
	1.396	808	441	0.5476	0.0482	3.60	1061.57	1.83	0.0063	4.03	0.0009	1.83	0.45	6.14	0.12	
	1.200	844	358	0.4198	0.0475	3.44	1029.87	1.72	0.0064	3.85	0.0010					
	2.076	1322	551	0.4212	0.0495	2.91	870.32	1.84	0.0080	3.45	0.0011					
	0.328	157	82	0.5233	0.0481	8.53	846.74	2.43	0.0077	8.88	0.0012					
	1.056	1001	244	0.2488	0.0481	2.19	847.46									
	0.372	127	73	0.5790	0.0531	5.88	672.04									
	0.284	171	50	0.2941	0.0509	5.94	627.35									
	1.205	336	223	0.6734												
	0.688	277	127	0.4610												
	1.045	458	192	0.4082												

ST14-5-37	0.739	451	133	0.2975	0.0473	2.23	603.50	2.07	0.0108	3.04	0.0017	2.07	0.68	10.76	0.22	+
ST14-5-54	0.967	580	167	0.2908	0.0481	1.94	602.77	2.02	0.0109	2.80	0.0017	2.02	0.72	10.76	0.22	+
ST14-5-32	1.106	924	212	0.2298	0.0481	1.77	601.32	1.74	0.0111	2.48	0.0017	1.74	0.70	10.79	0.19	+
ST14-5-14	0.749	261	127	0.4852	0.0492	4.73	598.44	1.92	0.0115	5.10	0.0017	1.92	0.38	10.81	0.21	+
ST14-5-12	0.888	698	152	0.2188	0.0474	2.42	597.01	1.65	0.0111	2.93	0.0017	1.65	0.56	10.87	0.18	+
ST14-5-56	0.980	306	126	0.4115	0.0617	12.98	579.71	1.97	0.0148	13.13	0.0017	1.97	0.15	10.99	0.24	+
ST14-5-36	1.063	716	184	0.2571	0.0485	2.57	588.58	1.68	0.0115	3.07	0.0017	1.68	0.55	11.01	0.19	+
ST14-5-9	0.810	715	137	0.1961	0.0498	2.70	587.54	1.81	0.0116	3.25	0.0017	1.81	0.56	11.01	0.20	+
ST14-5-28	1.118	476	182	0.3798	0.0487	3.16	584.45	2.37	0.0115	3.95	0.0017	2.37	0.60	11.08	0.26	+
ST14-5-15	0.615	621	106	0.1695	0.0476	2.10	585.14	2.13	0.0114	2.99	0.0017	2.13	0.71	11.09	0.24	+
ST14-5-22	0.952	259	160	0.6173	0.0485	4.59	565.61	1.73	0.0120	4.90	0.0018	1.73	0.35	11.44	0.20	+
ST14-5-16	1.722	662	289	0.4255	0.0457	2.22	564.97	1.90	0.0112	2.92	0.0018	1.90	0.65	11.50	0.22	+
ST14-5-38	1.428	740	226	0.3082	0.0476	1.84	546.45	1.66	0.0120	2.48	0.0018	1.66	0.67	11.86	0.20	+
ST14-5-19	4.049	292	668	2.2472	0.0493	3.92	540.54	2.02	0.0128	4.41	0.0019	2.02	0.46	11.90	0.24	+
ST14-5-52	6.600	1181	1034	0.8842	0.0472	1.81	535.91	1.76	0.0122	2.53	0.0019	1.76	0.70	12.08	0.21	+
ST14-5-40	1.030	265	140	0.5297	0.0491	3.73	482.63	2.03	0.0138	4.25	0.0021	2.03	0.48	13.39	0.27	+
ST14-5-55	2.412	409	313	0.7692	0.0474	2.22	465.33	2.18	0.0141	3.11	0.0021	2.18	0.70	13.90	0.30	+
ST14-5-39	1.042	376	140	0.3762	0.0475	3.85	464.47	1.49	0.0141	4.13	0.0022	1.49	0.36	13.94	0.21	+
ST14-5-43	1.132	291	155	0.5350	0.0477	2.81	455.17	1.89	0.0144	3.39	0.0022	1.89	0.56	14.21	0.27	+
ST14-5-41	1.686	369	215	0.5831	0.0469	2.65	429.92	2.39	0.0151	3.57	0.0023	2.39	0.67	15.05	0.36	+
ST14-5-59	2.698	723	305	0.4216	0.0470	1.92	413.91	1.76	0.0154	2.60	0.0024	1.76	0.68	15.64	0.28	+
ST14-5-26	0.445	145	41	0.2786	0.0498	3.29	324.46	2.23	0.0214	3.97	0.0031	2.23	0.56	19.85	0.44	+
ST14-5-44	0.242	662	31	0.0457	0.0485	1.19	86.88	2.33	0.0776	2.62	0.0115	2.33	0.89	73.78	1.71	+
ST14-5-13	42.400	819	175	0.2110	0.0579	0.84	13.15	1.69	0.6107	1.88	0.0760	1.69	0.89	471.76	7.78	+
ST14-5-35	16.970	91	63	0.6906	0.0596	1.09	11.89	1.96	0.6940	2.24	0.0841	1.96	0.87	519.46	9.93	+
ST14-5-30	12.720	134	48	0.3570	0.0581	1.01	11.68	1.85	0.6910	2.10	0.0856	1.85	0.88	529.47	9.54	+
ST14-5-45	29.500	235	105	0.4405	0.0580	0.89	11.66	1.93	0.6880	2.13	0.0858	1.93	0.91	534.31	9.58	+
ST14-5-48	11.900	179	40	0.2075	0.0581	0.93	11.57	1.84	0.6875	2.06	0.0864	1.84	0.89	548.81	9.23	+
ST14-5-29	17.770	230	65	0.2818	0.0590	0.82	11.25	1.72	0.7253	1.91	0.0889	1.72	0.90	548.81	9.23	+
ST14-5-27	23.080	537	140	0.2565	0.1387	0.83	8.50	2.97	2.2630	3.09	0.1176	2.97	0.96	652.88	18.81	+
ST14-5-17	38.320	221	68	0.3071	0.0758	0.83	5.68	1.54	1.8500	1.75	0.1760	1.54	0.88	1043.19	15.51	+
ST14-5-42	18.950	22	20	0.9132	0.1070	0.99	3.22	1.76	4.6330	2.02	0.3103	1.76	0.87	1741.47	30.00	+

AsH3 (ST14_24_Ash): 24.55477 °S; 65.87158 °W; Elevation: 2696 m

ST14-24-8	0.177	331	471	1.3004	0.4670	8.81	26525.20	8.84	0.0025	12.48	0.0000	8.84	0.71	0.18	0.04	0.218
ST14-24-40	0.221	159	267	1.6474	0.6310	13.01	11976.05	10.96	0.0076	17.02	0.0001	10.96	0.64	0.19	0.07	0.007
ST14-24-11	0.460	160	108	0.6711	0.7560	9.02	5988.02	30.56	0.0177	31.87	0.0002	30.56	0.96	0.19	0.10	0.014
ST14-24-22	0.489	560	1183	2.1053	0.4970	10.29	17211.70	13.14	0.0041	16.68	0.0001	13.14	0.79	0.19	0.05	0.05
ST14-24-21	0.486	1039	3909	3.7383	0.0780	16.68	27624.31	3.53	0.0004	17.05	0.0000	3.53	0.21	0.20	0.04	0.04
ST14-24-3	0.029	173	134	0.7663	0.2600	76.93	39682.54	14.73	0.0007	78.32	0.0000	14.73	0.19	0.20	0.06	0.06
ST14-24-52	0.054	297	358	1.1960	0.1530	52.95	39215.69	9.88	0.0006	53.86	0.0000	9.88	0.18	0.21	0.04	0.04
ST14-24-9	0.165	762	1407	1.8474	0.0670	31.35	35087.72	4.38	0.0003	31.66	0.0000	4.38	0.14	0.22	0.04	0.04
ST14-24-45	0.190	318	375	1.1876	0.4360	11.95	20964.36	7.02	0.0028	13.86	0.0000	7.02	0.51	0.23	0.04	0.04
ST14-24-54	0.020	174	87	0.4909	0.1500	113.34	41152.26	12.81	0.0002	114.06	0.0000	12.81	0.11	0.23	0.05	0.05
ST14-24-35	0.111	467	870	1.3699	0.1260	30.96	33783.78	6.20	0.0005	31.57	0.0000	6.20	0.20	0.23	0.04	0.04

ST14-24-14	0.057	269	385	1.4124	0.1200	47.51	32786.89	6.99	0.0005	48.02	0.0000	6.99	0.15	0.24	0.04	+
ST14-24-37	0.139	1531	859	0.5634	0.1520	26.33	37453.18	3.75	0.0005	26.59	0.0000	3.75	0.14	0.24	0.04	+
ST14-24-28	0.285	960	663	0.6930	0.2810	11.76	24330.90	5.72	0.0015	13.08	0.0000	5.72	0.44	0.27	0.04	+
ST14-24-50	0.241	650	1457	2.2371	0.1000	14.02	23809.52	3.32	0.0006	14.41	0.0000	3.32	0.23	0.28	0.04	+
ST14-24-34	0.026	99	105	1.0650	0.1000	170.00	26595.74	12.29	0.0005	170.45	0.0000	12.29	0.07	0.30	0.07	+
ST14-24-17	1.324	228	176	0.7740	0.7490	4.20	3215.43	3.73	0.0335	5.62	0.0003	3.73	0.66	0.30	0.09	+
ST14-24-36	0.319	109	206	1.8839	0.6290	13.69	6024.10	24.13	0.0152	27.74	0.0002	24.13	0.87	0.32	0.14	+
ST14-24-47	0.130	1224	729	0.5992	0.0840	13.11	26246.72	2.37	0.0004	13.33	0.0000	2.37	0.18	0.32	0.04	+
ST14-24-55	0.184	1354	859	0.6227	0.0932	9.90	23562.68	2.46	0.0005	10.20	0.0000	2.46	0.24	0.34	0.04	+
ST14-24-1	0.174	437	456	1.0246	0.2100	15.73	18621.97	8.10	0.0016	17.69	0.0001	8.10	0.46	0.35	0.04	+
ST14-24-2	0.057	307	143	0.4389	0.1770	19.79	20876.83	5.56	0.0011	20.55	0.0000	5.56	0.27	0.35	0.04	+
ST14-24-53	0.018	50	39	0.7599	0.1400	321.43	20000.00	26.03	0.0006	322.48	0.0001	26.03	0.08	0.37	0.20	+
ST14-24-20	0.853	361	234	0.6485	0.6020	3.56	6337.14	4.47	0.0131	5.72	0.0002	4.47	0.78	0.39	0.05	+
ST14-24-5	0.420	340	224	0.6549	0.0863	10.11	2443.79	2.31	0.0048	10.37	0.0004	2.31	0.22	2.59	0.07	+
ST14-24-13	0.776	436	533	1.2077	0.0616	7.18	2466.09	1.74	0.0035	7.38	0.0004	1.74	0.24	2.63	0.06	+
ST14-24-27	1.636	903	743	0.8230	0.0536	3.80	1588.06	1.66	0.0047	4.14	0.0006	1.66	0.40	4.10	0.08	+
ST14-24-10	0.900	625	246	0.3871	0.0850	14.13	1515.15	2.44	0.0079	14.34	0.0007	2.44	0.17	4.14	0.12	+
ST14-24-26	0.824	289	101	0.3479	0.1603	3.14	1353.73	1.76	0.0162	3.60	0.0007	1.76	0.49	4.17	0.09	+
ST14-24-44	0.750	503	303	0.6059	0.0625	9.94	1464.99	1.53	0.0059	10.06	0.0007	1.53	0.15	4.39	0.08	+
ST14-24-4	0.405	243	132	0.5294	0.0476	6.55	1117.32	1.88	0.0058	6.82	0.0009	1.88	0.28	5.85	0.12	+
ST14-24-16	1.393	701	459	0.6523	0.0483	2.98	1023.33	1.34	0.0065	3.27	0.0010	1.34	0.41	6.36	0.09	+
ST14-24-18	3.052	425	841	1.9685	0.0690	14.51	882.61	2.06	0.0109	14.66	0.0011	2.06	0.14	7.13	0.18	+
ST14-24-60	1.463	466	413	0.8913	0.0488	3.35	862.66	1.39	0.0078	3.63	0.0012	1.39	0.38	7.52	0.11	+
ST14-24-7	0.335	190	90	0.4715	0.0476	5.92	862.07	1.70	0.0074	6.16	0.0012	1.70	0.28	7.55	0.13	+
ST14-24-24	0.812	288	222	0.7669	0.0479	5.47	838.93	1.46	0.0079	5.67	0.0012	1.46	0.26	7.74	0.12	+
ST14-24-33	2.109	1469	587	0.4034	0.0466	1.99	820.41	1.34	0.0078	2.40	0.0012	1.34	0.56	7.94	0.16	+
ST14-24-41	1.213	529	282	0.5348	0.0470	6.41	638.98	1.46	0.0109	6.58	0.0016	1.46	0.22	10.13	0.18	+
ST14-24-51	9.570	1528	192	1.3055	0.0463	2.19	620.31	1.35	0.0103	2.57	0.0016	1.35	0.52	10.44	0.14	+
ST14-24-42	1.520	528	306	0.5865	0.0535	9.93	607.90	1.51	0.0121	10.04	0.0016	1.51	0.15	10.59	0.18	+
ST14-24-48	0.950	453	182	0.4026	0.0459	3.13	613.50	1.38	0.0103	3.42	0.0016	1.38	0.40	10.60	0.15	+
ST14-24-46	0.960	467	183	0.3948	0.0467	4.13	608.38	1.30	0.0106	4.33	0.0016	1.30	0.30	10.68	0.14	+
ST14-24-23	3.290	373	216	0.5821	0.1550	9.06	516.26	2.85	0.0417	9.50	0.0019	2.85	0.30	10.85	0.38	+
ST14-24-39	0.840	210	165	0.7610	0.0483	4.20	594.88	1.37	0.0109	4.42	0.0017	1.37	0.31	10.88	0.15	+
ST14-24-19	1.161	383	240	0.6219	0.0679	6.52	558.35	1.88	0.0169	6.78	0.0018	1.88	0.28	11.31	0.22	+
ST14-24-59	1.158	164	137	0.8347	0.0958	5.47	518.94	1.73	0.0256	5.74	0.0019	1.73	0.30	11.71	0.22	+
ST14-24-31	3.323	649	523	0.8026	0.0467	2.25	471.70	1.39	0.0137	2.65	0.0021	1.39	0.53	13.72	0.19	+
ST14-24-30	1.972	444	299	0.6653	0.0474	2.83	464.25	1.39	0.0140	3.15	0.0022	1.39	0.44	13.94	0.20	+
ST14-24-25	2.170	362	313	0.8511	0.0489	2.55	456.41	1.43	0.0148	2.92	0.0022	1.43	0.49	14.14	0.20	+
ST14-24-57	1.416	370	206	0.5977	0.0474	2.63	452.16	1.27	0.0144	2.92	0.0022	1.27	0.43	14.31	0.18	+
ST14-24-58	1.271	219	182	0.8292	0.0474	3.86	446.03	1.40	0.0146	4.11	0.0022	1.40	0.34	14.50	0.21	+
ST14-24-56	1.712	269	244	0.9025	0.0463	4.38	439.75	1.37	0.0146	4.59	0.0023	1.37	0.30	14.72	0.21	+
ST14-24-29	1.090	176	93	0.5316	0.0791	9.38	419.82	2.00	0.0261	9.59	0.0024	2.00	0.21	14.79	0.33	+
ST14-24-49	0.191	76	25	0.3307	0.0441	9.32	439.17	1.88	0.0137	9.51	0.0023	1.88	0.20	14.80	0.29	+
ST14-24-12	6.860	130	146	1.0965	0.3050	5.62	170.36	3.45	0.2520	6.59	0.0059	3.45	0.52	25.50	1.20	+

Appendix

ST14-24-32	1203	185	93	0.5013	0.0514	6.65	213.68	4.23	0.0328	7.88	0.0047	4.23	0.54	30.01	1.27	+
ST14-24-43	46370	244	195	0.7981	0.0580	0.81	12.12	1.29	0.6525	1.52	0.0825	1.29	0.85	510.73	6.42	+
ST14-24-38	47,800	195	170	0.8658	0.0644	1.31	11.26	1.45	0.7820	1.95	0.0888	1.45	0.74	544.80	7.75	+
ST14-24-6	19950	155	67	0.4325	0.0657	0.86	11.15	1.30	0.8056	1.56	0.0897	1.30	0.83	549.20	7.00	+